The University Of Sheffield.

HR-pQCT scanning of the human calcaneus

Early development and validation of assessment of calcaneal trabecular microstructure

By:

Louis Michael Metcalf

A thesis submitted in partial fulfilment of the requirements for the degree of Doctor of Philosophy

The University of Sheffield
Faculty of Medicine, Dentistry and Health
Department of Oncology and Metabolism

Submission Date: March 2018

Contents

Thesis abstract

Non-invasive assessments of the calcaneus, by techniques such as quantitative ultrasound (QUS) and dual x-ray absorptiometry (DXA), have been used as predictors of fracture risk assessment and to monitor the response to mechanical loading and treatments for osteoporosis. However, these current devices lack the sensitivity to measure microstructural changes in the bone. High-resolution peripheral quantitative computer tomography (HR-pQCT) has been specifically developed to provide volumetric bone mineral density (vBMD), geometry, trabecular and cortical microstructure measurements, revealing DXA-independent predictors of fracture risk and compartment-specific adaptations to environmental stimuli.

This thesis describes the development of a procedure to quantitate calcaneal vBMD and trabecular microstructure using HR-pQCT (first generation XtremeCT), in order to overcome limitations with previous quantitative devices.

Studies using human cadaveric feet and participants *in vivo* were used to develop the procedure and determine measurement accuracy and precision. Regional differences in calcaneus trabecular bone were found, with ~2-fold higher trabecular vBMD at the superior compared to the inferior region of the bone *in vivo*. The superior region of the calcaneus had better HR-pQCT measurement accuracy compared to the middle and inferior regions, due to fewer tissues surrounding the region and a higher trabecular density. Increasing HR-pQCT scans integration time (100 to 200ms) improved trabecular microstructure accuracy *ex vivo*; acceptable quality images could be obtained with a 200ms integration time *in vivo*. Calcaneus vBMD and trabecular microstructure could be measured with good relative precision in premenopausal women (vBMD, 0.9-1.9%; trabecular microstructure 1.4-1.8%), where it was necessary to correct for positional errors using image registration.

In conclusion, calcaneus vBMD and trabecular microstructure can be quantified using HR-pQCT *in vivo*. Continued development of the positioning apparatus would benefit the future application of the method, to enable greater flexibility with the region measured and enable image acquisition at a 200ms scan integration time.

Acknowledgements

I wish to thank my primary supervisor, Professor Eugene McCloskey, for always making time for me, and for providing a balance that allowed me to be creative to achieve the project aims. I have taken on a tremendous amount of knowledge from your supervision that I will take forward into my career. I extend these thanks to my second supervisor, Professor Graham Kemp, for taking me on as a student part the way through my PhD and providing valuable advice in our exchanges.

I have a number of colleagues and collaborators who have dedicated significant time to the project and my development – it's been a great privilege to work with you all. I am indebted to Dr Margaret Paggiosi for the continued encouragement, support and training, particularly your insight into conducting clinical research; Dr Enrico Dall'Ara, for invaluable technical expertise and guidance, and for welcoming me to work within your group; John Rochester, for the enthusiasm and trust in using donor limbs for our study ideas; Dr Nicolas Vilayphiou, for the guidance and patience in using the XtremeCT, and the commitment shown in the project development; Sister Angela Green, Sister Julie Walker and Jill Thompson, for your time in the study management tasks; and the Sheffield Clinical Research Office, for the advice on obtaining ethical approval for the clinical studies.

I wish to thank all colleagues within the MRC-Arthritis Research UK funded Centre for Integrated research for Musculoskeletal Ageing and the Academic Unit of Bone Metabolism. I have learned a great deal in many aspects of research through the exceptional training programmes and continued knowledge exchange. I'd also like to acknowledge the MRC and Arthritis Research UK, and the Impact, Innovation and Knowledge Exchange Collaborative R&D Award for funding the research.

I would like to thank the participants who took part in the studies, as well as those who offered to participate. The insights that I gained from you have inspired me to continue within clinical research and I hope that we gave you a positive research experience! Also, a special thank you to the donor families; the work in this thesis would not have been possible without your consent.

Finally, I wish to thank my family and friends. My parents and grandparents for instilling an attitude to make the most of every opportunity and supporting every decision that I have made – I hope that this thesis is a demonstration of what you have enabled me to achieve; friends that I have made in Sheffield and those down South for giving me an outlet from work and dragging me away from my laptop – questions like, "have you finished your PhD yet?" and "are you *still* a student?"

never grew old; and Steph, for your caring nature, patience, encouragement and for always looking out for my best interests – I hope that this work justifies my decision to move to Sheffield and work the odd weekend. We can now start to make up for any lost time!

Thesis communications

Publication

LM Metcalf, E Dall'Ara, MA Paggiosi, JR Rochester, N Vilayphiou, GJ Kemp & EV McCloskey. Validation of calcaneus trabecular microstructure measurements by HR-pQCT, *Bone* (2017), doi: 10.1016/j.bone.2017.09.013.

Oral communications

LM Metcalf, JA Fogden, RH Patel, MA Paggiosi, GJ Kemp & EV McCloskey. Optimising the quantification of bone microstructure in the human calcaneus using HR-pQCT. *21st International Bone Densitometry Workshop / 7th European Symposium on Ultrasonic Characterization of Bone 2017*; Kloster Banz, Germany.

LM Metcalf, JR Rochester, N Vilayphiou, MA Paggiosi & EV McCloskey. Method development to scan the calcaneus using high-resolution peripheral quantitative computed tomography. *CIMA/CMAR Annual Meeting 2015*; University of Nottingham, UK.

Oral poster

LM Metcalf, E Dall'Ara, MA Paggiosi, JR Rochester, N Vilayphiou, GJ Kemp & EV McCloskey. Determining the accuracy of calcaneum trabecular microstructure measurement by HR-pQCT. *Mellanby Centre Annual Research Day 2016*; University of Sheffield, UK.

Poster presentation

LM Metcalf, E Dall'Ara, MA Paggiosi, JR Rochester, N Vilayphiou, GJ Kemp & EV McCloskey. Validation of calcaneus trabecular microstructure measurements by HR-pQCT. *Mellanby Centre Bone Imaging Workshop 2017*; University of Sheffield, UK.

LM Metcalf, E Dall'Ara, MA Paggiosi, JR Rochester, N Vilayphiou, GJ Kemp & EV McCloskey. Validation of calcaneus trabecular microstructure measurements by HR-pQCT. *44th European Calcified Tissue Society Congress 2017*; Salzburg, Austria.

LM Metcalf, MA Paggiosi, GJ Kemp & EV McCloskey. A procedure to scan the calcaneus using high-resolution peripheral quantitative computed tomography. *National Osteoporosis Society Conference 2016*; Birmingham, UK.

LM Metcalf, JR Rochester, N Vilaphiou, MA Paggiosi & EV McCloskey. Method development to scan the calcaneus using high-resolution peripheral quantitative computed tomography. *Mellanby Centre Annual Research Day 2016*; University of Sheffield, UK.

LM Metcalf, JR Rochester, N Vilayphiou, MA Paggiosi & EV McCloskey. Examining the Calcaneus Using HRpQCT: Method Reproducibility and Regional Trabecular Variation. *American Society for Bone and Mineral Research Annual Meeting 2015*; Seattle, USA.

LM Metcalf, JR Rochester, N Vilaphiou, MA Paggiosi & EV McCloskey. Examining the calcaneus using HR-pQCT: method reproducibility and regional trabecular variation. *Bone Research Society Annual Meeting 2015*; Edinburgh, UK.

Other works

LM Metcalf, TJ Aspray & EV McCloskey. The effects of parathyroid hormone peptides on the peripheral skeleton of postmenopausal women. A systematic review, *Bone* (2017), 99, 39-46, doi: 10.1016/j.bone.2017.09.013.

J Alsayednoor, LM Metcalf, JR Rochester, E Dall'Ara, EV McCloskey & D Lacroix. Comparison of HR-pQCT and microCT based finite element models for the estimation of the mechanical properties of the calcaneus trabecular bone, *Biomechanics and Modeling in Mechanobiology*, Submitted.

Abbreviations

ALP – Alkaline phosphate
BHC – Beam hardening correction
BMC – Bone mineral content
BMD – Bone mineral density
aBMD – Areal bone mineral density
vBMD – Volumetric bone mineral density
BMI – Body mass index
BMU – Basic multicellular unit
BUA – Broadband ultrasound attenuation
BV/TV – Bone volume/Total volume
CPU – Central processing unit
CSA – Cross-sectional area
CT – Computed tomography
CTX – C-telopeptide of type I collagen
CV – Coefficient of variation
$CV\%_{RMS}$ – Root mean square error of the coefficient of variation
DXA – Dual-energy x-ray absorptiometry
FE – Finite element
GOBJ – Graphical Object
HR-pQCT – High-resolution peripheral quantitative computed tomography
ISCD – International Society for Clinical Densitometry
HRT – Hormone replacement therapy
kVp – Peak kilovoltage
LSC – Least significant change
µA – Microamperes
mA – Milliamperes
µSv – Micro Sievert
mSv – Milli Sievert
Micro-CT – Micro computed tomography
MRI - Magnetic resonance imaging
OPG – Osteoprotegrin
PINP - N-terminal propeptide of type I procollagen
PTH – Parathyroid hormone
pQCT – Peripheral quantitative computed tomography
QCT – Quantitative computed tomography
QUS – Quantitative ultrasound
RANKL – Receptor activator of NF-κB ligand
SD – Standard deviations
SD_{RMS} – Root mean square error of the standard deviation
SOS – Speed of sound
Tb.N – Trabecular number
Tb.Sp – Trabecular spacing
Tb.Th – Trabecular thickness

List of figures

List of tables

CHAPTER 1 INTRODUCTION

Background

1.1 The skeleton

The skeleton is essential to living vertebrate's and is made up of varied sizes and types of bones that accommodate its function. Long bones (such as the humerus, femur, radius, tibia) support weight and provide levers to facilitate movement from the skeletal muscles and tendons. The short bones (such as the carpals and tarsals) support movement. Flat bones (such as the skull, sternum, ribs and scapulae) provide organ protection. Irregular bones have complex shapes and specific functions, such as the vertebrae that protect the spinal column. Sesamoid bones (such as the patella and pisiform) provide attachments for tendons across joints. Bones are also a reservoir for the storage and release of minerals that maintains the body's homeostasis, such as calcium, magnesium and phosphorus, and contain bone marrow within its cavities that produce red blood cells.

1.1.1 Bone anatomy

The bone has a hierarchal structure from the nano- (<1μm) to macro-structural level (>500μm) (Figure 1.1). At the nano-structural level, the bone is a composite material primarily formed by mineralised collagen fibrils, containing collagen proteins (85-90%) with hydroxyapatite mineral platelets [$Ca_{10}(PO_4)_6(OH)_2$], water and non-collagenous organic proteins, such as osteopontin, sialoprotein, osteonectin and osteocalcin (10-15%) [1]. These material properties give bone a stiff, but flexible structure. The mineralised collagen fibrils are arranged in a planar fashion to form lamellae (3-7μm). The lamellae are arranged to form different types of bone microstructure (<200μm), such as Haversian systems and single trabeculae.

Haversian systems contain blood vessels and are tightly packed together to form the cortical bone compartment. The cortical compartment is surrounded by a membranous layer on the inner (endocortical) and outer (periosteal) surfaces, which contains bone cells (discussed in Section 1.1.2), blood vessels and nerve fibres. The endocortical surface forms a transitional zone with the trabecular bone. Single trabeculae are inter-connected, with a network-like appearance that is surrounded by bone marrow, blood vessels and nerve bundles. Here, the trabecular bone has a larger surface area compared to cortical bone. The proportion of trabecular and cortical bone varies between skeletal sites and is highly dependent on its function.

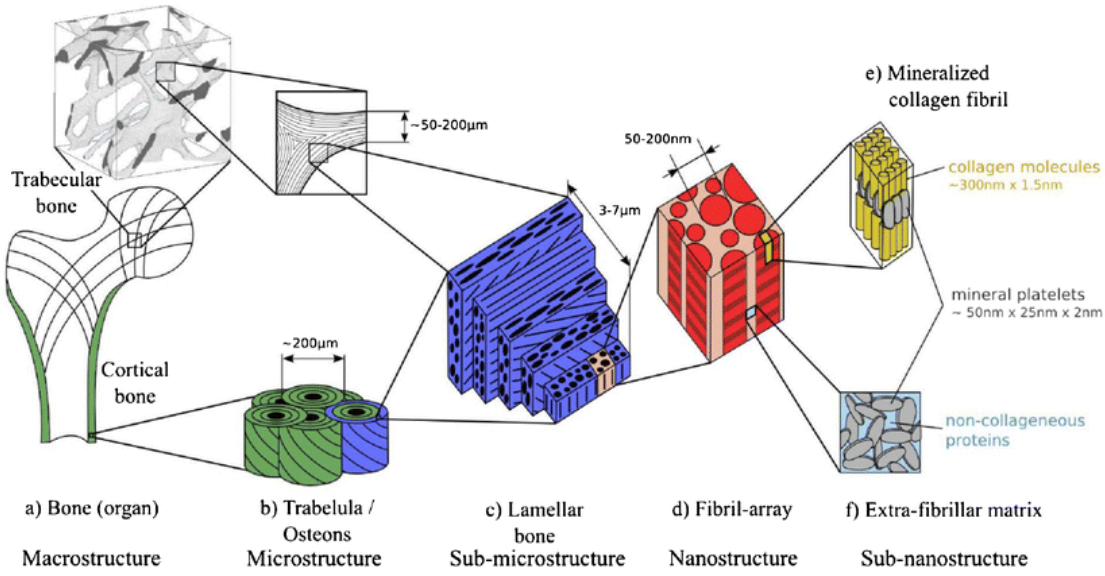

Figure 1.1. The hierarchy of the structural organisation of bone from the macro (proximal femur) to nano-structure.

Sourced from Pahr and Zysset [2].

1.1.2 Bone physiology

Bone is a metabolically active tissue that responds to extrinsic (external to the bone, e.g. endocrine, genetic and senescence) and environment stimuli (external to the body, e.g. pharmacologics, exercise and diet). There are three cells that regulate bone tissue, which are contained in a microenvironment called the basic multicellular unit (BMU) (Figure 1.2). Within the unit there is the: (1) osteoclast, which resorbs (removes) bone from the skeleton; (2) the osteoblast, which forms (deposits) new bone for the skeleton; and (3) the osteocyte, which is a mechano- and hormonal-sensory cells embedded and connected in the bone matrix. Osteocytes are responsible for sensing the stimuli and signalling BMU activity. The balance between osteoclast and osteoblast activity can determine a person's bone quantity over the lifespan.

During growth, bone modelling is dominant until the skeleton reaches maturity. Modelling adapts a bone's size, shape and spatial mineralisation with bone deposition but without previous bone resorption. Long bones during growth serves as an excellent example of bone modelling; with an increase in bone length, bone diameter and cortical thickness by late adolescence, followed by a plateau in bone geometry and smaller increases in trabecular and cortical compartment BMD with consolidation until post-puberty [3-6]. Heritability (genetics), hormones, weight and

lifestyle factors [7] govern the attainment of peak bone mass at the end of skeletal maturation, which is typically between 25 to 30 years of age [3, 8, 9]. The dimorphism in bone strength between males and females is evident at this stage; males typically have larger cross-sectional area and cortical area, thicker cortex and higher trabecular BV/TV, and subsequently higher estimated bone strength [10].

Bone remodelling is the process by which bone tissue is continuously renewed. Bone resorption and formation are typically balanced and occur at lower rates than seen than prior to maturity [11]. It permits the replacement of old or damaged bone through spatially and temporally dependent resorption and formation (i.e. coupling) within the BMU (Figure 1.2, Sims and Martin [12]).

Bone remodelling begins when the osteocytes orchestrate the retraction of the bone lining cells and reveal the bone matrix. This signals for the multinucleated osteoclasts (driven by increase RANKL:OPG cytokine expression ratio) to attach to the bone surface, which creates a sealed zone. The osteoclasts create an acidic environment by secreting hydrochloric acid within the sealed zone. This creates an optimal pH 2 for the enzyme, cathepsin k, to degrade type I collagen in the mineralised bone matrix – at each remodelling site, bone resorption occurs over a period of approximately 3 weeks. In the reversal phase, osteoblasts are recruited directly to the resorbed cavity via mechanisms that include the release of osteogenic growth factors from the matrix, cell-to-cell contact and secreted signals from osteoclasts – this occurs over approximately 5 weeks at the remodelling site. Osteoblasts deposit osteoid, which contains type I procollagen and additional non-collagenous proteins. The addition of hydroxyapatite mineralises the newly deposited osteoid forming bone matrix – bone formation occurs over approximately 3-4 months. Before returning to quiescence, the osteoblast has 3 fates: it undergoes apoptosis, becomes a bone-lining cell or differentiates within the bone matrix and becomes an osteocyte.

Bone resorption and formation (turnover) can be measured using biochemical markers. PINP and serum CTX-I are recommended as reference markers for bone formation and bone resorption, respectively [13, 14]. PINP is the cleavage of type I procollagen molecules prior to assembly into collagen fibrils and CTX-I is a c-terminal product from the breakdown of type I bone collagen. There are other biochemical markers available to measure bone remodelling, related to type I collagen degradation (NTX-I), matrix formation (osteocalcin) and osteoclast (TRAP5b) and osteoblast enzyme activity (bone ALP) [15]. These biochemical

markers are useful in monitoring how bone tissue may change in response to extrinsic and environmental factors.

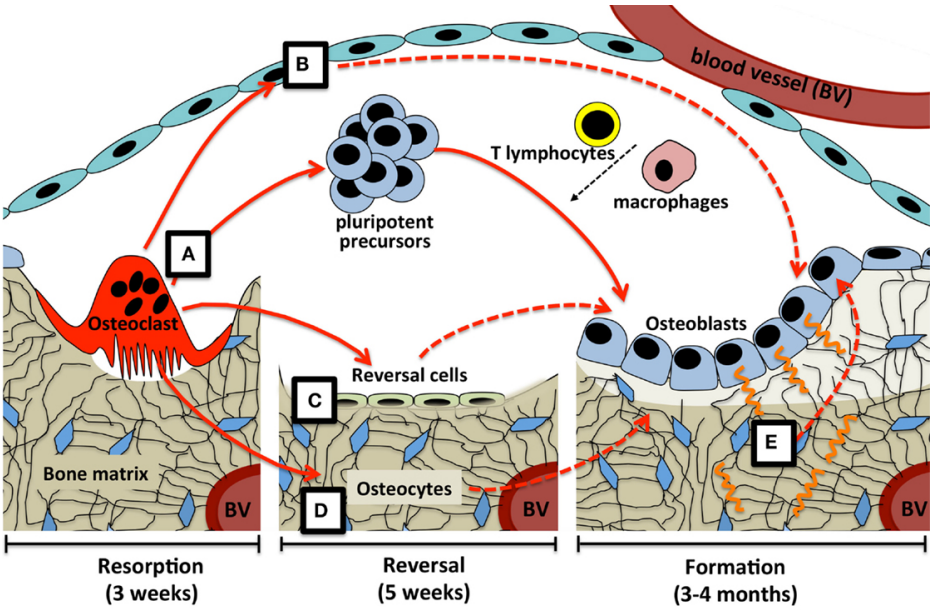

Figure 1.2. Bone remodelling within the basic multicellular unit.

Osteoclast secreted signals initiate the differentiation of osteoblast progenitors (A). Osteoclast secreted signals may lead to the indirect activation (dashed line) of osteoblast precursors and mature osteoblasts through the bone lining cells (B), the reversal cells on the bone surface (C) and the osteocytes (D and E).
Sourced from Sims and Martin [12].

1.1.3 The functional adaptation of bone

The functional adaptation of bone was first proposed in the 19th century by Julius Wolff, who observed that the trabecular patterns followed lines of principal stress in weight-bearing bones of the lower-limbs and foot (adapted version [16]), where regions have distinct geometrical structures based on stresses experienced [17]. Evolving from Wolff's findings, Harold Frost proposed the mechanostat theory for the control and remodelling of bone [18]. The theory proposed that bone operates in a negative feedback system, where strain is sensed and the bone modelled/remodelled to adequately adapt to the strength of the stimulus to resist structural failure.

Bone tissue is exposed to compressive, tensile and shear stresses (Figure 1.3). Via mechanotransduction and bone deformation (strain) these initiate bone modelling and remodelling to functionally adapt the bone. This can occur through extracellular

fluid creating fluid shear stress across the osteocytes, activating receptors associated with bone resorption (e.g. RANKL) and formation (e.g. sclerostin), and through microdamage to trabecular and cortical bone surfaces, such as linear microcracks (~ 50-100μm) or diffuse damage (clusters of sublamellar-sized cracks**)**. Linear microcracks are a result of higher loads (compressive and shear stress), which can lead to osteocyte apoptosis and the initiation of remodelling at that site [19]. Diffuse damage is a result of lower loads (tensile stress), which does not necessarily cause osteocyte apoptosis and can be followed by bone modelling rather than remodelling [20].

There are several examples of how the human skeleton functionally adapts. People with a high BMI carry a greater load and have higher BMD at central and peripheral sites of the skeleton compared to normal weight people [21-23]. There is deterioration in trabecular and cortical bone following the removal of weight-bearing compressive stress at the distal tibia with disuse [24] and spaceflight [25]. Studies have also shown that the humeral diaphysis from the racket arm of tennis players has geometrical asymmetries to the non-racket arm from bending, caused by compressive and tensive stress from striking the ball [26-28]. Functional adaptations at these sites may alter the customary strain stimulus for further adaptation, which may also be affected with changes in extrinsic and environmental factors. [29].

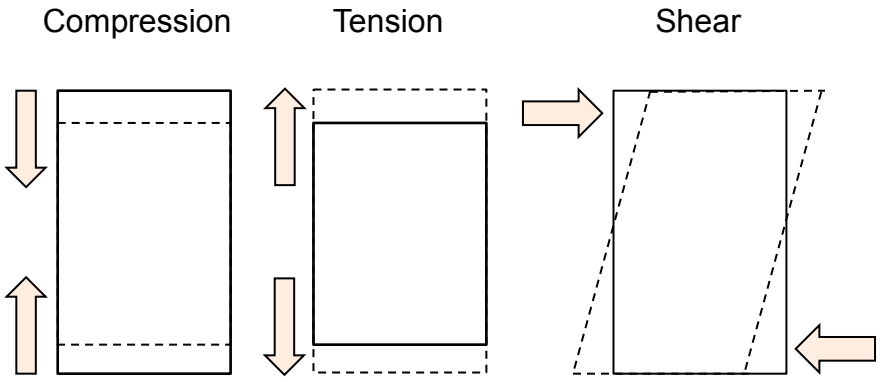

Figure 1.3. The biomechanical effect of compression, tension and shear stress.

Stress (arrows) is the force applied to a material and strain (dotted line) is the change in length or deformation of the material.
For a long bone, compression and tension would occur along the bone axis, whereas shear stress is perpendicular to the bone axis.

1.1.4 Bone fracture

Bone fracture occurs when the loading conditions exceed the capacity that the bone can resist i.e. its strength. Figure 1.4 shows the mechanics behind the fracture of bone with load-displacement behaviour (A) and stress-strain behaviour (B).

The point at which bone failure occurs is dependent on intrinsic characteristics, such as the mass, geometry, tissue integrity and material properties. For example: with a higher amount of healthy bone mass there is a greater quantity of tissue to absorb energy without fracturing, as shown by the higher failure load at the distal tibia compared to the distal radius [30, 31]; the accumulation of unrepaired microdamage affects tissue integrity and is associated with lowering the load/stress required for bone failure [32]; changes in the tissue material properties, such as the mineralisation, can alter bone stiffness; the degree of porosity and osteonal area fraction can also influence crack navigation, particularly at the cement lines and lamellar patterns in the osteons [33, 34].

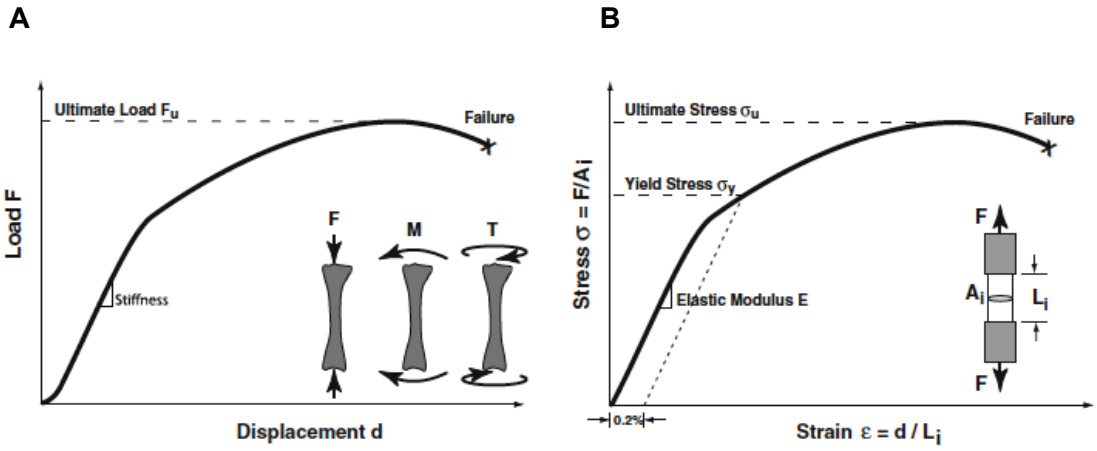

Figure 1.4. Mechanical properties of bone fracture.

A − Load-displacement behavior. Stiffness = linear region. Stiffness remains linear until transition to non-linear behaviour (yield point), causing permanent deformation and damage to the bone. Ultimate load = peak of the curve, which precedes failure of the bone (i.e. fracture). Work-to-failure = area under the load-displacement curve.
B − Stress-strain behavior. Elastic modulus = linear elastic region; yield stress = transition from linear to nonlinear behavior; ultimate stress (strength) = peak of stress-strain curve prior to failure. The energy needed to cause a fracture is calculated from the area under the stress-strain curve.
Sourced from Cole and van der Meulen [35].

It is well established that bone size is critical to whole bone strength at several skeletal sites [1-3]. Additionally, the characteristics of the trabecular and cortical compartment also contribute to bone strength. Cowin [4] stated that trabecular (cancellous) bone had 20-30% lower stiffness than cortical bone, proposing that

this was the result of different microstructural orientation and distribution (as shown in Figure 1.1). The relative contribution of the trabecular and cortical compartments to bone strength varies depending upon the skeletal site. For example, vertebrae are primarily composed of trabecular bone, which are orientated in an axial direction within a thin cortex. Trabecular thickness and the plate-rod conformation, as well as total BMD, significantly determines the vertebral failure load, whereas individual cortical parameters have a much smaller influence [2]. In contrast, cortical bone is more influential on peripheral bone strength; for example, the distal tibia and distal radius strength and stiffness is dependent on cortical thickness, as well as the trabecular BV/TV and connectivity [1]. There is also inter-site heterogeneity in the contribution of trabecular and cortical bone to proximal femur strength. In femoral neck fracture cases, large focal losses in trabecular vBMD have been reported. For trochanteric fractures there are focal losses in trabecular and cortical vBMD [5], as well as an association with trochanteric cortical area, as shown in mechanical testing experiments [3].

1.2 Osteoporosis

1.2.1 Definition and diagnosis

Osteoporosis is 'a systemic skeletal disease characterised by low bone mass and microarchitectural deterioration of bone tissue, with a consequent increase in bone fragility and susceptibility to fracture' [36]. A BMD T-score value 2.5 SD below the young adult female mean is used to assist the diagnosis of osteoporosis [37, 38] – there is more detail of this measurement in Section 1.3.1. The T-score is seen as a useful tool, as fracture risk increases by 1.5 to 3-fold with every T-score reduction by 1 SD [39].

Osteoporosis is, however, a multi-factorial disease and the -2.5 SD BMD T-score does not capture all fractures [40]. Other independent risk factors for osteoporosis include age, sex, BMI, parental history of fractures, personal history of prior fracture, current tobacco smoking status, glucocorticoid use, rheumatoid arthritis, alcohol consumption >3 units per day [41]. The combination of these factors with the BMD T-score can enhance fracture risk prediction [42]. In order to obtain a quantitative measurement of an individual's absolute 5-10 year fracture risk, the clinical risk factors, with or without BMD, have been integrated into different computational algorithms, such as FRAX®, QFracture and Garvan, each of which has different

input characteristics. Currently, QFracture and Garvan capture individuals falls rate; a key contributor to fracture incidence. Nonetheless, FRAX is more commonly used worldwide, as it has 68 population-specific calculators currently available [43].

1.2.2 Prevalence and impact

With an ageing population the prevalence and cost of osteoporosis-related fractures is predicted to increase worldwide. It has been estimated that 22 million women and 5.6 million men have osteoporosis in Europe [45]. There were also approximately 3.5 million new osteoporosis-related fractures in 2010: 610,000 hip fractures, 520,000 vertebral fractures, 560,000 forearm fractures and 1.8 million at other sites [45]. The direct annual cost was estimated at €24 billion, rising to €37 billion with indirect costs, such as long term care and pharmacological therapies for osteoporosis management [45]. In a UK populations study, it is estimated than one in two women and one in five men past 50 years of age will have an osteoporosis-related fracture in the rest of their lifetime (Figure 1.5) [44, 46].

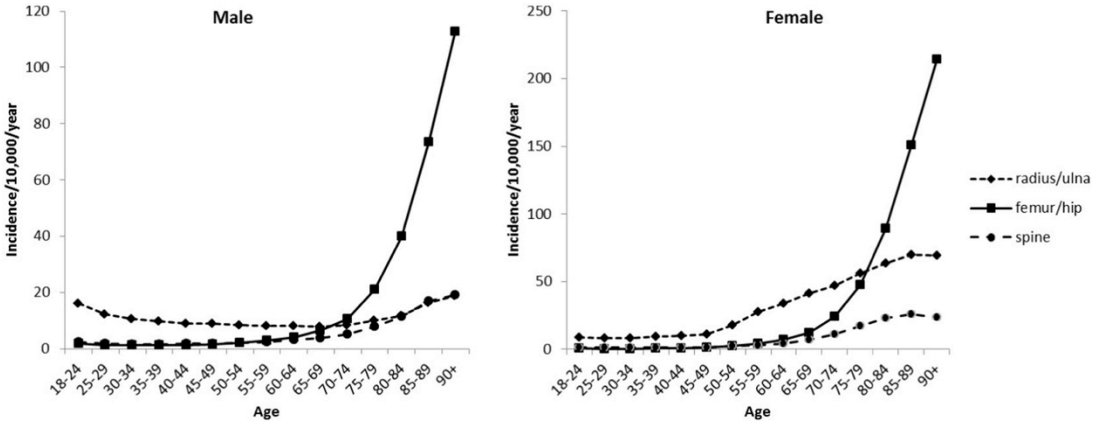

Figure 1.5. Age- and sex-specific incidence rates of fracture at the radius/ulna, femur/hip and spine (1988-2012).

Sourced from Curtis et al., [44].

1.2.3 Disease characteristics

The dimorphism in osteoporosis between women and men begins during puberty, in obtaining peak bone mass, and is primarily caused by differences in sex steroids. During growth and at skeletal maturation, males tend to have high BMD at the spine and hip, as well as larger bones, higher trabecular BMD and thicker cortices (Burt, Gabel, Lorentzon?). Following maturation, oestrogens and androgens restrain the rate of bone remodelling [47, 48], which assist with the maintenance of bone mass. Oestrogen deficiency that occurs with the menopause in women results in an increased number of activated BMUs; also mediated by proinflammatory cytokines [49]. This increases the number of differentiated osteoclasts and osteoblasts; but there is an imbalance between the resorbed and deposited bone, which leads to a net bone loss [50]. Men, on the other hand, do not have a rapid change in bone remodelling like women, but can lose substantial amounts of bone with ageing, associated with lower bioavailable oestrogen and testosterone [48, 51]. Collectively, these hormonal changes can result in the deterioration of trabecular and cortical microstructure.

Examples of the impact of trabecular and cortical bone loss that is associated with osteoporosis are shown in Figure 1.6. In the right image of Figure 1.6A, the trabecular bone appears less dense in the inner and outer medullary compartment. This can be caused by a conversion of plate- to rod-like trabeculae, the complete loss of trabeculae (i.e. lower number) and a loss of trabecular connectivity. In Figure 1.6B, there are examples of significant cortical remodelling and loss of cortical mass. This can be demonstrated by greater cortical porosity and the trabecularisation at the endocortical surface. There is also an accumulation of microcracks, which can be apparent in trabecular and cortical bone.

A

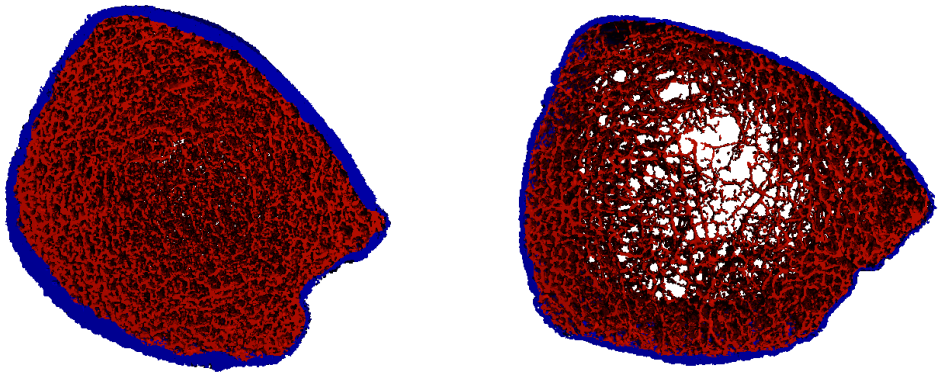

B

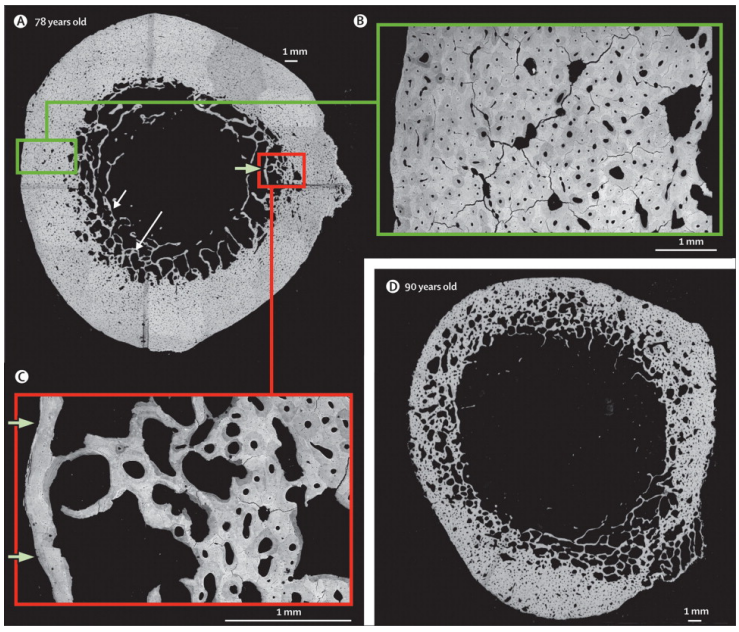

Figure 1.6. Images of trabecular and cortical microstructure.

A − Images of the distal tibia. The trabecular bone compartment is in red and the cortical bone compartment is in blue. The image on the left has a dense trabecular region, whereas the image on the right has had a noticeable loss in central meduallary area and towards the endocortical bone surface.
B − Micrograph of distal radius specimens from a 78 year old and 90 year old women. The green image shows the high number of cortical pores, and a high number of microcracks that surround and go through osteons. The red images shows an area of endocortical trabecularisation. The bottom right image shows that there is a greater number of larger pores in distal radius micrograph from the 90 year old woman (sourced from Zebaze et al., [52]).

1.2.4 Disease management

The prevention and management of osteoporosis has been improved by the development of pharmaceutical therapies. The prescription of licensed anti-resorptive and anabolic therapies accounts for 5% of the total spend on osteoporosis in Europe [45].

Anti-resorptive treatments prevent bone resorption and lower bone turnover, thus to some extent retaining ‘old’ bone and suppressing the formation of new bone. Anti-

resorptive therapies include oral and intravenous bisphosphonates, denosumab, calcitriol, raloxifene and hormone replacement therapy (HRT). Available anabolic therapies promotes bone formation and increase bone turnover by increasing the BMU activation frequency. Therefore, it has the opposite mechanistic action to anti-resorptives. Currently teriparatide, a 1 to 34 fragment of parathyroid hormone (PTH), is the only licensed anabolic treatment in the UK. Other anabolic treatments include abaloparatide (binds to PTH 1 receptor), which has been recently approved by the FDA, and romosozumab (anti-sclerostin antibody), which is undergoing phase III review.

The anti-fracture efficacy of anabolic and anti-resorptive treatments has been evaluated in comparative analyses of different studies and, more recently, direct head-to-head trials. In one of the latest comparative analyses of fracture reduction between treatments and placebo in postmenopausal women, bisphosphonates, denosumab and teriparatide had a relative risk reduction of 40-60% for vertebral fractures and 20-40% reduction for non-vertebral fractures [11]. However, in recent head-to-head trials there appears to be better anti-fracture efficacy of anabolic compared to anti-resorptive therapies in postmenopausal women with osteoporosis. In the VERO trial, there was a pooled 52% lower vertebral and non-vertebral fragility fracture risk with teriparatide compared to risedronate [12], and, in the ARCH trial, romosozumab lowered vertebral fracture risk by 48% and non-vertebral fracture risk by 19% when compared to alendronate [13]. This is promising for finding more efficacious treatments for patients, but more evidence is required to influence treatment decision-making.

Guidance on the prescription of osteoporosis treatments has been provided by NICE and the National Osteoporosis Guideline Group [41, 56]: oral bisphosphonates (alendronate and risedronate) are first line treatments for the prevention of fractures, due to a 3-fold lower cost-utility ratio (pounds per Quality of Life Year to prevent one fracture) compared to teriparatide. Intravenous bisphosphonate (zoledronic acid) and denosumab are recommended if oral bisphosphonates are contraindicated or not tolerated. Finally, teriparatide is a second/third line therapy for individuals that are unresponsive to bisphosphonates, have contraindications for bisphosphonates, or have a T-score ≤ -3.5 SD with a history of fragility fractures. A NICE technology appraisal is currently in progress, which includes abaloparatide.

1.3 Non-invasive assessment of bone

The ‘gold standard’ for measuring bone strength is mechanical loading until failure (i.e. fracture). Clearly, this cannot be achieved clinically. Non-invasive assessments have been important to predict bone strength by measuring the intrinsic characteristics of bone, particularly how these characteristics may adapt with extrinsic and environmental stimuli.

X-ray is the most common method used for the non-invasive assessment of bone. X-ray photon beams are attenuated based on the electron density (atomic number which in turn depends on mass density) of the body tissues. Bone mineral strongly attenuates x-rays as it has a high electron density, whereas soft tissues (e.g. fat and muscle) have low electron densities and are low attenuating tissues. The photon attenuations are detected and reconstructed into a radiographic image, where its detail is dependent on the physical properties of the assessment device. The contrast achieved between bone and soft tissues is essential to bone edge detection and measurement accuracy. Whilst the estimation of bone mineral by x-ray is not perfect, it provides a measurement that is more feasible than measuring the bone mineral ash weight. Other non-x-ray based assessments of bone (i.e. not dependent on bone mineral) include magnetic resonance imaging (MRI) and ultrasound. These are advantageous, as they do not irradiate the participants.

Devices used for the non-invasive assessment of bone have different capabilities and limitations. The key assessments are summarised within this section.

1.3.1 Dual-energy x-ray absorptiometry (DXA)

DXA is a quantitative radiological procedure for measuring areal (2D-based) (a)BMD. The accessibility of DXA, its low effective radiation dose and its capability of measuring BMD at the lumbar spine and proximal femur has established the assessment device as integral in diagnosing osteoporosis (Section 1.2.1, T-score measurement), estimation of fracture risk and monitoring of BMD changes over time [57]. Other non-BMD applications have been used from DXA images, such as vertebral fracture assessment, hip structural analysis, trabecular bone score and the measurement of body composition.

There are some technical limitations to using DXA. DXA assumes that all high-density overlying material imaged is bone [58], such as abdominal aortic calcification and surgical implants. Degenerative changes with arthritis and fracture can also cause artefacts and typically overestimate aBMD [58]. DXA also assumes

that soft tissue is homogenous; composition can change in response to extrinsic or environmental stimuli (e.g. hydration, weight loss), which affects x-ray attenuation. Subsequently, this may distort the segmentation of the bone from the soft tissue with image analysis. Soft tissue thickness can also attenuate x-rays, in which simulated fat-layering has been reported to increase DXA phantom aBMD [59]. Finally, areal DXA measurements cannot take into account bone depth, which can underestimate and overestimate aBMD in small and large bones, respectively, and does not discriminate between the trabecular and cortical compartments.

1.3.2 Quantitative Computed tomography

Quantitative computed tomography (QCT) can obtain volumetric (3D) measurements of bone, such as volumetric (v)BMD and bone geometry, therefore overcoming some of the limitations found with DXA.. QCT can also obtain some measurements of trabecular and cortical microstructure; however the accuracy of these measurements is dependent on the tomographic slice thickness and pixel size. Scans are generally of a shorter duration than DXA and the precision error for QCT is also low [60].

An advantage of QCT is that it can assess compartmental changes associated with fractures and response to treatment. For example, lower trabecular vBMD at the femoral neck and the trochanteric region, as well as focal cortical thinning and lower cortical vBMD towards the superior region of the femoral neck, have been reported with hip fractures [61-63]. Femoral neck and medial trochanter trabecular vBMD have also been shown to predict hip fracture, independently from total hip aBMD, age and BMI [61]. When QCT has been applied to monitor the response to osteoporosis treatment, an increase in integral vBMD and trabecular vBMD at the spine was 2 and 5-fold higher, respectively, with teriparatide compared to alendronate [64]. Localised increases in proximal femur cortical vBMD has been associated with regions of high compressive and tensile stress with teriparatide, highlighting the specificity that can be achieved using QCT assessments [65]. QCT images of the spine and hip have also been used to estimate failure loads and fracture under specific loading conditions using finite element (FE) modelling; which has been supported by the ISCD to monitor age- and treatment-related changes [66].

Preventing the more routine used of QCT in osteoporosis diagnosis and in studies is the substantially higher radiation dose per scan compared to DXA, due to the greater amount of soft tissue at the central sites. This radiation dose is even higher

with more specialised high-resolution QCT, which has superior spatial resolution. The radiation dose is an issue if completing longitudinal monitoring, especially in younger populations. Even with this improved spatial resolution, trabecular bone microstructure (number, thickness and spacing) or the geometry of cortical pores cannot be quantified. QCT devices are also more expensive compared to DXA. Taking these limitations into account, QCT appears to be complementary to DXA for fracture risk prediction and monitoring, rather than replacing DXA [67].

1.3.3 Peripheral QCT (pQCT)

pQCT obtains either a single slice or multiple slices at the extremities of the skeleton. The single slice pQCT devices (such as the Stratec XCT2000 and XCT3000) have a standard slice thickness of 2 mm, with an in-plane voxel size from 200-800 μm [68]. Multi-slice CT and cone beam CT, which are more commonly available in hospitals, can image a greater proportion of the peripheral site of interest and can also image the bone under weight-bearing conditions [69]. Subsequently, multi-slice images have greater effective radiation doses than single slice images. An advantage of pQCT scanners, particularly the Stratec XCT range, is that is has an open gantry, meaning it has great accessibility to image a number of distal-proximal sites along the extremities.

pQCT cannot be used to diagnose osteoporosis, but can be used for fracture risk assessment and monitoring interventions (loading and treatment). Radius and tibia cortical geometry and estimated biomechanical strength measured by pQCT can independently predict incident fractures in older men and women, following adjustment for proximal femur aBMD and other clinical risk factors [70, 71]. pQCT can also provide measurements of soft tissue and can be applied to image the muscle-bone relationship, such as with exercise interventions and musculoskeletal diseases [72, 73].

One of the main limitations to pQCT is that it is restricted to imaging the extremities. However, as it is limited to the extremities', the radiation dose is lower when compared to central sites using standard QCT. Variability in participant repositioning can cause measurement imprecision, such as through a slight alteration in the limb angle or with distal-proximal movement along the extremity [74-76]. The spatial resolution of pQCT means that trabecular microstructures and cortical pores cannot be quantified. Furthermore, the cortical bone density is sensitive to in-plane pixel size and may not be accurately quantified when it's thickness is low [68], such as at the radius metaphysis or with higher cortical bone loss.

1.3.4 High-resolution peripheral QCT (HR-pQCT)

HR-pQCT is a progression of pQCT that obtains multi-slice images with a superior voxel size (isotropic 82 and 61 μm, first and second generation XtremeCT, respectively). This has enabled the more accurate measurement of trabecular and cortical microstructure [77], which has identified compartmental differences in trabecular number, cortical thickness and porosity in individuals with similar DXA aBMD measurements [78]. The radiation dose per HR-pQCT scan is also low. HR-pQCT also appears to have better short and long-term measurement precision compared to pQCT [76, 79], potentially due to the improved spatial resolution and the removal of misalignments between repeat images with the manufactures' software.

HR-pQCT is not used for osteoporosis diagnosis, but appears to have a wide applicability in bone research. Measurements such as radius and tibia total, trabecular and cortical vBMD, cortical area and thickness, trabecular number, and bone strength (estimated by FE modelling) have all been independently associated with postmenopausal fracture risk [80-83]. In monitoring treatments responses an increase in HR-pQCT measured cortical porosity (and decrease in cortical vBMD) has been observed with teriparatide [84, 85], and cortical pore infilling with anti-resorptives [84-86]. The device has had the sensitivity to detect deterioration in trabecular and cortical microstructure with just 6-weeks disuse at the distal tibia [24] and detect compartment-specific abnormalities associated with type 2 diabetes [87], corticosteroid-induced osteoporosis [88] and with kidney transplantation [89]. Image acquisition and evaluation procedures have also been adapted to image joint geometry and microstructure at the metacarpals in patients with rheumatoid arthritis [90-92] and in patients developing knee osteoarthritis [93].

HR-pQCT has a number of potentially clinically relevant measurements, but also has limitations. It is a specialised device and less accessible than DXA and QCT. Only the extremities can be measured, particularly towards distal regions due to the restricted size of the gantry. The scan duration is 2-2.8 minutes (depending on the scanner), which is longer than pQCT devices. The longer scan duration can lead to movement artefacts and lead to repeat image acquisitions when image quality is unacceptable. Movement artefacts can cause measurement imprecision, particularly for microstructural measurements [94, 95]. Also, whilst there is good accuracy of most trabecular and cortical measurements, there are issues with measuring structures that are at or below the spatial resolution (95-150 μm [96, 97]), such as trabecular thickness and cortical pore size [77, 97, 98]. HR-pQCT does not have the

spatial resolution to detect microdamage (requires voxel size < 5 μm). This can only be achieved using micro computed tomography; however this cannot be used for the non-invasive assessment of human bone.

1.3.5 Magnetic resonance imaging (MRI)

MRI is typically used to image non-osseous tissue. The imaging of bone by MRI is largely dependent on visualising the bone marrow and surrounding soft tissues. The pulse and duration of the magnetic field, dictated by the radiofrequency, determine the spin and relaxation of the protons in the tissues. Bone has low proton abundance and has a negative signal (appears black) where as the marrow and soft tissues have higher proton abundances and a positive signal (appears white).

The advantage of MRI is that it invovles no ionizing radiation exposure and is available in hospital settings. As it in non x-ray-based, it cannot quantify BMD. Instead, it measures trabecular and cortical bone volume and microstructure. MRI has commonly been applied at peripheral sites as a better spatial resolution can be achieved (150 μm in-plane pixel size and a 300 μm slice thickness [68]), where as the spine and hip is challenging due to the abundance of soft tissue, which impact signal-to-noise ratio, the spatial resolution and scanning duration. Measurement at central, fragility fracture sites may be feasible using a higher magnetic field strength (7 tesla) [99], however these protocols are still relatively underdeveloped compared to those using lower magnetic field strength (1, 1.5 and 3 tesla) at the peripheral sites [76, 79, 100, 101].

MRI is not used in osteoporosis diagnosis, but has been applied in research studies to evaluate microstructural changes with fracture risk and treatment. Postmenopausal women with hip fractures have been reported to have lower BV/TV and increased trabecular spacing at the calcaneus [101] and the radius [102] compared to controls. More advanced image processing with MR images has detected an apparent conversion of trabeculae to rod-like phenotypes and trabeculae disconnection at the distal radius in women after the menopause, which was attenuated with estrogen therapy [103]. Maintenance in MR-measured BV/TV and trabecular microstructure has also been reported following 24 months of alendronate treatment, which was consistent with DXA aBMD at central sites [104].

The added complexity of imaging bone microstructure using MRI explains its lower use compared to x-ray based devices. HR-pQCT appears to be easier to use to measure bone microstructure, as shown by the superior short and long-term precision of measurements compared to MRI [76, 79]. MRI spatial resolution also

has an impact on its measurement of microstructure; there is reasonable accuracy for trabecular microstructure [105] but quantifying cortical pores pose challenges [106]. The scan duration needs to be longer to improve signal-to-noise and assist microstructure measurement. However, in turn, this increases the likelihood of movement artefacts during the image acquisition.

1.3.6 Quantitative ultrasound

Quantitative ultrasound (QUS) was introduced to quantify bone properties using ultrasonic waves [107]. The transmission of the waves and its absorption and scattering can be interpreted as bone properties, such as the attenuation of the waves (broadband ultrasound attenuation (BUA)) and speed that the waves transmit through the bone (speed of sound (SOS)). QUS measurements have been used to study BMD and bone microstructure, including trabecular separation, anisotropy and connectivity [108, 109], as well as cortical thickness and porosity [110]. Such in an osteoporotic bone, BUA and SOS would be lower than that measured from a dense bone without microstructural deterioration.

QUS is highly accessible; it is inexpensive, portable and ionizing radiation free. There are a number of QUS devices that measure different sites of the peripheral skeleton, such as the radius, tibia, calcaneus and phalanges. Specifically, calcaneal QUS is able to predict fracture risk independent from central DXA BMD (described in more detail in Section 1.4.3). Fracture risk prediction using calcaneal QUS is comparable to using femoral neck aBMD [111, 112] and QUS thresholds have been recommended as a useful tool for osteoporosis screening in locations that do not have access to DXA [113]. QUS measurements are also continuing to be developed, with a particular focus on measuring the proximal femur [114, 115] and the extremities where the focus is on cortical bone thickness and porosity [110].

There are limitations to QUS, which have been documented by the ISCD [113]. The technical diversity between devices, such as the number of detectors, within-site variation of the region of interest, measurement algorithms and the skeletal site assessed, can limit the interpretation of the results in clinical applications [113, 116]. This makes study comparisons challenging. Also, improper coupling between the ultrasound medium and the skin, skin temperature and soft tissue thickness can all affect QUS measurements. In prospective studies, ultrasound drift can lead to measurement imprecision. Subsequently, the relative measurement precision has been reported to be 2.3-7.1% for BUA and SOS between devices [113], which compromises the detection of clinically significant changes in monitoring studies.

1.3.7 Summary

Non-invasive assessments can help to determine a person's fracture risk and monitor the response to an extrinsic and environmental stimulus. Different devices can be used to achieve this (Table 1.1). DXA is integral to osteoporosis diagnosis and an essential tool in the management of the disease. However, the amalgamation of trabecular and cortical compartments limits DXAs sensitivity to detect intrinsic changes in bone. Ideally, QCT would be applied in these scenarios, particularly at major osteoporotic fracture sites (spine and hip). Measuring these sites using QCT would expose people to high ionising radiation doses and be unsuitable for monitoring or with multiple measurements in longitudinal study designs. pQCT devices (including HR-pQCT) offer significantly lower radiation doses. Whilst these devices are limited to the peripheral skeleton, and may not be entirely representative of the central sites [117, 118], meaningful measurements have been reported with disease and in response to interventions. MRI may offer an alternative to measure bone microstructure, but it complex to use and has issues with precision. QUS also has issues with precision in detecting changes in the bone. At this present moment, HR-pQCT is preferred for the measurement of peripheral bone microstructure in research settings.

Table 1.1. A summary of the devices for the non-invasive assessment of bone that are described in the Chapter.

		DXA	QCT	pQCT	HR-pQCT	MRI	QUS
Technical	Areal or volumetric	Areal	Volumetric	Volumetric	Volumetric	Volumetric	N/A
	Effective radiation dose	1–50 µSv	0.06–3 mSv	1–22 µSv	3–6 µSv	None	None
	Pixel size	1 mm^2	0.1–3 mm^2	100–800 μm^2	61–82 μm^2	150–300 μm^2	N/A
	Slice thickness	N/A	1–8 mm	2 mm	61–82 µm	0.30–1 mm	N/A
	Scan durations	10–30 sec	< 10 sec	< 10 sec	2–2.8 min	~ 20 min	< 10 sec
Application	Common sites measured	Central, extremities, whole-body	Central, extremities	Extremities[§]	Extremities[§]	Central, extremities[§]	Extremities[§]
	BMD	Yes	Yes	Yes	Yes	No	No (estimate)
	Trabecular and cortical bone*	No	Yes	Yes	Yes	Yes	No
	Other measurements	VFA, TBS, HSA, body composition, FEA	VFA, FEA	Biomechanical indicies, muscle	FEA	Soft tissue composition	BUA, SOS

Information for the table has been obtained from references in this Chapter.
Notes: 1000 µSv = 1 mSv. 2400 µSv or 2.4 mSv = 1 years background radiation. * Trabecular and cortical measurements depend on the slice thickness and pixel size. [†] Measurements made that are not BMD or microstructure. [§] Limitations on what site of the extremities that can be measured due to the physical properties of the device i.e. gantry size and field of view.
Abbreviations: BMD, bone mineral density; VFA, vertebral fracture assessment; TBS, trabecular bone score; HAS, hip structural analysis; FE, finite element analysis; BUA, broadband ultrasound attenuation; SOS, speed of sound.

1.4 Calcaneus

1.4.1 Anatomy

The calcaneus, or heel bone, is a weight-bearing bone. It is the largest tarsal bone and has distinct macroscopic features and geometry (Figure 1.7). It forms two joints with other bones of the foot: the subtalar joint with the talus at the posterior and middle facets of the sustentaculum tali, and the calcaneocuboid joint with the cuboid at the anterior facet. It has numerous ligament origins and insertions [119]: the calcaneo-fibula ligament attaches at the calcaneus from the fibula; the plantar fascia ligament originates from the plantar surfaces of the calcaneus tuberosity and attaches to the proximal phalanges via the metatarsals; the longitudinal plantar ligaments attach to the metatarsal via the cuboid; the calcaneo-navicular plantar ligaments attach at the navicular bone; the calcaneo-cuboid plantar and dorsal ligaments attach to the cuboid; the calcaneo-navicular bifurcate and calcaneo-cuboid bifurcate attach at the navicular and cuboid, respectively; the tibio-calcaneal ligament from the tibia. The triceps surae muscles also attach to the posterior portion of the calcaneus via the Achilles tendon.

The calcaneus is largely composed of trabecular bone with thin cortices [120]. The trabecular orientation is highly heterogeneous reflecting the applied mechanical loads. Gefen and Seliktar [121] summarised the intrinsic characteristics of the calcaneus in relation to the applied strains: the calcaneus subtalar articular surfaces are exposed to high compressive strains that occur from weight bearing and locomotory activities, which the trabeculae align to in the superior half and towards the inferior half of the bone. Trabeculae also follow tensile stress lines in the inferior half of the calcaneus from the Achilles tendon attachment, which bears strains through maintaining balance in the standing posture. There is a mix of tensile and compressive strains from ground reaction force on the plantar-posterior surface of the calcaneus cortex, and there are smaller tensile strains from the deep and superficial plantar ligaments towards the anterior region of the calcaneus.

The non-invasive assessment of the calcaneus has been undertaken in several areas of osteoporosis research, using devices such as DXA, MRI and QUS. The site has been primarily used to study the effects of mechanical loading, assess fracture risk and monitor response to treatments for osteoporosis management.

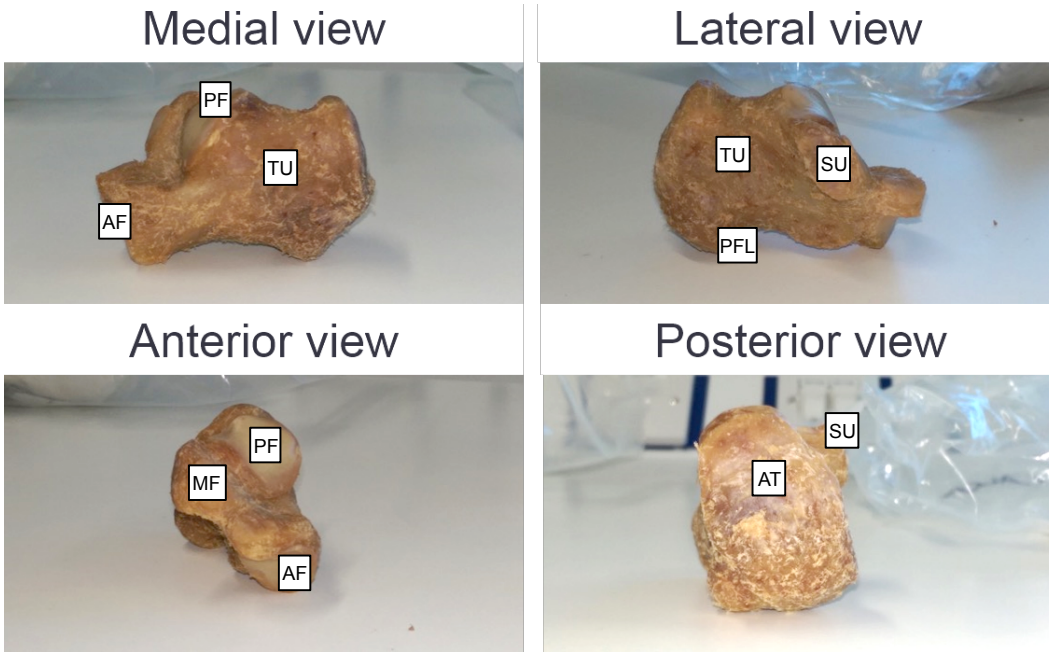

Figure 1.7. Calcaneus specimen with anatomical landmarks.

Landmarks: AF, anterior facet; MF, middle facet; PF, posterior facet, TU, tuberosity; SU, sustentaculum tali; PFL, plantar fascia ligament attachment; AT, Achilles tendon attachment.

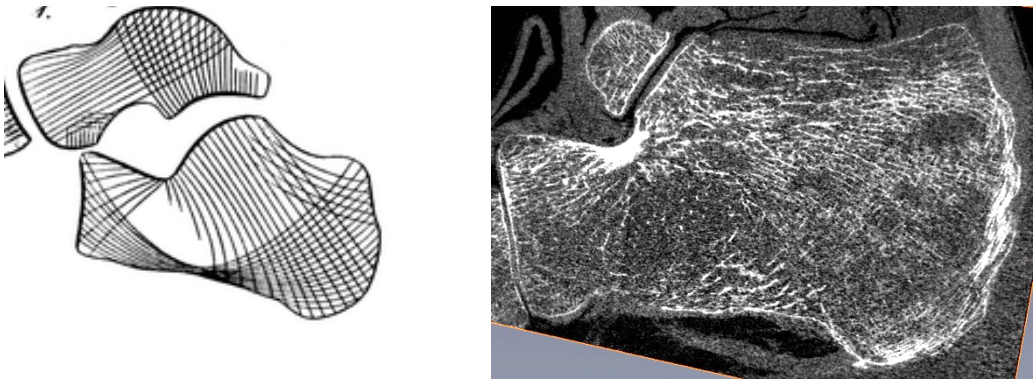

Figure 1.8. A sagittal slice through the calcaneus.

Left − sketch of the calcaneus and the trabecular orientation (adapted from Von Meyer [16]).
Right − slice of the calcaneus from a human cadaveric specimen captured using HR-pQCT.

1.4.2 Mechanical loading and unloading

The calcaneus is a mechano-responsive bone and has formed a surrogate site in a number of large physical activity/performance studies.

Blanchet and colleagues [122] reported that BUA and SOS were higher in active (≥3 sessions per week) postmenopausal women compared to sedentary counterparts,

independent from age, BMI, HRT use, smoking and alcohol intake. The associations between physical activity and QUS measurements were also independent of lumbar spine and femoral neck aBMD [122]. In younger adult men, time spent doing physical activities was positively associated with calcaneal BMD, with adjustment for age, height, weight, calcium intake and smoking status [123]. Men that had ceased activity or had continued to be active for at least 10 years had higher calcaneal BMD than those who have always been inactive [123]. Lower calcaneal BMD has also been reported in young women following the discontinuation of rigorous exercise over a 3-year period [124].

Physical performance and daily step count have also been predictive of calcaneal aBMD and QUS measurements. Pettersson and colleagues [123] found that total work capacity attenuated the prediction of BMD by history of physical activity levels in young men (10.1% without, 7.6% with total work capacity); although both parameters were likely closely correlated. Furthermore, in older men (60±11 years old), those who took longer to walk 50 feet had lower BUA and SOS, following adjustment for age, weight, alcohol consumption, smoking status [125]. Also, in older men and women (65-84 years old), a loss of QUS stiffness (parameter derived from both BUA and SOS) was dependent on physical activity levels over a 5-year follow-up [126]. The latter study also reported higher QUS stiffness in individuals completing over 8800 steps per day (or > 25 minutes of activity at > 3 metabolic equivalents), following adjustment for age, body mass and baseline calcaneus ultrasonic stiffness, in comparison to very sedentary individuals (< 4,000 steps per day).

Studies in larger cohorts, with varied populations, indicate that the characteristics of the calcaneus are dependent on physical activity and physical performance, as well as age and weight [122, 125, 127].

Higher calcaneal aBMD and BUA have been reported in participants that undertake sporting activities in comparison to controls. In particular, activities that expose the weight-bearing sites to high ground force impacts (football, squash, volleyball, dancing, gymnastics and running) [128-132]. Furthermore, in the same studies, the relative between-group differences in calcaneus measurements were comparable to other sites of the lower limbs (proximal femur to the distal tibia) [128, 130-132].

In prospective studies, the performance of high-impact activities increases calcaneal BMD in premenopausal women [133] and attenuates the loss of calcaneal BMD and BUA in peri- and postmenopausal women [130, 134] – similar trends in BMD were

reported at central sites [133, 134]. The effect of whole-body vibration, a low-impact activity, has had indifferent responses at the calcaneus [135, 136], as well as other sites of the central skeleton and extremities [137]. Methodological differences in the population recruited (children, young adults, postmenopausal women), the intervention duration, and uncertainties about the optimal magnitude and frequency (vibration intensity), and the duration (time exposed to vibration) may have contributed to the varied skeletal responses to whole-body vibration [137]. Considering the proximity of the calcaneus to the device platform, a response could be expected at this location with an 'osteogenic' protocol, mimicking the strains impacted during high-impact activities.

The removal of a weight-bearing stimulus also leads to a loss of calcaneal BMD. With 60 days of bed rest, the relative loss of calcaneus aBMD measured by DXA was equivalent to the tibia and greater than that reported at central sites of the skeleton [138]. With ~120 days of bed rest, the relative loss of calcaneal BMD exceeded peripheral and central sites, including the tibia [139]. There appeared to be high variability in the changes in calcaneus BMD with bed rest, but also with reambulation following bed rest in these studies. Whilst these could be due to individualised bone turnover responses, which has been recently highlighted [25], there may also be reproducibility issues due to difficulties in standardising a region to quantify in relation to the heterogeneous trabecular microstructure.

1.4.3 Fracture risk prediction

Calcaneus measurements have been used in the assessment of fracture risk, particularly using QUS. In a meta-analysis of prospective studies (55,164 women, 13,1742 men) with a total follow-up of 279,124 per years, the relative risk of hip fracture was 69% and 96% higher for every SD decrease in BUA and SOS, respectively [140]. Even when adjusted for DXA aBMD, there was still an independent association between BUA and fracture risk (34% higher for every SD decrease). QUS can also independently predict fracture incidence at individual sites such as the vertebrae, distal forearm and humerus/elbow [111]. The predictive ability of QUS appears to decrease over time, whereas that of femoral neck aBMD remains stable [111], suggesting that calcaneal QUS measurements may have a more limited long-term association with fractures.

BMD measurement of the calcaneus has also been associated with fractures, albeit in fewer studies compared to QUS. In the Study of Osteoporotic Fractures recruiting women older than 65 years, both calcaneal BUA and BMD had significant relative

risk increases, per SD decrease, for non-spine (30% and 40%, respectively) and hip (100 and 120%, respectively) fracture with a 2 year follow-up [141]. Calcaneal BMD appeared to have a slightly better association with fracture risk than BUA. Furthermore, calcaneal BMD was still associated with non-spine and trochanteric fractures following adjustment for calcaneal BUA and femoral neck BMD. With ~10 years follow-up in this study, containing a larger number of fractures, hip, wrist and spine fracture risk was 71%, 71% and 79% higher for every SD decrease, respectively [142]. Calcaneal BMD performed comparably to distal radius BMD for fracture prediction, but did not perform as well as central site BMD for predicting central site fractures (106-137% higher for every SD decrease). There is little doubt that measured characteristics of the calcaneus can be associated with fracture risk.

1.4.4 Treatment response

There is good evidence that the calcaneus bone is responsive to pharmaceutical treatments for osteoporosis. Postmenopausal women treated with HRT for 4 years maintained calcaneus BUA and SOS in comparison to a control group, where group-differences were between 6-10% [143]. Furthermore, male and female patients beginning treatment with oestrogen and bisphosphonate had an increase in BUA and SOS, whereas controls had a loss in these measurements [144]. QUS was, however, less sensitive to detect a relative change due to poorer precision error (technical limitations discussed in Section 1.3.6). Here, Sahota and colleagues [143] reported that QUS measurements had a 3-fold higher relative precision error than DXA, and Frost and colleagues [144] found that a lower proportion of patients exceeded the threshold for a clinically significant change compared to the lumbar spine. These findings partly support why QUS is not recommended for treatment monitoring by the ISCD [113].

Calcaneal BMD also changes with bisphosphonate treatment. Ringe and colleagues [145] reported an increase in calcaneal BMD of 15.5% (±10.7%) following a 24-month treatment with ibandronate in men and women with corticosteroid-induced osteoporosis, which was approximately 8% higher than patients treated with alfacalcidol. Leal et al., [146] showed 12 months of zoledronic acid treatment in women with breast cancer increased calcaneal BMD by 2%, with no change in the control group. Paggiosi et al., [147] found that postmenopausal women with osteoporosis prescribed oral bisphosphonates for 96 weeks had a significant increase in calcaneal aBMD than that reported at baseline (+2.0±4.4%), albeit a similar mean change was observed in a to premenopausal control group (+1.7±2.5%). However, changes from baseline were not apparent for other

peripheral sites (radius-ulna BMD, tibia vBMD at the 4% and 33% site), apart from a smaller increase (+0.4±1.2%) in total vBMD at the radius diaphysis.

While some of these trials demonstrated a treatment-response of the calcaneal BMD and/or QUS, the effect was small compared to those observed at the lumbar spine and, to a lesser extent, the proximal femur. The greater variance observed in the calcaneus compared to the central sites, may reflect the poorer precision of measurement techniques rather than actual biological changes in calcaneal aBMD.

1.4.5 Summary

It has been shown that measurements of the intrinsic characteristics of the calcaneus measured using aBMD and QUS, are reflective of loading, fracture risk and treatment/intervention responses. The devices that have been used to quantify the calcaneus have great applicability in large population studies, particularly in associating measurements with physical activity and fracture risk. However, these methods appear to lack sensitivity to detect changes and have questionable precision.

Thesis rationale

The thesis rationale can be summarised from previous sections:

- The calcaneus provides an accessible site of the peripheral skeleton, which appears to be readily responsive to loading and pharmacological intervention.
- Methods used to measure the intrinsic characteristics of the calcaneus lack sensitivity to quantify bone microstructure.
- HR-pQCT is currently the best available technique for compartmental measurements of trabecular and cortical bone at a low radiation dose.

Developing a method to image and quantify the intrinsic characteristics of the calcaneus using HR-pQCT has not been undertaken previously. Improving upon aspects from other non-invasive assessment devices, related to sensitivity and precision, may give greater purpose to using the calcaneus as a surrogate in interventional research studies, particularly those assessing the effects of mechanical loading and unloading alone or in combination with pharmacological therapies.

There have been suggestions of mechano-interactions with teriparatide (anabolic) treatment by comparing the response at the radius and tibia using HR-pQCT [148], and at the proximal femur using QCT [65]. Anabolic treatment may lower the customary strain stimulus required for mechanical adaptations. If this concept is proven, the combination of teriparatide and exercise could be important for populations that cannot undertake high-impact activities e.g. osteogenic. The calcaneus is exposed to high compressive (subtalar articular surface) and tensile stress (Achilles tendon attachment), and investigation with HR-pQCT may help to confirm whether these interactions are present.

In the wider context, the resources required for interventional mechanical loading studies can lead to high study costs. Novel methods are therefore sought after to detect microstructural changes in bone using a lower number of participants and earlier measurement endpoints. Calcaneus HR-pQCT measurements may provide a new alternative option for these studies.

Aims and objectives

The aim of the work described in this thesis was to develop a protocol to quantify bone density and bone microstructure in the human calcaneus. The method was developed using HR-pQCT as the imaging device. After this Introduction and the Chapter described in the Methods, Chapters 3-6 represents a chronological overview of the work.

Chapter 3 − To develop a protocol to scan the calcaneus using HR-pQCT in human cadaveric specimen.

1. To optimise foot positioning for the calcaneus HR-pQCT scans.
2. To compare trabecular vBMD and trabecular microstructure measurements between the inferior, middle and superior regions of the calcaneus tuberosity.
3. To evaluate trabecular vBMD and trabecular microstructure measurements with 5 (0.41 mm), 10 (0.82 mm) and 20 slice (1.64 mm) deviation in the measurement region in the calcaneus tuberosity.

Chapter 4 − To validate the calcaneus HR-pQCT measurements with respective to micro-CT measurements.

1. To determine the accuracy of trabecular bone volume and microstructure measurements using HR-pQCT, at the superior, middle and inferior regions of the calcaneus tuberosity, with respect to gold standard micro-CT measurements.
2. To characterise the effect of scan integration time on trabecular microstructure measurements on calcaneus HR-pQCT scans, with respect to gold standard micro-CT measurements.
3. To determine whether surrounding bones of the foot affect the accuracy of calcaneus trabecular bone volume and microstructure measurements using HR-pQCT.

Chapter 5 – To optimise the quantitative assessment of the calcaneus using HR-pQCT in vivo.

1. To compare image movement artefact grades between the 100ms and 200ms integration time calcaneus HR-pQCT scans.
2. To compare volumetric bone mineral density and trabecular microstructure between the 100ms and 200ms integration time calcaneus HR-pQCT images.

3. To compare the volumetric bone mineral density and trabecular microstructure between the superior and inferior region of the calcaneus HR-pQCT images.
4. To identify practical issues in positioning of the participant and the lower-limb that would compromise the application of the calcaneus HR-pQCT *in vivo*.

Chapter 6 – To determine the short-term measurement precision error for calcaneus HR-pQCT images.

1. To determine the short-term precision errors for volumetric bone mineral density and trabecular microstructure in calcaneus HR-pQCT images.
2. To compare measurements' coefficient of variation between unregistered, cross-sectional area (CSA)-based registered and 3D registered HR-pQCT images.
3. To compare volumetric bone mineral density and trabecular microstructure between the non-dominant and dominant calcaneus HR-pQCT images.
4. To compare volumetric bone mineral density and trabecular microstructure between calcaneus, distal radius and distal tibia HR-pQCT images.
5. To test associations between calcaneus, distal radius and distal tibia volumetric BMD measurements, and lumbar spine and proximal femur areal BMD measurements.

CHAPTER 2 METHODS: SCAN ACQUISITON AND EVALUATION

2.1 Dual-energy x-ray absorptiometry

DXA was used to determine aBMD of the lumbar spine (L1-L4), total hip and the calcaneus using a Discovery A densitometer (Hologic Inc.: Bedford, MA, USA) using Hologic software (version 12.6). This obtains a single 2D projection of the anatomical site of interest where outcomes such as bone area, bone mineral content (BMC) and aBMD are measured. aBMD is used to calculate T-scores to diagnose osteoporosis and is therefore incorporated into the clinical decision making process for determining fracture risk.

2.1.1 Principles

DXA uses the two different photon beam (x-ray) energies (high and low) to determine the attenuations from two different reference materials: bone mineral hydroxyapatite ($Ca_5(PO_4)_3OH$) and soft tissue (which have different electron densities, Section 1.3). Energies are typically set at a level just above the attenuation level for the material (K-edge filter) so that photons drop dramatically once they are transmitted through the material. Following transmission where photons are absorbed (photoelectric absorption) or scattered (Compton), photons are detected by a linear multi-detector array. An absorbed photon that uses up all its energy will not scatter, where as a partially absorbed photon will change direction (or scatter) with less energy and in a different detector. The detected photons are converted into a pixel intensity map representing the site that was scanned with attenuations (i.e. different greyvalues) that are dependent on the low and high energies.

Blake and Fogelman [149] described the attenuation of bone and soft tissues at the two different energies using the following formula:

$$\text{Low energy: } I' = [I'_0 \exp] - (\mu'_S M_S + \mu'_B M_B) \qquad \text{Equation 2.1}$$

$$\text{High energy: } I = [I_0 exp] - (\mu_S M_S + \mu_B M_B) \qquad \text{Equation 2.2}$$

where, I is the beam intensity, $'$ is for low energy, μ is the mass attenuation coefficient, M is the areal density, and $_B$ and $_S$ represent bone and soft tissue, respectively.

Blake and Fogelman [149] then placed J in place of the logarithmic transmission factor of I_0 to calculate the areal bone density (M_B):

$$M_B = \frac{(J' - kJ)}{(\mu_S' - k\mu_S)} \quad \text{Equation 2.3}$$

where:

$$k = \frac{\mu_S'}{\mu_S} \quad \text{Equation 2.4}$$

Edge-detection algorithms are used to identify bone edges on the pixel intensity maps, which precede the calculation of aBMD, bone area and BMC from the scans.

The M_B across the scan region of interest is then computed as aBMD, in grams per centimetre squared (g/cm^2). The bone area is the sum of the pixels in the region of interest (cm^2). The total mass of bone hydroxyapatite is expressed as BMC (g), and is calculated using aBMD and bone area [149]:

$$\text{BMC (g)} = \text{aBMD} \times \text{bone area} \quad \text{Equation 2.5}$$

The primary application of aBMD at central sites has been for diagnostic purposes and for the assessment of fracture risk. In this application, gender- and ethnicity-specific Z-scores and T-scores are calculated, which compares the individuals aBMD to an age-matched mean or a young, normal adult mean, respectively [37]. Equation 2.6 and Equation 2.7 shows how a Z-score and T-score is calculated using aBMD, respectively:

$$\text{Z-score} = \frac{\text{Measured aBMD} - \text{Age-matched mean aBMD}}{\text{Age-matched population SD}} \quad \text{Equation 2.6}$$

$$\text{T-score} = \frac{\text{Measured aBMD} - \text{Young adult mean aBMD}}{\text{Young adult population SD}} \quad \text{Equation 2.7}$$

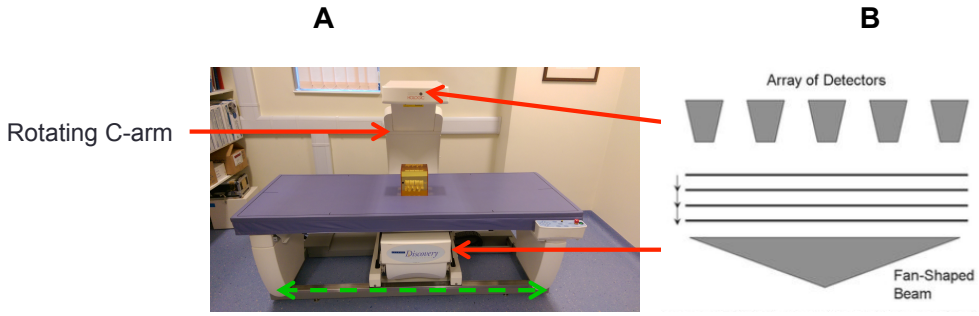

Figure 2.1. The Hologic Discovery dual-energy x-ray absorptiometry scanner (A) with fan-beam and detector technology (B).

The x-ray fan beam and rotating C-arm can move along the side to scan optimise positioning (green, dashed arrow).
Figure 2.1B sourced from Bonnick and Lewis [150].

2.1.2 Image acquisition and analysis

All DXA images were obtained using the manufacturer's standard procedures for each skeletal site, as described previously within our Research Group [21, 147, 151]. Participants' scans were obtained in the posterior-anterior projection using a dual-energy, low 100 peak kilovoltage (kVp) and high 140 kVp, x-ray with a current of 10 milliampere (mA).

2.1.2.1 Lumbar spine

Participants were positioned on the DXA scan bed in a supine, straight and central position with arms rested flat on either side (Figure 2.2). Legs were raised on a scan-positioning block provided by the manufacturer. The C-arm was positioned level with the participants' iliac crest using the DXA cross-hairs. Scout views were obtained from the mid-L5 to the mid-T12 so that vertebrae L1-L4 were captured: if required, the C-arm was repositioned to ensure the lumbar spine was within the scanning reference limits. Once in the correct position, the array mode was used for the DXA scan.

For image analysis, the global region of interest was positioned from the T12-L1 intervertebral space to the L4-L5 intervertebral space (white borders). The operator manually altered the L1-L4 intervertebral borders if there were clear positional discrepancies, and no changes were made to the L1-L4 right-left borders, unless vertebrae were excluded if they were deemed to be fractured or had severe degenerative changes. Sub-region analysis was then completed of each lumbar vertebra.

A B

Figure 2.2. Lumbar spine DXA scan.

A – Participant positioning for the lumbar spine scan.
B – Region of interest placement for the lumbar spine pixel intensity map.

2.1.2.2 Proximal femur

Participants were positioned on the DXA scan bed in a supine, straight and central position with arms on the chest (Figure 2.3). The limb being measured was rotated inwards by 15 to 20° using an angled foot positioning device provided by the manufacturer (Figure 2.3). This positioning is critical for positioning reproducibility of the proximal femur: the aim was to (i) achieve parallel positioning of the femoral neck to the scan bed and (ii) to ensure only a small portion of the lesser trochanter was seen on the scan image. Correct positioning was confirmed through obtaining a scout view prior to the DXA scan acquisition. The acquisition was completed in the array mode and included the entire femoral head, neck and approximately 3cm of the femoral shaft below the lesser trochanter.

For image analysis, the global region of interest was positioned in relation to anatomical features of the proximal femur from the left limb (Figure 2.3): (i) the upper border was positioned 5 scan lines away from the edge of the femoral head; (ii) the bottom border was positioned 10 scan lines below the lesser trochanter; (iii) the medial border was 5 scan lines from the edge of the femoral head; (iv) the lateral border was 5 scan lines from the edge of the greater trochanter. Sub-region analysis was completed to identify the central hip axis, the femoral neck box and the greater trochanteric region (Figure 2.3).

A B

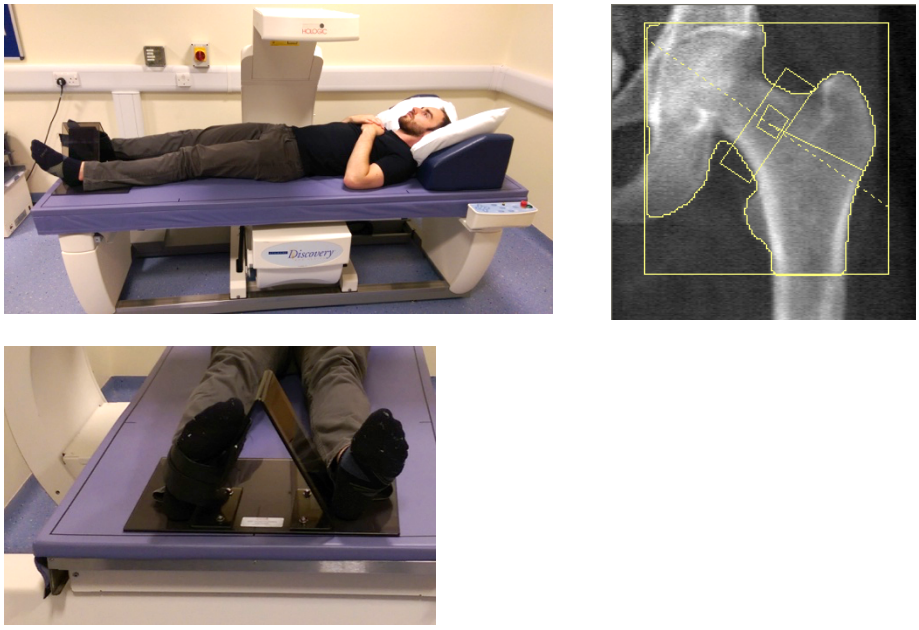

Figure 2.3. Proximal femur DXA scan.

A – Participant positioning for the proximal femur scan.
B – Region of interest placement for the proximal femur pixel intensity map.

2.1.3 DXA outcome precision error

The precision error, expressed as the coefficient of variation, for the lumbar spine DXA scans in our Research Group are 1.2% for bone area, 1% for aBMD and 2.2% for BMC, for adults with normal body mass index. The scan technician completing the measurements is certified by the ISCD, which requires a minimum precision of 1.8% at the total hip and 2.5% at the femoral neck from DXA image measurements.

2.1.4 DXA quality control checks

One highly trained operator performed all DXA scans, eliminating inter-operator reliability. Procedures employed by the Research Group ensure daily quality control checks of the scanner, in accordance with manufacturer recommendations. Quality control checks are completed with an anthropomorphic spine phantom, containing four single density, semi-hydroxyapatite 'vertebrae'. All measurements (bone area, aBMD and BMC) were within the limits of agreement set by the manufacturer and the coefficient of variations were below 0.8% over the period of which the scans were obtained (Appendix Figure 9.1).

2.2 Computed tomography

2.2.1 Principles

CT is an x-ray based technique that enables the three-dimensional quantification of tissue. Similar to DXA, photons pass through the participant and have different attenuations based on the tissues they pass through. The detected attenuation coefficient of the voxels is transformed into a CT number, known as Hounsfield Units (HU) for describing radiodensity. Here, water is defined as zero HU and air is defined as -1000 HU [60]:

$$CT\ number\ [HU] = (\frac{\mu - \mu_{water}}{\mu_{water}}) \times 1000 \qquad \text{Equation 2.8}$$

where μ is the average linear attenuation coefficient for the voxel, μ_{water} is the linear attenuation coefficient of distilled water at room temperate. There is a spread of HU for different tissues based on the HU scale transformation: the most distinctly attenuated tissue is bone. Several parameters in the CT acquisition and reconstruction can impact the discrimination between the bone and marrow phases. Key parameters include [60, 152]:

X-ray tube voltage (kilovolt peak, kVp) – Determines the maximum voltage or photon energy. This also impacts BMD calibration when used quantitatively.

X-ray tube current (milliamperes, mA, or microamperes, μA) – Determines the total number of photons that each tomographic projection is exposed to.

Scan integration time (ms) – Determines the exposure duration for each tomographic projection (i.e. shutter open time).

Reconstruction field of view – Determines the voxel size in the image matrix to which grey-values are assigned.

Slice thickness (mm or μm) – Determines the smallest thickness of the 2D CT slices.

Exposure factors (i-iii) dictate the radiation exposure and scan duration. Optimising the x-ray intensity (ii and iii) is important to improve image signal-to-noise ratio. Reconstruction factors (iv and v) determine the voxel size and spatial resolution in the images, and are critical to the accurate quantification of bone composition using CT [77, 153].

QCT is used to measure bone properties from CT images. To quantify BMD, calibration phantoms containing hydroxyapatite rods are able to convert the HU into BMD (g/cm^{-3}) using a regression slope and intercept. Here, three-dimensional volumetric densitometry and morphological information on bone can be obtained using post-scan processing methods.

The primary advantage of QCT over DXA is that the attenuated photons are detected over multiple projections, rather than one. This is achieved by multiple detectors rotating around the participant during image acquisition, resulting in multi-slice images of tissues that are reconstructed as volumes. Several advantages have been found using QCT over DXA to quantify bone properties, such as measuring bone shape and size and quantifying trabecular and cortical bone compartments. An additional advantage is that CT is free from inaccuracies due to extra-osseous calcification and degenerative changes, such as in the spine, which becomes amalgamated and consequently identified as bone using DXA. CT scanners can also be equivalently calibrated, as water has a QCT number of 0, unlike DXA.

There are also disadvantages associated with CT, such as the high ionizing radiation exposure at the spine and hip (upto 3 mSv), the expense and accessibility compared to DXA, and its ability to measure microstructural properties of bone *in vivo*. QCT, like DXA, is also unable to quantify bone material properties beyond bone mineral, such as collagen fibre organisation, and therefore excludes an important component of fracture risk.

2.3 High-resolution peripheral quantitative computed tomography

HR-pQCT was used to quantify vBMD and bone microstructure at the radius, tibia and calcaneus, using the first generation XtremeCT device and the SCANCO Image Processing Language (IPL, version 5.08-B) (SCANCO Medical AG: Brüttisellen, Switzerland). The advantages of HR-pQCT compared to multidetector-CT are that there is superior signal-to-noise ratio and spatial resolution, the radiation dose is significantly and does not involve radiating organs located in proximity to the axial skeleton. However, this also highlights its disadvantages compared to CT, as it is limited to peripheral sites of skeleton, where the lumbar spine and proximal femur carry a large proportion of the osteoporotic fracture burden.

The image acquisition, reconstruction and evaluation is outlined in this Methods Chapter and is consistent with clinical studies using this version of the device.

2.3.1 Image acquisition

HR-pQCT image acquisition for the distal radius and distal tibia followed the standard protocol provided by manufacturer.

HR-pQCT uses cone beam technology and obtained projections by one single rotation of the x-ray source and detector around 180º. The standard operational settings for clinical scans were an x-ray tube potential of 60 kVp, an x-ray tube current of 95 mA, and collection of 750 projections at an integration time of 100 ms. Each HR-pQCT scan was 9.02 mm in length, which was equivalent to 110 slices when considering the first generation XtremeCT isotropic voxel size of 82 µm. This resulted in a scan duration of 2.8 minutes and a radiation dose of 3 µSv per scan, which was equivalent to half a normal day's background radiation.

2.3.1.1 Distal radius HR-pQCT procedure

Self-report was used to identify the hand dominance for the distal radius HR-pQCT scans, by asking, "What hand do you write with?" The participant was then asked if they have suffered a previous fracture at the non-dominant location. If so, the dominant side was used and noted. The participant was seated and the forearm was placed in the forearm cast, with the hand lightly clasping the handle (Figure 2.4). Foam and positioning aids were used to secure the form and minimise movement. The cast was secured in the scanning gantry and a scout view was performed. The scout view start and end position was set to 90 mm and 120 mm, respectively. A reference line was placed on the slight curvature of the articular surface between the scaphoid and lunate fossae of the radiocarpal joint [154]; a fixed offset of 9.5 mm [1] was applied from the reference line to identify the measurement region.

Participants were asked to remain motionless during the image acquisition. At the end of each scan, the operator assessed the image quality of a single slice using a visual grading system, described by Engelke and colleagues [155]:

Grade 1 = Perfect: No noticeable artefacts.
Grade 2 = Slight artefact: small streaking.
Grade 3 = Pronounced artefact: large streaking, particularly near the cortex.
Grade 4 = Unacceptable artefacts: discontinuity at the cortex.

[1] A fixed offset is used for the standard HR-pQCT protocols (distal radius and distal tibia) in our Research Group. There have been recent publications using relative offsets based on participants' anatomy to remove positional errors due to radius and tibia length. This method has not yet been tested in our Research Group and was therefore not applied in the thesis.

Images given a grade 3 were repeated to see if the image quality could be improved; if the image quality was not improved, the grade 3 image was used for evaluation. Images given a grade 4 were repeated; if the repeated image quality was graded 4, the images were removed from the evaluation. Here, only images with a grade 1, 2 and 3 were used for evaluation.

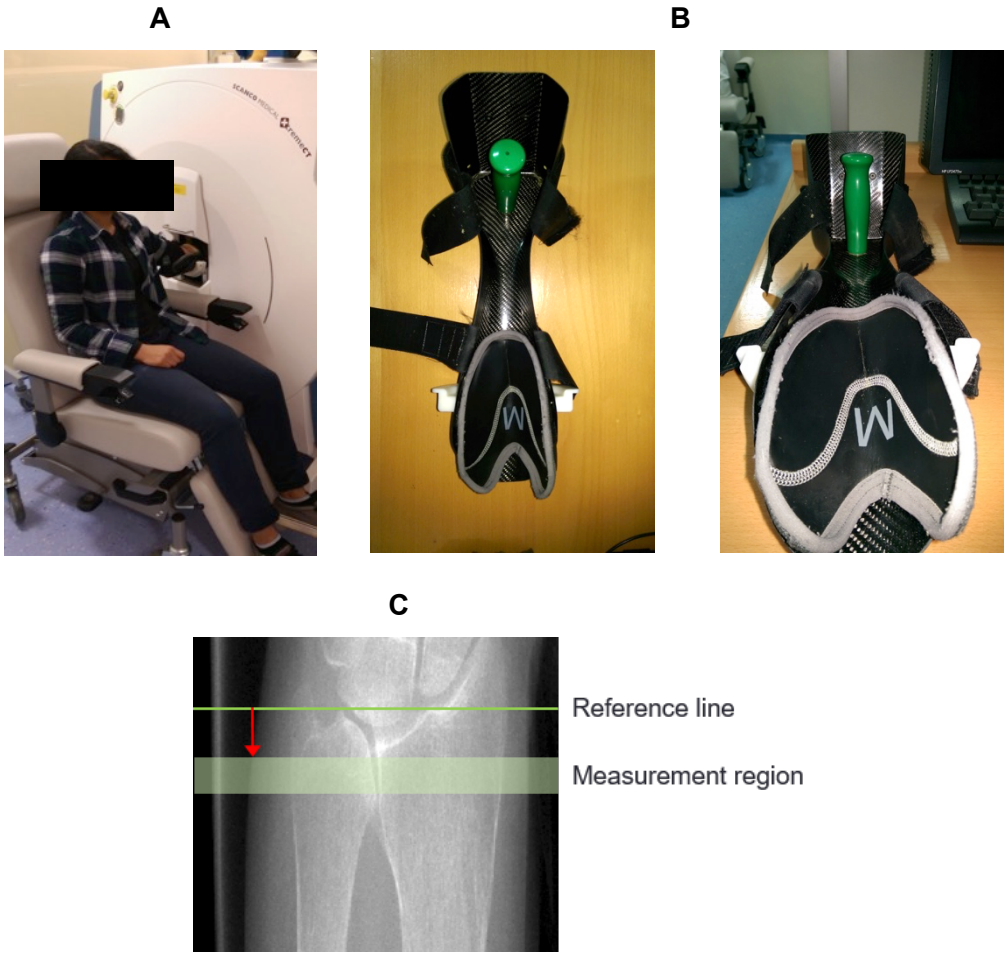

Figure 2.4. Participant positioning for distal radius HR-pQCT scans.

A – Participant positioning.
B – Upper-limb cast from two different viewpoints.
C – Scout view for the distal radius with the reference line placement and measurement region. The XtremeCT elongates the radiograph automatically.

2.3.1.2 Distal tibia HR-pQCT procedure

Self-report was used to identify the foot dominance for the distal tibia HR-pQCT scans, by asking, “What foot would you kick a ball with?” The participant was then asked if they have suffered a previous fracture at the non-dominant location. If so, the dominant side was used and noted. The participant was seated and the lower-limb was placed in the tibia cast, with the foot placed flat on the bottom of the cast

(Figure 2.5). Similar to the radius, foam and positioning aids were used to secure the lower-limb in the cast. The cast was secured in the scanning gantry and a scout view was performed. The scout view start and end position was set to 73 mm and 103 mm, respectively. A reference line was placed at the peak of the tibial articular plateau at the tibiotalar joint [154]; a fixed offset of 22.5 mm was applied from the reference line to identify the measurement region. The image acquisition and assessment of image quality was identical to that for the distal radius HR-pQCT procedure.

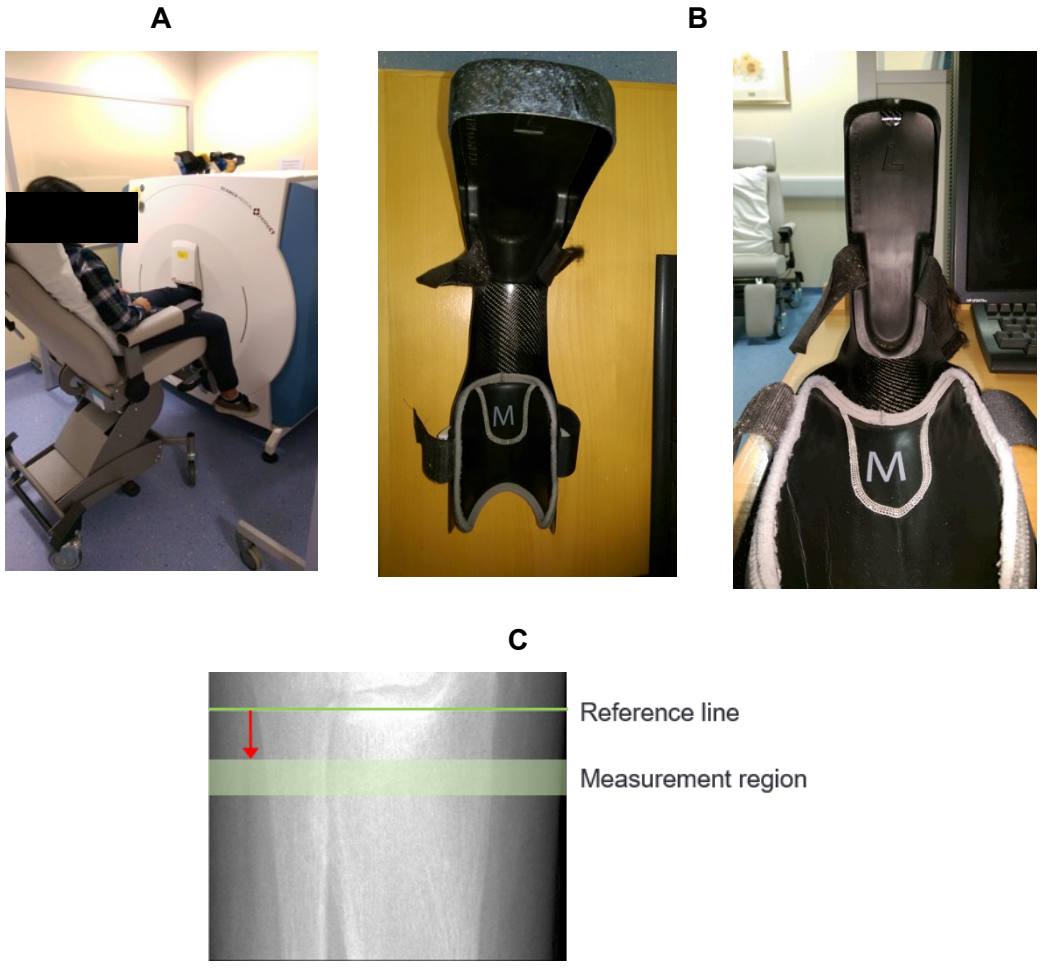

Figure 2.5. Participant positioning for distal tibia HR-pQCT scans.

A – Participant positioning.
B – Lower-limb cast from two different viewpoints.
C – Scout view for the distal tibia with the reference line placement and measurement region. The XtremeCT elongates the radiograph automatically.

2.3.2 Image reconstruction

HR-pQCT image reconstruction followed the standard protocol provided by manufacturer.

A beam hardening correction (BHC) filter with a 200 mg HA/cm^{-3} step wedge function was applied during image reconstruction [156]. The BHC filter aims to mitigate the beam hardening artefacts caused by preferential attenuation of low energy beams, which can result in a 'cupping profile' and can cause inaccuracies in attenuation measurements e.g. BMD (Figure 2.6); this is a common artefact with polychromatic x-ray sources.

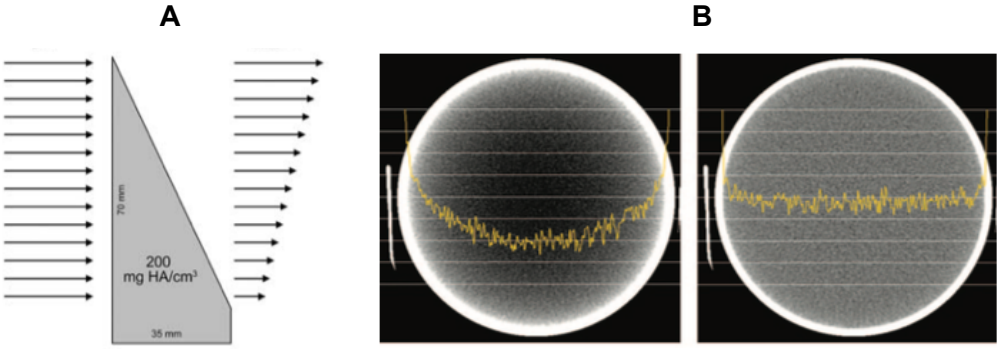

Figure 2.6. Beam-hardening correction.

A – 200 mg HA/cm^{-3} beam hardening step wedge phantom (sourced, Burghardt et al., [157]).
B – Example of a CT slice without beam hardening correction (left) and after beam hardening correction (right) (sourced from Barrett & Keat [158]).

The corrected reconstructed linear attenuation was mapped onto a 1536 x 1536 matrix over a 126 x 126mm field of view, yielding an isotropic 82 µm voxel size. Calibrations of the densities were performed on a weekly basis using a phantom supplied by the manufacturer, which has a soft tissue density (0 mg HAcm^{-3}) and HA rods at 100, 200, 400 and 800 mg HAcm^{-3} embedded in resin (Figure 2.7B). In comparison to the standard quality control procedure, which recommends that the error for the highest density rod error is within 1% i.e. ±8 mg HA/cm^{-3} [81], the error for the highest HA density rod was towards the lower limit of error for the duration of the study period (Figure 2.8).

In a multi-centre study, the spatial resolution of reconstructed images was reported as approximately 120 to 150 µm at the centre of the field of view, and between a mean 140 to 170 µm at a distance of 30 mm from the field of view centre [96].

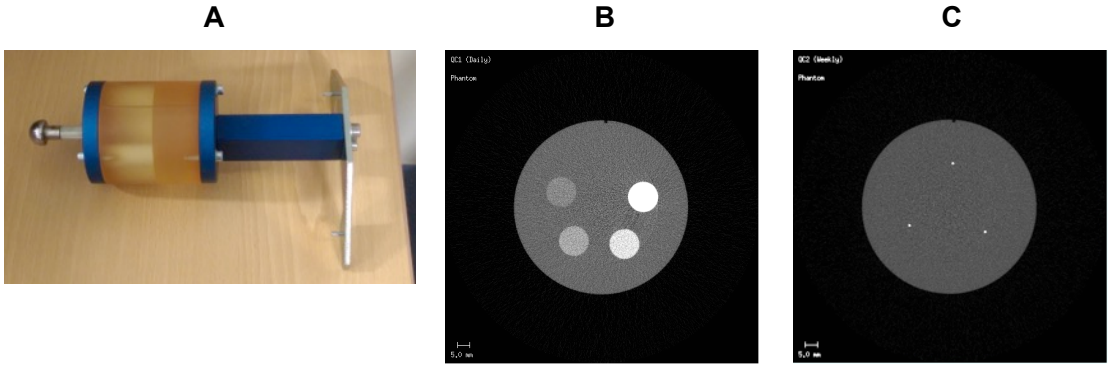

Figure 2.7. HR-pQCT calibration equipment and images.

A – The HR-pQCT phantom.
B – Image of the density phantom.
C – Image of the alignment phantom.

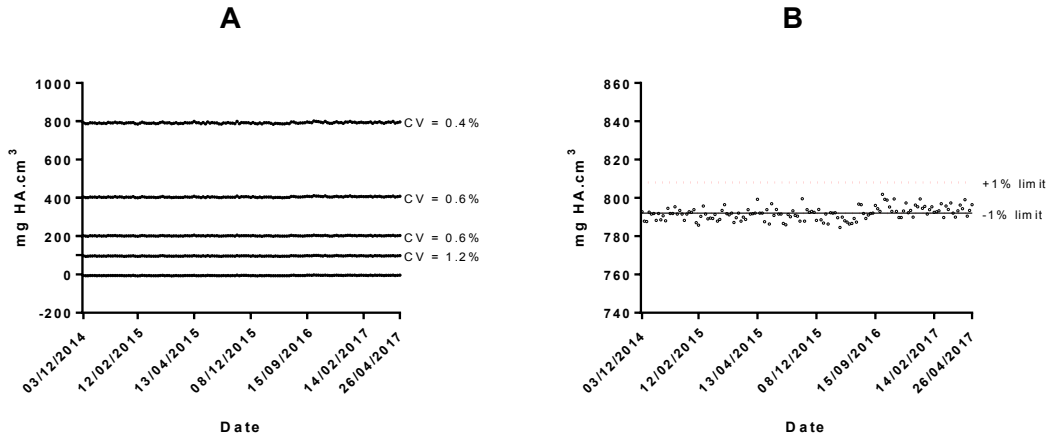

Figure 2.8. Quality control plots for the HR-pQCT density phantom over the study period.

A – Measurements for the hydroxyapatite rods with % coefficient variations.
B – Comparison of the 800 mg HA/cm^{-3} measurement to the limits of error.

2.3.3 Image evaluation

Following image reconstruction, a series of steps were performed to segment the image and obtain HR-pQCT measurements using the Scanco IPL.

2.3.3.1 Image segmentation

The operator performed a semi-automated contouring procedure around the periosteal boundary of the bone for all HR-pQCT image slices. First, a graphical object (GOBJ) was created in close proximity to the periosteal boundary. An automated edge detection algorithm was run, using the default settings for edge detection and a '2 times' iteration setting, to 'snap' the GOBJ to the periosteal boundary. The automated algorithm was stopped at 10 to 20 slice intervals to check

the quality of the periosteal edge detection on each slice; if results were unsatisfactory the GOBJ was manually corrected. The time to create an accurately placed GOBJ around the radius and tibia HR-pQCT images was approximately 60 minutes.

2.3.3.2 Image quantification

HR-pQCT images were quantified using the manufacturers 'standard clinical evaluation' script, specific to the first version of the XtremeCT; this uses a Laplace-Hamming filter to smooth the image and enhance edges, and then applies a 40% fixed, global threshold to segment (binarise) the bone from marrow phase [159].

From the greyscale HR-pQCT images, total vBMD, including both the trabecular and cortical bone, was calculated from the average mineral density in milligrams of hydroxyapatite per centimetre cubed (mg HA/cm^{-3}). Trabecular vBMD is further compartmentalised into inner and outer trabecular vBMD; the inner measurement is calculated as the inner 40% of trabecular area, and the outer measurement in the outer 60% of trabecular area. vBMD measurements were calculated using a calibration of HU attenuation values to HA density using a linear conversion, based on the measurements made on the manufacturer's calibration phantom.

A separate procedure was used to quantify the trabecular and cortical bone compartments using the manufacturers 'standard clinical evaluation', which has been outlined by Davis and colleagues [160]; a Gaussian filter (sigma = 2, support = 3) is applied to remove the finer trabecular bone structures from the medullary compartment, whilst preserving the cortical shell. A fixed global threshold (16% of the range) is then applied to segment the cortical from the trabecular bone compartment. However, thin segments of cortical bone can be lost with the Gaussian blurring and the accuracy of the fixed threshold may be perturbed if mineralisation of the bone changes with disease or pharmaceutical treatment [160]. A 'dual-threshold' algorithm is also used to better estimated cortical bone volume and thickness [161], as well as measuring cortical porosity [162]. Nonetheless, it has been reported that there is still good agreement between measurements extracted from the trabecular bone phases from the manufacturers 'standard clinical evaluation' and the 'dual-threshold' methods [161], such as trabecular bone volume fraction (BV/TV), trabecular number (Tb.N*), trabecular thickness (Tb.Th) and trabecular spacing (Tb.Sp).

Measurements of trabecular bone microstructure are computed, rather than measured directly, due to the closeness of the physical dimensions of individual

trabeculae (~200 μm) to the spatial resolution (120-150 μm [96])[2]. Direct quantification results in partial volume effects affecting measurement accuracy, leading to a 2-3 fold overestimation of BV/TV and Tb.Th [159, 163, 164]. In order to provide more accurate estimations, the following methods were used and are a part of the 'standard clinical evaluation':

BV/TV is derived from the *trabecular vBMD* divided by 1200 mg/cm^3 hydroxyapatite (now abbreviated to *BV/TV^d*); the figure is chosen to represent mineralised bone, and the calculation assumes all trabeculae have a this density [159].

From the binary HR-pQCT image, the mean *Tb.N** is computed using a mid-axis transformation to find the trabecular ridges [165] and the distance transformation method to calculate the distances between the ridges of a skeletonised binary image [166] (Equation 2.9 and Figure 2.9):

$$TbN = \left(\frac{1}{p} \sum_{j=1}^{i=p} DT(MAT(Image))_j \right) \qquad \text{Equation 2.9}$$

where, *p* is the distances between the ridges, expressed as an average over all inter-ridge voxels, *DT* is the distance transform between the trabecular bone ridges that is calculated from the diameter of a sphere, and *MAT* is the mid-axis transformation between the trabecular bone ridges that is calculated by a sphere [100].

Tb.Sp and *Tb.Th* are derived (from now on abbreviated to *Tb.Sp^d* and *Tb.Th^d*) using plate-model assumptions [167, 168], as shown in Equation 2.10 and Equation 2.11. Therefore, the accurate measurement of *trabecular vBMD* and *Tb.N** are critical to the measurement of trabecular microstructure from images obtained using the first generation XtremeCT.

$$\text{Tb.Th}^d = \frac{BV/TV^d}{Tb.N^*} \qquad \text{Equation 2.10}$$

$$\text{Tb.Sp}^d = \left(\frac{\left(1-BV/TV^d\right)}{Tb.N^*}\right) \qquad \text{Equation 2.11}$$

[2] The second generation XtremeCT has been recently made available commercially (2014), and has an isotropic voxel size of 61 μm and a spatial resolution of 95 μm. With the improved spatial resolution, this device directly measures BV/TV and the trabecular microstructure.

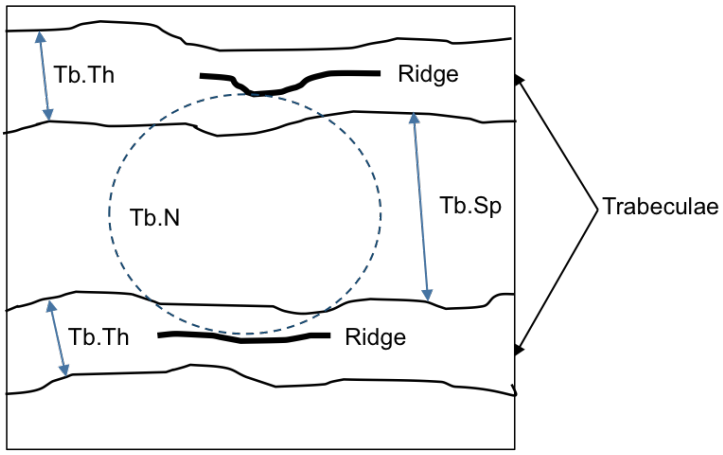

Figure 2.9. Schematic of trabecular number calculation.

The sphere between the trabeculae ridges is a visual representation of the Equation 2.9.

2.4 Micro-computed tomography

Micro-CT was used to quantify trabecular BV/TV and bone microstructure in samples dissected from human cadaveric calcanei (SkyScan 1172, Brüker: Kontich, Belgium). Micro-CT images were used as the 'gold standard' in order to validate measurements obtained from HR-pQCT images (Chapter 4). This section will describe the micro-CT procedure that was used to quantify trabecular microstructure of human bone samples.

Micro-CT has similar properties and uses similar components to HR-pQCT (Figure 2.10). Most desktop micro-CT devices use a cone beam technology and a polychromatic x-ray source, exposing samples to a range of photon energies. Monochromatic beam is also possible using synchrotron radiation micro-CT, but is only available at a few specialist centres worldwide. An advantage of micro-CT is that it can operate at a smaller voxel size (down to 1 μm) compared to HR-pQCT, and therefore a higher spatial resolution. Here, micro-CT can provide a good representation of trabecular and cortical microstructure compared to bone histomorphometry [169, 170], without using a destructive procedure to obtain serial sections of bone. However, its application in humans is limited to samples *ex vivo*, such as bone biopsies or samples extracted from cadaveric specimens.

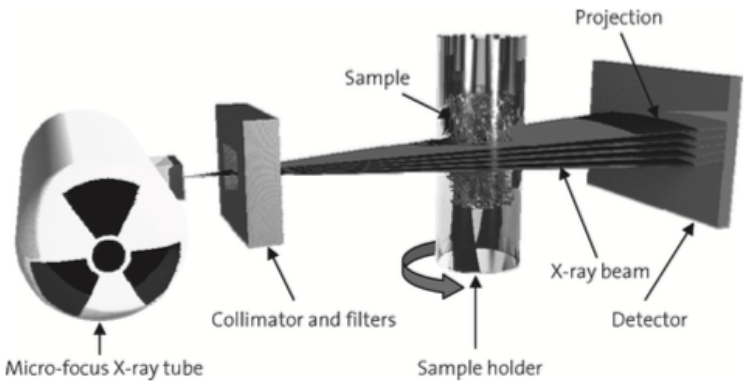

Figure 2.10. The main components of micro-CT scanning.

Sourced from Stauber and Müller [171].

2.4.1 Image acquisition

The SkyScan 1172 was used for micro-CT image acquisitions. Standard components of the micro-CT include: an 11 megapixel X-ray camera that can scan a matrix of up to 8000 x 8000 pixels per slice; a fixed x-ray tube and detector; a motorised sample holder that rotates 360° within the field of view during the acquisition of radiographic projections. The scan settings that were used had been previously optimised in the Mellanby Centre for Bone Research, Skelet.AL (Skeletal Analysis Laboratories), Department of Oncology and Metabolism at the University of Sheffield, using a bovine trabecular bone sample (Figure 2.11).

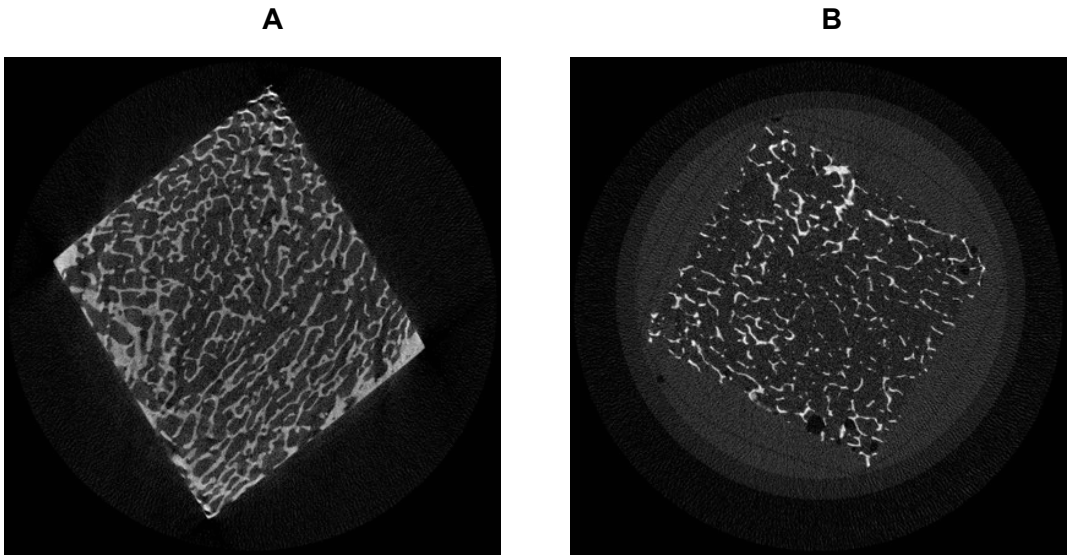

Figure 2.11. 2D micro-CT scan slice of the bovine bone (A) and human cadaveric calcanei (B) tissue.

Contrast added to improve image quality for printing.

Images, collected with an x-ray tube potential of 100 kVp and an x-ray tube current of 100 microampere (μA), were calibrated with flat field corrections to minimise ring-artefact. The scanning camera was set to medium (2000 x 1048 pixel level), which equated to an isotropic in plane pixel size of 17.4 μm; 3 to 4 voxels have been recommended to quantify trabeculae [152] to minimise quantitative bias from partial volume effects (Figure 2.12). This voxel size was comparable to previous studies that have quantified human trabecular bone [77, 169, 172]. A 1.0 mm aluminium foil filter was selected to filter the lower-energy photons to minimise beam-hardening artefact. The scan integration time for each projection was set at 2950 ms and the number of times each projection was repeated (frame averaging) was set at 2. The sample was rotated from 0° to 180° with a 0.7° rotation step. Random movement was turned off. The scan time per field of view was 44 minutes, where each sample was split into 2 or 3 field of views.

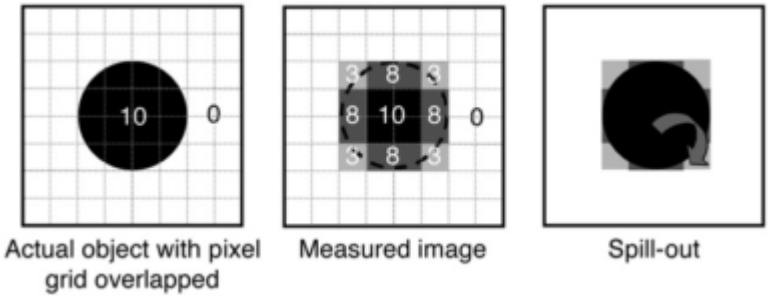

Figure 2.12. Example of partial volume effects.

Pixels containing part tissue and part background have their signal intensities averaged, causing 'spill out'.
Sourced from Soret et al., [173].

Prior to image acquisition, a scout view of the sample was obtained (Figure 2.13). The sample holder was then rotated 359 degrees (one scale marker short of full rotation i.e. the samples original position) to check for lateral movement of the sample; if the sample sides breached the scout view edges, the sample tube was removed and re-glued to the holder. Once these checks had been passed, a reference line was positioned that determined the start position of the scans, ensuring the cortical bone of the calcaneus sample was included.

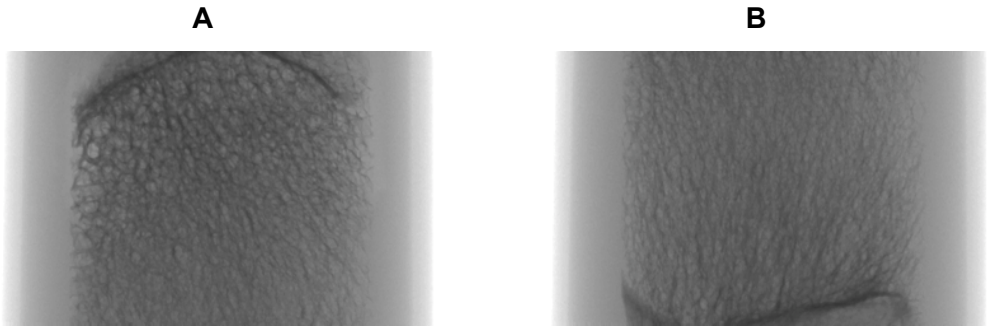

Figure 2.13. Scout view of the sample prior to micro-CT image acquisition.

A – First field of view.
B – Second field of view.
Cortical bone is apparent at the top of image A and at the bottom of image B.

2.4.2 Image reconstruction

The raw micro-CT projections were reconstructed into cross-sectional image slices in the NRecon software (Brüker: Knotich, Belgium).

The image contrast depth was set to 16-bit (with 65,536 grey levels). Here, the minimum grey level for the histogram scale was computed as zero, and the maximum grey level output was computed by the maximum value of the automated histogram multiplied by 0.714; this resulted in an image contrast range from 0 to approximately 0.035. To remove common polychromatic imaging artefacts found with micro-CT, ring artefact removal was set to 10% and a polynomial BHC was set to 30%. The reconstructed images were saved as a TIF format and in DICOM format, and exported to an external hard drive (1 terabyte, Seagate Expansion, Seagate Technology PLC: California, USA).

2.4.3 Image evaluation

The reconstructed DICOMs were imported to the XtremeCT I workstation. Here, the micro-CT images were quantified using the Scanco IPL and the manufacturer's standard methods.

2.4.3.1 Image segmentation

All micro-CT images were evaluated using a square GOBJ that was morphed over a range of 2D slices to create a cubic volume of interest. High frequency noise was removed from the micro-CT images using a Gaussian filter (kernel 1.2, support 2) [152, 163]. Individual slices from each sample were visually examined to test a

range of single-level, global thresholds; this was then optimised at 330/1000 or 33% of the maximum greyscale value (Figure 2.14). Following segmentation, a despeckle algorithm was applied to remove isolated 'bone' regions with a volume lower than 10 voxels (Figure 2.15); this additional filter can remove small islands of noise that may not be removed by the Gaussian filter and the threshold.

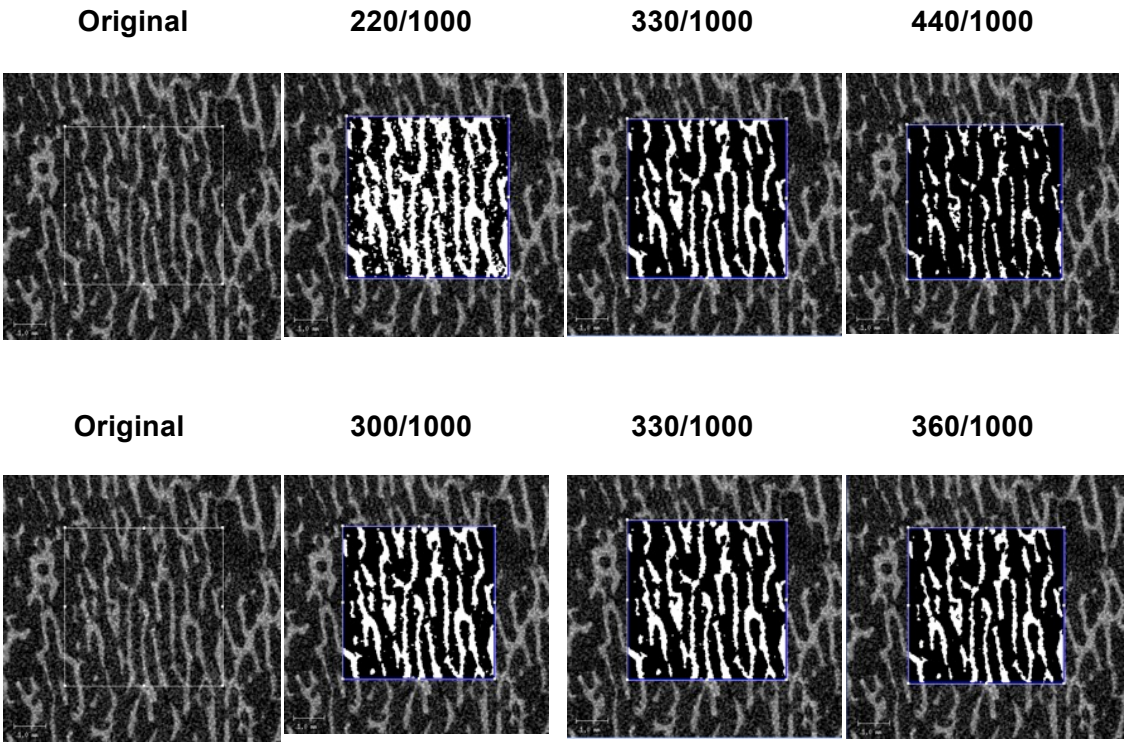

Figure 2.14. Testing the micro-CT image segmentation, following Gaussian filtering.

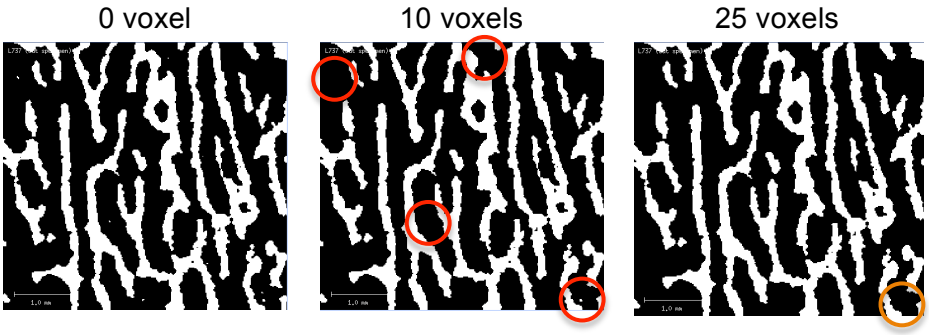

Figure 2.15. Application of the despeckle algorithm.

Red circles indicate the removal of noise from the original scan using a 10-voxel filter. The orange circle indicates the removal of noise using a 25-voxel filter.

2.4.3.2 Image quantification

Standard measurements reported from micro-CT evaluation of trabecular bone were similar to those reported from HR-pQCT scans. Measurements were, however, calculated using a 3D model-independent algorithm in the SCANCO IPL, rather than indirectly for some measurements (i.e. using plate-model assumptions). BV/TV was determined by dividing the number of bone voxels by the total number of voxels in the region of interest (TV). The average measurement for trabecular microstructure is computed from the images, as well as a standard deviation. Trabecular microstructure (Tb.N, Tb.Th and Tb.Sp) were measured using the distance transformation method, where maximal spheres are filled into the segmented image [166].

2.5 Summary of the bone densitometry methods

Table 2.1. Summary of the bone densitometry modalities.

		DXA	HR-pQCT	Micro-CT
Application		Lumbar spine, proximal femur	Radius, tibia and calcaneus*	Calcaneus **
Technical	Areal or volumetric	Areal	Volumetric	Volumetric
	X-ray tube potential	100 and 140 kVp	60 kVp	100 kVp
	X-ray current	10 mA	95mA	100 µA
	Pixel size	1 x 1 mm	82 x 82 µm	17.4 x 17.4 µm
	Slice thickness	N/A	82 µm	17.4 µm
	Scan durations	10 – 30 seconds	2.8 minutes	88 to 132 minutes

Notes: * the details for the calcaneus HR-pQCT scans are provided in Chapter's 3 and 5 of the thesis. ** imaged in human cadaveric calcaneus samples

2.6 Registration of the computed tomography images

The registration of HR-pQCT to micro-CT images was performed in Chapter 4 to enable the validation of HR-pQCT measurements of the calcaneus using Amira (version 6.0, FEI; Oregon, USA). The registration of HR-pQCT to HR-pQCT images was performed in Chapters 5 and 6, to compare HR-pQCT measurements of the calcaneus with different integration times (Chapter 5) and quantify calcaneus HR-pQCT measurements precision (Chapter 6), using the SCANCO IPL registration module (version 1.07).

2.6.1 Principles

Image registration is an important application in medical imaging. Hill et al., [174] defined *registration* as "determining the spatial alignment between images of the same or different subjects, acquired with the same or different modalities". A common 'intra-subject' application is to find the common region, or volume, between prospectively collected images to accurately monitor a person's physiology.

When images are spatially aligned, a *transformation* is obtained that maps the image to its new coordinates. By aligning the two images after the transformation and with a perfect registration, there should be two values at each voxel location.

The registration process can be broadly summarised into the following principles, which have been applied in two registration processes, registering HR-pQCT images and registering HR-pQCT to micro-CT images: *pre-processing*, to align the images being registered; *transformation type*, to define the geometric transformation from one image to the other; *similarity metric*, to determine the spatial alignment between the images; *optimisation*, to maximise the similarity between the images; and *interpolation*, to transform the registered image to its new spatial coordinates

2.6.2 Pre-processing

In the pre-processing of image registration it can be important to define landmarks of interest that can be used to overlap the images prior to spatial alignment.

First, the operator defined the *reference* and *moving* images; here, the *moving* image was spatially aligned to the *reference* image. Second, the *moving* image was aligned to the *reference* image based on the centre of mass and/or its principle axes. This automated image alignment reduced the distance that is searched for registering the images, thus reducing computing time. The operator adjusted the

alignment manually on a case-by-case basis, depending on the quality of the automated alignment, to further reduce the parameter space (image voxels) that was searched: for example, aligning the periosteal landmarks on the QCT scans.

2.6.3 Transformation type

A rigid body transformation is the most common form of registration that is used and preserves the distance between any two points of the images being transformed [174, 175], as shown in Figure 2.16. The rigid transformation (*T*) is defined by 3 rotations (*r*) and 3 translations (*t*) about the x, y and z-axes in each coordinate. This 4x4 matrix contains the information to spatially align and map the coordinates to its new position (Equation 2.12). This is an advantage of registering bone or a tissue enclosed in bone, such as the brain in the skull, due to its rigid structure, and has been frequently applied in studies registering HR-pQCT images [89, 176, 177] and HR-pQCT-to-micro-CT images [77, 163, 164]. Rigid body transformations were therefore applied for the image registration procedures.

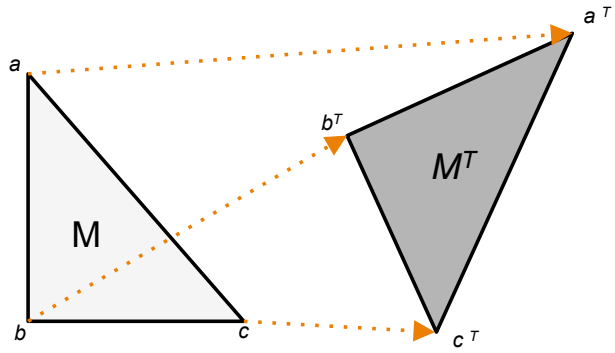

Figure 2.16. Example of rigid body transformation

The distances and angles between *a*, *b* and *c* are preserved in the transformed image (a^T, b^T and c^T)

$$T = \begin{bmatrix} rxx & rxy & rxz & tx \\ ryx & ryy & ryz & ty \\ rzx & rzy & rzz & tz \\ 0 & 0 & 0 & 1 \end{bmatrix}$$

Equation 2.12

2.6.4 Similarity metric

The type of similarity metric used is key to minimising the distance between coordinates of the *moving* and *fixed* images. A voxel-based similarity approach aims to register images based on the degree of shared information by the image

attenuations and intensities (e.g. grey-value histograms). This metric is not as susceptible to registration errors that may be present in feature-based similarity metrics, as it is more robust to changes in the structure i.e. growth with skeletal development or degradation with disease.

The similarity metric used for voxel-based approaches with HR-pQCT has followed earlier work using micro-CT images [178, 179]. For mono-modality images, similarities from the grey-level histogram can be used, such as correlation coefficient method that searches for a linear relationship between the intensities. This is available through the Scanco IPL and performs well in short-term repeat intra-subject HR-pQCT scans [177]. Therefore, the correlation coefficient metric has been applied in the HR-pQCT to HR-pQCT image registrations (Chapter 5 and 6).

The mutual information metric uses voxel intensity to measure how much information, or entropy, one image has about another image [180]. The metric is recommended for multi-modality image registration for diagnostic purposes [175], and has been specifically selected to register HR-pQCT and micro-CT images [30, 77, 163, 164, 181]. The individual voxel grey values of an image can be weighted and interpreted as a probability distribution i.e. how often does a grey value occur in the image and dividing those by the total number of occurrences [175]. This is known as *Shannon entropy* and is calculated for two images, *M* and *N*, as follows [180]:

$$H(M) = -\sum_{m \in M} p(m) \log p(m) \qquad \text{Equation 2.13}$$

$$H(N) = -\sum_{n \in N} p(n) \log p(n) \qquad \text{Equation 2.14}$$

In Equation 2.13 and Equation 2.14, $m \in M$ and $n \in N$ represents the whole set of voxel values for the respective images. $p(m)$ is the probability that a voxel of image M has the intensity m and $p(n)$ is the probability that a voxel of image N has the intensity n.

The *joint entropy* of two images, the content of the combined entropies of H(M) and H(N), can then be calculated as follows [180]:

$$H(M,N) = -\sum_{m \in M} \sum_{n \in N} p(m,n) \log p(m,n) \qquad \text{Equation 2.15}$$

In Equation 2.15, $p(m,n)$ is the joint probability of the images M and N. As the image alignment improves (H(M) and H(N)), the joint entropy decreases, resulting in a lower error in the image overlap. However, joint entropy also decreases as the image overlap decreases, which led to the proposal of the *mutual information* metric to overcome this error [180]:

$$I(M,N) = H(M) + H(N) - H(M,N) \qquad \text{Equation 2.16}$$

The equation can also be interpreted using a Venn diagram (Figure 2.17).

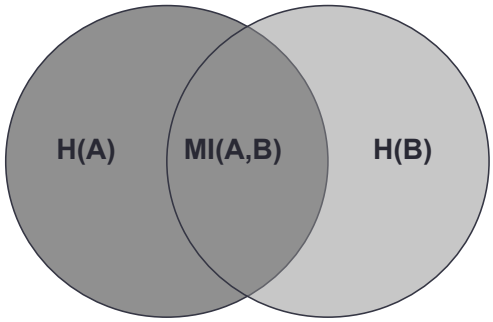

Figure 2.17. Graphical representation of the mutual information metric.

Studholme, Hill and Hawkes [180] also proposed the metric of *normalized mutual information*, which is more robust to entropy error than mutual information, as the marginal ($H(M)$ and $H(N)$) and joint $H(M,N)$ entropies are normalised as a ratio:

$$Y(M,N) = H(M) + H(N) \div H(M,N) \qquad \text{Equation 2.17}$$

The *normalized mutual information* metric has been used as the similarity metric in Amira to register the HR-pQCT to the micro-CT images (Chapter 4).

2.6.5 Optimisation

The range for rotations (radians) and translations (mm) was set prior to the registration within each axis; a larger rotation and translation search would increase the central processing unit (CPU) time. These rotations and translations are

performed over a range of iterations, which have a similar impact on CPU time. A pyramid workflow was applied to the voxel size during the iterations; this is initially performed at a coarse voxel size so that common landmarks can be identified. The transformation search at this level was completed once the tolerance level was met, where there were no further improvements in the spatial alignment. The voxel size was then scaled down to optimise the registration, following similar steps, with a final step of completing the iterations at the actual voxel size, in this case 82 μm.

2.6.6 Interpolator

Once the transformation has been optimised, an interpolator function was responsible for "pulling" the *moving* image to its new coordinates. This was completed by determining the pixel intensity in the transformed image in relation to the corresponding intensity in the original image [182]. Figure 2.18 depicts examples of a cropped HR-pQCT slice that has been transformed using the three kinds of interpolator considered here: the *nearest neighbour*, *linear* and *Lanczos* interpolators.

Nearest neighbour is one of the simplest interpolators, assigning transformed image intensity values to the new coordinate point. This preserves image intensity, but can cause a 'jagged' appearance and can lead to errors in measurements quantified from micro-CT images of bone [183].

The *linear interpolator* computes a weighted average of the grey values from the nearest neighbours of the pixel, typically 8 neighbouring pixels, in the transformed image. The grey value of the moving image is then linearly interpolated to the averaged pixel that is closest the original intensity value [184]. This removes the 'jagged' appearance found with the nearest neighbour interpolator, but it can also remove high frequency intensity values, leading to errors in the 'original' trabecular microstructure from untransformed images [183, 185].

The use of more computationally complex and time expensive interpolators, such as *cubic spline* and *Lanczos* (sinc) (Figure 2.19), can minimise image artefacts [182]. A *cubic spline interpolator* minimises errors in bone microstructure to less than 1.4%, and has superior performance to nearest neighbour and linear interpolators [183]. The *Lanczos interpolator* has also been used to transform micro-CT images to study bone microstructure and remodelling [186, 187]. The available interpolators can depend on what software is used; for instance, the *Lanczos* interpolator is used in Amira, as are the nearest neighbour and linear interpolators (Figure 2.18).

Alternative methods have been proposed to avoid interpolating the images analysed by transforming the HR-pQCT and micro-CT image mask [77, 89, 177, 179]. This is known as an *inverse transformation* and removes any potential error in the interpolation of bone microstructure. This method can be applied using the SCANCO IPL [177] and was applied in the HR-pQCT to HR-pQCT image registration (Chapter 5 and 6). Further details of the HR-pQCT to micro-CT interpolator function are provided in section 2.6.7.2.

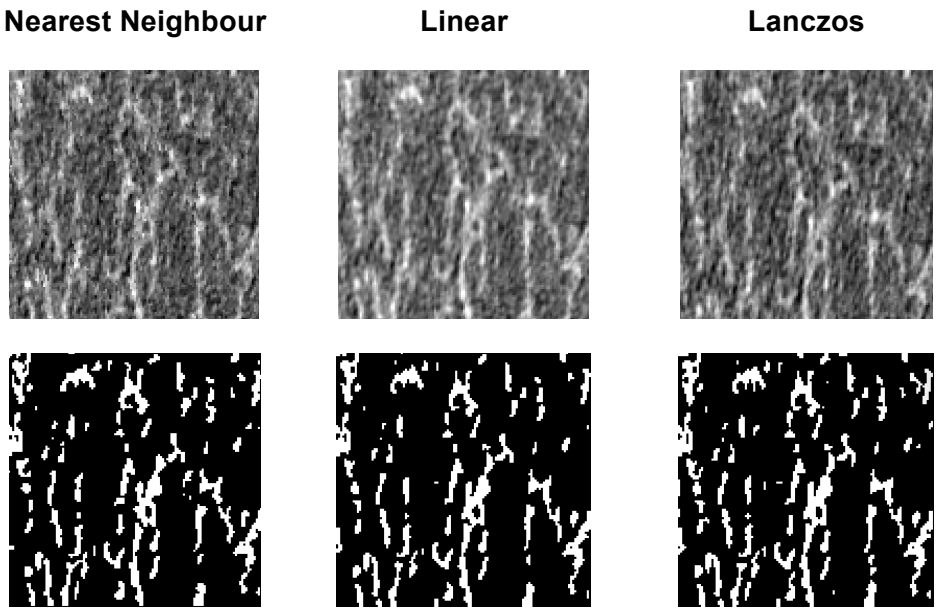

Figure 2.18. Examples of registered HR-pQCT slice images that have been transformed with 3 different interpolators using the Amira Image Registration modules.

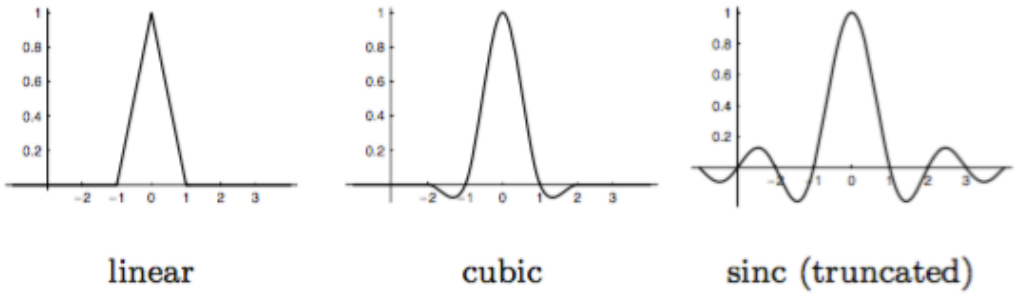

Figure 2.19. Example of three types of image interpolators.

Sourced from Pluim et al., [175]

2.6.7 Optimised experimental registration procedures

2.6.7.1 HR-pQCT to HR-pQCT registration

Step 1: Registration

The process is presented schematically in Figure 2.20. The registration settings followed default settings recommended by the manufacturer. For the registration the steps were as follows:

I. The 'baseline' and follow-up' images, as well as their GOBJs, were called into the IPL. Including the GOBJs in the registration is recommend to shorten registration time and maximise the registration accuracy between the scans.
II. The 'follow-up' image (moving) was registered to the 'baseline' (fixed) HR-pQCT scan. Within the registration, the centre of mass and moment of inertia was aligned and so the initial rotation and translation were set to default values.
III. The correlation coefficient similarity metric was used with a simplex search method [177], so that intensity similarities were searched over fine levels.
IV. The image was resampled to 10x, 4x and 1x the voxel size with the tolerance set to 0.0001.
V. The minimum required value for the correlation coefficient between the two scans was set to 0.5: the coefficients were recorded after each registration for quality control purposes.
VI. A transformation matrix for the registration was obtained.

Step 2: Transformation of the 'follow-up' GOBJ

In order to avoid interpolating the HR-pQCT image, the 'follow-up' GOBJ was transformed and overlaid on the 'baseline' HR-pQCT image:

I. The transformation matrix was applied to the 'follow-up' GOBJ. This was interpolated using linear interpolation [177, 188].
II. The 'baseline' and the transformed 'follow-up' GOBJs were concatenated to create a 'combined' GOBJ, containing both masks.
III. A threshold was applied to the 'combined' GOBJ to identify the common volume between the images.
IV. The GOBJ of the common volume was then overlaid on the 'baseline' HR-pQCT image.

V. The common volume was established by identifying all GOBJs that surrounded the periosteal perimeter of the bone. Any partial GOBJs were deleted.

Step 3: Transformation of the 'baseline' GOBJ

Following transformation of the 'follow-up' GOBJ to the 'baseline' image, the same procedure is applied in reverse:

I. The same transformation matrix was inverted and applied to the 'baseline' GOBJ. This was also interpolated using linear interpolation.
II. The transformed 'baseline' and the 'follow-up' (original, not transformed) GOBJs were concatenated to create a 'combined' GOBJ containing both masks.
III. A threshold was applied to the 'combined' GOBJ to identify the common volume between the images.
IV. The GOBJ of the common volume was then overlaid on the 'follow-up' HR-pQCT image.
V. The common volume was established by identifying all GOBJs that surrounded the periosteal perimeter of the bone. Any partial GOBJs were deleted.

Step 4: Evaluation of the common volume

The manufacturers' guidelines set a cut-off for the common volume between HR-pQCT images of 70%. For instance, 70% of the 110 HR-pQCT slices that are collected between two repeat images must be the same. Other studies have reported using a 75% [9] and 80% cut-off [189-191]. The 70% cut-off is used by our Research Group for the distal radius and distal tibia HR-pQCT scans. Once the common volume is established, only that region is evaluated (methods described in Section 2.3.3) between the repeat HR-pQCT images.

Two methods can be applied to quantify the common volume of interest (), which have been used in the literature [9, 177, 188]: (1) the maximised method, which includes all GOBJ slices that appear on the bone; (2) the cropped method, which only includes GOBJ slices that are overlapped on the periosteal boundary of the bone This is recommended for FE analysis of the HR-pQCT images, as the surfaces of the evaluated image need to be flat.

On the manufacturer's recommendation, the cropped method was used for the evaluation of the common volume in the thesis, as it is applicable to all measurements that can be made using the Scanco IPL.

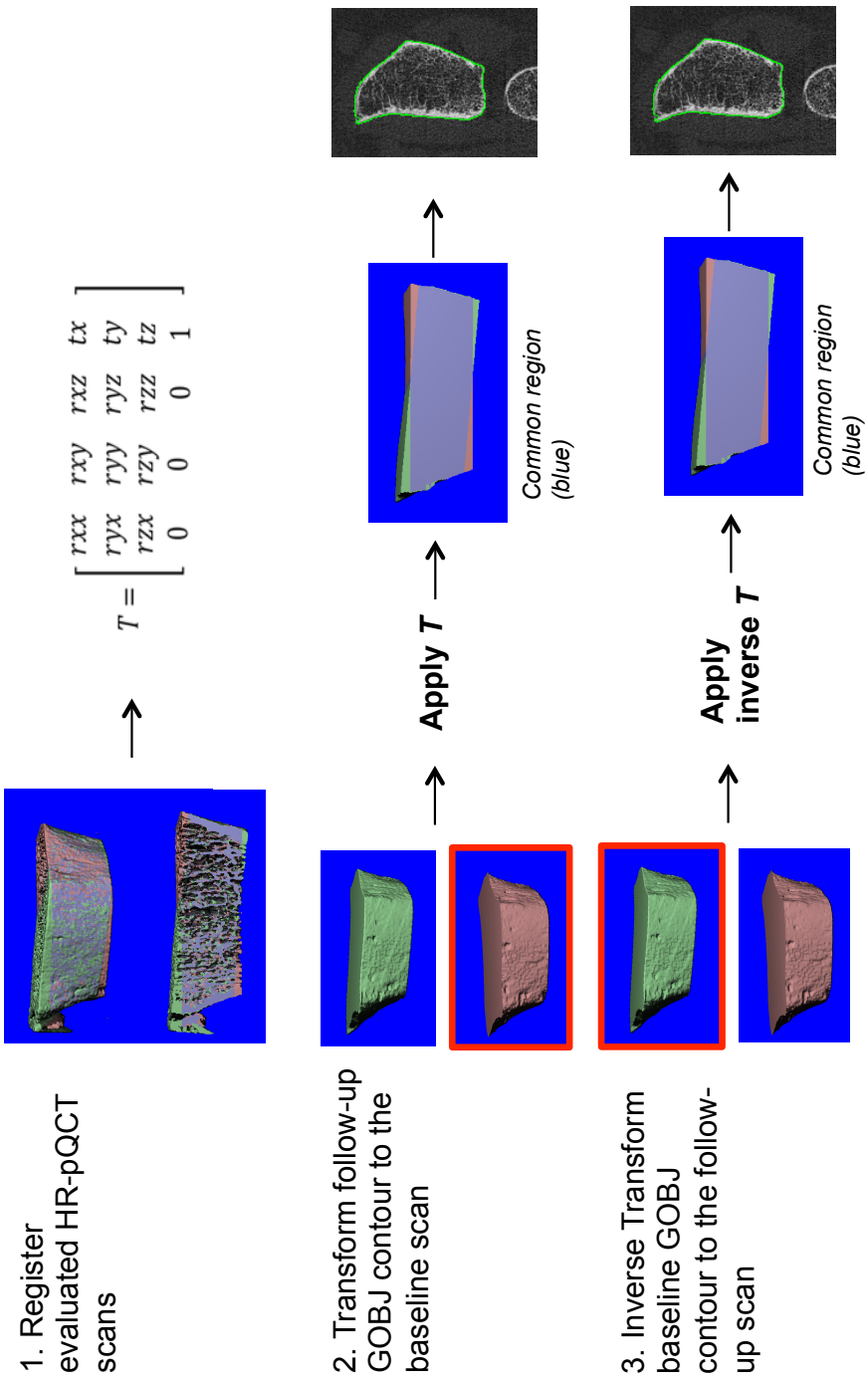

Figure 2.20. 3D rigid registration procedure applied to HR-pQCT scans using the SCANCO Medical AG Image Processing Language.

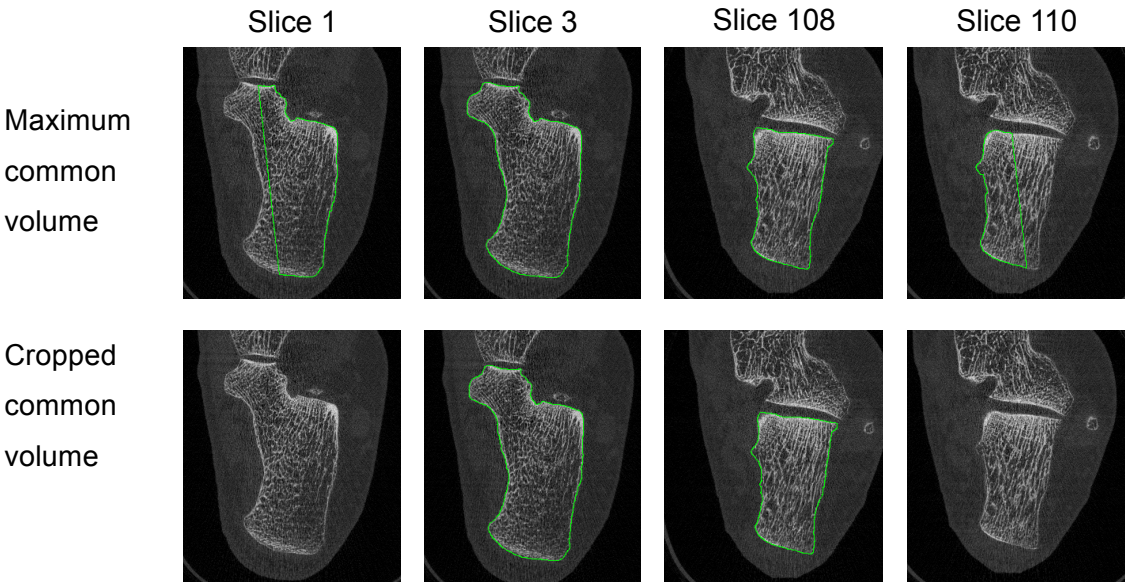

Figure 2.21. Maximised and cropped GOBJ for evaluation following 3D image registration

Maximised common volume – the GOBJ (green line) is only partially in contact with the periosteal surface on some of the slices. Slice 1 and slice 110 show the GOBJ covering approximately half of the calcaneus. These slices are included in the evaluation of the images using the maximised common volume method.
Cropped common volume – the GOBJ is in contact with the calcaneus periosteal surface on all of the evaluated HR-pQCT slices. The GOBJs that were in partial contact with the periosteal surface of the HR-pQCT slices, in the maximum common volume method (slice 1 and 110 in this example), are removed prior to analysis.

2.6.7.2 HR-pQCT to micro-CT registration

Step 1: Registration

The HR-pQCT image was pre-aligned with the micro-CT scan by finding the centre of mass, then manually translating and rotating the scan to find similar cortical landmarks. This order uses the highest resolution scan as the template for initial registration and prevents the potential manipulation of the micro-CT scan parameters, considering the aim of the micro-CT scan as to best represent the 'true' bone microstructure.

A rigid transformation was applied with a normalised mutual information metric, as in with previous studies looking at multi-modal CT registration [77, 163]. The minimum and maximum optimizer steps were set to 0.01 and 0.0625, respectively, for finer translation and rotation of the HR-pQCT scan. (Lowering the numbers of steps did not improve the registration metric). The HR-pQCT scan was resampled in a pyramid fashion at 16, 8, 4 and then at the original (x 1) voxel size. (A resampling

limit below 27 led to longer computation time per scan and no improvement in the registration metric).

Step 2: Transformation

A Lanczos interpolator was chosen to transform the registered HR-pQCT image voxels to their new coordinates. The Lanczos interpolator minimised changes in trabecular microstructure compared to the nearest neighbour and linear interpolators (Figure 2.22), which is in line with Schulte et al., [183], who used a more complex interpolator with micro-CT scans. The isotropic 82 µm voxel size was preserved following completion of the transformation.

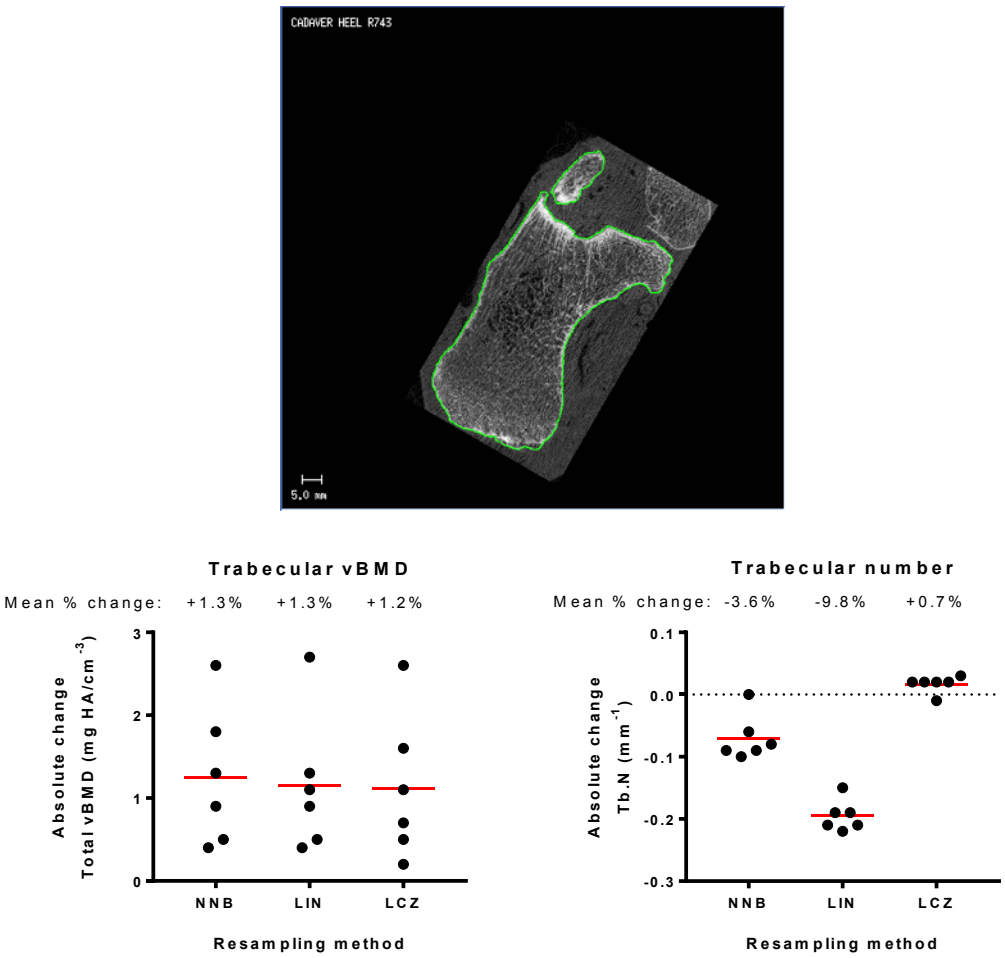

Figure 2.22. Comparison of trabecular vBMD and trabecular number using three different resampling methods.

Using Amira, HR-pQCT images of the calcaneus were manually rotated and resampled using three different interpolators: nearest neighbour (NNB), linear interpolation (LIN) and Lanczos (LCZ). Each resampled HR-pQCT scan was imported into the XtremeCT workstation and evaluated using the standard patient analysis. Measurements from the resampled calcaneus HR-pQCT images were compared to the original HR-pQCT scans (n=6) – the absolute and percentage change from the original is shown.

CHAPTER 3 HR-PQCT METHOD DEVELOPMENT USING HUMAN CADAVERIC CALCANEUS

3.1 Introduction

Chapter 3 outlines the method to image the calcaneus using HR-pQCT, which has been developed in human cadaveric specimen.

3.1.1 Imaging the calcaneus

The imaging of calcaneus microstructure has previously been performed using CT and MRI. The application of CT has the advantage of obtaining a scan of the whole calcaneus in a short duration (< 10 seconds) [192]. In conventional multi-slice CT participants lay supine and have the lower leg and foot fixed in position during the scan. A more recent application of cone beam CT can image the calcaneus (including ankle and foot) in weight-bearing conditions (i.e. standing) and at a lower effective radiation dose per scan compared to multi-slice CT (2-14 µSv vs. 21 µSv) [69]. Furthermore, cone beam CT can reconstruct the images at a smaller voxel size compared to multi-slice CT (isotropic ≥ 0.15 mm vs. ≥ 0.2 mm pixel size and ≥ 0.5 mm slice thickness) with a similar-sized Field of view [69].

The application of MR to image the calcaneus has the advantage of avoiding exposure to ionising radiation. Measurement at the calcaneus has been reported to achieve an in-plane spatial resolution of 156 x 156 µm and slice thickness of 0.5 mm [100, 105, 193], which is similar to multi-slice CT scans. Participants lie supine during calcaneus MR image acquisition with the leg secured in a holder. Sagittal and/or axial slices of the calcaneus have been obtained in reported scan durations of 12 to 20 minutes [101, 193, 194]. This is significantly longer than a calcaneus CT scan and does not obtain an image of the whole bone.

A protocol to image the calcaneus using HR-pQCT has not yet been described. HR-pQCT has a superior voxel size (isotropic 82 µm) to multi-slice CT and cone beam CT, however HR-pQCT requires a longer scan duration (2.8 minutes) to obtain just a 9 mm region of interest *in vivo*. The effective radiation dose is 3 µSv with a standard HR-pQCT scan [195] and is therefore equivalent to a cone beam CT scan of the ankle and foot at an isotropic voxel size of 0.3 mm [69]. Whilst HR-pQCT has a superior spatial resolution with a lower effective radiation dose compared to cone beam CT, the HR-pQCT scanner gantry (and field of view) is narrower. Therefore, optimising the positioning of the foot and the calcaneus for the HR-pQCT scans would be essential prior to any application *in vivo*.

3.1.2 Calcaneus microstructural heterogeneity

The calcaneus has a heterogeneous bone microstructure, evident in both transverse CT slice images [196] and sagittal histological sections of the calcaneus [120, 197]. Quantitative analysis has found BV/TV, Tb.Th and Tb.N to be 2-4 fold higher at superior regions (near the posterior facet) compared to anterior regions of the calcaneus (below the anterior process) in cadaveric specimens using micro-CT [197]. Approximately 2-fold higher BV/TV and apparent Tb.Th has been reported between similar regions of the calcaneus in healthy subjects using MRI [198]. Lin and colleagues [198] reported heterogeneity within superior, anterior and posterior regions of the calcaneus across participants as coefficient of variations (CV), in which BV/TV ranged from 22 to 28%, apparent Tb.Th ranged from 24 to 54%, apparent Tb.Sp from 22 to 41% and apparent Tb.N from 12 to 16% within the regions. The heterogeneity in calcaneus microstructure appears to be greater along the superior-inferior axis [197, 198], than in the anterior-posterior axis of the bone [101, 199]. Few studies have performed a regional quantitative analysis of the calcaneus [101, 197-199] and no study has performed this using HR-pQCT.

The measurement of calcaneus microstructure using HR-pQCT would use different quantitative methods to those applicable to MRI or micro-CT. MRI uses direct voxel counting for BV/TV measurement and calculates the mean intercept length as an index for apparent Tb.Th [200]. Plate-model assumptions are then used to calculate apparent Tb.N (area fraction of bone/Tb.Th) and apparent Tb.Sp ((1/Tb.N) – Tb.Th) [200]. Quantitative differences have been reported between co-registered HR-pQCT and MRI images of the radius and tibia; BV/TV and Tb.Th were 3 to 4-fold higher with MRI, and Tb.N* and $Tb.Sp^d$ were higher using HR-pQCT [100]. Furthermore, the correlation between the measurements obtained using MRI and HR-pQCT at the radius and tibia ranged from an R^2 of 0.18 to 0.52, highlighting the weak agreement for the same microstructural parameters between the two modalities. Agreement between HR-pQCT and micro-CT measurements is stronger [77, 163], which could be expected, as HR-pQCT is essentially a clinical micro-CT device. However, the greater HR-pQCT voxel size leads to an overestimation of Tb.N*, and an underestimation of Tb.Th and Tb.Sp [77, 163, 164, 201]. Therefore, measurements of calcaneus microstructure obtained using HR-pQCT may not completely reflect those obtained using other modalities.

3.1.3 Positional variation and microstructure heterogeneity

The heterogeneity that has been established at the calcaneus could affect measurement precision with improper positioning of the region that is evaluated. Within the standard region obtained using HR-pQCT at the distal radius and distal tibia, there can be large variability in total vBMD, trabecular vBMD and cortical thickness. Kazakia and colleagues [100] found the mean percentage variation in BV/TV^d to range from 8 to 58% at the distal radius and 8 to 40% at the distal tibia, depending on the HR-pQCT slice that was evaluated within a 9 mm region of interest. The highest heterogeneity in this region was found in cortical thickness (~152% and ~71% across all participants' radius and tibia, respectively). These findings have been confirmed by Boutroy et al. [202] and Boyd [203], who identified similar regional differences in total, trabecular and cortical vBMD, as well as Tb.N*, $Tb.Th^d$ and cortical thickness. An important finding by Boyd [203] was that distal radius total vBMD changed by up to ±6% with 0.5 mm of proximal or distal movement of the region of interest. A similar region of interest movement at the distal tibia caused total vBMD, Tb.N* and cortical thickness to change by approximately ±2%, which increased by up to ±6% with ~1.7 mm of region movement. Positional variation is therefore critical using HR-pQCT at the radius and tibia, and the same could be anticipated at the calcaneus.

3.1.4 Summary

A protocol to image and quantify the calcaneus using HR-pQCT has not been proposed in the literature. Imaging the bone using HR-pQCT provides different challenges to those found with CT (scan duration, positional variation and larger field of view) and MRI (positional variation), but does provide advantages in microstructure quantification due to its superior spatial resolution. Quantitative measurements using micro-CT and MRI have identified a heterogeneous calcaneal trabecular microstructure between different regions of the bone, which could be anticipated using HR-pQCT. This heterogeneity could impact measurement error with improper positioning of the foot and positional variation with the start of the measurement region.

3.2 Aims and objectives

The aim of Chapter 3 is to develop a protocol to scan the calcaneus using HR-pQCT in human cadaveric specimen.

The objectives of Chapter 3 are:

1. To optimise foot positioning for the calcaneus HR-pQCT scans.
2. To compare trabecular vBMD and trabecular microstructure measurements between the inferior, middle and superior regions of the calcaneus tuberosity.
3. To evaluate trabecular vBMD and trabecular microstructure measurements with 5 (0.41 mm), 10 (0.82 mm) and 20 slice (1.64 mm) deviation in the measurement region in the calcaneus tuberosity.

3.3 Methods and Materials

3.3.1 Study design

Professor Eugene McCloskey, Dr Margaret Paggiosi and I designed the study The study was undertaken using anonymised human cadaveric specimen, where consent had been obtained in life and bodies were donated to the Medical Teaching Unit at the University of Sheffield for anatomical study. Specimen limbs were transported to and from the Clinical Research Facility, Northern General Hospital by the Designated Individual (Mr John Rochester). The use of the limbs was carried out under direct supervision of the Designated Individual, authorised under the Human Tissue Act (Code 4). The study was given favourable ethical opinion by the University of Sheffield Medical Research Ethics Committee (Application 007375).

The specimen limbs were used in three separate visits to the Clinical Research Facility: visit 1 was completed using a single specimen limb (Section 3.4); visits 2 and 3 were completed using a number of specimen limbs (Section 3.5). Dr Margaret Paggiosi performed the HR-pQCT image acquisitions. I completed the HR-pQCT image analysis.

3.3.2 Materials

At the Medical Teaching Unit, the specimen were formaldehyde fixated using embalming fluid number 4 (Vickers Laboratories Ltd, Pudsey, UK) by infusion through the arterial system: 25-30 litres was used in a 70 kg cadaver. Specimens were stored at 1-4°C and were later dissected at room temperature (18-24°C). Prior to transportation to the Clinical Research Facility, specimens were divided through

the proximal 2/3 point of the tibia (n = 16) or between the talus and tibia endplate (n = 6) at the Medical Teaching Unit. No medical history was available and specimens were not examined for the presence of metabolic bone disease or any abnormality.

3.4 Development with a single human calcanei

3.4.1 Materials

The lower limb of one human cadaveric specimen with the tibia present (*in situ*) was used to develop the foot positioning for the calcaneus HR-pQCT scans.

3.4.2 Image acquisition

3.4.2.1 Specimen positioning

With studies previously reporting that participants were comfortable in the position for the distal tibia HR-pQCT scans [204], a similar position was selected for the calcaneus HR-pQCT scans. The lower limb cast, used for distal tibia scans and provided by the manufacturer, was used to fix the cadaveric limb in place. In an attempt to achieve similar positioning to that used with other imaging modalities [194, 205], the sole of the specimen foot was placed flat on the bottom of the lower-limb cast, with no plantar or dorsi-flexion at the ankle joint (i.e. neutral), and similar to the position used for the distal tibia scans.

A two-dimensional x-ray (scout view) was obtained (Figure 3.1). Whilst this position aligned the tibia endplate parallel to the scout view, the calcaneus was at an angle. The advantage of this position is that it was similar to the distal tibia scan. However, the main limitation was that it led to surrounding bones of the foot crossing the XtremeCT field of view. This can cause scattering of the x-ray photons and cause incomplete tomographic projections as the CT source rotates around the foot [158]. Plantar flexion at the ankle joint overcame this problem and aligned the calcaneus superior and inferior surfaces with the field of view (Figure 3.1); this was a similar position to that used with QUS and with specialised calcaneus DXA (DXL Calscan, Demetech AB: TÄBY, Sweden), which have both received considerable use *in vivo*.

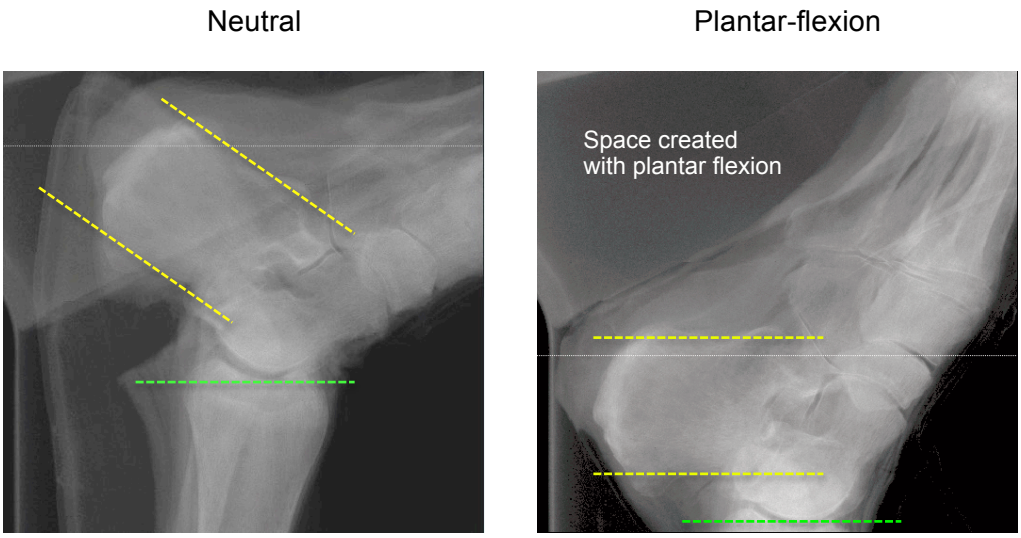

Figure 3.1. Two-dimensional x-ray scans of the foot with neutral foot position and with plantar-flexion.

Calcaneus superior and inferior surface (yellow dotted lines); Tibia endplate (green dotted line).

3.4.2.2 Scout view

The additional advantage with plantar flexion at the ankle joint was that main body of the calcaneus bone was parallel to the scanning region. The scanning region can only be placed parallel to the scout view, which would lead to different regions being scanned in the neutral and plantar-flexed foot positions. Figure 3.2 shows the differences between the region of the calcaneus that is imaged in the neutral and plantar-flexed positions. The plantar-flexion at the ankle joint led to an improvement in contrast between the bone and the soft tissue, which would benefit the calcaneus periosteal perimeter detection; this was supported by an improved definition between the air and bone peak of the bimodal histogram (Figure 3.3).

The size of the scout view required adaptations for the calcaneus HR-pQCT images. The start and end position in the control files for the radius and tibia scout views are set to 90 mm and 120 mm, and 73 mm and 103 mm, respectively. With the calcaneus superior and inferior surfaces that are parallel to the scout view, the start and end positions were widened to 0 mm to 150 mm. This ensured that the scan technician could visualise the whole calcaneus and also check the position of the surrounding bones of the foot in relation to the field of view.

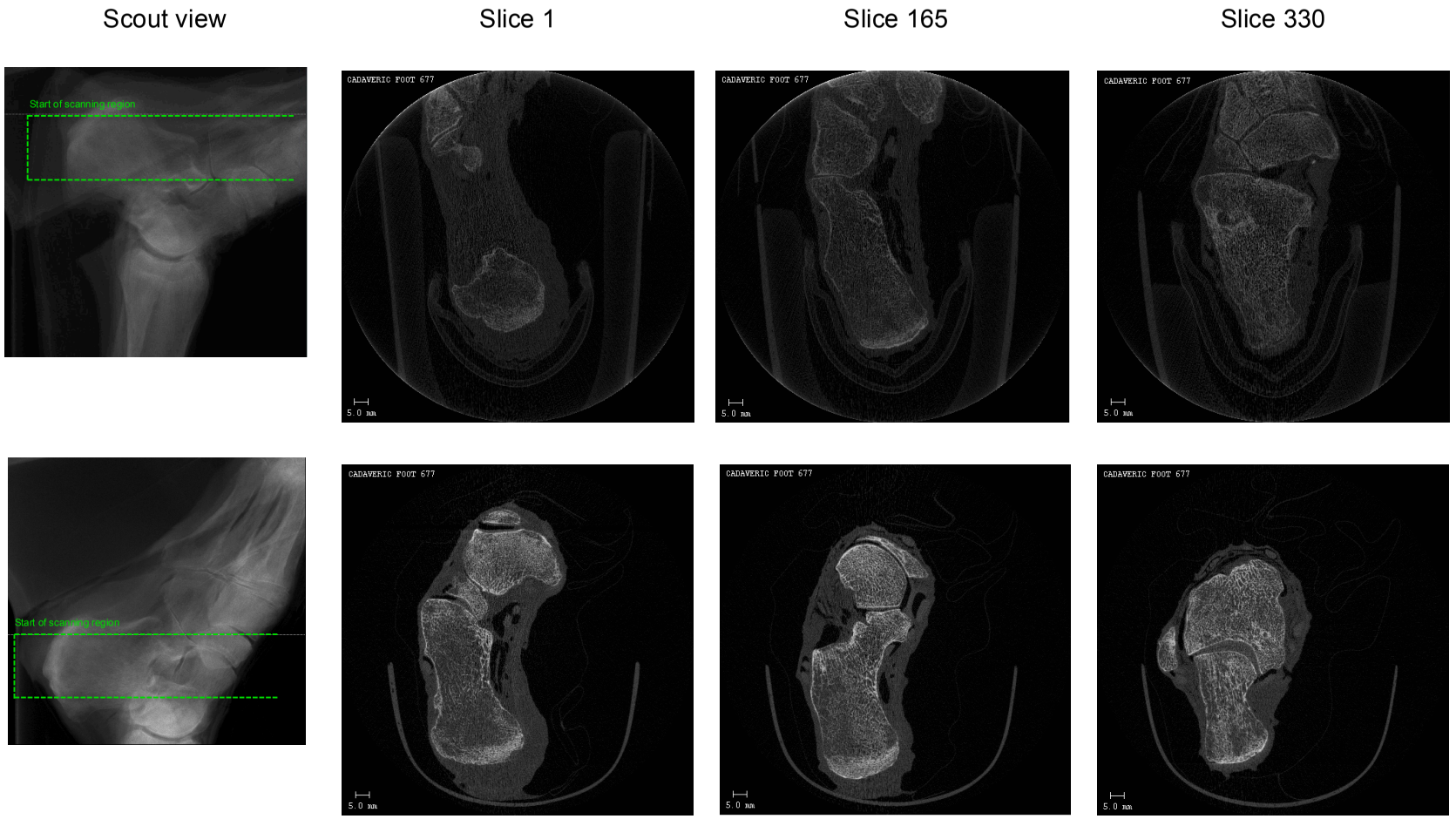

Figure 3.2 Comparison of the calcaneal HRpQCT slices for the neutral (upper panel) and plantar-flexed (lower panel) foot positions.

HR-pQCT images obtained using the standard manufacturer operational settings for HR-pQCT image acquisition (Section).

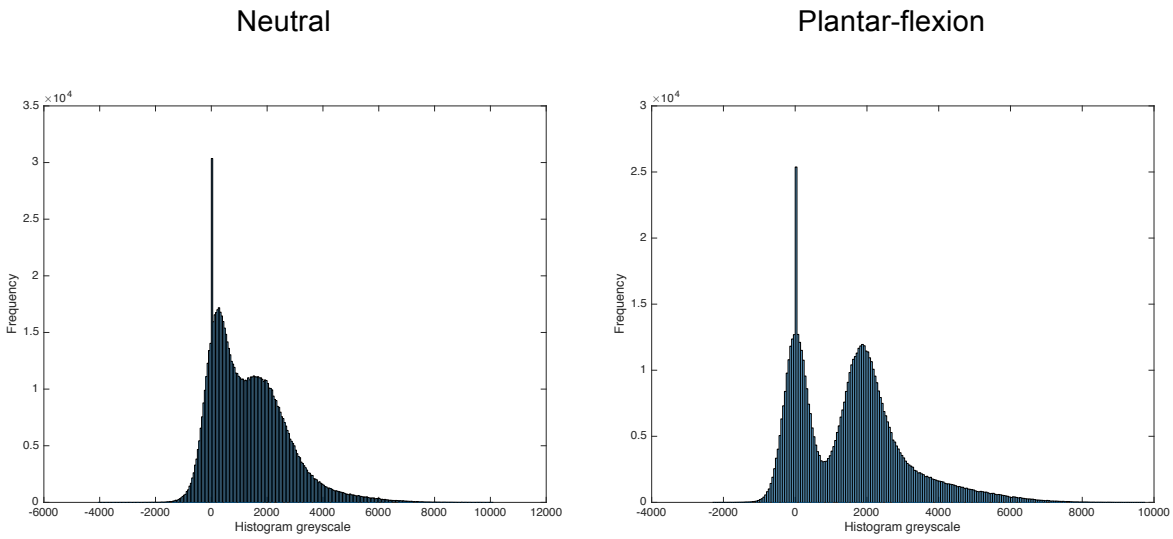

Figure 3.3. Frequency of the Hounsfield units from the neutral and plantar-flexion calcaneus HRpQCT images.

Hounsfield units were exported from the calcaneus HR-pQCT slice images. These were exported from the calcaneus only apply a GOBJ around the calcaneus periosteal surface.

3.5 Application in multiple human cadaveric calcaneus

3.5.1 Materials

The lower limbs from 21 human cadaveric specimens (*in situ*) were used to (1) further test the development of the foot positioning, (2) test the scanning region identification and (3) evaluate the volumetric BMD and trabecular microstructure of the calcaneus using HR-pQCT.

3.5.2 Image acquisition

The specimens were positioned in the lower-limb cast with plantar-flexion at the ankle joint. The foot was fixed in the position using pieces of foam and the Velcro straps attached to the lower limb cast. The scout view size (or scaling) was set to a start position of 0 (zero) and an end position of 150. The standard manufacturer operational settings for HR-pQCT image acquisition were used (Section 2.3.1): an x-ray tube potential of 60 kVp, an x-ray tube current of 95mA, collecting 750 projections at an integration time of 100ms.

Two different regions of interest were obtained in the 21 specimens. At visit 2, 15 specimens had the whole calcaneus imaged using HR-pQCT, with up to 770 slices captured (at an isotropic voxel size of 82 μm). At visit 3, 6 specimens had a 330-

slice region captured around the mid-point of the calcaneus between the superior peak of the tuberosity and the plantar fascia attachment (Figure 3.4). A smaller region was collected at visit 3 due to time and scheduling constraints.

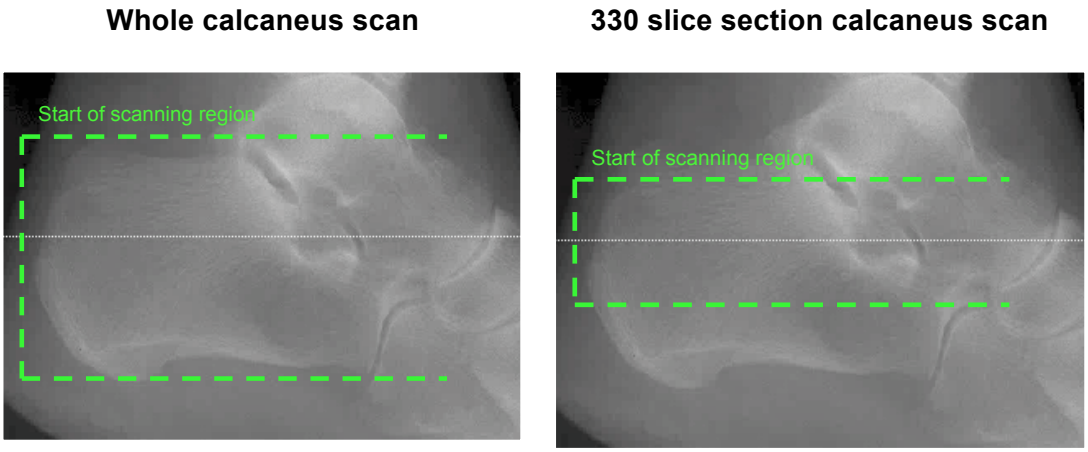

Figure 3.4. Regions for the calcaneal HR-pQCT scans.

3.5.3 Image reconstruction

Calcaneus HR-pQCT image reconstruction followed the standard protocol provided by the manufacturer (Section 2.3.2).

3.5.4 Image evaluation

All image evaluations were completed within the XtremeCT Evaluation Software.

3.5.4.1 Volume of interest size and positioning

A protocol to position the volume of interest was developed to quantify the calcaneus trabecular microstructure. Previous studies using three-dimensional imaging methods [194, 198, 206] have used circular, square and rectangular regions of interest to measure trabecular BV/TV and trabecular microstructure heterogeneity in the calcaneus. These analyses have excluded cortical bone, which could be due to the difficulty in measuring the thin cortex in comparison to the method's spatial resolution. Using HR-pQCT, the cortical bone could be visually identified in the transverse slices of the bone. The semi-automated contouring procedure with the dual-threshold algorithm [161, 162] (Section 2.3.3) was performed on one cadaveric specimen. The performance of the endocortical boundary detection was poor and required high manual input to correct its position on every slice (Figure 3.5). For simplicity, the semi-automated contouring was not

applied in Chapter 3 and a GOBJ was positioned to quantify trabecular bone and exclude cortical bone.

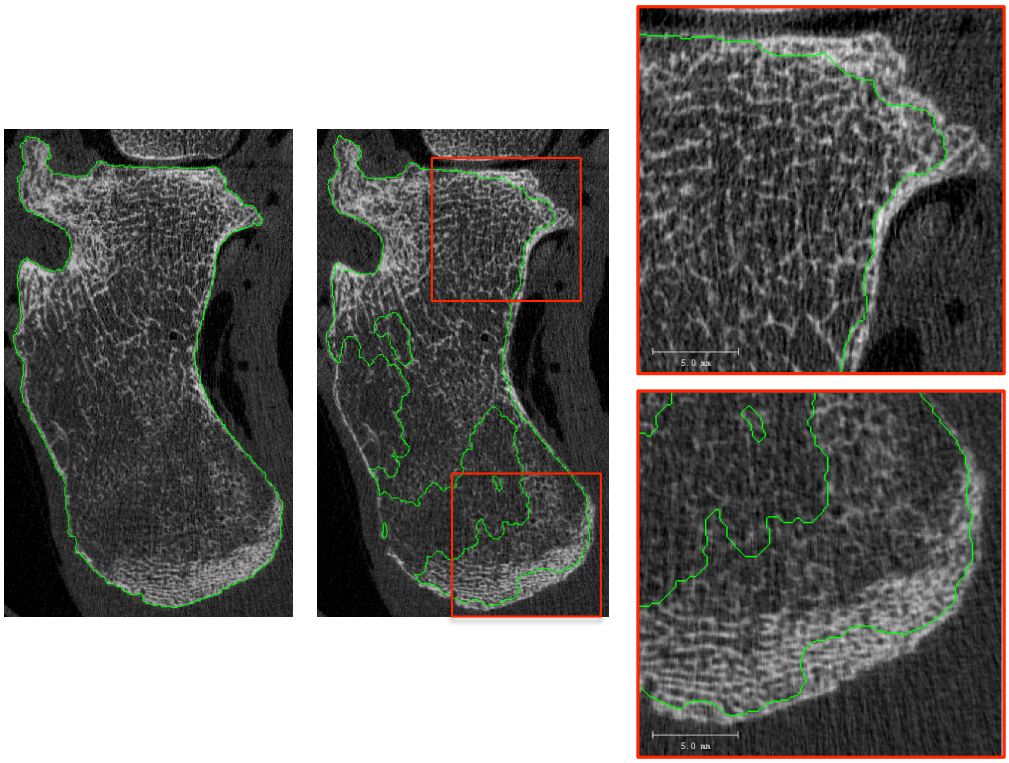

Figure 3.5. Example of the dual-threshold segmentation algorithm on calcaneus HR-pQCT slices.

The left image shows the GOBJ (green line) in contact with the periosteal surface of the calcaneus. The central image shows the automated performance of the cortical segmentation method, in which the GOBJ should be in contact with the endocortical surface. The right images represent the red squares within the central image and further highlight the improper positioning of the GOBJ.

The GOBJ size and position was piloted across all specimens. A fixed sized GOBJ was used, with dimensions of (X) 12.25 mm x (Y) 12.25 mm x (Z) 9.02 mm (Figure 3.6A). The Z-dimension was equivalent to the number of slices measurement at the distal radius and distal tibia *in vivo*, representing a 2.8 minute scan duration [195]. The X and Y dimensions were tested at larger sizes (up to 25 mm), however the GOBJ overlapped the periosteal perimeter at medial-lateral surfaces of the calcaneus across different specimen. This was particularly apparent at superior and inferior regions of the bone, where the medial-lateral widths were narrow in all specimens. Increasing the Y-dimension was also tested (up to 40 mm), however the GOBJ then encroached areas of the calcaneus that are subjected to high mechanical strains, such as those near the Achilles tendon attachment and near the

posterior facet. These regions have been found to have 1.5-2 fold higher BV/TV compared other regions of the calcaneus tuberosity [197, 198].

3.5.4.2 Volume of interest evaluation

Objective 1: To compare trabecular vBMD and trabecular microstructure measurements between the inferior, middle and superior regions of the calcaneus tuberosity.

Six different regions of the calcaneal tuberosity body were evaluated. An eight-step process was applied to position the GOBJ, which is depicted in Figure 3.6B-C:

Step 1. A single GOBJ was placed on the middle slice of the bone between the superior tuberosity peak and the plantar fascia attachment. To avoid areas that are subjected to high mechanical strains, the anterior edge of the single GOBJ was positioned at 60% of the slice length.

Step 2. The single GOBJ was then translated in the medial-lateral direction to ensure that the GOBJ had an equal distance either side to the medial and lateral periosteal surfaces.

Step 3. The GOBJ was then morphed through 330 slices in a fixed coordinate position of the HR-pQCT slice images, using the 'Contouring: Range: Morph function'.

Step 4. The morphed GOBJs were then divided into superior (1 to 110 slices), middle (111 to 220 slices) and inferior regions (221 to 330 slices).

Step 5. The single GOBJ, used in the first step, was then translated in the anterior direction to create a new region of interest. There was a one-voxel difference between the anterior edge of the original GOBJ and posterior edge of the new GOBJ.

Step 6. The new single GOBJ was translated in the medial-lateral direction to ensure that the GOBJ had an equal distance either side to the medial and lateral periosteal surfaces, similar to step 2.

Step 7. The new single GOBJ was then morphed through 330 slices in a fixed coordinate position of the HR-pQCT slice images, similar to step 3.

Step 8. The newly morphed GOBJs were then divided into superior (1 to 110 slices), middle (111 to 220 slices) and inferior regions (221 to 330 slices).

The GOBJ regions created in step 4 and step 8 were labelled 'posterior' and 'anterior' regions, respectively: posterior-superior, posterior-middle posterior-inferior,

anterior-superior, anterior-middle, anterior-inferior. The volume covered by these regions was similar to that used to identify trabecular heterogeneity in the main body of the calcaneus tuberosity in previous work [198].

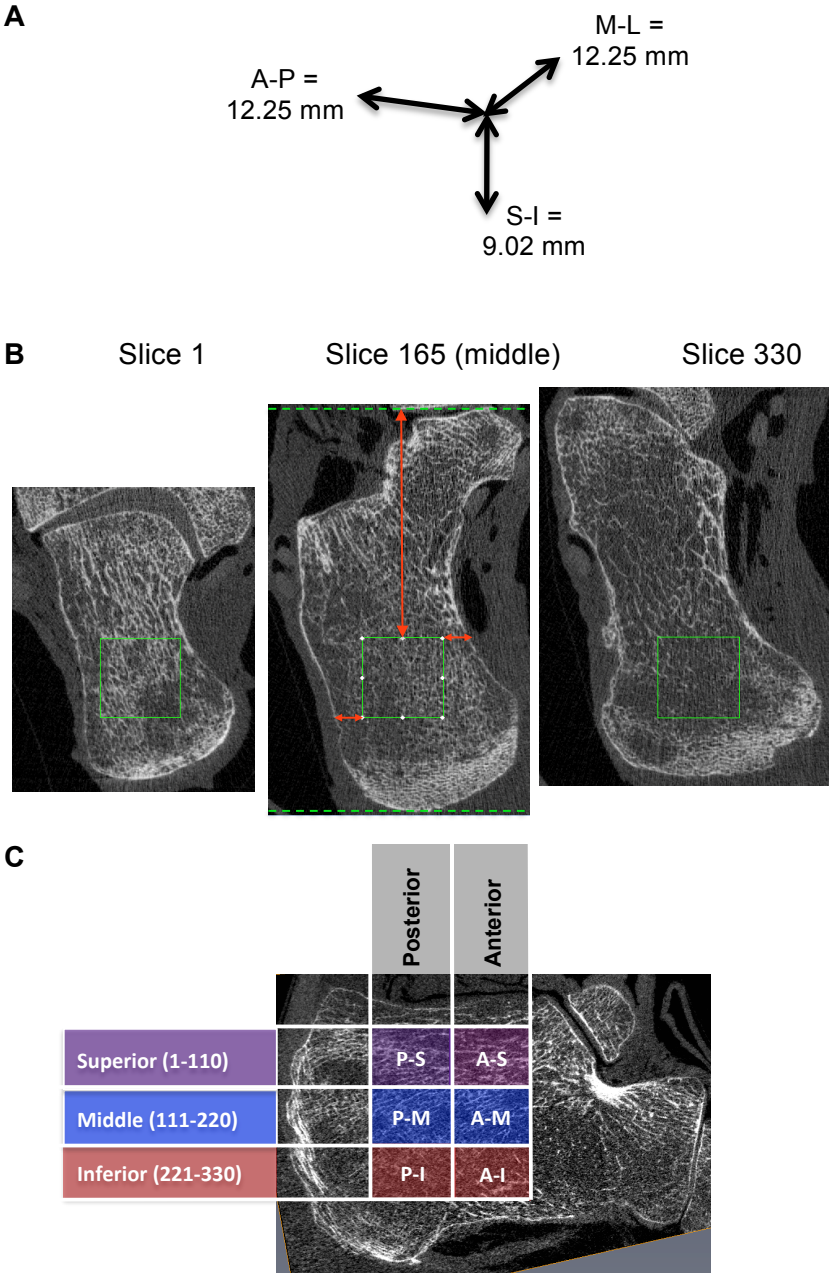

Figure 3.6. Location of the volume of interest for the scan evaluation.
A − The dimension of the GOBJ was 15 mm^2: Anterior-Posterior = 12.25, Medial-Lateral = 12.25 mm, Superior-Inferior = 9.02 mm).
B − The GOBJ position on the middle slice was morphed through slice 1 to 330 at fixed coordinates on the HR-pQCT field of view. Note the change in calcaneus morphology through this slice range.
C – Approximate position of the six GOBJs relative to a sagittal slice of the calcaneus.

Objective 2: To evaluate trabecular vBMD and trabecular microstructure measurements with 0.41 mm, 0.82 mm and 1.64 mm deviation in the measurement region in the calcaneus tuberosity.

The reference GOBJ within each posterior region (posterior-superior, posterior-middle and posterior-inferior region) was translated ±5 (±0.41 mm), ±10 (±0.82 mm) and ±20 slices (±1.64 mm) in the superior and inferior direction. These three translations were within the ranges reported by [203] at the distal tibia, in which total vBMD and Tb.N* changed by up to ±6% with ~1.7 mm of GOBJ movement. The GOBJ with each movement was evaluated in comparison to the reference GOBJ. This aimed to represent the potential differences of landmark selection by the scan technician and how this may impact measurement error. This was performed in subset of cadaveric specimens with the tibia present that has HR-pQCT scans of the whole calcaneus completed (n=10).

3.5.4.3 Image quantification

The HR-pQCT images were quantified for trabecular vBMD, Tb.N*, $Tb.Th^{d}$ and $Tb.Sp^{d}$ (* – directly computed; ^{d} – derived) using the 'standard clinical evaluation' script (Section 2.3.3).

3.5.5 Statistical analysis

Statistical analyses were completed in GraphPad Prism (7.0, GraphPad Software: La Jolla California, USA) and SPSS statistics package (version 21, IBM: New York, USA). A $p<0.05$ indicated statistical significance, unless indicated otherwise. HR-pQCT measurements were visually checked for normality, and then statistically checked using a Shapiro-Wilk test. Normally distributed measurements were presented as a mean with a 95% confidence interval (95% CI) and non-normally distributed measurements were presented as a median with an interquartile range (IQR); parametric and non-parametric tests were applied accordingly.

3.5.5.1 Repositioning error between repeated scans

The region of interest placement is related to the identification of the midpoint between the superior and inferior surfaces of the calcaneus. Here, reproducibility will be impacted by the positioning errors that alter the apparent distance between the two surfaces. This has been explored by repositioning the calcaneus between two repeat image acquisitions. The total number of slices in each image was

counted to provide a measure of calcaneal height (82µm x total number of slices)[3]. The root mean square error of the standard deviation (SD_{RMS}) of the calcaneus height (mm) was calculated from the two images to represent the variability in the positioning. This analysis was only completed in images of the whole calcaneus (n=16).

3.5.5.2 Regional evaluation of the calcaneus tuberosity

Two separate regional evaluations were performed. First, the percent CV (CV%) was calculated for the 6 regions combined for each measurement to provide a heterogeneity measurement within the main body of the calcaneus tuberosity [198]:

$$CV\% = \frac{measurement\ standard\ deviation\ within\ the\ regions}{measurement\ mean\ within\ the\ regions} \times 100 \qquad \text{Equation 3.1}$$

Second, measurements from the six 110-slice volumes of interest (Figure 3.6B) were compared to one-another. Normally distributed measurements (trabecular vBMD and $Tb.Th^d$) were compared using a one-way repeated measures analysis of variance (ANOVA) with Bonferroni post-hoc tests ($p<0.008$; 0.05/6). Non-normally distributed measurements ($Tb.N^*$ and $Tb.Sp^d$) were compared using a Friedman's test with adjusted Dunn's multiple comparison post-hoc tests (p values corrected to $p<0.05$ for post-hoc analyses).

3.5.5.3 Systematic adjustment of the volume of interest

Measurements from the translations of the GOBJ (±5, 10 and 20 slices) were compared to the original posterior-superior, posterior-middle and posterior-inferior region measurements, and expressed as a percentage change. Linear regression analyses were performed to evaluate the correlation between the percentage change in measurements from the translations of the GOBJ (trabecular vBMD, $Tb.N^*$, $Tb.Th^d$ and $Tb.Sp^d$) and the translations of the GOBJ (±5, 10 and 20 slices). The coefficient of determination (r^2), equation slope and intercept, and root mean square error (RMSE) were calculated.

[3] This analysis was completed before the method to measure repositioning error for the reference line placement was proposed by Bonaretti and colleagues (2016). This has been adapted accordingly with updated software for the HR-pQCT image acquisition in Chapter 5 and 6.

3.6 Results

3.6.1 Repositioning error between repeated scans

Figure 3.7 shows the calcaneus height for the individual specimens between the plantar fascia attachment (first HR-pQCT slice) and the superior peak of the tuberosity (last HR-pQCT slice) for the repositioned HR-pQCT images of the whole calcaneus. The SD_{RMS} in the calcaneus height between these images was 1.77 mm (equivalent to 22 HR-pQCT slices). There was difficulty in repositioning the specimens without a tibia. When the reproducibility errors were calculated separately for specimens with the tibia present and absent, there was a greater variation in mean difference in specimens with the absent tibia (95% CI: tibia absent = 0.37, 5.4%; tibia present = 0.2, 0.8%). The SD_{RMS} in the calcaneus height between the images in which the tibia was present, was 0.24 mm (equivalent to 3 HR-pQCT slices).

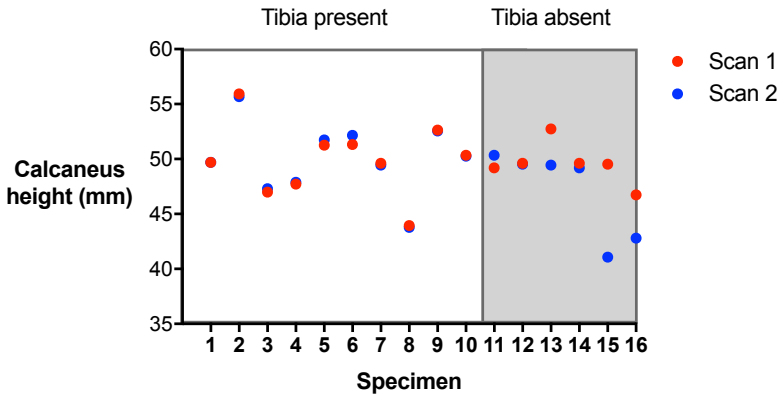

Figure 3.7. Calcaneal height of repositioned HR-pQCT scans for the individual calcanei.
Calcaneal height was calculated by multiplying the number of slices between the superior peak of the tuberosity and the plantar fascia attachment by the HR-pQCT slice thickness (0.082 mm, 82 µm).

3.6.2 Regional evaluation of the calcaneus tuberosity

16 specimens were used in the analysis as 5 were excluded due to air bubbles in the volumes of interest. These specimens had negative trabecular vBMD, which would subsequently affect the calculation of $Tb.Th^{d}$ and $Tb.Sp^{d}$.

Table 3.1 shown the descriptive statistics and CV% for the 6 combined regions of interest. Figure 3.8 shows the trabecular vBMD and trabecular microstructure

between the different regions of the calcaneus that were evaluated using HR-pQCT. There was noticeably higher CV% for trabecular vBMD and Tb.Th^{d} in comparison to Tb.N* and Tb.Sp^{d}. The regional heterogeneity was further supported by statistical analysis between the 6 regions. A statistically significant effect of the calcaneus region was found on trabecular vBMD ($F(2.28, 34.2) = 29.2$, $p<0.001$, $R^2 = 0.66$) and Tb.Th^{d} ($F(2.86, 42.9) = 50.9$, $p<0.001$, $R^2 = 0.57$), as well as Tb.N* ($X^2(5) = 13.4$, $p=0.02$) and Tb.Sp^{d} ($X^2(5) = 17.3$, $p=0.004$). Superior regions (both anterior and posterior) were found to have significantly greater trabecular vBMD and Tb.Th^{d} than the middle and inferior regions (both anterior and posterior). There were no differences in trabecular vBMD and Tb.Th^{d} between the anterior and posterior regions. There were found to be no significant differences between the individual regions for Tb.N* (p=0.09-1). Tb.Sp^{d} at the anterior-superior region was significantly lower than the posterior-inferior region. Tb.Sp^{d} at the posterior-superior region was lower than the posterior-inferior (p=0.03). Tb.Sp^{d} was not statistically significant between the other calcaneal regions (p=0.16-1.00).

Table 3.1. Summary statistics and coefficient of variation (%) for trabecular vBMD and trabecular microstructure in the 6 regions.

	Mean (95% CI) / Median [IQR]	CV% (95% CI)
Tb.vBMD, mg HA/cm^{-3}	129 (117, 141)	41% (32, 56%)
Tb.N*, mm^{-1}	3.1 [2.5, 3.6]	11% (8, 13%)
Tb.Th^{d}, µm	34 (24, 46)	40% (33, 48%)
Tb.Sp^{d}, µm	288 [240, 362]	13 (10, 16%)

Trabecular vBMD (Tb.vBMD) and Tb.Th^{d} – mean (95% CI); Tb.N* and Tb.Sp^{d} – median [IQR].

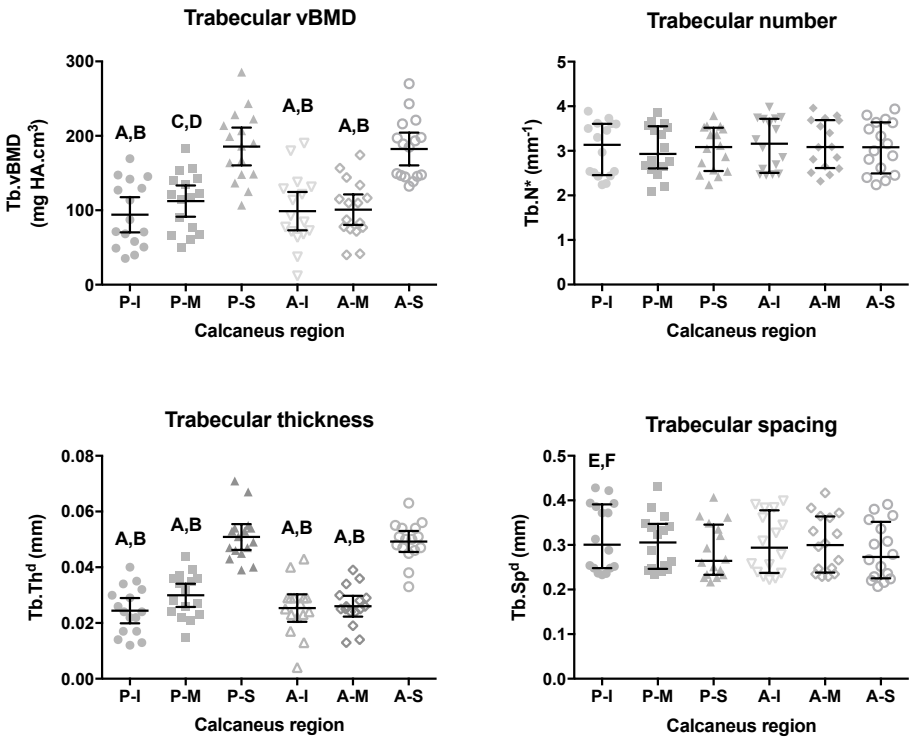

Figure 3.8. Trabecular volumetric BMD and trabecular microstructure measured at different regions of the calcaneus tuberosity body by HR-pQCT.

Abbreviations: P-S, posterior-superior; P-M, posterior-middle; P-I, posterior-inferior; A-S, anterior-superior; A-M, anterior-middle; A-I, anterior-inferior.
Bonferroni corrected p value set at p<0.008 (= 0.05/6): A, p<0.001 to P-S; B, p<0.001 to A-S; C, p=0.003 to P-S; D, p=0.003 to A-S.
Adjusted Dunn's p value set at p<0.05: E, p=0.03 to P-S; F, p=0.007 to A-S.

3.6.3 Systematic adjustment of the volume of interest

The trabecular vBMD, Tb.N*, Tb.Th^{d} and Tb.Sp^{d} for each reference volume of interest is reported in Table 3.2. The percentage change in the reference volume of interests with adjustment (±0.41 (5 slices), ±0.82 (10 slices) and ±1.64 mm (20 slices)) is reported as a linear regression analysis in Table 3.3 and graphically in Figure 3.9.

Trabecular vBMD was sensitive to changes in the volume of interest in all regions. There was a positive, moderate-strong correlation for the superior (r^2=0.72, p<0.001) and middle region Tb.vBMD (r^2=0.73, p<0.001) with the volume of interest adjustment. Here, a positive shift (superior direction) of the volume of interest increased the trabecular vBMD, and a negative shift (inferior direction) of the volume of interest decreased the trabecular vBMD. At the inferior region there was a negative, weak correlation for trabecular vBMD (r^2=0.22, p<0.001), as well as a higher RMSE. This was influenced by little or no change in trabecular vBMD with a

+20-slice shift to a -5-slice shift, with trabecular vBMD increasing from a -5 to -20 slice shift. $Tb.Th^d$ followed similar trends to the trabecular vBMD. Positive slice shifts in the superior and middle regions increased $Tb.Th^d$, and negative slice shifts decreased the superior and middle regions $Tb.Th^d$ (r^2=0.80, p<0.001 and r^2=0.79, p<0.001, respectively). There was a negative, weak correlation for $Tb.Th^d$ at the inferior region, which was influenced by an increase in $Tb.Th^d$ from -5 to -20 slices.

The Tb.N* and $Tb.Sp^d$ were relatively stable with the slice shifts of the reference volume of interest. There was no significant correlation for Tb.N* at the superior and middle region, where as the inferior region had a very weak correlation, favouring an increase in Tb.N* from a -5 to -20 slice shift (r^2=0.08, p=0.03). $Tb.Sp^d$ had very weak correlations at the superior, middle and inferior regions. There was a reduction in $Tb.Sp^d$ with a positive slice shift at the superior and middle regions, and a decrease with a negative slice shift at the inferior region.

Table 3.2. Region trabecular vBMD and trabecular microstructure measurements for the reference volume of interest that were compared to measurements following slice shifting.

	Superior	Middle	Inferior
Tb. vBMD, mg HA/cm^{-3}	148 (114, 182)	110 (86, 134)	83 (52, 114)
Tb.N*, mm^{-1}	2.8 (2.6, 3.1)	2.9 (2.6, 3.2)	2.8 (2.4, 3.1)
$Tb.Th^d$, µm	43 (36, 49)	31 (26, 36)	23 (16, 30)
$Tb.Sp^d$, µm	320 (280, 360)	320 (290, 360)	350 (300, 400)

Data presented as mean (95% confidence intervals).
N = 10, tibia present in all specimens.

Table 3.3. Linear regression analysis of the systematic adjustment of the calcaneus HR-pQCT volume of interest.

	Tb.vBMD	Tb.N*	$Tb.Th^d$	$Tb.Sp^d$
Superior	R^2 = 0.72*** RMSE = 3.9% Y = 0.465*X-0.112	R^2 = NS RMSE = 1.6% Y = -0.017*X+0.181	R^2 = 0.80*** RMSE = 3.3% Y = 0.499*X-0.227	R^2 = 0.11** RMSE = 2.0% Y = -0.052*X-0.276
Middle	R^2 = 0.73*** RMSE = 2.8% Y = 0.345*X+0.275	R^2 = NS RMSE = 1.3% Y = 0.000*X+0.040	R^2 = 0.79*** RMSE = 2.6% Y = 0.365*X+1.04	R^2 = 0.08* RMSE = 1.5% Y = -0.032*X-0.135
Inferior	R^2 = 0.22*** RMSE = 6.2% Y = -0.248*X+1.750	R^2 = 0.08* RMSE = 2.1% Y = -0.046*X+0.282	R^2 = 0.14** RMSE = 5.6% Y = -0.172*X+2.38	R^2 = 0.14** RMSE = 2.4% Y = 0.072*X-0.440

RMSE – Root mean square error. Significance * ≤0.05, ** ≤0.01, *** ≤0.001

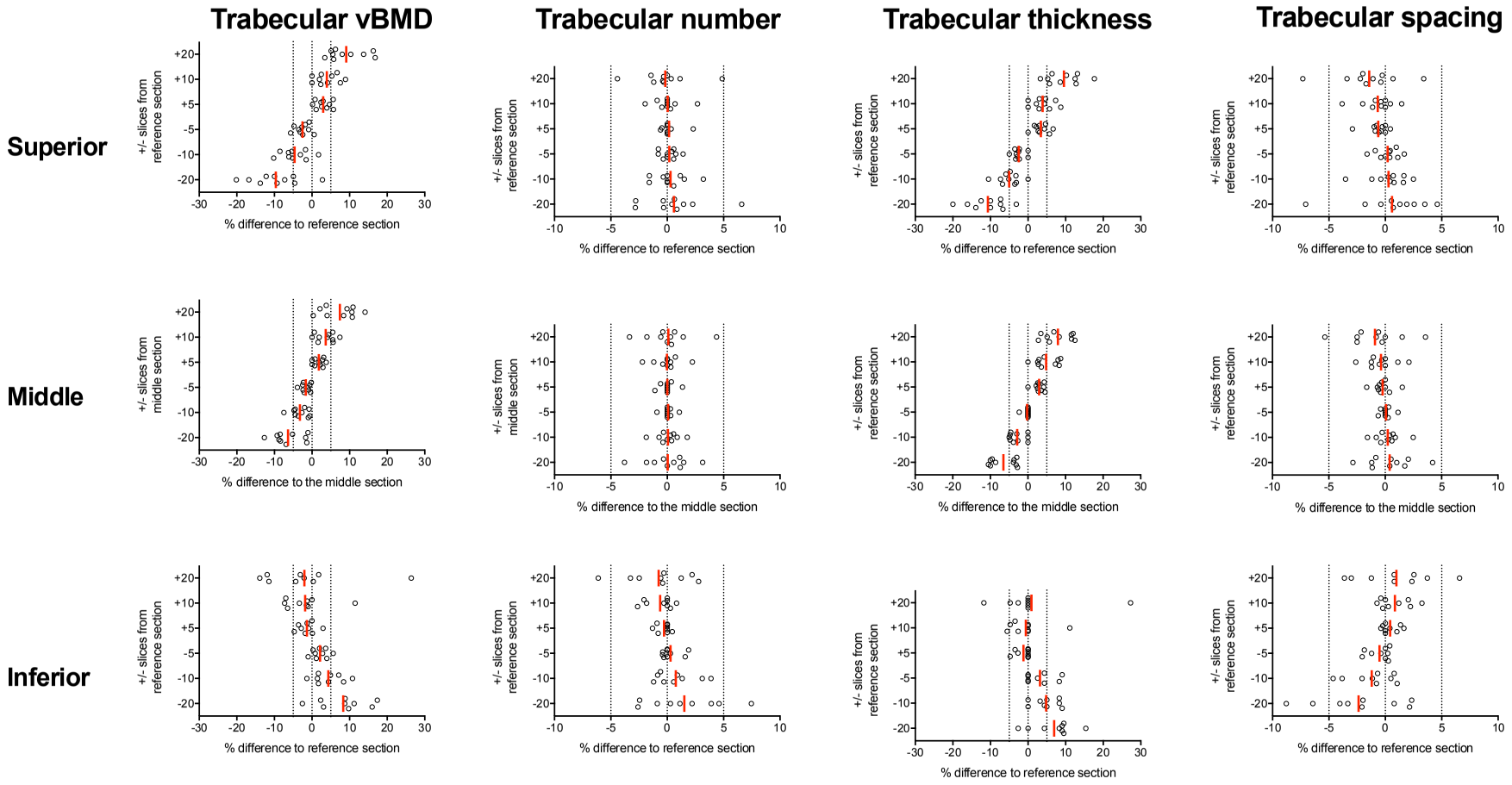

Figure 3.9. Percentage changes in calcaneus trabecular vBMD and trabecular microstructure with upto ±20 slice shifting of the posterior-superior, -middle and -inferior volumes of interest.

Mean (red line) and individual data points presented. Slice shifts: ±5 slices = ±0.41 mm; ±10 slices = ±0.82 mm; ±20 slices = ±1.64 mm.

3.7 Discussion

This Chapter described preliminary findings for the use of HR-pQCT at the calcaneus from human cadaveric specimen. The foot was positioned to ensure that the calcaneus and surrounding bones of the foot were within the field of view. Regional differences were found in the main body of the calcaneus tuberosity, specifically relating to trabecular vBMD and $Tb.Th^d$, which was significantly greater in superior regions compared to the middle and inferior regions of the bone. The heterogeneous trabecular vBMD and $Tb.Th^d$ highlights the importance in standardising the position of the reference line to identify the start of the image region (as shown for the distal radius and distal tibia in Section 2.3.1) to minimise calcaneus HR-pQCT measurements precision error.

It was apparent that the analysis of the calcaneus HR-pQCT images was more complex than the radius and tibia. The calcaneus cross-sectional area was noticeably larger (in comparison to radius and tibia scans collected from other studies in our Research Group) and therefore took longer to check the automated edge-detection performance. Some specimens, given their cadaveric source, also had low trabecular vBMD and a thin cortex, with cortical thickness approaching the width of individual trabeculae in specific regions on visual inspection of the slices (example Figure 3.6A). The low cortical thickness may had led to the large inaccuracies in the detection of the endocortical surface by the 'dual-threshold' algorithm, where similar errors have been reported at the ultradistal radius slices in osteoporotic individuals, with cortical thickness ranging from 200 to 300 μm [162]. Whereas radius cortical thickness increases with proximal movement from the ultradistal slices [100, 202, 203], which makes segmentation easier, the calcaneus cortical thickness was fairly uniform throughout the bone. Previous studies using MRI [193, 194, 198] and QCT [206, 207] have not evaluated calcaneus cortical bone. With the lower spatial resolution in these devices compared to HR-pQCT, separating the trabecular and cortical bone compartments may have been even more challenging. The condition of the calcaneal specimens in this Chapter may be a limiting factor in its application.

The natural variation in calcaneus trabecular vBMD and microstructure was demonstrated across representative regions that could be visualised and measured *in vivo*. Large regional differences in trabecular vBMD and $Tb.Th^d$ were apparent in the main body of the calcaneus tuberosity, as demonstrated by a CV% of ~60%.

These differences were mainly apparent along the superior-inferior axis of the calcaneus, rather than the anterior-posterior axis, which was consistent with studies using different quantitative imaging modalities [197, 198, 208]. Large distal-to-proximal differences have also been demonstrated at the radius and tibia, specifically in cortical thickness [202, 203, 209]. Bearing these anatomical differences in mind, adaptations have been made to HR-pQCT protocols to image different regions in clinical studies assessing fracture risk [87, 210] and pharmaceutical treatment response [211], as well as monitoring fracture healing [212]. It would be simpler to measure an extended region of interest at the calcaneus, or even the whole bone, however the increased likelihood of movement artefacts would be an issue with the increased scan duration (~20 minutes in the calcaneus specimens). At this stage, establishing a reproducible protocol for regional assessment of the calcaneus using scan duration comparable to current clinical studies is of importance. Once a protocol similar to that used routinely at the distal radius and distal tibia has been established, attempts could be made at larger region imaging and longer scans duration *in vivo*.

Different foot positioning was tested in the cadaveric specimen to ensure that the surrounding bones of the foot were within the XtremeCT field of view. With the aim of developing a protocol to enable the regional assessment of the calcaneus, standardised foot positioning was critical. The repositioning error of the scans was 0.24 mm (in specimen with the tibia present), based on the distance between two fixed anatomical landmarks. This is equivalent to 3 HR-pQCT slices at an 82 μm slice thickness. Based on the measurements from the positional variation, the change in trabecular vBMD would be on average 3% at the superior region and 1-2% at the middle and inferior regions of the calcaneus tuberosity. This variation was slightly higher than that reported in trabecular vBMD at the distal tibia (±1%) and distal radius by Boyd [203], however the reference trabecular vBMD was lower compared to the calcaneus specimens (tibia = 43 mg HA.cm^{-3}; radius = 39 mg HA.cm^{-3}) and the larger positional errors reported for total vBMD were dependent on cortical thickness. Larger positional variation at the calcaneus tuberosity led to more noticeable changes, with the mean percentage change in trabecular vBMD with a ±20 slice (±1.64 mm) shift reaching approximately 10% (superior region), which has also been reported for trabecular vBMD at the radius and tibia [203]. Image registration techniques may ameliorate these positional errors in multiple measurements of the same calcaneus, such as in longitudinal studies.

There are technical aspects of the calcaneus HR-pQCT imaging protocol that need to be considered for the application *in vivo*. Beam hardening and scatter artefacts from the polychromatic x-ray source could influence the trabecular vBMD measurement from the calcaneus HR-pQCT images. Sekhon and colleagues [156] reported that the manufacturers BHC algorithm was not sufficient to correct for beam hardening artefact, with trabecular vBMD overestimated by upto 41% in a customised HR-pQCT phantom with inserts containing a range of trabecular vBMD (60-360 mg HA/cm^{-3}) and cortical thickness (0.5-2.5 mm). Tissue with a larger size and quantity can also lead to cupping artefact from beam hardening, which can underestimate attenuation coefficients i.e. density measurements [213, 214]. The larger calcaneus size, combined with the greater quantity of bone in the field of view (talus, navicular and cuboid), could enhance beam-hardening artefact and lead to erroneous measurements using a similar protocol to that used for the radius and tibia HR-pQCT image acquisition and reconstruction. This is an important consideration for microstructural accuracy, as $Tb.Th^{d}$ and $Tb.Sp^{d}$ are dependent on trabecular vBMD. Additionally, the greater quantity of bone in the field of view may have compromised the image signal-to-noise ratio, as photons would be attenuated in surrounding bones and soft tissue. Increasing the x-ray intensity or frame averaging can improve signal-to-noise ratio [152, 214]; different x-ray intensities and its effect on the accuracy of the calcaneus trabecular vBMD (BV/TV^{d}) and trabecular microstructure measured by HR-pQCT, in comparison to a 'gold standard' reference, are investigated in Chapter 4.

A practical concern was the correct participant positioning for the HR-pQCT image acquisitions. It was established that the participant's body position would be similar to that with the tibia HR-pQCT scans, but with different foot positioning. This is unlike participant's position for MRI and conventional CT imaging of the calcaneus, where the body is supine on a couch. Furthermore, CT and some MRI devices have a larger gantry than the XtremeCT, which enables the foot to be more easily positioned for the image acquisitions. Whilst the pilot experiment was completed using cadaveric lower limbs *in situ*, other practical issues could be apparent *in vivo*. A pilot and familiarisation study for the developing measurement is described in Chapter 5.

3.8 Conclusion

This Chapter has presented preliminary findings for imaging the calcaneus *in situ* using HR-pQCT. The anticipated participant position for the calcaneus HR-pQCT scans would be similar to the distal tibia scans, with adaptations to the foot positioning to benefit image quality. The data generated from the cadaveric specimens indicate large heterogeneity in calcaneus tuberosity trabecular vBMD and $Tb.Th^{d}$, with differences shown over small (~1.64 mm) and large (~18 mm) positional variation of cubed volumes of interest. The appreciable positional variation has highlighted the importance of standardising the reference line positioning for the calcaneus HR-pQCT scans.

Technical and practical limitations have been highlighted and are addressed in the following Results Chapters: measurement validation with regards to the HR-pQCT scan settings and image reconstruction (Chapter 4); piloting the calcaneus HR-pQCT image acquisition *in vivo* and further testing the image analysis procedures (Chapter 5 and 6); short-term precision error for calcaneus HR-pQCT measurements (Chapter 6).

CHAPTER 4 VALIDATION OF CALCANEUS HR-PQCT MEASUREMENTS

This Chapter has been published: Metcalf LM, Dall'Ara E, Paggiosi MA, Rochester JR, Vilayphiou N, Kemp GJ, McCloskey EV, Validation of calcaneus trabecular microstructure measurements by HR-pQCT, *Bone*, doi: 10.1016/j.bone.2017.09.013.

As the author of this manuscript, permission to use the manuscript in the thesis is granted by Elsevier for personal use only. The published manuscript has been adapted so that it is consistent with the format of the thesis. A proportion of the Introduction, Methods and some parts of the Results have been reported in Chapter 3, and will be referred to when necessary to avoid repeating similar information.

Additional analyses have been included in the Appendix and are referred to within the Methods and Results sections.

4.1 Introduction

Chapter 3 presented preliminary findings from imaging the calcaneus using HR-pQCT *in situ*. Notable differences in trabecular vBMD and $Tb.Th^{d}$ were observed in the superior region compared to middle and inferior regions of the calcaneus tuberosity. Whilst observing these regional differences, it was clear that the calcaneus is anatomically and structurally different compared to the radius and tibia; the calcaneus CSA is larger and has several close-lying bones of the foot (talus, navicular and cuboid). This may make keeping the surrounding bones of the foot in the field of view challenging. Because there is likely to be a different quantity of bone and surround tissues in the field of view of the calcaneus HR-pQCT scans compared to the radius and tibia, the HR-pQCT scan settings may not be appropriate for optimal signal-to-noise ratio, due to x-ray artefacts such as beam hardening and photon scatter [156, 213, 214]. Adaptation of the x-ray intensity is known to improve signal-to-noise ratio, but it is unknown how changing the x-ray intensity may influence HR-pQCT measurements.

X-ray artefacts can affect quantitative measurement accuracy. Beam hardening can cause low attenuation values towards the centre of the field of view, leading to underestimations of vBMD [156]. Photon scatter may increase noise within the HR-pQCT images, which could be quantified as bone voxels following the application of the segmentation procedure [172]. As a distance-transformation method is used for Tb.N* measurement, higher bone voxels as noise may artificially increase Tb.N* [172]. This may subsequently lower $Tb.Th^{d}$ and lower $Tb.Sp^{d}$ calculations when using plate-model assumptions with the first generation XtremeCT. Considering the

differences mentioned above, the accuracy of distal radius and distal tibia HR-pQCT measurements [30, 77, 163, 164, 216] may not reflect those at the calcaneus.

4.2 Aims & Objectives

The aim of Chapter 4 is to validate the calcaneus HR-pQCT measurements with respective to micro-CT measurements.

The objectives of Chapter 4 are:

1. To determine the accuracy of trabecular bone volume and microstructure measurements using HR-pQCT, at the superior, middle and inferior regions of the calcaneus tuberosity, with respect to gold standard micro-CT measurements.
2. To characterise the effect of scan integration time on trabecular microstructure measurements on calcaneus HR-pQCT scans, with respect to gold standard micro-CT measurements.
3. To determine whether surrounding bones of the foot affect the accuracy of calcaneus trabecular bone volume and microstructure measurements using HR-pQCT.

4.3 Methods

4.3.1 Study design

Professor Eugene McCloskey, Dr Margaret Paggiosi, Dr Enrico Dall'Ara and I designed the study. The study design followed that reported in Section 3.3.1. I completed the calcaneus sample preparation for the micro-CT scans, the micro-CT scanning, and the image registration and analysis.

4.3.2 Materials

Ten lower limbs were obtained from cadavers (n=5, all female, age range 85 to 101 years); all had been divided through the proximal 2/3 point of the tibia. The specimens' preparation has been described in Section 3.3.2.

4.3.3 Calcaneus HR-pQCT imaging

4.3.3.1 Image acquisition

The specimen positioning was consistent with that reported in Section 3.4.2.1. Scans of the whole calcaneus were obtained between the superior peak of the

tuberosity and the plantar fascia attachment to the calcaneal tuberosity at an isotropic voxel size of 82 µm (maximum of 660 slices) using the standard clinical operational settings (Section 2.3.1).

As part of the method development, each calcaneus was scanned with different integration times; *in situ* (with the calcaneus in the intact limb) scan projections were collected twice at 100 ms and once each at 150 and 200 ms integration times, labelled IS100, IS150 and IS200, respectively. The range of integration times was tested to determine the potential gains in microstructure assessment of more prolonged exposure, while limiting the upper scan time to 4.2 minute to minimize potential movement artifacts when the protocol would be used *in vivo* in future clinical settings. Isolated (*ex vivo*, with the calcaneus removed from the limb, soft tissue removed but no cleaning of the bone marrow) scan projections were collected at 100 ms integration time, labelled EV100, to determine whether measurements would be affected by the surrounding bones of the foot. For these scans, the calcaneal samples were placed in sealed polythene bags and supported by foam, in order to obtain a similar anatomical position to scans *in situ*.

The calibration of the HR-pQCT density phantom is shown in the Appendix (Figure 9.2).

4.3.3.2 Image reconstruction

Calcaneus HR-pQCT image reconstruction followed the standard protocol provided by the manufacturer (Section 2.3.2).

4.3.4 Calcaneus micro-CT imaging

4.3.4.1 Sample preparation

The dissected calcanei were cut into rectangular prism samples (18 x 18 x 40 mm) preserving cortical bone at the superior and inferior surfaces, using a diamond-coated bandsaw under constant water irrigation (EXAKT: Norderstedt, Germany). Each sample was submerged and fixed in a 50 ml holder containing saline solution and was vacuumed for 20 minutes to remove air bubbles prior to each scan.

4.3.4.2 Image acquisition

Calcaneus micro-CT image acquisition followed the protocol reported in Section 2.4.1.

4.3.4.3 Image reconstruction

Calcaneus micro-CT image reconstruction followed the protocol reported in Section 2.4.2.

4.3.5 Rigid image registration

HR-pQCT scan DICOMs were registered to their respective micro-CT scans in a two-step process (Amira 6.0, FEI: Oregon, USA): step 1, an IS100 HR-pQCT scan was pre-aligned and registered to the micro-CT scan using a normalized mutual information metric and resampled using a Lanczos interpolator (Figure 4.1A). This has been described in Section 2.6.7.2. In step 2, the remaining HR-pQCT scans (IS100, IS150, IS200 and EV100) were registered using similar settings to the pre-registered IS100 HR-pQCT scan. This spatially registered all HR-pQCT scans to the micro-CT scan and, importantly, to the same reference system. The HR-pQCT scans from step 2 were used for morphological evaluation.

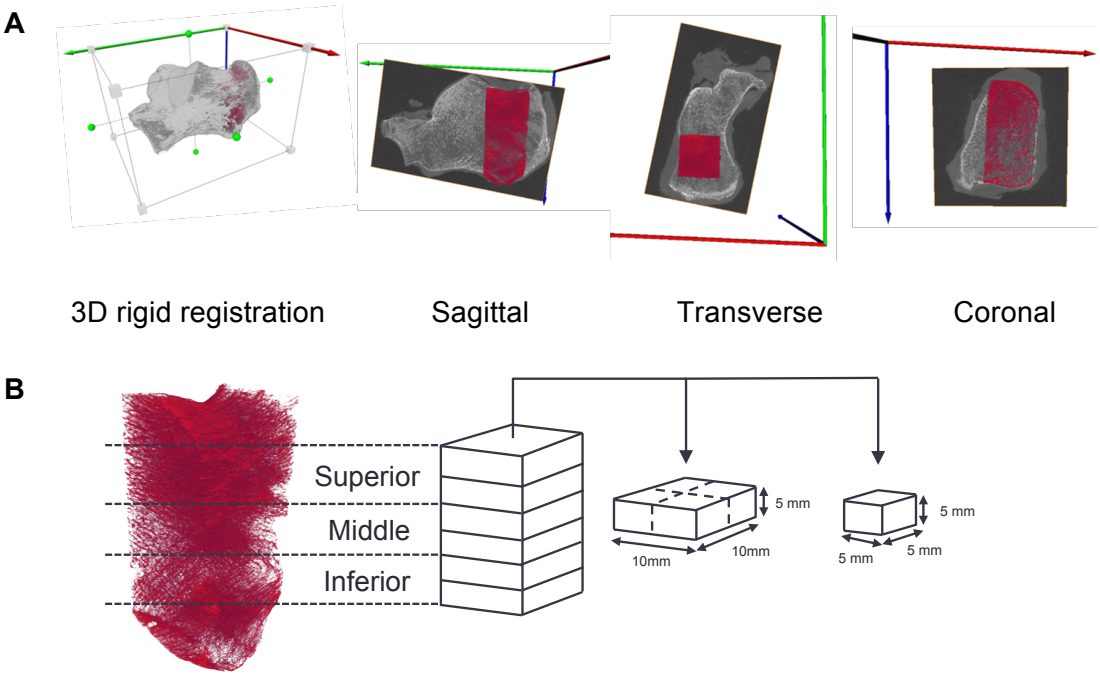

Figure 4.1. Methodology for registration and identifying the cubed regions of interest for HR-pQCT and micro-CT image analysis.

A) The HR-pQCT images were rigidly registered to the micro-CT image (red). Examples of the micro-CT and HR-pQCT images following transformation are shown in all 3 planes (sagittal, transverse and coronal).
B) Scans were split into six 10 x 10 x 5 mm regions along the superior-inferior axis. The 6 regions were sub-divided into four equal sized cubed volumes of interest (5 x 5 x 5 mm), which were used in the evaluations. Two of the 10 x 10 x 5 mm regions were combined into superior, middle and inferior regions: there were eight 5 x 5 x 5 mm-cubed volumes of interest in these regions.
Superior = region 1 to 8; middle = region 9 to 16; inferior = region 17 to 24.

4.3.6 HR-pQCT and micro-CT image evaluation

A custom cropping procedure was performed at the common region between the scan modalities, along the superior-inferior axis. The aim of the procedure was to increase the likelihood of evaluating a wider range of BV/TV [216, 217] as there had been significant bone loss in some specimens. Images were divided into regions of interest approximately 5 x 5 x 5 mm in dimensions: HR-pQCT, 60 x 60 x 60 voxels and micro-CT 284 x 284 x 284 voxels (Figure 4.1B). 24 cubical regions of trabecular bone were isolated in each scan, virtually dividing the central portion of each micro-CT image in six 5 mm thick slices, which were divided into four cubes (Figure 4.1). All registered HR-pQCT scans and the micro-CT scans were then imported into the XtremeCT for evaluation.

The HR-pQCT images were quantified for trabecular vBMD, BV/TV^{d}, Tb.N*, $Tb.Th^{d}$ and $Tb.Sp^{d}$ (* – directly computed; ^{d} – derived) using the manufacturers 'standard clinical evaluation' script (Section 2.3.3). The micro-CT images were quantified for BV/TV, Tb.N, Tb.Th and Tb.Sp (all directly measured) using the SCANCO IPL (Section 2.4.3). Examples of the HR-pQCT and micro-CT scans segmentation are presented in Figure 2.

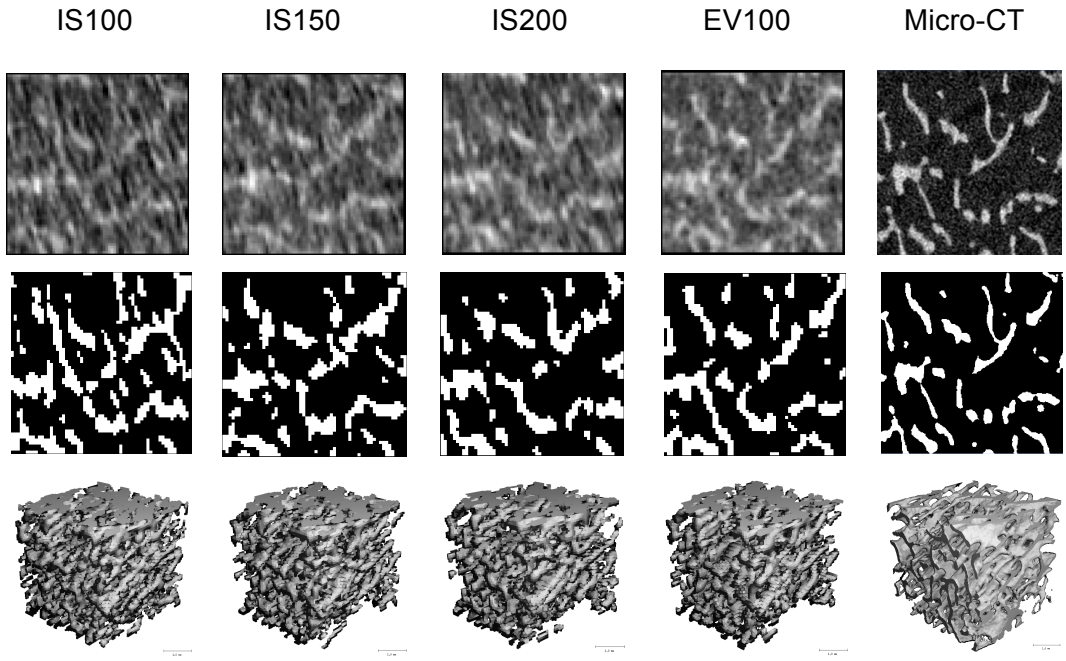

Figure 4.2. Segmentation of representative regions of interest in the calcaneus using HR-pQCT and micro-CT.

A slice is shown for a representative HR-pQCT and micro-CT image. The HR-pQCT scan is separated into the condition (*in situ* (IS) and *ex vivo* (EV)) and scan integration time (100, 150 and 200ms). This includes a greyscale and segmented slice, and the 3D volume of interest.

4.3.7 Statistical analysis

Statistical analyses were completed in GraphPad Prism (7.0, GraphPad Software: La Jolla California, USA) and R Studio (1.0.44: Boston, USA). A $p<0.05$ indicated statistical significance, unless stated otherwise. Morphometric measurements were non-normally distributed following visual and statistical checks (Shapiro-Wilk test), therefore median and interquartile ranges were calculated for each measurement. Wilcoxon-Rank tests were performed to compare the paired HR-pQCT and micro-CT scans (IS100, IS150, IS200, EV100 vs. micro-CT). Friedman's test with post-hoc between-pair analyses using Dunn's multiple comparisons tests was performed to compare the four HR-pQCT scans.

Linear regression analyses were performed to evaluate the correlation between the measurements performed on the HR-pQCT and micro-CT images; coefficient of determination (r^2), equation slope and intercept, root mean square error (RMSE) and the largest difference between the predicted and morphological parameters (max. error) were calculated. A region was treated as an outlier and removed from the regression analyses if all comparisons (IS100, IS150, IS200 and EV100) exceeded the Cook's distance (4/number of regions). Regression slopes were compared between the HR-pQCT scans using a one-way ANOVA and t-tests with Bonferroni corrections, to account for multiple tests i.e. between scan conditions (0.05/4) and between regions (0.05/3). Passing-Bablok regression was also performed as part of the HR-pQCT and micro-CT method comparison of each morphological parameter. Bland-Altman methods were performed to test for bias (mean ± SD) between the paired HR-pQCT scans and the micro-CT scan [218].

4.4 Results[4]

4.4.1 Descriptive comparisons

In total, 108 matched regions were evaluated between all HR-pQCT scans and the micro-CT scans, after removal of HR-pQCT scans with visible air bubbles or negative trabecular vBMD values. Table 4.1 contains the descriptive statistics for the morphological measurements from the scans. All estimates of BV/TV^d, $Tb.Th^d$ and $Tb.Sp^d$ derived from HR-pQCT images (IS100, IS150, IS200 and EV100) were

[4] Please note, the Results for this Chapter has been copied from the published manuscript. Figures and Tables from the supplemental information of the manuscript are included in this Results section.

significantly lower than the corresponding measures obtained from micro-CT images (all p<0.001). In contrast, Tb.N* measured in all HR-pQCT images was significantly overestimated (p<0.001) when compared to the micro-CT measurements. No differences were found among the trabecular vBMD and BV/TV^{d} measurement performed on the *in situ* HR-pQCT images across the 3 integration times, but Tb.N*, Tb.Th^{d} and Tb.Sp^{d} measured from IS100, IS150 and IS200 images were all significantly different to one another (p<0.001); as the integration time increased, Tb.N* decreased and Tb.Th^{d} and Tb.Sp^{d} increased. Trabecular vBMD, BV/TV^{d} and Tb.N* measured from the *in situ* HR-pQCT images were significantly higher, and Tb.Sp^{d} was significantly lower, compared to the measurements from the EV100 HR-pQCT image (p<0.001). Tb.Th^{d} measured from the IS100 and IS150 was significantly lower than measurements from the EV100 HR-pQCT image (p<0.001), but there was no difference between the IS200 and EV100 measurement (p>0.99).

Table 4.1. Descriptive statistics for the micro-CT and HR-pQCT scan images.

Measurements	Micro-CT	HR-pQCT			
		IS200	IS150	IS100	EV100
Tb.vBMD (mg HA/cm^3)	-	102^{c} (64, 132)	104^{c} (67, 127)	104^{c} (64, 131)	99 (61, 132)
BV/TV (%)	**13.6 (10.2, 16.2)**	8.7^{c} (5.4, 10.7)	8.7^{c} (5.5, 10.6)	8.7^{c} (5.4, 10.9)	8.2 (5, 11)
Tb.N (mm^{-1})	**1.49 (1.37, 1.62)**	1.98^{c} (1.72, 2.44)	2.14^{bc} (1.84, 2.89)	2.51^{abc} (2.24, 3.32)	1.79 (1.48, 1.97)
Tb.Th (mm)	**0.128 (0.119, 0.135)**	0.044 (0.028, 0.053)	0.040^{bc} (0.025, 0.05)	0.034^{abc} (0.02, 0.046)	0.046 (0.029, 0.056)
Tb.Sp (mm)	**0.64 (0.56, 0.7)**	0.46^{c} (0.38, 0.55)	0.42^{bc} (0.33, 0.49)	0.36^{abc} (0.28, 0.41)	0.51 (0.45, 0.62)

Abbreviations: *in situ* 100ms (IS100); *in situ* 150ms (IS150); *in situ* 200ms (IS200); *ex vivo* 100ms (EV100); trabecular vBMD (Tb.vBMD), bone volume fraction (BV/TV), trabecular number (Tb.N), trabecular thickness (Tb.Th), trabecular spacing (Tb.Sp).
N = 108 matched regions. Data are presented as median (25%, 75% percentile). Shaded areas indicate measurements that were directly measured.
Measurements in bold are significantly different to all HR-pQCT scans (all p<0.001).
[a] different to IS150, [b] different to IS200, [c] different to EV100 (all p<0.001).

4.4.2 Regression analyses in the common whole sample

Regression analyses for all evaluable regions are shown in Table 2. There were strong correlations between BV/TV measured in the micro-CT images and BV/TV^{d} computed from both *in situ* and *ex vivo* HR-pQCT images (r^2 = 0.95-0.98). There was no difference between the BV/TV versus BV/TV^{d} regression slopes (p=0.94) and the RMSEs were similar (0.8-0.9%). The BV/TV^{d} maximum errors obtained from

the *in situ* HR-pQCT images were similar (2-2.3%), and the value measured from the *ex vivo* HR-pQCT image was apparently lower (1.4%).

Weak to moderate correlations were found between Tb.N measured in the micro-CT and the *in situ* HR-pQCT images; the correlations were dependent on integration time (r^2 = 0.33 for IS100 and r^2 = 0.61 for IS200) with significant differences between the IS100 and IS200 regression slopes ($p<0.01$). There seemed to be lower RMSE and maximum error when the *in situ* integration time was increased from IS100 to IS200 (0.19 to 0.15 mm^{-1} and 0.67 to 0.46 mm^{-1}, respectively). The Tb.N correlation improved further when measured by the *ex vivo* HR-pQCT image in comparison to the micro-CT image (r^2 = 0.79) and the regression slope was significantly different to that obtained with the *in situ* comparisons (IS100, IS150 and IS200, $p<0.001$). Tb.N* measured from the *ex vivo* HR-pQCT image also seemed to have lower RMSE (0.11 mm^{-1}) and maximum error (0.30 mm^{-1}) compared measurements from the *in situ* HR-pQCT images.

Moderate correlations were found for $Tb.Th^d$ estimated in all HR-pQCT images with respect to the respective micro-CT measurements (r^2 = 0.53-0.59). There were no significant differences between the $Tb.Th^d$ regression slopes ($p=0.73$), and the RMSE and maximum error were all similar between the different HR-pQCT integration times. Weak to moderate correlations were found for $Tb.Sp^d$ estimated in all HR-pQCT images with respect to Tb.Sp micro-CT measurements; *in situ* correlations were dependent on the integration time (r^2 = 0.33 for IS100 and r^2 = 0.55 for IS200) and the correlation was found to increase when measured in the *ex vivo* HR-pQCT image (r^2 = 0.66). There were no differences in $Tb.Sp^d$ regression slopes ($p=0.64$), and the $Tb.Sp^d$ RMSE and maximum error were all similar.

Method comparison analyses using the Passing-Bablock regression for all regions found that linearity between HR-pQCT BV/TV^d and $Tb.Th^d$, in all scan conditions, and micro-CT BV/TV and Tb.Th could not be rejected (Table 9.1). HR-pQCT Tb.N* and $Tb.Sp^d$ at IS100 compared to micro-CT Tb.N and Tb.Sp could be rejected from linearity, whereas increasing integration time (IS150 and IS200) and dissecting the calcaneus from the foot (EV100) could not be rejected from linearity.

Table 4.2. Regression analysis for the HR-pQCT vs. Micro-CT trabecular measurement across all regions.

Sample	r^2	Intercept	Slope	RMSE	Max. error
Bone volume/total volume[d] (1) (n=104)					
IS200	0.96	0.050	1.000	0.009	0.021
IS150	0.95	0.050	1.010	0.009	0.023
IS100	0.96	0.050	1.000	0.008	0.020
EV100	0.98	0.053	1.020	0.008	0.014
Trabecular number (mm^{-1}) (n=106)					
IS200	0.61	0.805	0.347[§]	0.15	0.46
IS150	0.44	0.921	0.263[§]	0.18	0.59
IS100	0.33	0.941	0.217*,[§]	0.19	0.67
EV100	0.79	0.678	0.469	0.11	0.30
Trabecular thickness[d] (mm) (n=107)					
IS200	0.55	0.103	0.588	0.009	0.025
IS150	0.53	0.104	0.607	0.010	0.026
IS100	0.55	0.106	0.663	0.009	0.023
EV100	0.59	0.102	0.586	0.008	0.022
Trabecular spacing[d] (mm) (n=107)					
IS200	0.55	0.367	0.556	0.07	0.21
IS150	0.43	0.401	0.530	0.08	0.23
IS100	0.33	0.402	0.627	0.09	0.24
EV100	0.66	0.348	0.517	0.06	0.21

Abbreviations: *in situ* 100ms (IS100); *in situ* 150ms (IS150); *in situ* 200ms (IS200); *ex vivo* 100ms (EV100); RMSE, root mean square error; max. error, maximum error from the regression equation.

All r^2 values are statistically significant, $p<0.001$. Comparison of the regression slopes between different HR-pQCT conditions: * $p<0.01$ compared to IS200; [§] $p<0.001$ compared to EV100.

4.4.3 Regression analysis in superior, middle and inferior regions of the calcaneus.

We completed a regional analysis by grouping the 5 mm^3 regions of interests into superior, middle and inferior regions of the calcaneal samples (Figure 4.1). A number of cubed regions from the inferior region were removed as the analysis returned a negative vBMD. The results within each of these regions for BV/TV^d and Tb.N*, the measurements used to compute $Tb.Th^d$ and $Tb.Sp^d$ from the HR-pQCT images, are shown in Table 4.3 and Table 4.4, respectively, with corresponding regression plots in the Figure 4.3. Data for $Tb.Th^d$ and $Tb.Sp^d$ are shown in the Table 4.5 and Table 4.6, respectively.

There were strong correlations at the superior, middle and inferior regions for BV/TV measured in the micro-CT images and BV/TV^d computed from both *in situ* and *ex vivo* HR-pQCT images (r^2 = 0.96-0.99, all $p<0.001$). The superior and middle region regression slopes for BV/TV^d were significantly different to the inferior region, within each respective integration time *in situ* ($p<0.017$). The BV/TV^d RMSE was below 1% in all regions. The maximum error was 1-2% for the *in situ* and *ex vivo* HR-pQCT images at the superior, middle and inferior regions.

For the Passing-Bablok regression, linearity could not be rejected at any of the regions and in any of the scanning conditions between HR-pQCT BV/TV^d and micro-CT BV/TV ($p > 0.05$) (Table 9.2). The intercepts indicated that there were systematic differences for all BV/TV measurements between HR-pQCT and micro-CT (all > 0), showing HR-pQCT BV/TV^d underestimated micro-CT BV/TV. The slopes indicated some proportional differences; at the superior region IS100 and IS200 had slopes slightly < 1 and the inferior region had proportional differences > 1 for the *in situ* HR-pQCT scans. There were no proportional differences for the middle region for the *in situ* and *ex vivo* HR-pQCT scans.

The correlation for Tb.N measured from micro-CT and HR-pQCT images was strongest in the superior region (r^2 = 0.70-0.93, all $p<0.001$) compared to the middle region (r^2 = 0.52-0.76, all $p<0.001$). No correlation was found for Tb.N in the inferior region (all $p\geq0.21$). The strongest correlations were found for Tb.N measured in the *ex vivo* HR-pQCT compared to the micro-CT image, and was the only HR-pQCT image to be significantly, albeit moderately, correlated with micro-CT in the inferior region. All superior region regression slopes were significantly different to the middle (apart from IS100) and inferior regions, within each respective integration time. All middle region regression slopes were also significantly different to the inferior

region, within each respective integration time. A lower RMSE and maximum error were apparent at the superior and middle region with increasing integration time *in situ*, but this was not apparent at the inferior region *in situ*.

For the Passing-Bablok regression, linearity could not be rejected at the superior and middle region for the *in situ* scans between HR-pQCT and micro-CT Tb.N ($p > 0.05$). At the inferior region, of the *in situ* scans, only IS200 could not be rejected for linearity, whereas the IS100 and IS150 were rejected (both $p = 0.04$). Linearity was also rejected for EV100 at the superior region ($p = 0.04$), even though this condition and region had the strongest correlation between the methods ($r = 0.92$). There were systematic differences for all Tb.N measurements between HR-pQCT and micro-CT (all > 0), showing HR-pQCT Tb.N overestimated micro-CT Tb.N. The overestimation of Tb.N by HR-pQCT was lowest for the EV100 HR-pQCT scan within all regions. Whilst there were at least moderate-strong correlations between the methods at the superior and middle regions, there were no correlations for the inferior region between the *in situ* HR-pQCT scans and the micro-CT scans. The slopes indicated proportional differences for all Tb.N measurements, where the slopes were all < 1. The slopes increased as the integration time for the *in situ* HR-pQCT scans increased; the EV100 had the highest slope value within each respective region. The Passing-Bablok regression results for Tb.Sp were also comparable to those found for Tb.N, due to the calculation that is used for HR-pQCT derived $Tb.Sp^d$ (Table 9.5).

Table 4.3. Bone volume fraction regression data for the different HR-pQCT conditions at the three different regions.

Sample	Median (IQR)	r^2	Intercept	Slope	RMSE	Max. error
Superior (n=42)						
Micro-CT	0.159 (0.139, 0.187)					
IS200	0.105 (0.081, 0.126)	**0.96**	0.069	0.862[§]	0.009	0.018
IS150	0.103 (0.083, 0.124)	**0.96**	0.070	0.857[§]	0.009	0.019
IS100	0.105 (0.084, 0.124)	**0.97**	0.066	0.880[§]	0.008	0.019
EV100	0.102 (0.082, 0.130)	**0.97**	0.063	0.927[*,§]	0.007	0.020
Middle (n=43)						
Micro-CT	0.125 (0.097, 0.153)					
IS200	0.078 (0.046, 0.103)	**0.96**	0.053	0.954[§]	0.007	0.020
IS150	0.077 (0.046, 0.102)	**0.96**	0.052	0.962[§]	0.008	0.022
IS100	0.077 (0.044, 0.100)	**0.96**	0.053	0.967[§]	0.007	0.021
EV100	0.071 (0.044, 0.095)	**0.99**	0.051	1.030	0.004	0.013
Inferior (n=21)						
Micro-CT	0.100 (0.075, 0.123)					
IS200	0.056 (0.036, 0.075)	**0.98**	0.035	1.160	0.005	0.010
IS150	0.058 (0.036, 0.075)	**0.98**	0.033	1.180	0.005	0.012
IS100	0.056 (0.035, 0.074)	**0.98**	0.035	1.160	0.005	0.010
EV100	0.050 (0.025, 0.071)	**0.99**	0.049	1.070	0.004	0.008

Abbreviations: *in situ* 100ms (IS100); *in situ* 150ms (IS150); *in situ* 200ms (IS200); *ex vivo* 100ms (EV100); RMSE, root mean square error; max. error, maximum error from the regression equation.

Median (interquartile range) bone volume fraction (1) is presented within each integration time at each region.

r^2 values in bold are statistically significant, $p<0.001$. Comparison of regression slopes between the regions, within the same integration time: * $p<0.017$ compared to the middle region; [§] $p<0.017$ compared to the inferior region.

Table 4.4. Trabecular number regression data for the different HR-pQCT conditions at the three different regions.

Sample	Median (IQR)	r^2	Intercept	Slope	RMSE	Max. error
Superior (n=41)						
Micro-CT	1.51 (1.37, 1.65)					
IS200	1.87 (1.64, 2.10)	**0.88**	0.565	0.499*§	0.10	0.20
IS150	2.02 (1.79, 2.28)	**0.82**	0.601	0.454*§	0.12	0.28
IS100	2.36 (1.95, 2.59)	**0.70**	0.632	0.385§	0.16	0.38
EV100	1.81 (1.55, 1.98)	**0.93**	0.461	0.584*§	0.07	0.17
Middle (n=44)						
Micro-CT	1.56 (1.37, 1.67)					
IS200	1.99 (1.67, 2.56)	**0.70**	0.860	0.317§	0.12	0.27
IS150	2.13 (1.89, 2.96)	**0.59**	0.916	0.264§	0.15	0.35
IS100	2.49 (2.29, 3.44)	**0.52**	0.822	0.258§	0.16	0.38
EV100	1.86 (1.51, 2.07)	**0.76**	0.680	0.460§	0.11	0.24
Inferior (n=21)						
Micro-CT	1.45 (1.32, 1.47)					
IS200	2.06 (1.88, 2.36)	0.00	1.430	-0.013	0.10	0.22
IS150	2.34 (2.19, 2.85)	**0.05**	1.510	-0.044	0.10	0.21
IS100	2.87 (2.61, 3.30)	**0.08**	1.560	-0.054	0.10	0.20
EV100	1.69 (1.13, 1.79)	**0.50**	1.110	0.196	0.07	0.20

Abbreviations: *in situ* 100ms (IS100); *in situ* 150ms (IS150); *in situ* 200ms (IS200); *ex vivo* 100ms (EV100); RMSE, root mean square error; max. error, maximum error from the regression equation.

Median (interquartile range) trabecular number (mm^{-1}) is presented within each integration time at each region.

r^2 values in bold in all regions are statistically significant, $p \leq 0.001$. Comparison of regression slopes between the regions, within the same integration time: * $p<0.017$ compared to the middle region; § $p<0.017$ compared to the inferior region.

Table 4.5. Trabecular thickness regression data for the different HR-pQCT conditions at the three different regions.

Tb.Th (mm)	Median (IQR)	r^2	Intercept	Slope	RMSE	Max. error
Region 1 to 8 (n=42)						
Micro-CT	0.135 (0.129, 0.146)					
IS100	0.047 (0.038, 0.051)	**0.30**	0.111	0.568	0.011	0.022
IS150	0.051 (0.043, 0.058)	**0.28**	0.111	0.497	0.011	0.024
IS200	0.054 (0.046, 0.062)	**0.30**	0.110	0.492	0.011	0.023
EV100	0.057 (0.050, 0.066)	**0.40**	0.106	0.528	0.010	0.020
Region 9 to 16 (n=42)						
Micro-CT	0.124 (0.115, 0.129)					
IS100	0.028 (0.021, 0.038)	**0.50**	0.105	0.617	0.007	0.013
IS150	0.032 (0.026, 0.043)	**0.45**	0.104	0.545	0.007	0.014
IS200	0.035 (0.029, 0.046)	**0.46**	0.103	0.526	0.007	0.014
EV100	0.041 (0.029, 0.048)	**0.57**	0.102	0.534	0.006	0.013
Region 17 to 24 (n=20)						
Micro-CT	0.120 (0.113, 0.130)					
IS100	0.018 (0.009, 0.025)	**0.45**	0.105	0.785	0.009	0.018
IS150	0.022 (0.012, 0.030)	**0.45**	0.104	0.684	0.009	0.016
IS200	0.025 (0.013, 0.034)	**0.47**	0.104	0.615	0.009	0.015
EV100	0.028 (0.017, 0.036)	**0.64**	0.103	0.619	0.007	0.014

Abbreviations: *in situ* 100ms (IS100); *in situ* 150ms (IS150); *in situ* 200ms (IS200); *ex vivo* 100ms (EV100); RMSE, root mean square error; max. error, maximum error from the regression equation.

Median (interquartile range) trabecular thickness (mm) is presented within each integration time at each region.

r^2 values in are statistically significant, $p<0.001$. Comparison of the regression slopes between the regions, within the same integration time: * $p<0.017$ compared to the middle region; § $p<0.017$ compared to the inferior region.

Table 4.6. Trabecular spacing regression data for the different HR-pQCT conditions over the three different regions.

Tb.Sp (mm)	Median (IQR)	r^2	Intercept	Slope	RMSE	Max. error
Region 1 to 8 (n=42)						
Micro-CT	0.62 (0.54, 0.69)					
IS100	0.37 (0.34, 0.46)	**0.54**	0.306	0.775§	0.08	0.18
IS150	0.43 (0.39, 0.50)	**0.71**	0.266	0.769§	0.06	0.13
IS200	0.46 (0.42, 0.52)	**0.80**	0.236	0.792*§	0.05	0.11
EV100	0.49 (0.44, 0.58)	**0.89**	0.190	0.845*§	0.04	0.07
Region 9 to 16 (n=44)						
Micro-CT	0.60 (0.55, 0.69)					
IS100	0.37 (0.28, 0.41)	**0.57**	0.324	0.847§	0.07	0.14
IS150	0.43 (0.31, 0.51)	**0.61**	0.379	0.572§	0.07	0.16
IS200	0.47 (0.35, 0.57)	**0.71**	0.366	0.544§	0.06	0.16
EV100	0.50 (0.43, 0.63)	**0.77**	0.292	0.628§	0.05	0.13
Region 17 to 24 (n=21)						
Micro-CT	0.67 (0.66, 0.72)					
IS100	0.33 (0.29, 0.36)	0.06	0.757	-0.187	0.06	0.13
IS150	0.38 (0.34, 0.43)	0.03	0.732	-0.091	0.06	0.13
IS200	0.45 (0.41, 0.50)	0.05	0.709	-0.033	0.06	0.13
EV100	0.56 (0.51, 0.87)	**0.34**	0.579	0.166	0.05	0.14

Abbreviations: *in situ* 100ms (IS100); *in situ* 150ms (IS150); *in situ* 200ms (IS200); *ex vivo* 100ms (EV100); RMSE, root mean square error; max. error, maximum error from the regression equation.

Median (interquartile range) trabecular spacing (mm) is presented within each integration time at each region.

r^2 values in bold in the superior and middle regions are statistically significant, $p<0.001$. The r^2 value in bold in the inferior region is statistically significant, $p=0.005$. Comparison of the regression slopes between the regions, within the same integration time: * $p<0.017$ compared to the middle region; § $p<0.017$ compared to the inferior region.

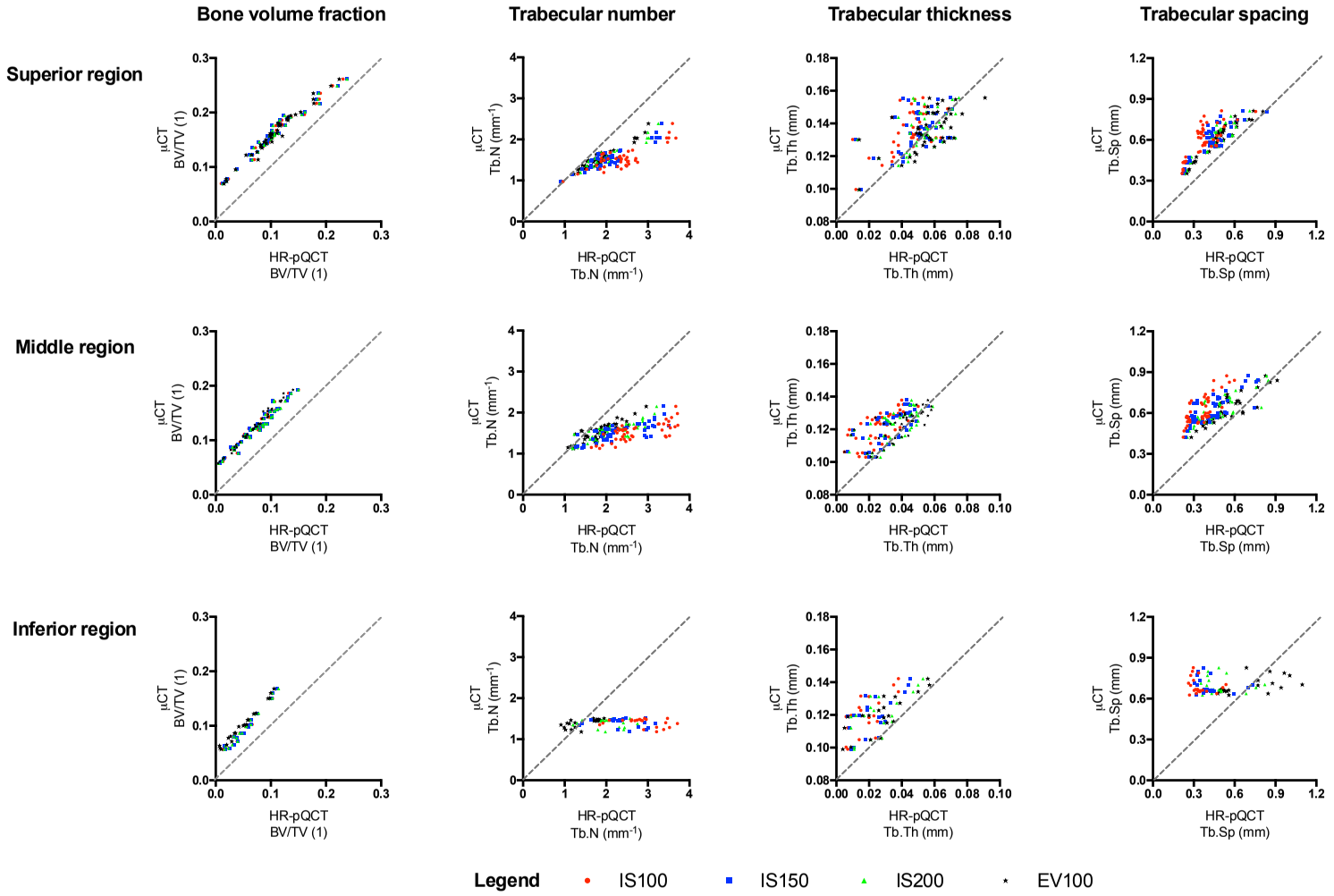

Figure 4.3. Regression plots for the comparison of measurements from calcaneus HR-pQCT and micro-CT images at the different regions.

Abbreviations: *in situ* 100ms (IS100); *in situ* 150ms (IS150); *in situ* 200ms (IS200); *ex vivo* 100ms (EV100).
Grey hashed line indicates the line of unity.

4.4.4 Bland-Altman method comparison

Bland-Altman plots for measurements in the superior, middle and inferior regions are presented for BV/TV^d and Tb.N* in Fig. 3. Plots for $Tb.Th^d$ and $Tb.Sp^d$ are available in the supplemental material 5. BV/TV^d computed from the HR-pQCT images underestimated BV/TV measured by micro-CT. The mean biases for the *in situ* and *ex vivo* HR-pQCT images were similar between the integration times and regions: approximately 4-5%. Tb.N* measured by HR-pQCT images systematically overestimated Tb.N measured from the micro-CT images. The mean bias for Tb.N* decreased as the integration time increased in the *in situ* HR-pQCT images at all regions. The Tb.N* mean bias was lower in the *ex vivo* HR-pQCT images compared to the *in situ* HR-pQCT images. The mean bias (±SD) for IS100 and IS150 increased from the superior to inferior regions (IS100: superior = −0.85 ± 0.40 mm^{-1}, inferior = −1.46 ± 0.55 mm^{-1}; IS150: superior = −0.56 ± 0.33 mm^{-1}, inferior = −0.98 ± 0.53 mm^{-1}), whereas the mean bias for IS200 increased from the superior to middle regions and was similar for the middle to inferior regions (superior = −0.44 ± 0.28 mm^{-1}, middle = −0.58 ± 0.42 mm^{-1}, inferior = −0.63 ± 0.41 mm^{-1}).

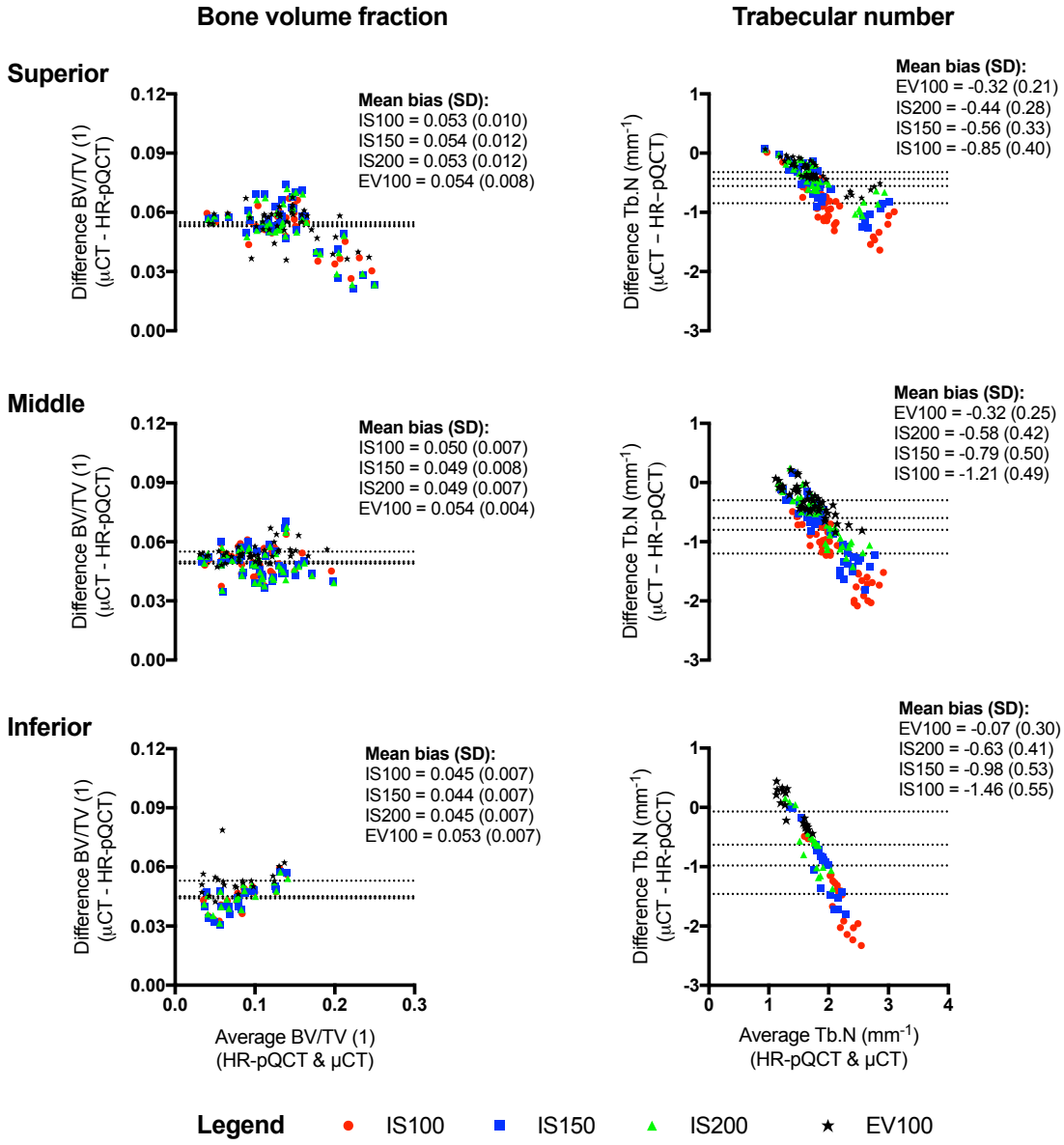

Figure 4.4. Bland-Altman plots for calcaneus bone volume fraction and trabecular number measured from HR-pQCT images (IS100, IS150 and IS200, and EV100) compared to micro-CT image at different regions (superior, middle and inferior).

Abbreviations: *in situ* 100ms (IS100); *in situ* 150ms (IS150); *in situ* 200ms (IS200); *ex vivo* 100ms (EV100).

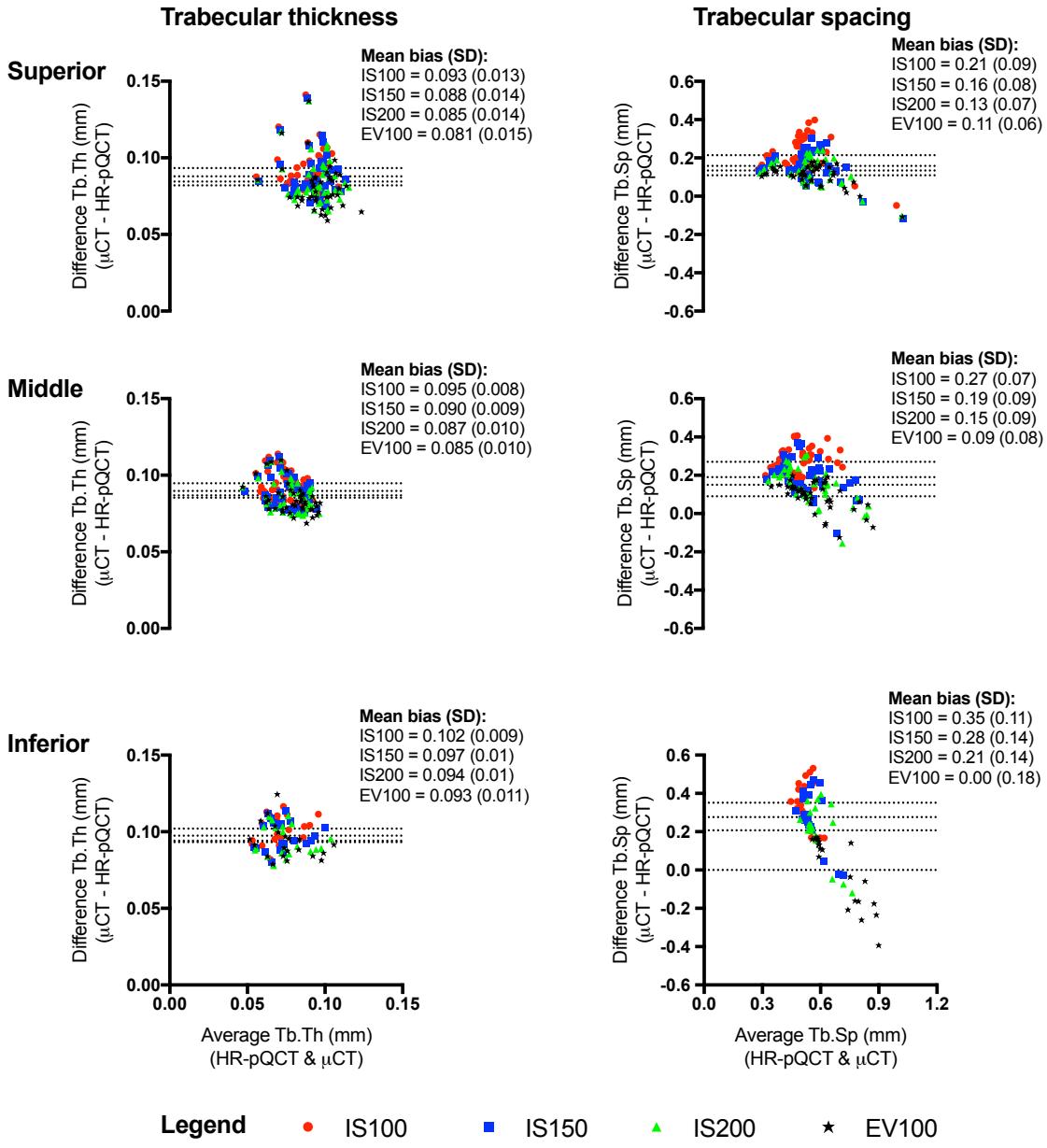

Figure 4.5. Bland-Altman plots for calcaneus trabecular thickness and trabecular spacing measured from HR-pQCT images (IS100, IS150 and IS200, and EV100) compared to micro-CT image at the different regions (superior, middle and inferior).

Abbreviations: *in situ* 100ms (IS100); *in situ* 150ms (IS150); *in situ* 200ms (IS200); *ex vivo* 100ms (EV100).

4.5 Discussion[5]

This Chapter describes the novel adaptation of HR-pQCT for the measurement of calcaneal BV/TV^d and microstructure. Calcaneus BV/TV^d and microstructure assessed at an isotropic 82 µm voxel size was validated against micro-CT at an isotropic 17 µm voxel size, which acted as a 'gold-standard' reference. HR-pQCT BV/TV^d had a strong correlation across all scan conditions, explaining 95 to 98% of micro-CT BV/TV, when all regions were combined. This is important, as BV/TV^d is a key measurement to predict bone strength [30, 164, 219] and has a strong association with fracture risk [220, 221].

The strong correlation and underestimation of BV/TV^d that was found with the calcaneus HR-pQCT scan images was consistent with previous studies at the distal radius and distal tibia [77, 163, 164]. The lower estimation of BV/TV^d, derived from trabecular vBMD measurement by HR-pQCT, could be caused by the global threshold used to define bone tissue and lower signal-to-noise ratio resulting in a higher number of partial volume voxels in the HR-pQCT images compared to the micro-CT images. It should also be remembered that the HR-pQCT measurements were made in the intact bone, so that beam hardening artifacts caused by the intact cortex and surrounding bone structures may have also impacted on trabecular vBMD measurement [156]. Trabecular vBMD was similar at the different integration times. On removing the calcaneus from the foot, the trabecular vBMD and BV/TV^d were significantly lower than the *in situ* scans, even though the absolute difference was relatively small. Dissection may have exposed the calcaneus to air bubbles that were undetectable in the HR-pQCT images, or else there may have been a reduction in image noise with removal of the surrounding bones and soft tissue. Nonetheless, a regression equation that is independent of integration time can be used to adjust calcaneus BV/TV^d computed from HR-pQCT images to that measured by micro-CT ($Y = 1.010*X + 0.050$).

Calcaneus Tb.N* was systematically overestimated, and $Tb.Th^d$ and $Tb.Sp^d$ subsequently underestimated when measured by HR-pQCT using the standard patient analysis, consistent with previous studies at the radius and tibia [77, 163, 164]. It has been well established that the accurate measurement of trabecular microstructure is dependent on the spatial resolution [77], which was equivalent to the calcaneus Tb.Th measured by micro-CT in the current study. The higher values

[5] The Discussion for this Chapter has been copied from the published manuscript.

of Tb.N* in purely trabecular samples measured by HR-pQCT compared to micro-CT are in keeping with previous reports [77, 164], probably reflecting factors such as decreased signal-to-noise ratio and partial volume effects; factors that are exacerbated at the shorter integration times as observed in our study. A similar increase in Tb.N* for individual specimens has been reported when comparing a 123 µm to 82 µm isotropic voxel size [77]. BV/TV^d may be less susceptible to such factors as it is derived from trabecular vBMD, in which the averaging per cm^{-3} is likely to suppress differences between integration times, as has been demonstrated by summing the voxels for BV/TV measurement [30, 216, 222].

The direct measurement of Tb.N* is fundamental to determining $Tb.Sp^d$ and $Tb.Th^d$ using plate-model assumptions. The HR-pQCT indirect patient analysis aims to preserve all trabeculae using a low global threshold in order to measure Tb.N* [172]. The caveat is that if an image has a low signal-to-noise ratio, image noise could be categorised as bone following application of the HR-pQCT threshold to segment to bone and marrow phases [159]; this is the possible mechanism of the greater overestimation of Tb.N* at lower integration times and in the inferior regions of the calcaneus. Increasing integration time improved the accuracy of Tb.N* in comparison to micro-CT, leading also to an improvement in $Tb.Sp^d$ accuracy. However, $Tb.Th^d$ was not improved, due to its equal-weighted dependency on BV/TV^d and Tb.N*. Weak correlations with $Tb.Th^d$ have been confirmed in studies at the radius and tibia despite strong correlations for BV/TV^d and Tb.N* [77, 163]; this study therefore further highlights a limitation in the use of the plate-model assumptions using the first generation XtremeCT. A better signal-to-noise ratio, provided by a higher trabecular vBMD, was also reflected in the improved accuracy of Tb.N* in the denser superior region of the calcaneus than in the middle and, particularly, inferior regions. Furthermore, the regions with thinner trabeculae (middle and inferior) could be more susceptible to errors with the global threshold applied by the indirect HR-pQCT analysis, which could also explain differences in trabecular measurement accuracy compared to other studies [30, 77, 163, 164, 172]. Other thresholds may improve the accuracy; for example, in femoral neck trabecular bone samples a local-derived direct assessment improved estimates of $Tb.Th^d$ and $Tb.Sp^d$, though the overall impact was relatively small [172].

The superior region scanned at 200 ms integration time had comparable correlation, slopes and accuracy for BV/TV^d, Tb.N* and $Tb.Sp^d$ compared to previous studies at the distal radius and distal tibia [77, 163, 164]. This is encouraging, as these validated protocols have been widely used in clinical studies [85, 220, 221, 223-

225]. In addition to lower bone volume in the middle and inferior regions, the signal-to-noise ratios may also be impacted by the surrounding bones of the foot at these levels in affecting the measurement of trabecular microstructure using HR-pQCT. The more marked differences in Tb.N* between the *in situ* and *ex vivo* scans at the inferior region suggest that this may be the case. In the same region, noise is likely to have contributed to the fact that although the *ex vivo* scan had similar Tb.N* values to the micro-CT, the correlation was still relatively weak. Additionally, the poorer estimation at these regions could be due to thinner trabeculae, which has been highlighted as an issue in a previous study comparing plate- and rod-like trabeculae at different voxel sizes [226].

The results reinforce using 200 ms integration time for the calcaneus HR-pQCT scans to compensate for the x-ray absorption from the surrounding tissues. Practically, there would still be a low radiation exposure per 110 slices (6 µSv per scan). However, scan duration would be 4.2 minute (per 110 slices using the XtremeCT I), which is longer than the distal radius and distal tibia scans (2.8 minute). This would increase the probability of participant movement and may consequently affect measurement precision error. Precision error of HR-pQCT measurements at the calcaneus has not been established *in vivo*. Distal radius and tibia error is already between 3 and 6% (least significant change 8-17%) for trabecular microstructure using rigid registration at 100 ms integration time [155, 176, 177]. However, it can be questioned whether the accuracy at lower integration times could be accepted to improve reproducibility, which could be the case if BV/TV^d, and possibly other volumetric measurements, were of primary interest. The comparison of different integration times *in vivo* therefore requires investigation.

We have attempted to best represent *in vivo* conditions by obtaining HR-pQCT scans *in situ*, with bones, soft tissue and marrow intact, to inform the clinical translation of the method. However, we recognize there are several limitations to the study. First, and as has been discussed, the study was free from movement artifact, which would be expected to affect measurement accuracy *in vivo*. Second, measurements may have been impacted by the deterioration of bone mineral given the advanced age of the donors. We found that BV/TV measured by micro-CT was comparable to previous studies that have evaluated similar regions and specimens of a similar age and gender [197, 227, 228]; preliminary *in vivo* HR-pQCT measurements suggest derived BV/TVs of ~26% (unpublished data) and this is likely to be greater in a younger cohort. Assessment of calcaneus cortical bone was not undertaken due to the extremely thin cortices observed in our cohort that

affected the segmentation of the calcaneus cortical bone (HR-pQCT example Figure 3.5; micro-CT example Figure 9.3); whether this would be possible in younger specimens remains to be determined. Third, in an attempt to broaden the BV/TV range that was validated, we evaluated smaller cubic regions of interest [216, 217], potentially increasing errors between modalities that would have been lessened by comparisons of larger cross-sectional area. Fourth, micro-CT analysis primarily used a fixed threshold, which was adapted for 4 regions (same specimen). Others have used an adaptive threshold for all samples [77] and this may be a factor in differences between the studies. Finally, we used the first generation XtremeCT device (isotropic voxel size = 82 μm, spatial resolution = 127-154 μm [96]) that uses plate model-assumptions to compute trabecular microstructure. The second generation XtremeCT device has a reported superior spatial resolution (isotropic voxel size = 61 μm, spatial resolution = 95 μm), which includes more independent measurements and may improve the direct estimation of trabecular microstructure [97]. Furthermore, the field of view is slightly larger and the scan time is shorter, which may better accommodate the quantification of calcaneus trabecular microstructure *in vivo*.

4.6 Conclusion

In summary, we have developed a protocol to scan the calcaneus using HR-pQCT that has achieved measurement correlation and accuracy comparable to previous validation studies performed at the distal radius and distal tibia. Here, scanning a superior region of the bone with a 200 ms scan integration time for the quantification of trabecular microstructure is preferred, based on the proposed protocol and integration times investigated in this study. Investigating inferior regions of the calcaneus and using lower integration time appears inaccurate. Future developments will include the testing of HR-pQCT integration times *in vivo* and determining measurement precision error, bearing in mind the potential for movement artifacts in longer scan durations. Such studies will determine whether calcaneus HR-pQCT scans could have a significant clinical utility in osteoporosis or podiatry research.

CHAPTER 5 QUANTIFYING CALCANEUS VOLUMETRIC BMD AND MICROSTRUCTURE IN VIVO

5.1 Introduction

Chapter 4 found that a 200 ms integration time achieved predictions of trabecular BV/TV^d and microstructure (mainly Tb.N*) at the calcaneus that were similar to those reported at the distal radius and distal tibia using the first generation XtremeCT [77, 163, 164]. There were also regional differences in the calcaneus tuberosity body (Chapter 3 and 4) and the prediction of trabecular microstructure (Tb.N* and $Tb.Sp^d$) was stronger at the superior region of the calcaneus compared to the middle and inferior regions of the bone (Chapter 4). Chapter 5 will present the translation of the developed method to a pilot study *in vivo*. Performing the HR-pQCT method *in vivo* presents several challenges that are not encountered in cadaveric experiments: the physical positioning of the participants, reproducible alignment of the scanning region and minimising image artefacts from movement.

5.1.1 Participant positioning

The correct positioning of the participant is essential to obtain images of an acceptable quality for quantitative analysis and to ensure that the measurement precision error is low. Participants must also understand what to expect, so that they are comfortable during the image acquisition. This requires the scan technician to explain the process and to describe the examination and its duration [229]. Reiteration of the scan duration is an important preparatory step for HR-pQCT imaging, as the scan duration for a 9 mm stack of tomographic slices is at least 2.8 minutes with the first generation XtremeCT. Therefore, minimising involuntary movements is fundamental to HR-pQCT image acquisition.

From previous HR-pQCT studies, it has been assumed that the positioning for the distal tibia scans allows a more comfortable position than the radius scans due to the neutrality of the body's position, i.e. similar to sitting in a chair (Figure 2.5). The body position for the calcaneus scans would be similar to distal tibia scan, however the positioning of the foot would be different, with plantar-flexion at the ankle joint rather than a neutral position (Chapter 3). The use of positioning aids made from low attenuation materials (foam wedges, plastic bags with foam pellets, and air-filled cushions) are encouraged to standardise positioning and minimise involuntary movements [158]. It is also important that contact between the positioning aid and skin is between firm and soft to ensure that comfort is optimal with the correct positioning [229]. Without these precautions, HR-pQCT measurement precision

error could be compromised through improper alignment [154, 176, 177] and image artefact caused by movement [94, 95].

5.1.2 Reproducible alignment of the scanned region

Reproducible alignment of the HR-pQCT scan region can minimise error between repeat scans. Once participants are positioned in the XtremeCT gantry, the start point of the HR-pQCT scanning region is identified on a scout view. Variability in the positioning of the reference line can induce error between measurements. With the first generation XtremeCT, experienced operators had a 0.20 mm and 0.38 mm same-day precision error for identifying the anatomical landmark (start point) on the same scout view image for scans at the tibia and radius, respectively [154]. The resulting precision errors from this small misalignment at these sites, ranged from 0.9-3.3% for measurements of volumetric BMD and from 2.5-12% for measurements of bone microstructure [154], which is supported by heterogeneous vBMD, Tb.N* and cortical thickness on a slice-by-slice basis [100, 203] and with ±2 mm (distal and proximal) movement of the region of interest at the radius and tibia [203, 230]. Heterogeneity in trabecular vBMD and trabecular microstructure is anticipated with errors in the reference line placement for calcaneus HR-pQCT scans (Chapter 3).

The misalignment of repositioned HR-pQCT images may lead to increased precision errors and compromise the detection of microstructure adaptations over time with interventions and disease. Image registration can overcome this limitation. Bonaretti and colleagues [154] demonstrated that removal of the positioning error with CSA-based (2D) registration in radius and tibia HR-pQCT images, significantly lowered the precision error for volumetric BMD (< 1.3%) and microstructure measurements (1.3-8.9%; the highest was for cortical porosity). The CSA-based matching of images incorporated into the evaluation using the manufacturers' standard methods does not take into account 'out of plane' differences. 3D registration, which does take into account image rotation and translation, has been reported to improve short-term measurement precision error compared to the CSA-based registration method [176, 177], although absolute differences were relatively small. The strength of 3D registration has been shown in bones with changing morphology, such as in mice with age and treatment [231] and in humans with disease [89]. The use of 3D registration identified greater radius cortical porosity in patients following kidney transplantation when compared to the CSA-based registration method, as well as identifying changes from positive non-linear to positive linear relationships between bone resorption markers and cortical porosity [89]. The improved sensitivity of 3D

registration could, therefore, be important in detecting small changes in trabecular microstructure from HR-pQCT images.

5.1.3 Minimising image artefacts

Movement is the primary cause of image artefact with HR-pQCT. At the end of each acquisition, the scan technician visually grades an image from a single reference slice taken from the centre of the HR-pQCT stack (more detail in 2.3.1.1). Severe artefacts that require the image acquisition to be repeated, based on manufacturer recommendations, include horizontal streaking, disruption of the cortical bone contiguity and smearing of the trabecular bone. Generally, there are lower frequencies of repeated measurements at the tibia compared to the radius, which has been associated with participant positioning [94, 95, 151, 155]. Movement has been associated with errors in volumetric BMD and microstructure measurements obtained with HR-pQCT. Between images without (best) and with severe artefacts (worst, and require repeating), the mean difference and precision error in measurements of trabecular microstructure increases, with discrepancies as high as 20-30% and 10-12%, respectively [94, 95]. Measurements of volumetric BMD (total, trabecular and cortical) are not as severely affected, with the mean difference and precision error ranging from 1-7% and 1-5%, respectively [94, 95]. Importantly, the magnitudes of the precision errors caused by movement, which are accepted for analysis, are equivalent to biological variations with disease, pharmaceutical interventions and between clinical populations [80, 89, 224, 232, 233]. Therefore, minimising participant movement is critical when using HR-pQCT *in vivo*.

5.1.4 Summary

Sources of the error that occurs with HR-pQCT imaging *in vivo* need to be controlled in order to establish whether a 200 ms would be an acceptable integration time to quantitate calcaneus volumetric BMD and trabecular microstructure.

Positioning is a source of error for HR-pQCT scanning. Participants need to be comfortable in the position that was tested in human cadaveric specimen. Reproducible identification of the anatomical landmarks to position the reference line would maximise the common volume between the repeat image acquisitions, although these positioning errors can be minimised by applying a 3D image registration procedure between the images. Image artefact caused by movement can be minimised using positioning aids to immobilise the limb, whilst maintaining participant comfort. The scan technician can control error from images with severe movement artefact by repeating the image acquisition or by removing the image

from the analysis. It is also important for the scan technician to develop familiarity with the imaging protocol to minimise precision errors.

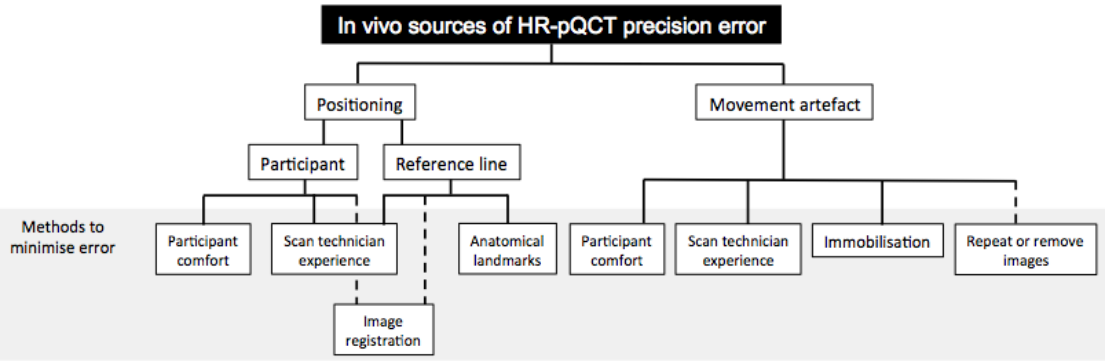

Figure 5.1. Summary of the *in vivo* sources of HR-pQCT precision error.

Dashed lines indicate measures that are undertaken to minimise errors following image acquisition.

5.2 Aims and objectives

The aim of Chapter 5 is to optimise the quantitative assessment of the calcaneus using HR-pQCT *in vivo*.

The objectives of Chapter 5 are:

1. To compare image movement artefact grades between the 100ms and 200ms integration time calcaneus HR-pQCT scans.
2. To compare volumetric bone mineral density and trabecular microstructure between the 100ms and 200ms integration time calcaneus HR-pQCT images.
3. To compare the volumetric bone mineral density and trabecular microstructure between the superior and inferior region of the calcaneus HR-pQCT images.
4. To identify practical issues in positioning of the participant and the lower-limb that would compromise the application of the calcaneus HR-pQCT *in vivo*.

5.3 Methods

5.3.1 Study design

Professor Eugene McCloskey, Professor Graham Kemp, Dr Margaret Paggiosi and I designed the study. The study had a cross-sectional, randomised design, and

required participants to attend for a single visit. This study was given a favourable ethical opinion and approval by the Yorkshire & Humber - Sheffield Research Ethics Committee (reference 15/YH/0401). Sister Angela Green and I completed the participant recruitment and informed consent. Dr Margaret Paggiosi performed the HR-pQCT image acquisitions. I completed the HR-pQCT image registration and analysis; Jenna Fogden and Rhea Patel assisted with the semi-automated contouring of the HR-pQCT images.

5.3.2 Positioning and Comfort Pilot study

Dr Margaret Paggiosi and I piloted the calcaneus HR-pQCT scanning procedure on 6 volunteer participants (using the same inclusion and exclusion criteria detailed in section 5.3.3) prior to obtaining 100 ms and 200 ms integration time HR-pQCT images. This pilot study was completed under the same ethics submission (reference 15/YH/0401). This enabled the scan technician to become familiar with performing the procedure and explaining it to the participant. This also enabled the investigator and scan technician to optimise the participants positioning, test different positioning aids and to ensure comfort during the image acquisition. Section 5.3.5 contains detail of the piloted procedure.

5.3.3 Participants

The sample size for the study was calculated from *ex vivo* experiments using human cadaveric specimens. According to these experiments, 5 samples were required to detect a mean reduction in Tb.N* by 0.5 mm^{-1} with the 200 ms compared to a 100 ms scan integration time, with an alpha of 0.05, with 80% power. Tb.N* was chosen as the endpoint, as it changes with integration time and is critical to the estimation of $Tb.Th^{d}$ and $Tb.Sp^{d}$ using the first generation XtremeCT. As the scans were collected in vivo, and due to the higher scan duration with 200 ms integration time compared to 100 ms, a higher risk of movement artefact was anticipated. The loss of either the 200 ms, or the 100 ms, integration time images would render the participant's other HR-pQCT images redundant from the analysis. Therefore, 10 participants were recruited to lower the risk of compromising study power due to high number of unacceptable HR-pQCT images.

5 female and 5 male participants were recruited. Female participants had to be postmenopausal and male participants had to be over the age of 50 years. Participants had to be ambulatory and were excluded from the study if they had:

- a BMI less than 18 or greater than 35 kg/m^2;

- a condition or local abnormality that would impede positioning of the foot in the XtremeCT scanner;
- or experienced previous bilateral fractures of the calcaneus.

All participants were telephone-screened using the study eligibility criteria prior to attending the Clinical Research Facility. Eligible participants provided written informed consent.

5.3.4 Descriptive statistics

Weight (kg) was measured to the nearest 0.1 kg using an electronic balance scale (Seca: Birmingham, UK). Height (cm) was measured to the nearest 0.1 cm using an electronic, wall-mounted stadiometer (Seca 242, Seca: Birmingham, UK). BMI was calculated as (weight (kg)/ (height (m))^2).

5.3.5 Calcaneus HR-pQCT imaging

5.3.5.1 Participant positioning

HR-pQCT imaging of the calcaneus was performed using the first generation XtremeCT. Participants were seated upright with full extension of the knee. The non-dominant foot (or dominant foot if there was a contraindication for using the non-dominant foot) was positioned in the carbon fibre, lower limb cast used for the distal tibia scans, with plantar-flexion at the ankle joint to align the superior and inferior surfaces of the bone with the scout view (Figure 5.2), following suggestions from Chapter 3 (Section 3.4.2). Furthermore, this was a useful guide for the scan technician to ensure that foot positioning was similar between participants.

To assist reproducible foot positioning, a customised, high-density foam wedge (6LB RECON, The Foam Shop: Taunton, UK) was placed underneath the foot. Foam wedges, with angles of 19.1 and 23.4°, were appropriate to align the calcaneus surfaces with the scout view (Figure 5.2B). The scan technician could then adjust the positioning with manual movement of the foot or by using smaller pieces of foam. Once positioning was optimised, the foot, ankle and lower calf were secured using pieces of foam and a thin bandage, which was wrapped around the lower calf and toes to minimise movement artefact during the scans. The same type of bandage was used across all participants, with consistent positioning. The bandage thickness was less than 2 mm and was no thicker than a sock. There was no evidence of x-ray attenuation by the bandage in the scout view or in HR-pQCT images.

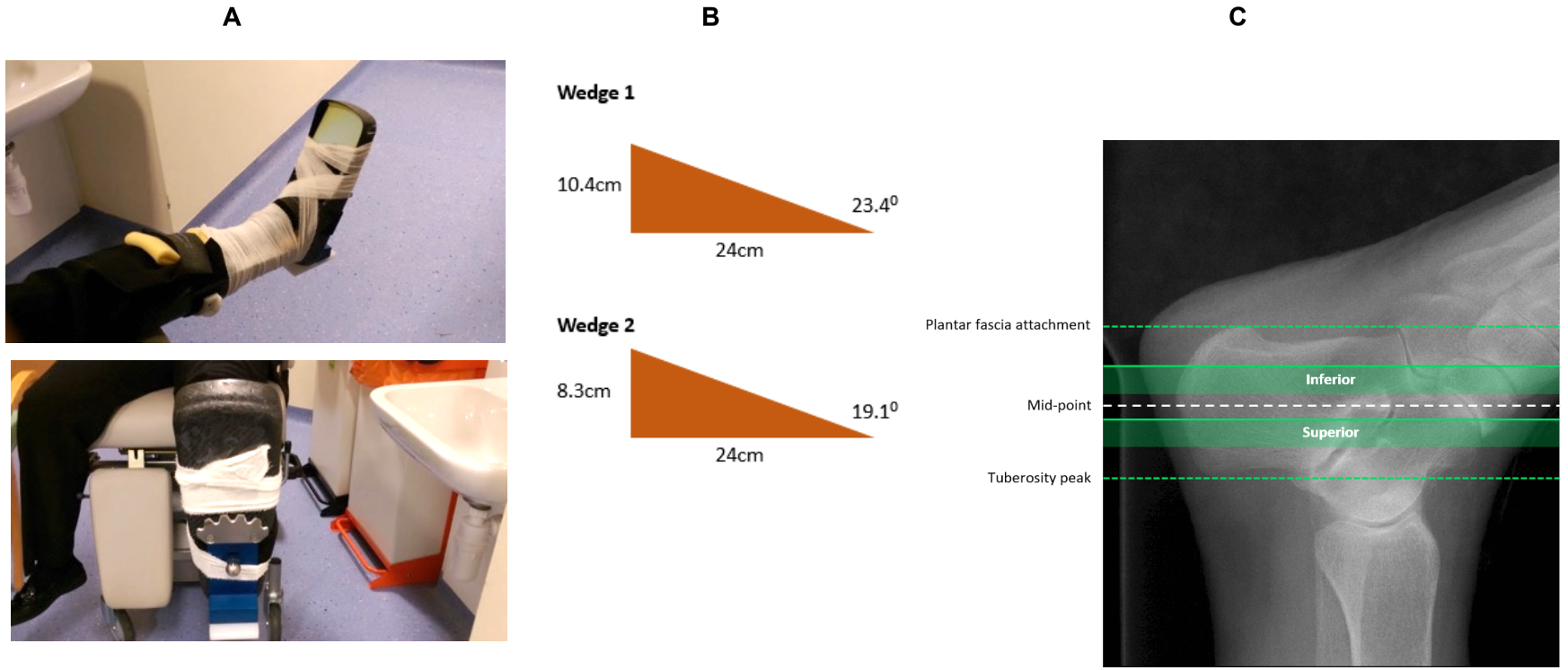

Figure 5.2. Foot positioning procedure prior to calcaneus HR-pQCT image acquisition.

A − Foot positioning setup used for calcaneus HR-pQCT scans.
B − Dimensions of the foam wedges on which the participant's foot rested during image acquisition to assist positioning.
C − Scout view of the foot: The dashed green lines indicate the location of the anatomical landmarks used to identify the mid-point of the calcaneus (white dashed line). The solid green lines at the top of the shaded green box indicate the start point for collection of the superior and inferior region images. The approximate size of the scanned region is indicated by the transparent green box.

5.3.5.2 Image acquisition

Prior to the pilot study starting, custom software and two control files were added to the XtremeCT workstation by SCANCO Medical AG, to assist with identifying the start point of the scanning region. On the scout view, the superior peak of the tuberosity and the plantar fascia attachment to the calcaneal tuberosity was identified using the software by the scan technician. A reference line was then automatically placed at the mid-point between these two landmarks by the software, with a value in millimetres that was recorded by the scan technician. To identify the start point for the superior region of the calcaneus, +4.51 mm (control file 1) was added to the reference line at the mid-point of the bone. Following superior region image acquisition, the scan technician completed the same procedure (scout view, landmark and mid-point identification) and subtracted -13.53 mm (control file 2) to identify the start point for the inferior region image acquisition. The locations of the regions of interest by the control files were similar to those evaluated in cadaveric specimen (Chapters 3 and 4).

HR-pQCT images of the calcaneus were collected using the standard clinical operational settings at the superior and inferior regions (Figure 5.2). The only adjustment was that the images were collected at 100 and 200 ms scan integration time, resulting in a 2.8 minute and 4.2 minute scan duration and an estimated radiation dose per scan of 3 and 6 μSv, respectively.

The order of the integration times was randomised by coin toss, which the scan technician performed prior to positioning the participant's foot in the XtremeCT scanning gantry. This enabled calibration of the XtremeCT with the correct integration time prior to each scan. The participant's lower limb was removed from the XtremeCT following image acquisition at the first integration time and prior to image acquisition at the second integration time: the foot was not repositioned in the lower-limb cast between the two scans. The scan technician recorded the integration time and the measurement numbers on a pre-prepared workbook sheet. The investigator evaluating the calcaneus HR-pQCT images was blinded from this information and was not present during participant positioning and the image collection. The investigator was unblinded after the images had been evaluated.

Immediately after the HR-pQCT image acquisition had finished, the scan technician qualitatively graded the image quality of the central slice of a low-resolution reconstruction from 1 to 4 (Figure 5.3). The image acquisition was repeated if the image grade was 3 or 4. If the best image grade was a 4, the image was excluded

from the study. There was only one repeat image acquisition per integration time, per region.

5.3.5.3 Image reconstruction

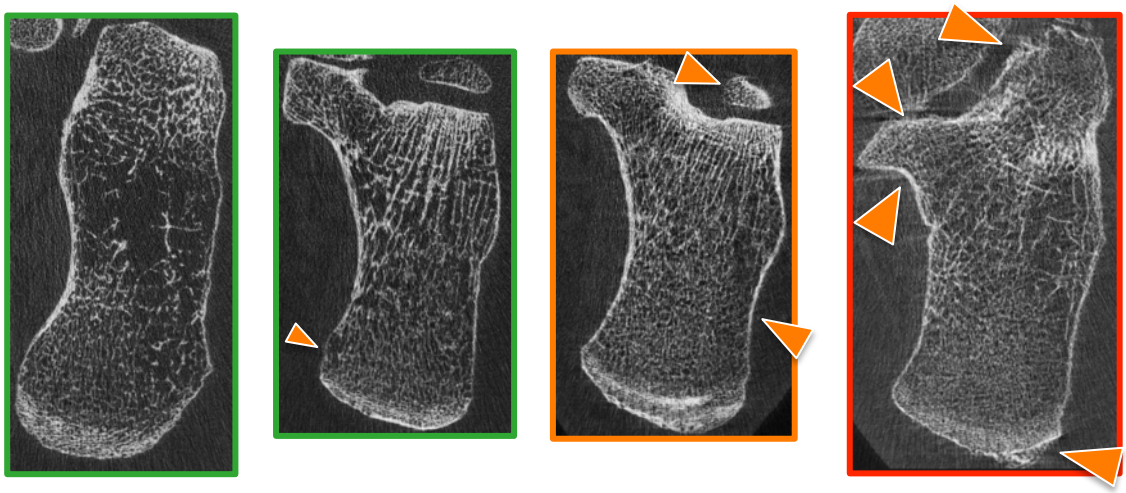

Grade 1 =	Grade 2 =	Grade 3 =	Grade 4 =
'No artefact'	'Slight'	'Pronounced'	'Unacceptable'

Figure 5.3 Examples of the different visual grading given to calcaneus HR-pQCT images.

From grade 2 to 4, there are discontinuities in the calcaneus cortex (orange arrows), which become more severe as the grade increases. The explanation of this grading has been sourced from Engelke et al. [155].

Calcaneus HR-pQCT image reconstruction followed the standard protocol provided by the manufacturer (Section 2.3.2).

5.3.5.4 Image evaluation

The semi-automated contouring of the calcaneus periosteal boundary was performed for all HR-pQCT image slices. The images were evaluated using the standard clinical evaluation script (Section 2.3.3) to segment the calcaneus from the marrow phase. Measurements reported from the evaluation were, total vBMD, trabecular vBMD, outer and inner trabecular vBMD, BV/TV^{d}, Tb.N*, $Tb.Th^{d}$ and $Tb.Sp^{d}$ (* – directly computed; ^{d} – derived).

5.3.6 Image registration

A 3D registration protocol was applied to minimise repositioning error between the 100 ms and 200 ms integration time HR-pQCT images using the SCANCO Medical

IPL registration module (Section 2.6.7.1). The maximised and cropped common volumes were calculated between the images (Figure 2.21). The cropped method was used to determine the common volume of interest for evaluation. The percentage common volume between the 100 ms and 200 ms integration time was compared to a 70% "cut off", as used within our Research Group. Due to the exploratory nature of completing repeat image acquisitions, and the scan technician's relatively little experience with the method, no images were excluded if the common volume of interest was below 70%.

5.3.7 Statistical analysis

Statistical analyses were performed in GraphPad Prism (7.0, GraphPad Software: La Jolla California, USA). A $p<0.05$ indicated statistical significance. HR-pQCT measurements were visually checked for normality, then statistically checked using a Shapiro-Wilk test. Normally distributed measurements were presented as a mean with a 95% confidence interval (95% CI) and non-normally distributed measurements were presented as a median with an interquartile range (IQR). Paired t-tests were used to compare normally distributed measurements and Wilcoxon-Rank tests to compare non-normally distributed measurements.

5.3.7.1 Mid-point reference line precision error

The SD_{RMS} of the mid-point reference line positions [154] was calculated between each superior and inferior region image acquisitions: 20 in total (10 x 100 ms integration time, 10 x 200 ms integration time).

5.3.7.2 Image quality grade comparison

The relative frequency for the image quality grades were presented for 100 and 200 ms integration time HR-pQCT images, at the superior and inferior regions of the calcaneus.

5.3.7.3 100 ms vs. 200 ms integration time HR-pQCT measurements

The percent common volume of interest was reported as a percentage of the number of slices in the common volume in comparison to the total number of slices that were obtained. Following the evaluation of the common volumes, the absolute difference for the HR-pQCT measurements was calculated between the 100 and 200 ms integration time images. Linear regression analyses were performed to evaluate the correlation between the 100 and 200 ms integration time measurements; the r^2, equation slope and intercept, and RMSE were calculated.

Bland-Altman methods were also performed to test for bias (mean and 95% Limits of Agreement (LoA)) between the 100 and 200 ms integration time measurements [218].

5.3.7.4 Superior versus inferior region comparison

The absolute difference for the HR-pQCT measurements was calculated between the superior and inferior regions in the unregistered images. Pearson's or Spearman's correlations were performed to test associations for the HR-pQCT measurements between the superior and inferior regions of the calcaneus.

5.4 Results

5.4.1 Participant characteristics

10 participated in the study, but only 9 completed the study and were included in the analysis. 1 participant was removed from the analysis due to discomfort in the hip joint when their limb was positioned in the XtremeCT scanning gantry. The participant had unacceptable image quality for a scan at the superior region of the calcaneus and a repeat could not be performed. Therefore, the results that are presented are from 9 participants (5 female and 4 male). The mean (±SD) age of participants was 62 (±5) years and the mean (±SD) BMI was 26.2 (±4.4) kg/m^2.

5.4.2 Mid-point reference line precision error

The mid-point reference line SD_{RMS} between the 18 separate acquisitions of the superior and inferior regions was 0.69 mm.

5.4.3 Image quality grades

Figure 5.4 shows the image quality grades from the calcaneus HR-pQCT images. Acceptable image quality grades were obtained at both integrations times and at both regions of the calcaneus. At 100 ms integration time, no HR-pQCT image acquisitions were repeated; at the superior region, 5 images had a 'no artefact' grade and 4 images had 'slight' artefacts. At 200 ms integration time, 4 HR-pQCT image acquisitions at the superior region were repeated due to 'unacceptable' image quality grades: these were all noted to be movement artefacts, rather than artefacts due to equipment errors. All repeat acquisitions at this integration time resulted in images with acceptable quality: 3 HR-pQCT images had a 'no artefact' grade and 6 HR-pQCT images had a 'pronounced' artefact grade. HR-pQCT images acquired at the inferior region of the calcaneus, at both 100 and 200 ms integration

times had an equal number of ‘no artefact’ and ‘slight’ artefact grades, 7 and 2, respectively.

Figure 5.4. Image quality grading for the HR-pQCT images at different regions and at different integration times.

Data shown for 9 participants.
Abbreviations: Sup – Superior; Inf – Inferior.

5.4.4 Common volume of interest

The median (IQR) for the image registration CPU time was 6 minutes (4, 11 minutes) for the superior region and 6 minutes (5, 8 minutes) for the inferior region.

For the maximised method, the median common volume between the 100 ms and 200 ms integration time HR-pQCT images was 100% at the superior region (range 92-100%) and 100% at the inferior region (95-100%) of the calcaneus. Figure 5.5 shows the common volume of interest for the cropped method between the 100 and 200 ms integration time HR-pQCT images – this method was used for the comparison of the images. The median (IQR) for the common volume was 84% (79, 96%) at the superior region and 88% (71, 94%) at the inferior region; there were no statistical differences in the common volumes between the regions (p=0.81).

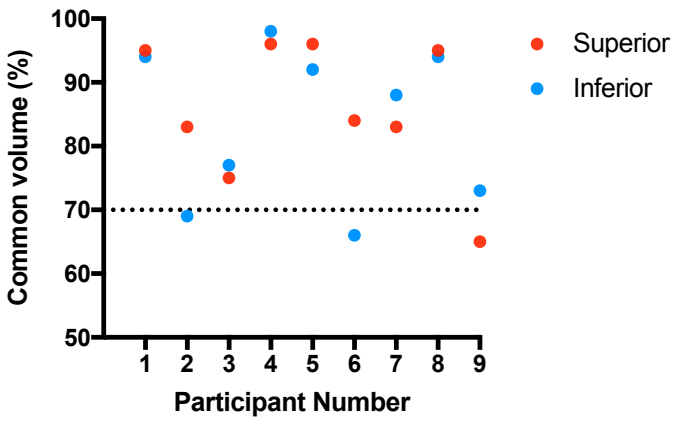

Figure 5.5. Common volume between the 100 ms and 200 ms integration time images using the cropped method.

A 'cut off' for the common volume of interest was set at 70%, as recommended by the manufacturer and used within our Research Group.

5.4.5 Integration time comparison

Figure 5.6 and Figure 5.7 shows superior and inferior images, respectively, obtained at a 100 and 200 ms integration times, with pixels coloured for each integration time image and the common volume between the images. Table 5.1 shows the results from the integration time comparisons for the HR-pQCT measurements from superior and inferior region images.

There were no differences in total vBMD, trabecular vBMD, outer trabecular vBMD and inner trabecular vBMD, and BV/TV^{d} between the 100 ms and 200 ms integration time HR-pQCT images at both the superior and inferior region. Tb.N* was significantly lower at a 200 ms integration time compared to 100 ms integration time with mean (95% CI) differences at the superior (-0.5 (-0.6, -0.5), p<0.001) and inferior regions (-0.8 (-0.9, -0.7), p<0.001) respectively. A reduction in Tb.N* was found in all participants. There was significantly higher Tb.Th^{d} (superior, p<0.001; inferior, p=0.004) and Tb.Sp^{d} (superior, p<0.001; inferior, p=0.004) in the 200 ms compared to the 100 ms integration time scans at the superior and inferior regions.

Superior region

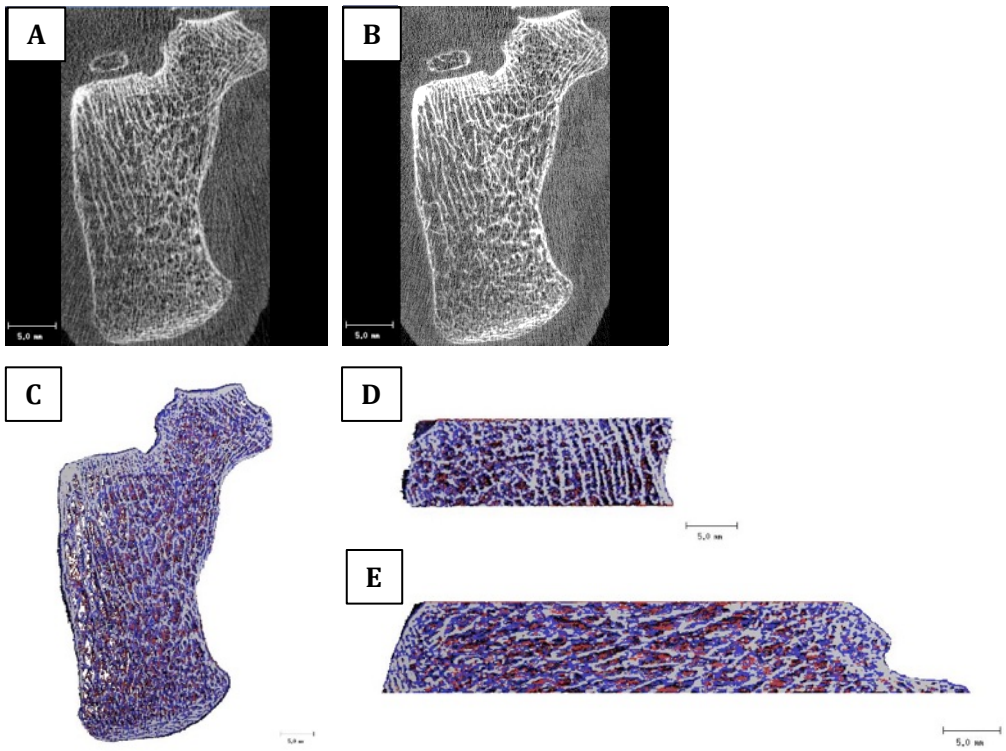

Figure 5.6. Calcaneus HR-pQCT images at the superior region performed at 100 ms and 200 ms integration times.

2D slices of the calcaneus at 100 ms (A) and 200 ms (B) integration times. 3D segmented images at the axial (C), anterior-posterior (D) and medial-lateral view (E). White pixels represent the common volume between the 100 ms and 200 ms images. The red and blue pixels represent the 100 ms and 200 ms integration time 3D segmented images, respectively.

Inferior region

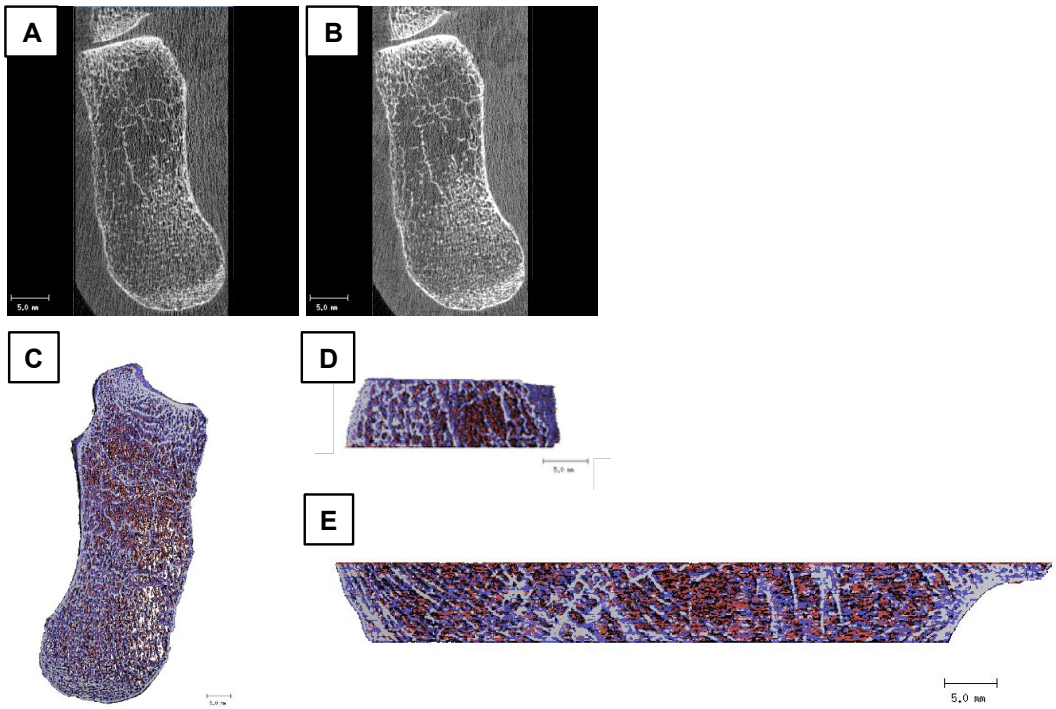

Figure 5.7. Calcaneus HR-pQCT images at the inferior region performed at 100 ms and 200 ms integration times.

2D slices of the calcaneus at 100 ms (A) and 200 ms (B) integration times. 3D segmented images at the axial (C), anterior-posterior (D) and medial-lateral view (E).
White pixels represent the common volume between the 100 ms and 200 ms images. The red and blue pixels represent the 100 ms and 200 ms integration time 3D segmented images, respectively.

Table 5.1. Comparison of measurements obtained from the common volume between calcaneus HR-pQCT images acquired at 100 ms and 200 ms scan integration times.

Superior region	100 ms	200 ms	Δ	p value
Total vBMD, mg HA.cm^{-3}	298 (260, 335)	297 (260, 334)	-1 (-7, 5)	0.727
Tb.vBMD, mg HA.cm^{-3}	240 (210, 271)	241 (208, 274)	1 (-4, 5)	0.681
Outer Tb.vBMD, mg HA.cm^{-3}	271 (251, 312)	271 (252, 315)	39, -6$^{\#}$	0.055
Inner Tb.vBMD, mg HA.cm^{-3}	213 (168, 240)	208 (169, 246)	22, -23$^{\#}$	>0.99
BV/TV^{d}, %	20 (17.5, 22.6)	20.1 (17.4, 22.8)	0.1 (-0.3, 0.4)	0.729
Tb.N*, mm^{-1}	3.2 (2.8, 3.6)	2.7 (2.3, 3)	-0.5 (-0.6, -0.5)	<0.001
Tb.Th^{d}, µm	60 (56, 71)	77 (67, 87)	14 (10, 18)	<0.001
Tb.Sp^{d}, µm	250 (210, 290)	313 (258, 369)	0, 45$^{\#}$	0.004
Inferior region	100 ms	200 ms	Δ	p value
Total vBMD, mg HA.cm^{-3}	183 (140, 225)	182 (142, 222)	-1 (-5, 4)	0.825
Tb.vBMD, mg HA.cm^{-3}	141 (110, 171)	142 (111, 172)	1 (-2, 4)	0.526
Outer Tb.vBMD, mg HA.cm^{-3}	204 (169, 234)	205 (168, 236)	1 (-1, 4)	0.210
Inner Tb.vBMD, mg HA.cm^{-3}	98 (67, 125)	104 (64, 124)	1 (-4, 5)	0.786
BV/TV^{d}, %	11.7 (9.2, 14.3)	11.8 (9.3, 14.3)	0.1 (-0.1, 0.3)	0.621
Tb.N*, mm^{-1}	3.1 (2.6, 3.6)	2.3 (1.7, 2.9)	-0.8 (-0.9, -0.7)	<0.001
Tb.Th^{d}, µm	38 (32, 43)	52 (46, 59)	15 (10, 19)	<0.001
Tb.Sp^{d}, µm	297 (243, 351)	426 (308, 543)	0, 45$^{\#}$	0.004

Data shown for 9 participants.
Δ (difference) = 200 ms minus 100 ms
Mean (95% CI) difference for total vBMD, Tb.vBMD, Outer and Inner Tb.vBMD (inferior region only), BV/TV, Tb.N* and Tb.Th^{d}.
$^{\#}$ non-normally distributed: median (IQR) and the number of positive (higher 100 ms) and negative (higher 200 ms) signed ranks for Outer and Inner Tb.vBMD (superior region only), Tb.Sp^{d}.

Figure 5.8 and Figure 5.9 shows the correlation and linear regression analyses between the 100 ms and 200 ms integration time HR-pQCT images. Total vBMD, trabecular vBMD, outer and inner Tb.vBMD was strongly correlated between the 100 ms and the 200 ms integration time HR-pQCT images ($r^2 \geq 0.97$), and the RMSE appeared to be proportional to the absolute values within the regions (i.e. superior higher than inferior). BV/TV^{d} was also strongly correlated ($r^2 = 0.95$) and had a small RMSE (0.4-0.5%) for both regions. Tb.N* and Tb.Sp^{d} were also strongly correlated between the 100 ms and 200 ms integration time HR-pQCT images ($r^2 \geq 0.98$). The Tb.N* and Tb.Sp^{d} RMSE was also higher for the inferior region compared to the superior region. Tb.Th^{d} in the superior region of the calcaneus was strongly

correlated between the 100 ms and 200 ms integration time HR-pQCT images, but was weakly correlated in the inferior region. The Tb.Th^{d} was similar between both regions.

Passing-Bablok regression was also performed between the 100 ms and 200 ms integration time scans, and the results were similar to those reported using linear regression, which is presented in the Appendix (Table 9.6).

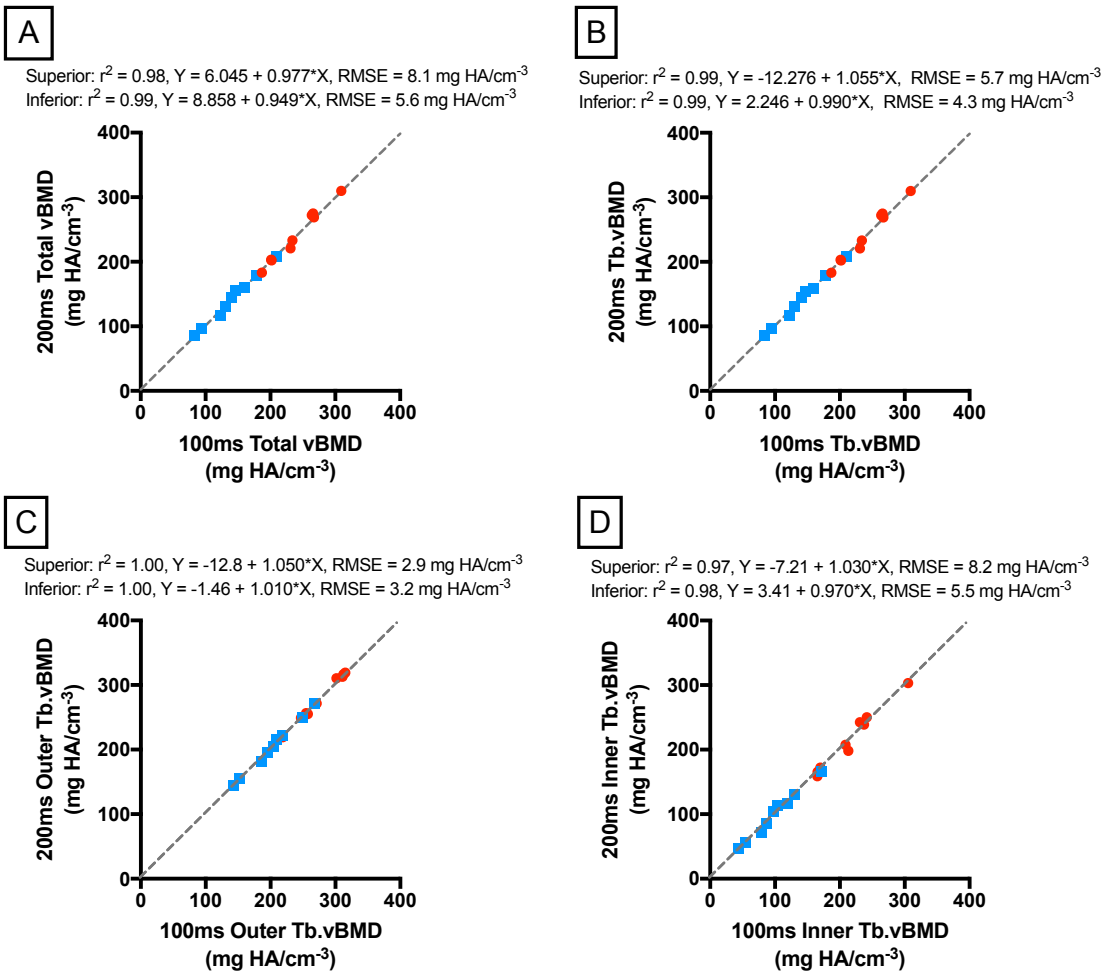

Figure 5.8. Correlations between volumetric bone mineral density measurements between the 100 ms and 200 ms integration time calcaneus HR-pQCT images.

A – Total vBMD; B – Tb.vBMD; C – Outer Tb.vBMD; D – Inner Tb.vBMD.
r^2, coefficient of determination; RMSE, root mean square error.
Red – Superior region; Blue – Inferior region. Dotted grey line indicates the line of unity.

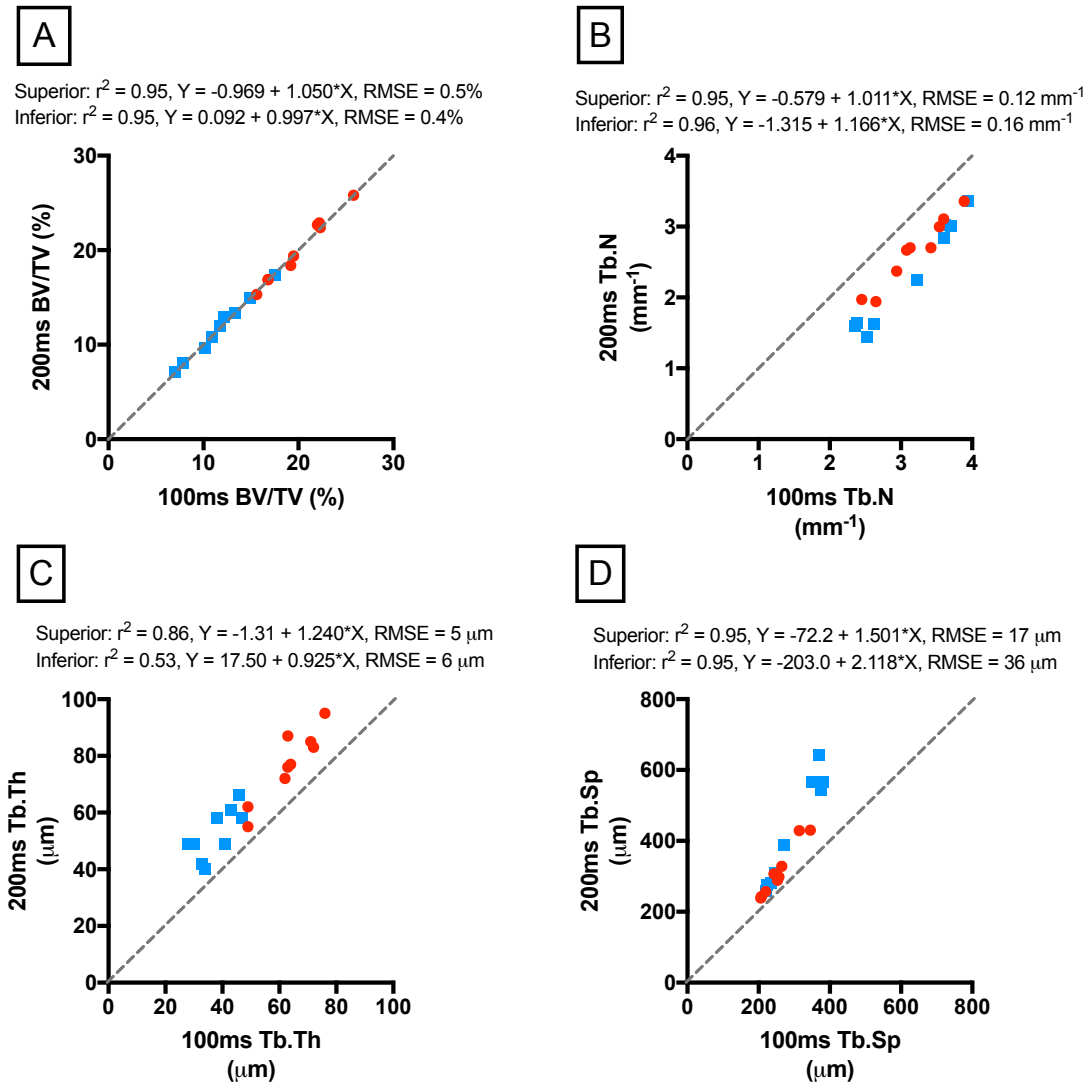

Figure 5.9. Correlations between bone volume fraction and trabecular microstructure measurements between the 100 ms and 200 ms integration time calcaneus HR-pQCT images.

A – BV/TV^{d}; B – Tb.N*; C – Tb.Th^{d}; D – Tb.Sp^{d}.
r^2, coefficient of determination; RMSE, root mean square error.
Red – Superior region; Blue – Inferior region. Dotted grey line indicates the line of unity.

Figure 5.10 shows Bland-Altman plots for the HR-pQCT measurements between the 100 ms and 200 ms integration time HR-pQCT images. No bias was present for total vBMD, trabecular vBMD, outer and inner trabecular vBMD, and BV/TV. Tb.N* had a fixed bias at the superior and inferior region, which appeared higher for the inferior region images (superior = 0.5 mm (95% LoA 0.3, 0.8 mm); inferior = 0.8 mm (95% LoA 0.4, 1.2 mm)). Tb.Th^{d} had a fixed bias at the superior and inferior regions, and there was little difference between the superior (-14 μm (95% LoA -24, -4 μm)) and inferior region (-15 μm (95% LoA -27, -3 μm)). Tb.Sp had a systematic bias; as the average Tb.Sp^{d} increased the difference in Tb.Sp^{d} increased. The 95% LoA for

Tb.Sp[d] were wider for the inferior region (-130 µm (95% LoA -300 µm, 40 µm)) compared to the superior region (-60 µm (95% LoA -110, 0 µm)).

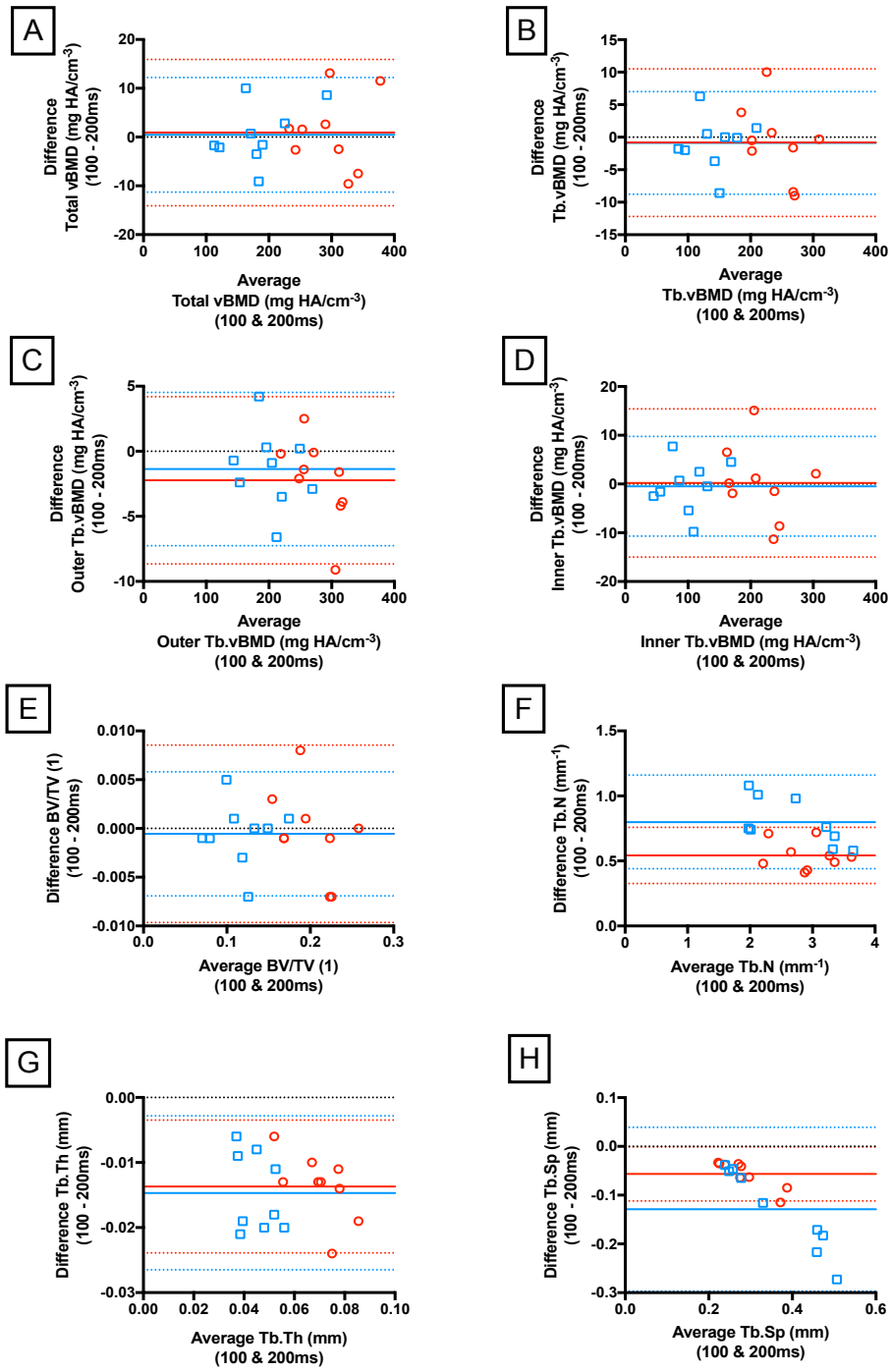

Figure 5.10. Bland-Altman plots between the 100 ms and 200 ms integration time HR-pQCT images.

A – Total vBMD; B – Tb.vBMD; C – Outer Tb.vBMD; D – Inner Tb.vBMD; E – BV/TV[d]; F – Tb.N*; G – Tb.Th[d]; H – Tb.Sp[d].
Superior region – Red; Inferior region – Blue; Mean bias – Solid line; 95% limits of agreement – dotted line.

5.4.6 Region comparison

Table 5.2 shows the results from the superior and inferior region comparison. The superior region of the calcaneus had significantly greater total and trabecular vBMD, greater outer and inner trabecular vBMD, greater BV/TV^{d}, and a greater Tb.N* and Tb.Th^{d}, in comparison to the inferior region. Tb.Sp^{d} was significantly lower in the superior region of the calcaneus compared to the inferior region.

Figure 5.11A-H shows the associations between the HR-pQCT measurements made at the superior and inferior regions of the calcaneus. All measurements had strong, positive correlations between the two regions.

Table 5.2. Comparison between HR-pQCT measurements from unregistered superior and inferior regions of the calcaneus collected at 200 ms scan integration time.

	Region		Absolute difference	
	Superior	Inferior	Δ	p value
Total vBMD, mg HA.cm^{-3}	293 (259, 328)	182 (143, 222)	-111 (-130, -92)	<0.001
Tb.vBMD, mg HA.cm^{-3}	239 (209, 269)	142 (113, 172)	-96 (-117, -76)	<0.001
Outer Tb.vBMD, mg HA.cm^{-3}	277 (251, 303)	205 (175, 236)	-72 (-94, -50)	<0.001
Inner Tb.vBMD, mg HA.cm^{-3}	213 (179, 247)	100 (71, 129)	-113 (-135, -90)	<0.001
BV/TV^{d}, %	19.9 (17.4, 22.4)	11.9 (9.4, 14.3)	-8 (-10, -6)	<0.001
Tb.N*, mm^{-1}	2.6 (2.3, 3)	2.3 (1.7, 2.9)	-0.3 (-0.6, 0)	0.034
Tb.Th^{d}, µm	77 (67, 86)	53 (46, 60)	-24 (-30, -18)	<0.001
Tb.Sp^{d}, µm	301 (251, 377)	425 (308, 541)	0, 45$^{\#}$	0.004

Data shown for 9 participants.
Δ (difference) = inferior minus superior.
Mean (95% CI) difference for total vBMD, Tb.vBMD, Outer Tb.vBMD, Inner Tb.vBMD, BV/TV^{d}, Tb.N* and Tb.Th^{d}.
$^{\#}$ non-normally distributed; median (IQR) and the number of positive (higher inferior) and negative (higher superior) signed ranks for Tb.Sp^{d}.

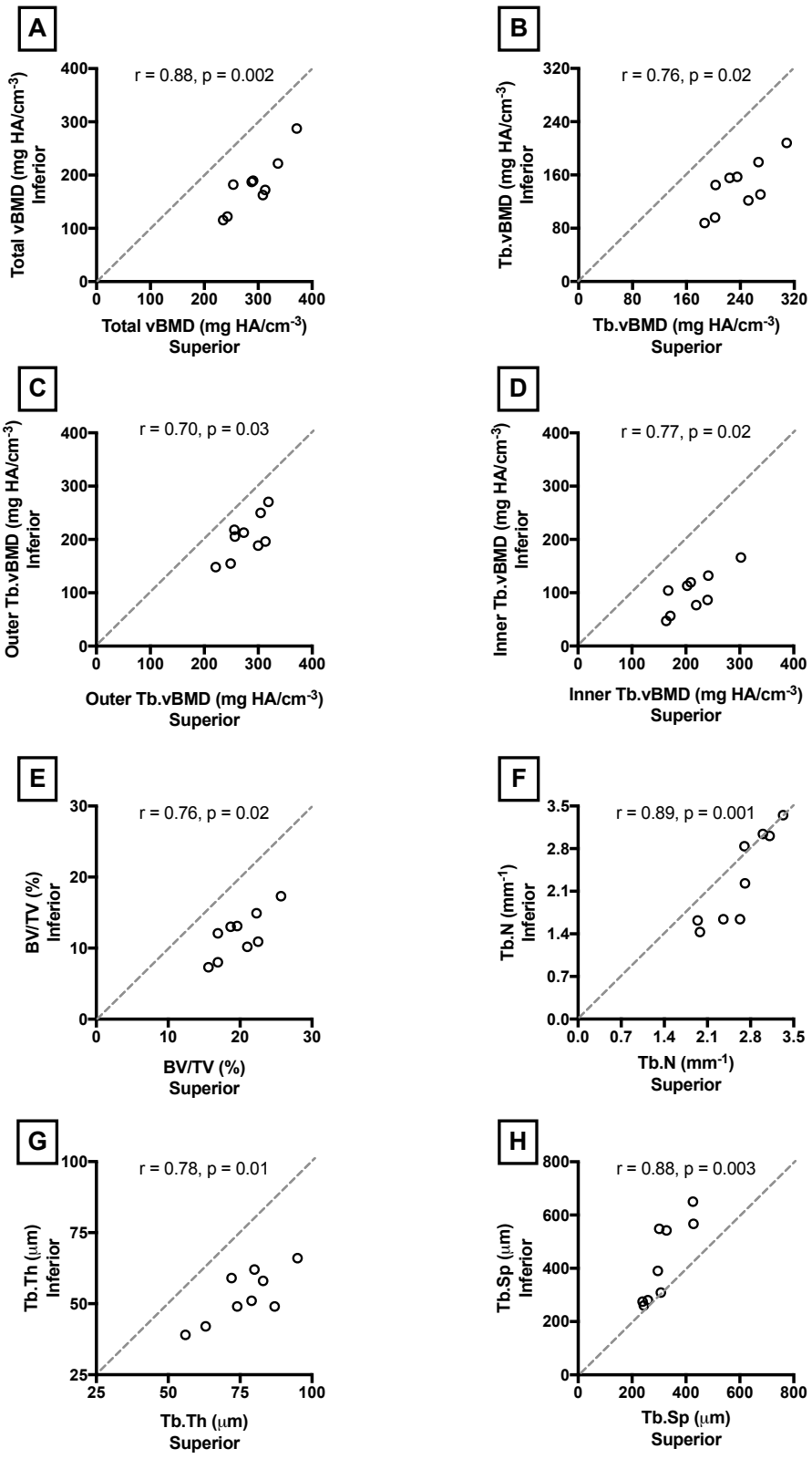

Figure 5.11. Correlations between volumetric bone mineral density and trabecular microstructure measurements between the superior and inferior regions of the calcaneus.

Pearson's correlation coefficient: A – Total vBMD; B – Tb.vBMD; C – Outer Tb.vBMD; D – Inner Tb.vBMD; E – BV/TV[d]; F – Tb.N*; G – Tb.Th[d].
Spearman's correlation coefficient: H – Tb.Sp[d].
Dotted grey line indicates the line of unity.

5.5 Discussion

This Chapter described the adaptation of HR-pQCT for the measurement of bone density and trabecular microstructure in the human calcaneus *in vivo*. The change in trabecular number using a 200 ms scan integration time consolidates findings obtained from human cadaveric calcanei (Chapter 4), and therefore appears to be an important adaptation to the standard clinical protocol if quantifying calcaneus trabecular microstructure is of interest. The scanning procedure and image acquisition was well tolerated by most participants and consequently image quality grades were consistent with previous studies undertaken at the distal radius and distal tibia [94, 95, 151, 155]

Increasing the exposure time of the HR-pQCT tomographic projections (integration time) led to significant changes in the recorded trabecular microstructure *in vivo*. With an increasing integration time, there was a decrease in Tb.N*. The magnitude of change in Tb.N* caused by this technical adaptation exceeded changes reported with biological variability. In context with studies completed in our Research Group that have used HR-pQCT, the mean difference exceeded that found between the different stages of skeletal development in males and females (16-18 years, 30-32 years and >70 years) by approximately 2-3 fold [151], and was equivalent to the magnitude of increase found in adults with an obese BMI compared to normal BMI [21]. Furthermore, the mean difference in Tb.N* exceeded (i) the loss reported at the distal radius with a 3 year follow-up in postmenopausal women [191], (ii) the loss observed at the distal tibia with 60 days of bed-rest [189], and (iii) was comparable to the difference in radius Tb.N* between females below 20 years of age and females in their 80's in a normative data collection [234]. The difference in Tb.N* by adapting the integration time for HR-pQCT image acquisition of the calcaneus can therefore be considered a technical adaptation that could produce 'clinically significant' changes.

There was strong correlations for Tb.N* and $Tb.Sp^{d}$ between 100 ms and 200ms HR-pQCT scans. There was also a strong correlation for $Tb.Th^{d}$ at the superior region, but weak at the inferior region. From this pilot sample, regression equations could be applied to remove differences between measurements of Tb.N* and $Tb.Sp^{d}$. Measurement bias appeared to exist between the 100 ms and 200 ms HR-pQCT images in the inferior region (systematic decrease in Tb.N*, systematic increase in $Tb.Sp^{d}$), where there was also a wider 95% LoA compared to the

superior region. This poorer agreement could be explained by greater noise in the inferior region images, as highlighted in Chapter 4, considering that there appeared to be less movement artefacts than the superior region images, particularly for the 200 ms integration time scans. The inferior region images also had greater regression errors for Tb.N* and Tb.Sp^{d}. Therefore, it may only be appropriate to adjust the trabecular microstructure measurements for the 100 ms integration time images from the superior region of the calcaneus.

The higher number of images graded with a 'pronounced' artefact from the superior region at 200 ms integration time did not affect the overall outcome for studying Tb.N*. The percentage reduction in Tb.N* at a 200 ms integration time (-17% superior, -26% inferior) exceeded, or was equivalent to, the percentage increase reported between images with 'no artefact' and 'pronounced' artefact [94, 95]. It is possible that the higher image artefact grade may have contributed to the different absolute difference between the superior (-0.5 mm^{-1}) and inferior regions (-0.8 mm^{-1}), and would be within the range of measurement differences reported by including images with and without 'pronounced' artefact [94, 155]. The larger change in Tb.N* at the inferior region could also be anticipated due to the anatomy of the calcaneus. Here, the inferior region encompassed the neutral area (Ward's triangle) of the calcaneus in most participants. There seemed to be a higher number of 'bone' voxels in this region at 100 ms integration time (Figure 5.7), which would be detected as trabeculae using the Tb.N* computational algorithm. The removal of these voxels (i.e. noise) with the 200 ms integration time (Figure 5.7) would increase the marrow space and subsequently lower the Tb.N*. This may also contribute to the systematic bias reported with increasing Tb.N* at the inferior of the calcaneus.

The heterogeneity in calcaneus trabecular BMD and microstructure between the superior and inferior regions was consistent with the regional variation reported in previous studies [197, 198]. For example, areas of low density (neutral area) have been identified by a lower inner trabecular vBMD at the inferior region by viewing the HR-pQCT images and measurements. The superior region of the calcaneus is exposed to high mechanical strains, which was reflected by the high total and trabecular vBMD; specifically, the outer trabecular vBMD would detect these regions at the sub-talar articular surfaces and at the Achilles tendon attachment. The variability in total vBMD between the superior and inferior region of the calcaneus was similar to the total vBMD difference reported between distal and proximal sites of the radius and tibia [87, 155, 203]. More proximal sites of the radius and tibia have a thicker cortex [87, 155, 203], which can facilitate the segmentation of the

endocortical boundary and therefore the separation of the cortical and trabecular bone phases for assessment of cortical thickness and porosity [155, 210]. However, it remains to be seen whether assessing different sites and/or envelopes of the same bone using HR-pQCT translates into a clinical impact. Whilst distinct differences between the superior and inferior region of the calcaneus were found, there were also strong, positive associations in measurements between the regions. It would be of interest to investigate the associations of the measurements change with osteoporosis, or pharmaceutical and lifestyle interventions.

Several practical considerations have been identified in obtained calcaneus HR-pQCT images *in vivo*:

The positioning of the foot presented challenges to the scan technician. Some participants with larger feet were unable to fit the surrounding bones of the foot in the scanner field of view when HR-pQCT images were obtained at the inferior region of the calcaneus. This was apparent in 4 participants, all male, and was not an issue in any participant when imaging the superior region of the calcaneus. Being unable to contain the surrounding tissues within the field of view may have produced greater noise in the inferior region images, which would have affected the estimation of Tb.N*, as well as $Tb.Th^{d}$ and $Tb.Sp^{d}$ [172]. However, this may be less of an issue when using the second generation XtremeCT, as the diameter of the field of view is 14 mm larger than the first generation XtremeCT device.

Using the lower limb cast for tibia image acquisitions also restricted positioning of the foot. The scan technician noted that the cast was too narrow at the location of the cast where the shank was positioned. This may have affected those with a larger foot size more. Customised positioning aids have been developed for HR-pQCT imaging at the radius and tibia, and also for scans of fractured radii [212], the knee [93] and the metacarpals [90]. Customising positioning aids for the calcaneus HR-pQCT scans may be an important development to pursue

A customised positioning cast might minimise image artefact caused by movement. Participants indicated that they could move their toes once in position for the calcaneus HR-pQCT image acquisition, in which additional foam wedges were then applied to restrict the movement. Movement of the fingers was also an issue highlighted with metacarpal HR-pQCT imaging, which has a 7-8 minute image acquisition duration. Barnabe and colleagues [90] subsequently proposed the use of a ridged splint combined with an inflatable positioning device to restrict this. A similar inflation device has also been used in studies monitoring fracture healing at

the distal radius, in which image acquisition lasted 5.6 minutes [212, 235]. When considering limitations in the agreement for inter-operator grading of HR-pQCT images [94, 155], minimising toe and foot movement to optimise calcaneus HR-pQCT image quality would be critical to the wider translation of the protocol. However, apparatus to minimise movement of the foot is currently unavailable for the calcaneus HR-pQCT scans.

The practical issue of positioning the foot was highlighted by the precision error (SD_{RMS}) for identifying the calcaneus mid-point (= 0.69 mm, equivalent to 8 to 9 slices at an 82 μm voxel size). Whilst this positional error could be removed by image registration in monitoring studies, it could cause errors when comparing different populations in cross-sectional studies. The equivalent measurements at the tibia and radius have been reported to be 0.2 mm (2-3 slices) and 0.38 mm (5-6 slices), respectively, using an 82 μm voxel size [154]. However, Bonaretti and colleagues [154] completed these measurements by analysing the same image twice (radii = 45, tibia = 46) in custom-built software, where as the current work obtained the mid-point positional error from 2 separate scout view acquisitions, either side of a 2.8-4.2 minute HR-pQCT scan. Therefore, the calcaneus mid-point positional error measured in this work could be overestimated if the participants moved between the 2 scout view image acquisitions.

There are also two technical adaptations that may explanation the greater mid-point positional error with the calcaneus scans. (1) The start and end position scaling was maximised for the calcaneus HR-pQCT scout view. This ensured that the scan technician could identify both anatomical landmarks and simultaneously check foot positioning. At the radius and tibia, the scout view scaling is smaller (i.e. more ‘zoomed in’), therefore providing greater anatomical detail for reference line positioning. (2) There could also be difficulties in selecting the two anatomical landmarks on the calcaneus, in order to identify the mid-point of the bone. Difficulties have also been reported for single landmark identification for the radius HR-pQCT scans [151, 154, 176]. The landmark identification may, however, enable a form of anatomical standardisation for relative positioning of the region of interest. This has been recommended at the distal radius and distal tibia to allow more relevant comparisons between populations of different sizes (e.g. across sexes and ethnicity) and for normative database development [230, 236, 237]. Relative positioning of the calcaneus HR-pQCT scanning region of interest would depend on obtaining an absolute value between the two anatomical landmarks, which is currently not available in the XtremeCT software.

Finally, the potential limitations from the scout view scaling and the landmark identification may explain some of the variability in the common volume between participants for the 100 ms and 200 ms HR-pQCT image acquisitions. In relation to the 'cut off' proposed to excluded repositioned HR-pQCT images (< 70%), 1 participant and 2 participants would have been removed from the analysis of the superior and inferior region of the calcaneus, respectively, without repositioning. Nevertheless, the median maximised common volume without repositioning of the foot was still higher than the 90-94% reported for repositioning at the radius and tibia [177, 188]. Some variability could have been expected due to the infancy of performing the protocol *in vivo*. Chapter 6 provides a more detailed insight into foot positioning and measurement precision error.

5.6 Conclusion

The Chapter reports work to determine a method to quantify calcaneus vBMD and trabecular microstructure *in vivo* using the first generation XtremeCT. HR-pQCT images have acceptable image quality grades at 100 ms and 200 ms integration times, in which a 200 ms integration time appears preferable for the quantification of trabecular microstructure, supporting findings from *ex vivo* experiments (Chapter 4).

CHAPTER 6 DETERMINING CALCANEUS HR-PQCT MEASUREMENT PRECISION

6.1 Introduction

Chapter 5 piloted the calcaneus HR-pQCT imaging method *in vivo*. Images of an acceptable quality were collected, although there were more movement artefacts at 200 ms compared to 100 ms integration time, and an image registration procedure was applied to correct for repositioning errors (i.e. foot position and anatomical landmark identification). Controlling for these factors has been shown to be important for minimising HR-pQCT measurement precision error. Quantifying the superior region of the calcaneus was recommended using the first generation XtremeCT, as it provides more accurate measurements (Chapter 4) and has fewer practical issues compared to the inferior region of the bone (Chapter 5). Chapter 6 will present the short-term HR-pQCT measurement precision error for the superior region of the calcaneus *in vivo*. It will also present a site comparison analysis using HR-pQCT between the non-dominant and dominant calcaneus, and the calcaneus, distal radius and distal tibia.

6.1.1 Precision error

Precision is the "ability to reproduce the same numerical result in the setting of no real biologic change when the test is repeatedly performed in an identical fashion" [150]. However, no quantitative measurement is perfect in these conditions, where device variability and human error are key factors in precision error. Glüer and colleagues [238] presented an extensive overview of calculating precision errors in bone densitometry. Here, precision errors from individual subjects are pooled based on root-mean square averages. These can be collected as short-term precision errors (SD of repeat measurements) or long-term precision errors (SEE of changes over time), and can be presented in absolute or relative values. An insufficient degrees of freedom in the calculations could underestimate the precision errors by as much at 41% [238]; at least 27 degrees of freedom was recommended to achieve an upper 90% confidence limit of +30% of the mean precision error. A more recent ISCD position paper recommended using 30 degrees of freedom to achieve an upper 95% confidence limit of the precision error that is no more than 34% greater than the calculated value [239]. Falsely identifying or missing a BMD or microstructural change may lead to incorrect decisions that could affect patient care.

Studies have calculated HR-pQCT measurement precision errors (Table 6.1). Those that have reported precision errors (as root mean square coefficient of variations, $CV\%_{RMS}$) with sufficient degrees of freedom [79, 151, 155, 177, 195, 240, 241], total

and trabecular vBMD ranged from 0.5-2.1% at the distal radius and 0.2-1.9% at the distal tibia, and trabecular microstructure ranged from 1.0-7.0% at the distal radius and 1.5-7.0% at the distal tibia. As previously highlighted in Chapter 5, participant and reference line positioning [154, 176, 177], and movement artefact [94, 95] contribute to these precision errors. Other contributing factors could be between-subject differences, for instance comparing an adult with a normal T-score and an adult with an osteoporotic T-score. The lower bone mass and microstructure deterioration in the osteoporotic subject may increase the relative precision error [151, 155, 240]. The estimation of short-term precision error could also be dependent on whether measurements were made on the same-day or between different days [74, 242]. Between-day scanning may include device fluctuations and remove enhanced recall by the operator and participant in terms of positioning [74]. Image registration may remove the positioning bias, which may explain why there seems to be minimal influence of timing on HR-pQCT precision errors (Table 6.1).

6.1.2 Least Significant Change

The least significant change (LSC) provides a statistical indication to whether the magnitude of change in a measurement represents a real biologic change [150, 243]. Changes that exceed a 95% LSC (2.77 times higher than the precision error) are considered biologically/clinically significant i.e. providing 95% confidence that a true biological change has occurred [243]. If applying the 95% LSC to the $CV\%_{RMS}$ precision error reported in previous studies (Table 6.1), a clinically significant change in total and trabecular vBMD would range from 1.4-5.8% at the distal radius and 0.6-5.3% at the distal tibia, and trabecular microstructure would range from 2.8-19.4% at the distal radius and 4.2-19.4% at the distal tibia. Examples of scenarios where the 95% LSC can be applied include: *disease monitoring,* where 3-year changes in distal radius cortical porosity, cortical area and trabecular area, and distal tibia cortical vBMD, cortical porosity and trabecular area exceeded the LSC in males and females over the age of 50 years [9]; *treatment responses*, where studies have reported statistically significant mean changes that were within the LSC's, such as cortical porosity with teriparatide [84, 244, 245], and total and trabecular vBMD with anti-resorptive treatments [84, 86, 245].

Table 6.1. HR-pQCT measurement precision error reported in the literature. Continued on the next page.

Author	Participants Gender and age	Scans and degrees of freedom (= df)	Short-term precision results		
			Method	Distal radius	Distal tibia
Boutroy [195]	F=15; 21-47 yrs.	3 scans*: Baseline, 1 week, 1 month. Radius and Tibia = 30.	$CV\%_{RMS}$	vBMD = 0.7-0.9%. Microstructure = 1.0-3.2%.	vBMD = 1.3-1.5%. Microstructure = 1.5-4.4%.
Kazakia [100]	F=52; 25-73 yrs.	3 scans ^{NR}: times not specified. Radius = 16; Tibia = 14.	CV%	BV/TV = 1.2%. Microstructure = 5.3-5.8%.	BV/TV = 0.3%. Microstructure = 1.4-1.5%.
MacNeil & Boyd [176]	F=15; 20-40 yrs. M=15; 20-37 yrs.	2 scans**: Baseline, 1 week. Radius & Tibia: Male = 14, Female = 15.	$CV\%_{RMS}$	F: vBMD = 0.4-0.5%. Microstructure = 3.0-3.2%.	F: vBMD = 0.7-0.8%. Microstructure = 3.3-3.5%.
				M: vBMD = 0.5-0.6%. Microstructure = 3.3-3.9%.	M: vBMD = 0.3-0.5%. Microstructure = 3.3-3.4%.
Engelke [155]	F=42; 63.7±8.0 yrs.	2 scans ^{NR}: same-day. Radius = 42; Tibia = 41.	$CV\%_{RMS}$	vBMD = 1.3%. Microstructure = 5.9-6.3%.	vBMD = 0.6-0.8%. Microstructure = 5.0-5.2%.
Kawalilak [240]	F&M=30; 19-48 yrs. F=34; 62-88 yrs.	2 scans*: within 24 hours. 19-48 yrs: Radius = 29; Tibia = 30. 62-88 yrs: Radius = 27; Tibia = 32.	$CV\%_{RMS}$	19-48 yrs: vBMD = 0.8-1.6%. Microstructure = 5.7-5.9%.	19-48 yrs: vBMD = 0.6-1.4%. Microstructure = 3.8-4.0%.
				62-88 yrs: vBMD = 1.2-2.1%. Microstructure = 5.4-6.1%.	62-88 yrs: vBMD = 0.9-1.9%. Microstructure = 6.2-6.8%.

Table 6.1 continued. HR-pQCT measurement precision error reported in the literature.

Author	Participants Gender and age	Scans and degrees of freedom (= df)	Short-term precision results		
			Method	Distal radius	Distal tibia
Ellouz [177]	F=15; 21-47 yrs.	3 scans**: Baseline, 1 week, 1 month. Radius and Tibia = 30.	$CV\%_{RMS}$	vBMD = 0.5-1.0%. Microstructure = 3.0-3.4%.	vBMD = 1.0-1.8%. Microstructure = 4.3-4.8%.
Paggiosi [151]	F=30 & M=30 per age group (16-18, 30-32, >70 yrs).	2 scans*: same-day F: Radius = 27, 27, 25; Tibia = 30, 29, 29. M: Radius = 27, 30, 27; Tibia = 30, 30, 30.	$CV\%_{RMS}$	F (16-18, 30-32, >70 yrs): vBMD: 0.9-1.4%, 1.1-1.2%, 1.1-1.2%. Microstructure = 4.7-5.2%, 3.8-4.4%, 5.9-6.8%.	F (16-18, 30-32, >70 yrs): vBMD: 0.7-0.9%, 0.8-1.0%, 1.1%. Microstructure = 6.3-6.7%, 6.6-7.0%, 4.6-5.2%.
				M (16-18, 30-32, >70 yrs): vBMD: 0.7-0.9%, 0.8-1.0%, 1.1%. Microstructure = 6.3-6.7%, 6.6-7.0%, 4.6-5.2%.	M (16-18, 30-32, >70 yrs): vBMD = 0.3-0.4%, 0.6-0.7%, 0.3-0.5%. Microstructure = 3.5-3.6%, 4.0-4.1%, 5.3-5.4%.
Wong [79]	F&M=32; 20-69 yrs	2 scans*: same-day Radius and Tibia = 31	$CV\%_{RMS}$	vBMD = 0.5-0.7%. Microstructure = 4.6-4.8%.	vBMD = 0.2-0.4%. Microstructure = 3.7-4.1%.
Zhou [241]	F&M=30; 45±14 yrs	2 scans ^{NR}: within 48 hours Radius and Tibia = 30	$CV\%_{RMS}$	vBMD = 1.2-1.3%. Microstructure = 4.9-5.4%.	vBMD = 1.2-1.6%. Microstructure = 6.0-6.7%.

Abbreviations: F – Female; M - Male
vBMD measurements reported for total, trabecular vBMD and BV/TV (as it is derived from trabecular vBMD); Microstructure measurements reported for BV/TV, Tb.N*, Tb.Th and Tb.Sp.
Scans: * analysed following CSA-based registration; ** analysed following 3D registration; ^{NR} not reported.
Degrees of freedom: There are discrepancies to the original number of participants as images were removed due to movement artefact.

6.1.3 HR-pQCT image registration

Image registration can lower HR-pQCT measurement precision error compared to no registration [177]. The comparison of precision errors following CSA-based (2D) registration and 3D registration in the same dataset has been undertaken twice at the distal radius and distal tibia, using different image registration methods and software [176, 177]. MacNeil and Boyd [176] transformed the grey-level HR-pQCT images using linear interpolation, which has been demonstrated in Chapter 2 to lower Tb.N* and potentially remove image noise (Figure 2.22). Ellouz et al., [177] transformed the masks (i.e. GOBJs) of the HR-pQCT images using the SCANCO IPL, therefore preserving the grey-level images (as described in Chapter 2 Section 2.6.6). By removing angular deviations between images into account, 3D registration may more accurately determine the common volume between HR-pQCT images [177, 246]. This may improve the sensitivity to detect microstructural changes with disease and with interventions [89, 246].

6.1.4 Dominance

Limb asymmetries have been established in humans. This is mostly apparent in individuals that have asymmetrical mechanical loads on their body, such as the upper extremities in young adult cricketers [247], tennis players [26-28], and in the take-off leg in conditioned jumpers (high, long and triple) [248]. Asymmetries have also been reported in the general population. Hildebrandt and colleagues [249] found significant, but small, asymmetries that favoured the dominant distal radius (cortical area +2.11%, failure load +3.00%) and non-dominant distal tibia (total vBMD +0.77%, cortical area +1.03% and cortical thickness +1.51%); the dominant limb defined by what hand participants write with and what foot participants would kick a ball with, respectively. In a large Korean population study (male = 815, female = 979), there were no distal radius asymmetries associated with dominance, apart from slightly higher aBMD in the non-dominant limb in male's ≥ 61 years (approximately +0.010 g/cm^{-2}), whereas the non-dominant calcaneus had significantly greater aBMD (mean ranged from 0.009-0.018 g/cm^{-2}) in males and females ≤ 20 years, 21-40 years and 41-60 years [127]. The 'cross-symmetry' of bone properties at the lower limbs (non-dominant greater than dominant) [127, 249] has been attributed to loading characteristics from stabilising the body weight to facilitate movement of the dominant limb in activities, such as kicking a ball, and greater motor neuron excitability [250]. Nonetheless, the significant differences reported in these studies were small. There may also be asymmetrical loading

characteristics in older adults with the use of walking aids, history of hip or lower extremity fractures and osteoarthritis, independent from dexterity [251]. Therefore, measuring the effects of limb dominance is important to develop a standardised bone densitometry protocol at these sites.

6.1.5 Site comparison

The calcaneus is the largest tarsal bone and has a very high ratio of trabecular to cortical bone, which varies across different regions of interest. Other sites imaged using HR-pQCT, such as the radius and tibia, are long bones and have different trabecular-cortical ratios depending on the region that is studied [87, 155, 252]. Macro- and micro-structure differences can be expected between the radius and tibia due to mechanical forces from bearing weight. The distal tibia has a larger total CSA, higher trabecular vBMD, a thicker cortex and higher cortical porosity in comparison to the distal radius, which is apparent in males and females across a wide age range [151, 195, 234]. The total, trabecular and cortical vBMD, and stiffness, between the distal radius and distal tibia are also moderately-strongly correlated to one another [253, 254], and are stronger than those found between HR-pQCT measurements at the radius and tibia and QCT measurements at the lumbar spine and proximal femur [253, 255]. Furthermore, correlations are generally weaker with distal radius and distal tibia vBMD compared to lumbar spine and proximal femur aBMD [253, 255, 256], potentially due to the comparison of volumetric and areal projections. Eckstein and colleagues [228] also reported meagre correlations between trabecular bone specimens from the calcaneus, distal radius, proximal femur sites and the lumbar vertebral body. These weaker peripheral-central correlations are likely influenced by different rates of bone loss between central and peripheral sites [117]. The relationship between calcaneus vBMD and trabecular microstructure compared to measurements at the distal radius and distal tibia has not been reported using HR-pQCT. Furthermore, although weak-moderate correlations have been reported between distal radius and distal tibia vBMD with central site aBMD, the relationship between calcaneus vBMD and central site aBMD has also not been previously reported.

6.1.6 Summary

In summary, quantifying the HR-pQCT measurements precision error at the superior region of the calcaneus will indicate the potential applicability of the method in clinical studies. This can be based on establishing upper boundaries for determining clinically significant changes (i.e. precision errors' 95% LSC) in calcaneus total and

trabecular vBMD, and trabecular microstructure. The precision errors could be dependent on the image registration method that is used and may highlight areas to improve the protocol. Establishing whether there are calcaneal asymmetries in relation to limb dominance would help justify site selection to propose a standardised protocol and determine whether the other limb could be imaged where fracture may compromise a participant's positioning. No study *in vivo* has quantified calcaneus vBMD and trabecular microstructure in comparison to peripheral sites using HR-pQCT and central sites using DXA.

6.2 Aims and objectives

The aim of Chapter 6 is to determine the short-term measurement precision error for calcaneus HR-pQCT images.

Primary objectives of Chapter 6 are:

1. To determine the short-term precision errors for volumetric bone mineral density and trabecular microstructure in calcaneus HR-pQCT images.
2. To compare measurements' coefficient of variation between unregistered, cross-sectional area (CSA)-based registered and 3D registered HR-pQCT images.

The Chapter also aims to present preliminary analysis of the calcaneus HR-pQCT image measurements in comparison to peripheral and central sites of the skeleton.

Secondary objectives of Chapter 6 are:

1. To compare volumetric bone mineral density and trabecular microstructure between the non-dominant and dominant calcaneus HR-pQCT images.
2. To compare volumetric bone mineral density and trabecular microstructure between calcaneus, distal radius and distal tibia HR-pQCT images.
3. To test associations between calcaneus, distal radius and distal tibia volumetric BMD measurements, and lumbar spine and proximal femur areal BMD measurements.

6.3 Methods

6.3.1 Study design

Professor Eugene McCloskey, Professor Graham Kemp, Dr Margaret Paggiosi and I designed the study. The study was a cross-sectional, observational design, with two

visits separated by approximately 4 weeks. The investigations were completed as a sub-study to the concurrent study 'Clinical data to inform the MultiSim Project: Development of a modelling framework focused on the human musculoskeletal system'. The MultiSim Project is collecting a range of biological assessments from postmenopausal women, such as HR-pQCT scans of the radius, tibia and calcaneus, CT scans of the proximal femur and MRI of lower limbs, physical function and real-time activity monitoring data, as well as bone turnover markers. The project aims to use this data create a framework to personalise clinical decision-making and improve the prediction of whether musculoskeletal disease would occur, and what treatment would be most suitable.

The study was given a favourable ethical opinion and approval by the East of England - Cambridge and Hertfordshire Research Ethics Committee (reference 16/EE/0049). Sister Angela Green and Sister Julie Walker completed the participant recruitment and obtained informed consent. Dr Margaret Paggiosi performed the HR-pQCT image acquisitions. I completed the HR-pQCT image registration and analysis.

6.3.2 Participants

15 healthy premenopausal women were recruited into the sub-study. The sample size was chosen to have at least 30 degrees of freedom for the assessment of calcaneus HR-pQCT short-term measurement precision error, as recommended by the ISCD [239]. Greater detail of the calculations is provided in the statistical analysis (Section 6.3.6.3). 25 postmenopausal women with T-score ≤ −1 aim to be recruited as part of the MultiSim Project, 10 with no history of fracture or recent falls and 15 with recent falls with and without fractures. Recruitment of the postmenopausal women is on going and therefore not included in the Chapter 6 analysis.

Inclusion and exclusion criteria were as developed for the MultiSim Project. Briefly, participants needed to be willing to participate and able to give informed consent. Participants were excluded if they had a BMI lower than 18 or higher than 35 kg/m^2; had a previous fracture of either calcaneus, bilateral fractures of the distal radius and/or tibia; a history of, or current, conditions known to affect bone metabolism and BMD, such as a diagnosed skeletal disease or arthritis, chronic hepatic or renal disease, coeliac and/or other malabsorption syndromes, hyperparathyroidism, hyperthyroidism and/or diagnosed endocrine disorders, hypocalcaemia or hypercalcaemia, diagnosed restrictive eating disorder, or diabetes mellitus; history

of, or current, severe ischaemic heart disease, rheumatoid arthritis, ankylosing spondylitis, or cancer (concurrent); history of, or current neurological diseases affecting the neuromuscular system including Parkinson's disease, stroke, muscular dystrophy, myopathies, myasthenia, cerebral trauma, or peripheral neuropathy; treatment for more than 3 months in a year or under treatment with oral corticosteroids; history of any long-term immobilisation (duration greater than three months); conditions or surgery which could prevent the acquisition or analysis of musculoskeletal images; use of medications or treatment known to affect bone metabolism other than calcium/vitamin D supplementation; alcohol intake greater than 21 units per week; any individual who has had a previous CT scan (regardless of time and site). Premenopausal women taking the contraceptive pill were not excluded from the study.

All participants were telephone-screened using the study eligibility criteria prior to attending the Clinical Research Facility. Eligible participants provided written informed consent.

6.3.3 Descriptive statistics

As described in Chapter 5, Section 5.3.4.

6.3.4 DXA Imaging

At visit 1, lumbar spine and proximal femur DXA imaging followed protocols described in Section 2.1.2.

6.3.5 HR-pQCT imaging

6.3.5.1 Distal radius and distal tibia image acquisition

At visit 1 (baseline), distal radius and distal tibia HR-pQCT images were collected and followed protocols described in Section 2.3.1.

6.3.5.2 Calcaneus image acquisition

The calcaneus HR-pQCT imaging followed the protocol described in Chapter 5, Section 5.3.5.

At visit 1 (baseline) the superior region of the calcaneus was imaged twice using HR-pQCT. The images were collected at 100 ms integration time. The 100 ms integration time was preferred to the 200 ms integration time, due to concerns of higher movement artefacts at a 200 ms integration time using the current imaging apparatus. Losing participants' HR-pQCT images due to movement artefacts would

have a negative affect on the statistical power of the precision error estimation. The 2 calcaneus HR-pQCT images were obtained from the non-dominant foot, with repositioning between the 2 image acquisitions i.e. removing the participants' lower limb from the XtremeCT scanner gantry, removing the foot from the lower-limb cast and standing out of the chair. The non-dominant foot was then placed back in the lower-limb cast, as previously described.

At visit 2 (4 weeks after baseline) 1 calcaneus HR-pQCT image was obtained from the non-dominant foot and then 1 calcaneus HR-pQCT image was obtained from the dominant foot. Dominance was identified using similar methods described in Chapter 2 (Section 2.3.1).

Short-term measurement precision error was obtained from the three non-dominant calcaneus HR-pQCT images. The first non-dominant calcaneus HR-pQCT image (collected at baseline) was used in the site comparison with the distal radius and distal tibia HR-pQCT images, and the lumbar spine and proximal femur DXA images.

6.3.5.3 Image reconstruction

All HR-pQCT images were reconstructed using the standard protocol provide by the manufacturers (Section 2.3.2).

6.3.5.4 Calcaneus image registration

Three different methods were used to compare the measurements from the three non-dominant calcaneus HR-pQCT images: (1) no registration, (2) CSA-based registration and (3) 3D registration.

The evaluation of the HR-pQCT images without registration would include repositioning errors into the short-term precision error measurements.

The CSA-based registration is a two-dimensional method that is the standard registration procedure implemented using the SCANCO IPL. This automatically matches the bone area on a slice-by-slice basis and translates the stack of slices to provide an optimal overlap and determine the common volume [165]. The slice shift and common volume using the CSA-based registration are automatically added to the HR-pQCT measurements datasheet that is exported from the XtremeCT workstation.

The 3D registration has been described in Section 2.6.7.1. Adaptations were made to the procedure to account for the third HR-pQCT image. The 3D registration code can be found in the thesis Appendix and is summarised in the following points:

I. The *baseline*, *same-day* and *4-week* images, as well as their GOBJs, were called into the IPL. Two separate registrations (*same-day to baseline*; *4-week to baseline*) were completed using the methods described in Section 2.6.7.1, Step 1, II to VI.
II. The *same-day* GOBJ was transformed and concatenated using the methods described in Section 2.6.7.1, Step 2, I and II.
III. A threshold was applied to identify the common volume between the combined *same-day to baseline* GOBJs.
IV. The *4-week to baseline* transformation matrix was applied to the *4-week* GOBJ.
V. The transformed *4-week* GOBJ was concatenated with the common volume of the *baseline to same-day* GOBJ. This created an image containing the three, spatially aligned, calcaneus HR-pQCT GOBJs (*baseline, same-day and 4-week*).
VI. A threshold was applied to identify the common volume between the three GOBJs.
VII. This common volume was then overlaid on the baseline HR-pQCT image. The respective transformation matrices were inverted and applied to overlay the common volume on the *same-day* and *4-week* HR-pQCT images.

No calcaneus HR-pQCT images were removed if the common volume for the CSA-based and 3D registration was below 70%, to ensure that the sample size was preserved for estimating the short-term measurement precision error.

6.3.5.5 Image evaluation

All HR-pQCT images were evaluated using the steps described in Section 2.3.3. Measurements reported from the evaluation were total vBMD, trabecular vBMD, outer and inner trabecular vBMD, BV/TV^{d}, Tb.N*, $Tb.Th^{d}$ and $Tb.Sp^{d}$ (* – directly computed; ^{d} – derived). Total CSA was available in the analyses, apart from the calcaneus HR-pQCT image comparisons to calculate short-term measurement precision error, as it is not provided in the registered analysis worksheets.

The unregistered and CSA-based registered calcaneus HR-pQCT images were evaluated using the procedure in section 2.3.3. The 3D registration only evaluated the common volumes following the procedure described in section 6.3.5.4.

For the site comparison analysis between the calcaneus, distal radius and distal tibia, the baseline, unregistered calcaneus HR-pQCT images were used. Calcaneus trabecular microstructure measurements were adjusted using regression equations derived from Chapter 5 (Equation 6.1, 6.2 and 6.3), to predict measurements using a 200 ms integration time from 100 ms integration time. This aimed to provide a more accurate estimation of trabecular microstructure measurements, in line with those found in validation studies at the distal radius and distal tibia [77, 163, 164], which has been reported in Chapter 4. These measurements have been labelled 'adjusted' Tb.N*, Tb.Th^{d} and Tb.Sp^{d}:

$$adjusted\ Tb.N^{*} = -0.579 + (1.011 \times (100ms\ Tb.N^{*})) \quad \text{Equation 6.1}$$

$$adjusted\ Tb.Th^{d} = -0.001 + (1.237 \times (100ms\ Tb.Th^{d})) \quad \text{Equation 6.2}$$

$$adjusted\ Tb.Sp^{d} = -0.072 + (1.501 \times (100ms\ Tb.Sp^{d})) \quad \text{Equation 6.3}$$

6.3.6 Statistical analysis

Statistical analyses were performed in GraphPad Prism (7.0, GraphPad Software: La Jolla California, USA), unless stated otherwise. A $p<0.05$ indicated statistical significance, unless stated otherwise. HR-pQCT measurements were visually checked for normality, and then statistically checked using a Shapiro-Wilk test. Normally distributed measurements were presented as a mean with a 95% CI and non-normally distributed measurements were presented as a median with an IQR.

6.3.6.1 Mid-point reference line precision error

The SD_{RMS} of the mid-point reference line positions [154] was calculated between each superior image acquisition: 45 in total (15 x baseline, 15 x same-day, 15 x 4-week). Please note that only the superior region HR-pQCT images are evaluated in this Chapter.

6.3.6.2 Image registration

The common volume for the calcaneus HR-pQCT images following the 3D registration was compared between scans obtained on the same-day (Scan 1-2), 4-weeks apart (Scan1-3) and all 3 scans combined (All scans) using a Friedman test with Dunn's multiple comparisons. A Mann-Whitney signed-rank test was used to compare the common volume between the CSA-based and 3D registration for all scans.

6.3.6.3 Calcaneus HR-pQCT measurement precision error

The relative frequency for the calcaneus HR-pQCT image quality grades was calculated.

Calculation of the calcaneus HR-pQCT measurements short-term precision error was performed in accordance with the ISCD recommendations [239], using the Advanced Precision Calculator (www.iscd.org). Measurements reported from the calculator were CV% (Equation 6.4), $CV\%_{RMS}$ (Equation **6**.**5**) and SD_{RMS} (Equation 6.6):

$$CV\% = \frac{SD_j}{\overline{x_j}} \times 100 \qquad \text{Equation 6.4}$$

$$CV\%_{RMS} = \sqrt{\sum_{j=1}^{m} \frac{CV\%_j^2}{m}} \qquad \text{Equation 6.5}$$

$$SD_{RMS} = \sqrt{\sum_{j=1}^{m} \frac{SD_j}{m}} \qquad \text{Equation 6.6}$$

where j refers to an individual participant, SD is the measurement standard deviations between the three calcaneus HR-pQCT images, and $\bar{x}$ is the measurement mean between the three calcaneus HR-pQCT images, and m is the number of participants in the analysis. These measurements were expressed as both absolute and relative values.

The LSC was calculated for each HR-pQCT measurement using a 95% confidence criterion [150]:

$$LSC = Pr \times 2.77 \qquad \text{Equation 6.7}$$

where Pr is the precision value (either SD_{RMS} or $CV\%_{RMS}$), 2.77 represents the 95% confidence level (1.96 i.e. ± 2SD), multiplied by the square root of 2 (= 1.414) to account for single precision singles undertaken at each time point. The LSC was also expressed as both absolute and relative values.

HR-pQCT measurement SD_{RMS} and $CV\%_{RMS}$ were calculated within each registration method (no registration, CSA-based and 3D registration). The CV% was used to statistical compare the three registration methods, as the SD_{RMS} and

$CV\%_{RMS}$ are geometric means and therefore only provide one value for each outcome [240]. A Friedman test with Dunn's multiple comparisons was performed to compare the CV% between the three registration methods.

Linear regression analyses were performed to evaluate the correlation between the absolute slice shift in HR-pQCT slices with BSA-based registration (dependent variable) and the percentage change in the HR-pQCT measurements from the slice (total vBMD, trabecular vBMD and Tb.N*; independent variable). The r^2, equation slope and intercept, and RMSE were calculated. This analysis aimed to determine whether the positive or negative slice shift from *in vivo* scans replicated the respective increase or decrease in trabecular vBMD reported in cadaveric specimen over a larger CSA (Section 3.6.3).

6.3.6.4 Non-dominant vs. dominant

Paired t-tests were performed to compare HR-pQCT measurements between the non-dominant and dominant calcaneus.

6.3.6.5 Site comparison

The relative frequency for the calcaneus, distal radius and distal tibia HR-pQCT image quality grades were calculated.

A one-way ANOVA with a Bonferroni correction was performed to compare total vBMD, trabecular vBMD, outer trabecular vBMD, BV/TV^d, Tb.N* and $Tb.Th^d$ between the calcaneus, distal radius and distal tibia ($p<0.017$). A Friedman test with a Dunn's multiple comparisons was performed to compare inner trabecular vBMD and $Tb.Sp^d$ between the calcaneus, distal radius and distal tibia. Similar tests were performed for the adjusted Tb.N*, $Tb.Th^d$ and $Tb.Sp^d$ at the calcaneus in comparison to the distal radius and distal tibia.

Pearson's correlation analysis (with 95% CI) was performed to test the association for total vBMD, trabecular vBMD, outer trabecular vBMD, BV/TV^d, Tb.N* and $Tb.Th^d$ between the calcaneus and the distal radius and distal tibia. Spearman's correlation analysis (with 95% CI) was performed to test the association for inner trabecular vBMD and $Tb.Sp^d$ between the calcaneus and the distal radius and distal tibia.

Pearson's correlation analysis was performed to test the association for total vBMD and trabecular vBMD from the calcaneus, distal radius and distal tibia, with lumbar spine aBMD. Spearman's correlation analysis was performed to test the association for total vBMD and trabecular vBMD from the calcaneus, distal radius and distal tibia, with total hip and femoral neck aBMD.

6.3.6.6 Anthropometry vs. HR-pQCT imaging measurements

Spearman's correlation analysis (with 95% CI) was performed to test the association between weight and height with the HR-pQCT measurements at the calcaneus, distal radius and distal tibia: total CSA, total vBMD, trabecular vBMD, outer trabecular vBMD, inner trabecular vBMD, BV/TV^{d}, Tb.N*, Tb.Th^{d} and Tb.Sp^{d}.

6.4 Results

6.4.1 Participant characteristics

Fifteen premenopausal women participated in the study. The participant's descriptive statistics and DXA imaging measurements are presented in Table 6.2.

Table 6.2. Participant descriptive statistics and DXA measurements.

Age, years	32 (5)
Height, m	1.64 (0.06)
Weight, kg	65.0 (13.9)
BMI, kg/m^{-2}	24.1 (3.9)
Lumbar spine aBMD, g/cm^{-2}	1.070 (0.899, 1.100)
Lumbar spine T-score	0.2 (-1.3, 0.5)
Total hip aBMD, g/cm^{-2}	0.951 (0.093)
Total hip T-score	0.1 (0.8)
Femoral Neck aBMD, g/cm^{-2}	0.796 (0.079)
Femoral Neck T-score	-0.5 (0.7)

Lumbar spine aBMD and T-score presented as median (IQR). All other data presented as mean (±SD)

6.4.2 Calcaneus HR-pQCT measurement precision error

6.4.2.1 Mid-point reference line precision error

For the 45 individual acquisitions, the SD_{RMS} was 1.26 mm, which corresponded to 14.0% of the total stack length. Figure 6.1 shows the individual data for the mid-point reference line placement between the first, second and third image

acquisitions as a CV%. There was no statistically significant effect of the image acquisition time on the mid-point reference line placement CV%.

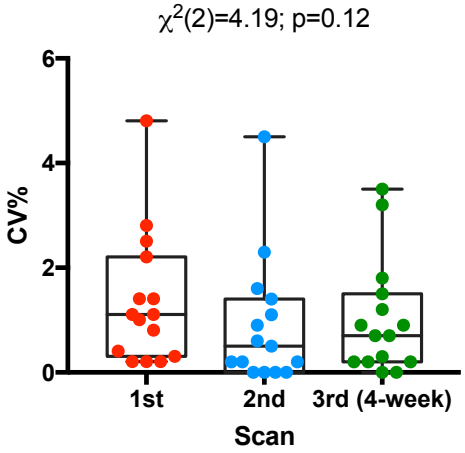

Figure 6.1. Box and Whisker plots for the mid-point reference line placement on the calcaneus HR-pQCT scout view.

The coefficient of variation (%) for each individual participant is presented within each time point, with pooled median, IQR, and minimum and maximum values. A Friedman test was performed with Dunn's corrected multiple comparisons.

6.4.2.2 Calcaneus HR-pQCT image quality

Figure 6.2 shows the relative frequency of the image quality grades from the calcaneus HR-pQCT image acquisitions, obtained for short-term measurement precision error analysis. An acceptable HR-pQCT image was obtained for each participant at each image acquisition time point.

From the baseline HR-pQCT image acquisitions, 32% has no artefact, 47% had slight and/or pronounced artefact, and 21% had unacceptable artefacts (definitions in Section 2.3.1). The 4 images with unacceptable artefacts were repeated. All repeats had pronounced image artefacts and were included in the analysis. 1 HR-pQCT image that had pronounced artefact was repeated, however the image grade did not improve. The scan technician deemed this acceptable for inclusion in the analysis.

From the same-day HR-pQCT image acquisitions, 44% had no artefact, 56% had slight and pronounced image artefacts, and no images had unacceptable artefacts.

1 HR-pQCT image that had pronounced artefact was repeated. The repeat had slight image artefact and was included in the analysis.

From the 4-week HR-pQCT image acquisitions, 37% has no artefact, 47% had slight and pronounced artefact, and 16% had unacceptable artefacts. 3 unacceptable image acquisitions were repeated. 1 repeat had no artefact and 2 repeats had pronounced image artefacts, and were all included in the analysis. 1 HR-pQCT image that had pronounced artefact was repeated. The repeat had a slight image artefact grade and was included in the analysis.

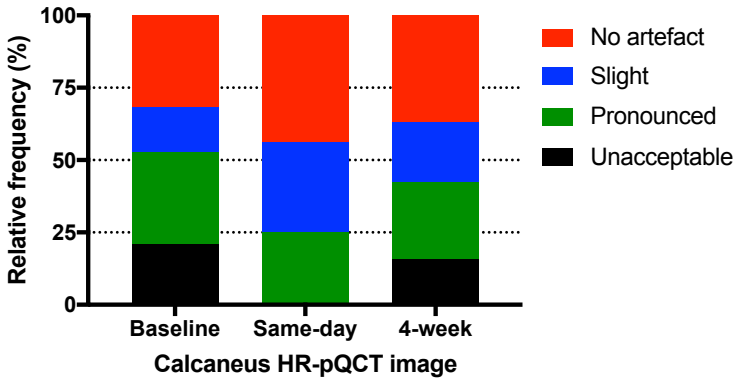

Figure 6.2. Image quality grades for the superior region calcaneus HR-pQCT images obtained for short-term measurement precision error calculation.

Participants = 15. The number of HR-pQCT image acquisitions including repeats: Baseline = 19; Same-day = 16; 4-week = 19.

6.4.2.3 Image registration

Figure 6.3 shows the common volume between the calcaneus HR-pQCT images following the 3D registration, with comparisons made between scans obtained on the same-day (Scan1-2), 4-weeks apart (Scan1-3) and all 3 scans combined (all scans).

There was a significant effect of the scan combination on the common volume. The common volume was higher between Scan1-2 than all scans (rank sum difference = 23.5, $p<0.001$). There were no differences in the common volume between the Scan1-2 and Scan1-3 (rank sum difference = 11, $p=0.13$), and between Scan1-3 and all scans (rank sum difference = 12.5, $p=0.07$).

Between the three repeated and repositioned calcaneus HR-pQCT image acquisitions, the median (IQR) common volume was significantly greater for the CSA-based registration (90% (89, 93%)) compared to 3D registration (76% (70, 79%)); sum of positive, negative ranks = 120, 0, p<0.001 (Figure 6.4).

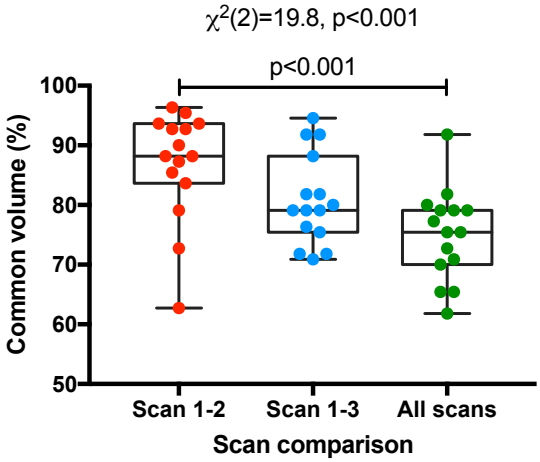

Figure 6.3. Box and Whisker plots for the common volume percentage between the 3D registered HR-pQCT images at the superior region of the calcaneus.

Scan 1-2 = baseline and same-day; Scan 1-3 = baseline and 4-week; All scans = baseline, same-day and 4-week.
Data are presented for each participant within each integration time, with the median, interquartile range, and minimum and maximum values. Friedman test was performed with Dunn's corrected multiple comparisons between the scan comparisons.

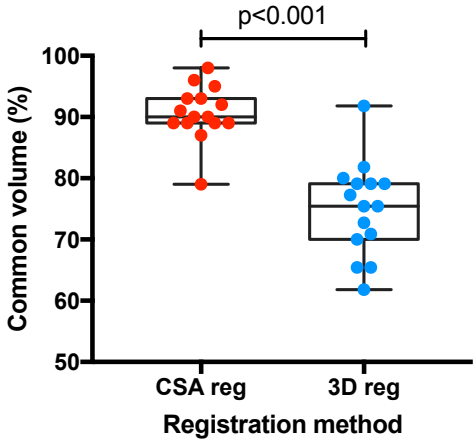

Figure 6.4. Box and Whisker plots for the common volume percentage between all scans at the superior region of the calcaneus following CSA-based and 3D registration.

Data are presented for each participant within each integration time, with the median, interquartile range, and minimum and maximum values. A Wilcoxon-signed rank test was performed between the registration methods.

6.4.2.4 Short-term precision error and the least significant change

Table 6.3 shows the descriptive calcaneus HR-pQCT measurements, and the short-term precision error (SD_{RMS} and $CV\%_{RMS}$) and associated LSCs without registration, with CSA-based and 3D registration. Total and trabecular vBMD measurements short-term precision error was generally lower with CSA-based and 3D registration, when compared to measurements with no registration. Without registration the SD_{RMS} ranged from 4-7 mg HA/cm^{-3} and the $CV\%_{RMS}$ ranged from 1.5-2.4%; with CSA-based registration the SD_{RMS} ranged from 2-5 mg HA/cm^{-3} and the $CV\%_{RMS}$ ranged from 0.8-1.6%; and with 3D registration the SD_{RMS} ranged from 2.4-4.9 mg HA/cm^{-3} and the $CV\%_{RMS}$ ranged from 0.9-1.9%. BV/TV^{d} and Tb.Th^{d} followed a similar pattern to trabecular vBMD, where as Tb.N* and Tb.Sp^{d} were similar between the three methods. The trabecular microstructure $CV\%_{RMS}$ precision error without registration ranged from 1.7-2.2%, with CSA-based registration ranged from 1.4-1.8% and with 3D registration ranged from 1.6-1.8%. LSC measurements followed similar relationships to the SD_{RMS} and $CV\%_{RMS}$.

Figure 6.5A-H shows the CV% for total vBMD and trabecular vBMD, BV/TV^{d} and trabecular microstructure measurements between the repeat, repositioned calcaneus HR-pQCT images with no registration, CSA-based and 3D registration. Post-hoc analyses are presented in the text as rank sum differences from the Friedman tests.

There was no statistically significant effect of the registration method on total vBMD CV%. There was, however, a statistically significant effect of the registration method on trabecular vBMD, outer and inner trabecular vBMD CV%. The trabecular vBMD CV% was lower with CSA-based registration compared to no registration (16.5, p=0.008), and there were no differences in the CV% between 3D registration and no registration (9.0, p=0.30) and the CSA-based and 3D registration methods (-7.5, p=0.51). The outer trabecular vBMD CV% were lower with CSA-based (15.0, p=0.02) and 3D registration (13.5, p=0.04) compared to no registration, whereas there was no difference between the CSA-based and 3D registration methods (-1.5, p>0.99). The inner trabecular vBMD CV% was lower with CSA-based registration compared to no registration (15.5, p=0.01), whereas there were no differences between the 3D registration and no registration (11.5, p=0.11), and between the CSA-based and 3D registration methods (-4.0, p>0.99).

There was a statistically significant effect of the registration method on BV/TV CV%, following a similar relationship to trabecular vBMD. The BV/TV CV% was lower with CSA-based registration compared to no registration (15.5, p=0.01), whereas there were no differences between the 3D registration and no registration (8.5, p=0.36), and the CSA-based and 3D registration methods (-7.0, p=0.60).

There were no statistically significant effects of the registration method on Tb.N*, $Tb.Th^{d}$ and $Tb.Sp^{d}$ CV%.

Table 6.3. Precision error measurements for volumetric BMD and trabecular microstructure of the superior region calcaneus without registration, after CSA-based registration and 3D registration.

	Descriptive statistics			SD_{RMS} (LSC)			$CV\%_{RMS}$ (LSC)		
	No	CSA	3D	No	CSA	3D	No	CSA	3D
Total vBMD, mg HA.cm^{-3}	344 (332, 356)	345 (333, 357)	347 (336, 359)	6.9 (19)	5.0 (13.9)	4.9 (13.5)	1.9 (5.3)	1.4 (3.8)	1.3 (3.7)
Tb.vBMD, mg HA.cm^{-3}	258 (251, 264)	259 (252, 265)	262 (255, 268)	4.9 (13.5)	2.9 (8.0)	3.3 (9.1)	1.8 (5.1)	1.1 (3.0)	1.2 (3.4)
Outer Tb.vBMD, mg HA.cm^{-3}	285 (279, 291)	286 (280, 292)	288 (282, 293)	4.2 (11.5)	2.2 (6.2)	2.4 (6.7)	1.5 (4.1)	0.8 (2.2)	0.9 (2.4)
Inner Tb.vBMD, mg HA.cm^{-3}	239 (232, 247)	241 (233, 248)	244 (236, 251)	5.9 (16.4)	4.0 (11.1)	4.8 (13.2)	2.4 (6.5)	1.6 (4.5)	1.9 (5.3)
BV/TV[d], %	21.5 (20.9, 22.0)	21.6 (21.0, 22.1)	21.8 (21.3, 22.3)	0.4 (1)	0.2 (0.7)	0.3 (0.7)	1.8 (5.1)	1.1 (3.1)	1.2 (3.3)
Tb.N*, mm^{-1}	3.2 (3.1, 3.2)	3.2 (3.1, 3.2)	3.2 (3.1, 3.2)	0.05 (0.15)	0.05 (0.14)	0.05 (0.14)	1.7 (4.7)	1.7 (4.6)	1.6 (4.4)
Tb.Th[d], µm	68 (66, 70)	68 (66, 70)	69 (67, 71)	2 (4)	1 (3)	1 (3)	2.2 (6.1)	1.4 (3.9)	1.4 (3.9)
Tb.Sp[d], µm	249 (243, 255)	249 (243, 255)	248 (243, 254)	10 (10)	10 (10)	10 (10)	1.9 (5.2)	1.8 (5.1)	1.8 (5.0)

Descriptive statistics (mean (95% CI)) is presented for each measurements within each registration method.
Short-term precision error abbreviations: SD_{RMS}, root-mean-square standard deviation; $CV\%_{RMS}$, root-mean-square coefficients of variation; LSC, least significant change.
Registration abbreviations: No, without registration; CSA, cross-sectional area registration; 3D, 3D registration.
N = 15.

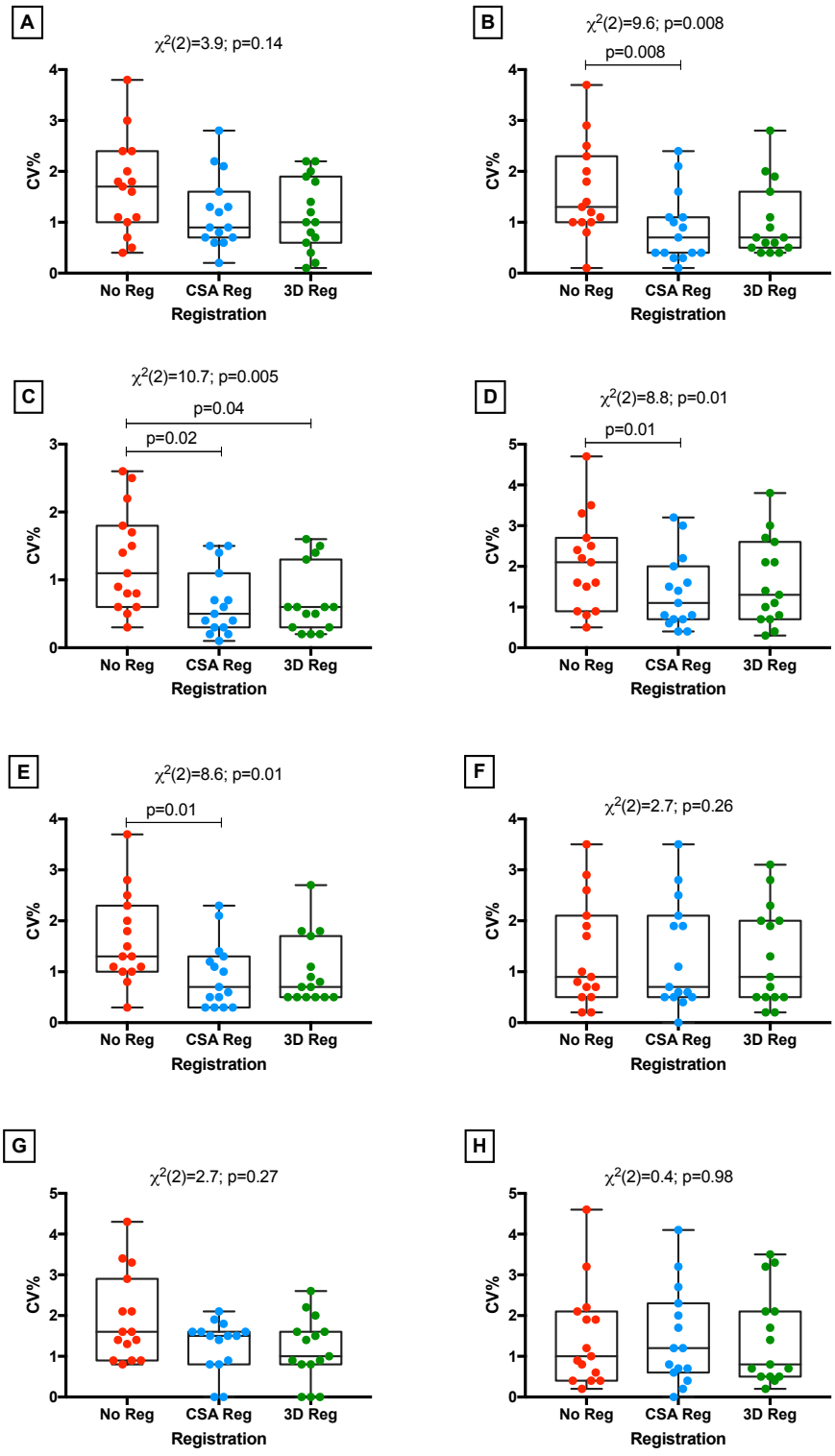

Figure 6.5. Box and whisker plots of the superior region calcaneus volumetric BMD measurement coefficient of variation between the three repositioned HR-pQCT scans, without registration, after CSA-based and 3D registration.

A − Total vBMD; B − Tb.vBMD; C − Outer Tb.vBMD; D − Inner Tb.vBMD; E − BV/TV^{d}; F − Tb.N*; G − Tb.Th^{d}; H − Tb.Sp^{d}.
Data are presented for each participant within each registration method, with the median, IQR, and minimum and maximum values. Friedman test's were performed with Dunn's corrected multiple comparisons.

Figure 6.6 shows the percentage change in total vBMD, trabecular vBMD and Tb.N* with positive and negative slice shifts of the volume of interest, following CSA-based registration. For total vBMD (Figure 6.6A) and trabecular vBMD (Figure 6.6B), there were trends for an increase with a positive slice shift (i.e. movement of the region of interest in the superior direction) and a decrease with a negative slice shift (i.e. movement of the region of interest in the inferior direction). A weak-moderate prediction of the percentage change in total vBMD (r^2 = 0.40, p<0.001), and a moderate prediction of the percentage change in trabecular vBMD (r^2 = 0.62, p<0.001) could be made with slice shifts using a regression equation. In Figure 6.6B, removal of the data point located at slice shift +21 and change in trabecular vBMD of +5.1% weakened the prediction (r^2 = 0.57, p<0.001), but had a minimal effect on the regression slope, intercept or RMSE (Y = 0.296*X − 0.155, RMSE = 1.6 mg HA/cm^{-3}). There were no significant correlations for Tb.Th^d and Tb.Sp^d.

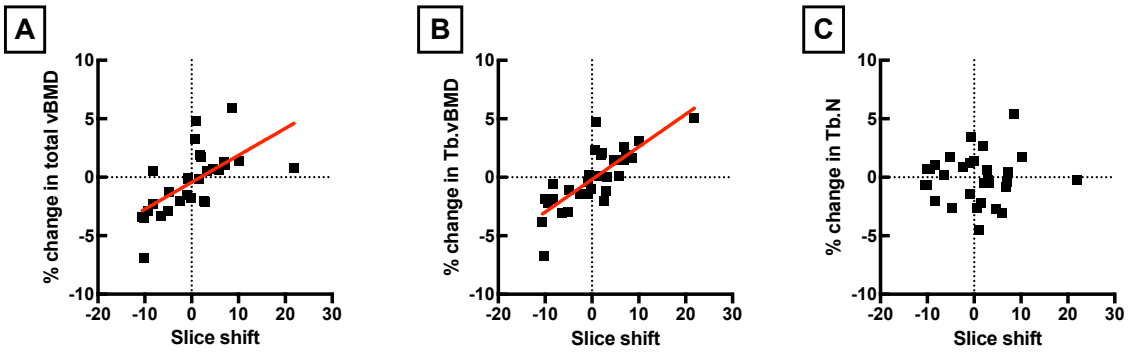

Figure 6.6. Percentage change in total volumetric BMD (A), trabecular volumetric BMD (B) and trabecular number (C) in relation to the slice shift in the superior region of the calcaneus.

The slice shift was record from the CSA registration between the baseline and same-day HR-pQCT images, and between the baseline and 4-week HR-pQCT images.
Linear regression analyses: Total vBMD – r^2 = 0.40 (p<0.001), Y = 0.231*X − 0.434, RMSE = 2.1 mg HA/cm^{-3}; Tb.vBMD – r^2=0.63 (p<0.001), Y = 0.279*X − 0.190, RMSE = 1.6 mg HA/cm^{-3}; Tb.N* – p=0.76.
N = 15 participants, with 2 measurements.

6.4.3 Non-dominant vs. dominant

Table 6.4 shows the comparison between the HR-pQCT measurements from the non-dominant and dominant calcaneus. There were no differences in the total CSA, volumetric BMD and trabecular microstructure between the non-dominant and dominant calcaneus region.

Table 6.4. Comparison of measurements obtained from the non-dominant and dominant superior region of the calcaneus HR-pQCT images.

	Calcaneus site		Mean (95% CI) absolute difference	
	Non-dominant	Dominant	Δ	p value
Total CSA, mm^{-3}	1266 (1183, 1348)	1287 (1170, 1403)	21.0 (-38.3, 80.3)	0.48
Total vBMD, mg $HA.cm^{-3}$	345 (324, 366)	340 (323, 358)	-4.8 (-15.9, 6.4)	0.37
Tb.vBMD, mg $HA.cm^{-3}$	258 (245, 271)	255 (244, 266)	-3.0 (-12.9, 6.8)	0.52
Outer Tb.vBMD, mg $HA.cm^{-3}$	285 (274, 297)	282 (274, 290)	-3.2 (-9.8, 3.5)	0.32
Inner Tb.vBMD, mg $HA.cm^{-3}$	240 (225, 254)	237 (222, 251)	-2.9 (-15.6, 9.7)	0.63
BV/TV^{d}, %	21.5 (20.4, 22.6)	21.3 (20.3, 22.2)	0.2 (-1.0, 0.5)	0.53
Tb.N*, mm^{-1}	3.17 (3.03, 3.30)	3.19 (3.06, 3.31)	0.02 (-0.04, 0.08)	0.42
$Tb.Th^{d}$, µm	68 (64, 72)	67 (63, 71)	-1 (-3, 1)	0.34
$Tb.Sp^{d}$, µm	249 (238, 261)	248 (238, 259)	-1 (-7, 5)	0.73

Data shown for 15 participants as mean (95% CI).
Δ (difference) = Dominant minus non-dominant.

6.4.4 Skeletal site comparison

6.4.4.1 HR-pQCT image quality

Figure 6.7 shows the HR-pQCT image quality grades between the calcaneus, distal radius and distal tibia image acquisitions. At the calcaneus, 21% of the scan images had an unacceptable image quality, 47% had a slight and pronounced image quality, and 32% had no artefact. At the distal radius, 54% of the scan image had an unacceptable image quality, 42% had a slight and pronounced image quality, and 4% had no artefact. At the distal tibia, 6% of the scan images had an unacceptable image quality, 13% had a slight and pronounced image quality, and 81% had no artefact. Repeat calcaneus and distal tibia HR-pQCT images had acceptable image quality grades. Of the 9 repeated distal radius image acquisitions, 3 still had unacceptable image quality.

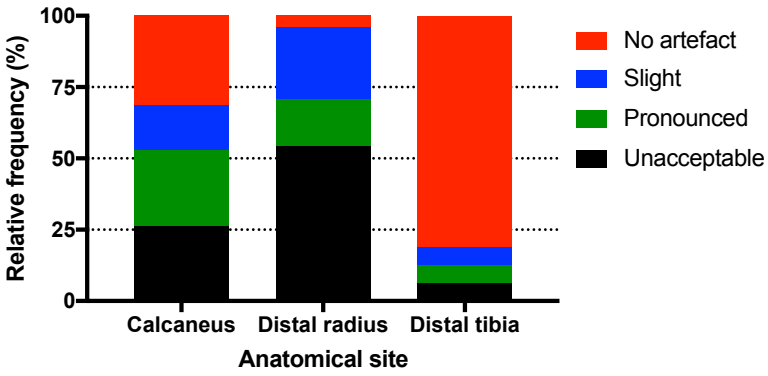

Figure 6.7. Image quality grades for superior region of the calcaneus, distal radius and distal tibia HR-pQCT images.

Participants = 15.
Number of HR-pQCT image acquisitions including repeats: Calcaneus = 19; Distal radius = 24; Distal tibia = 16.

6.4.4.2 HR-pQCT site comparison

12 participants with acceptable HR-pQCT image quality for the calcaneus, distal radius and distal tibia were included in the repeated measures analysis.

Figure 6.8A-E shows the total CSA, total and trabecular volumetric BMD comparison between the superior region of the calcaneus, distal radius and distal tibia. Post-hoc analyses are presented in text as mean (95% CI) differences from the one-way ANOVAs (total CSA, total vBMD, trabecular vBMD and outer trabecular vBMD) and rank sum differences from the Friedman tests (inner trabecular vBMD).

There were also significant effects of the skeletal site on total vBMD, trabecular vBMD, and outer and inner trabecular vBMD. Total vBMD was higher at the superior region of the calcaneus compared to the distal tibia (39 (17, 62) $p<0.001$), but not the distal radius (31 mg HA.cm^{-3} (-7, 69 mg HA.cm^{-3}), $p=0.13$). Trabecular vBMD was higher at the superior region of calcaneus compared to the distal radius (107 mg HA.cm^{-3} (92, 122 mg HA.cm^{-3}), $p<0.001$) and the distal tibia (94 mg HA.cm^{-3} (76, 112 mg HA.cm^{-3}), $p<0.001$). The superior region of the calcaneus also had higher outer and inner trabecular vBMD: outer trabecular vBMD compared to the distal radius (75 mg HA.cm^{-3} (60, 91 mg HA.cm^{-3}), $p<0.001$) and distal tibia (62 mg HA.cm^{-3} (40, 84 mg HA.cm^{-3}), $p<0.001$); inner trabecular vBMD compared to the distal radius (-20, $p<0.001$) and distal tibia (-16, $p=0.003$). There were no differences between distal radius and distal tibia total vBMD (-9 mg HA.cm^{-3} (-23, 41 mg HA.cm^{-3}), $p>0.99$), trabecular vBMD (-13 mg HA.cm^{-3} (-31, 5 mg HA.cm^{-3}), $p=0.22$), outer

trabecular vBMD (13 mg HA.cm^{-3} (-8, 34 mg HA.cm^{-3}), p=0.32) and inner trabecular vBMD (-4, p>0.99).

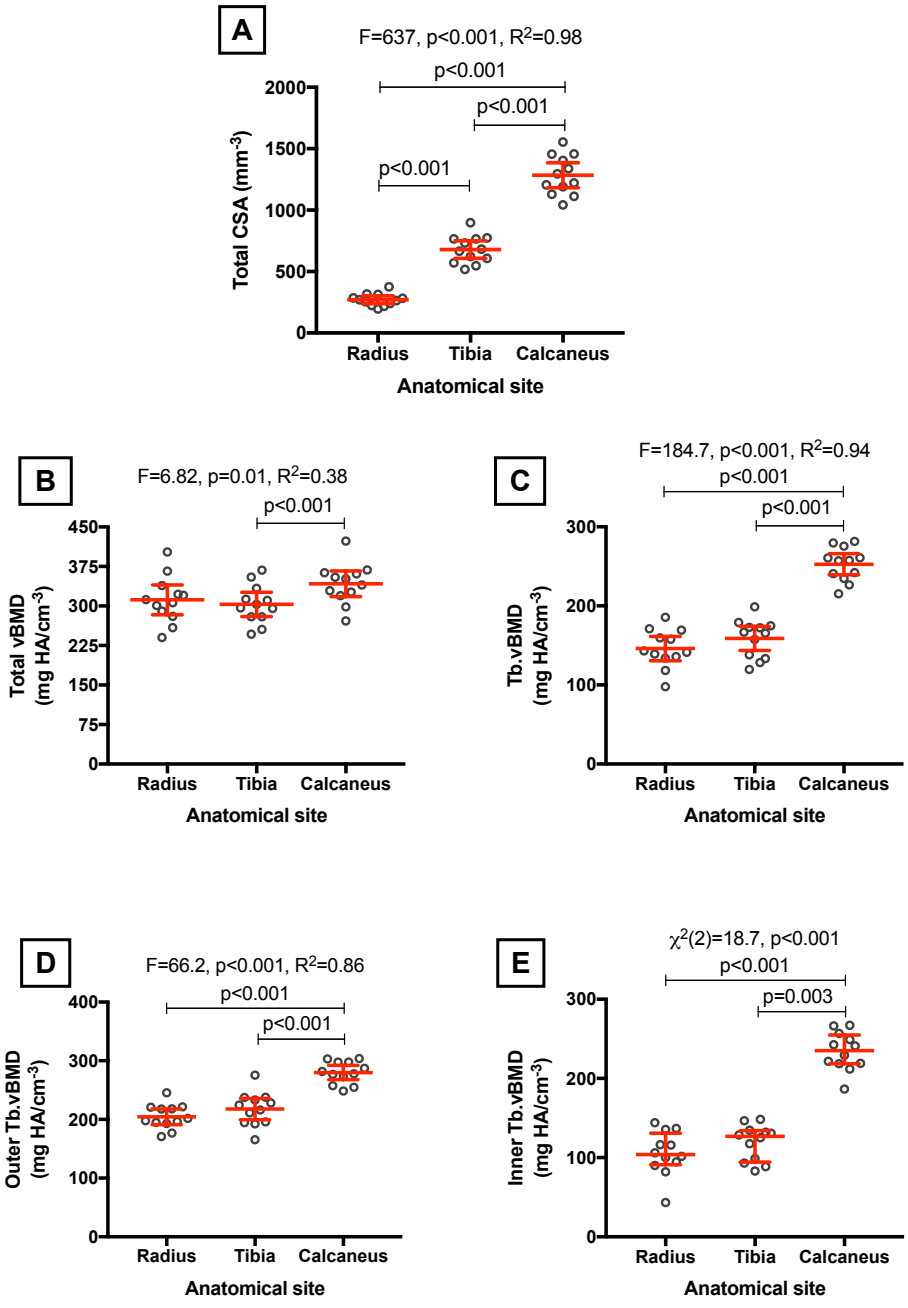

Figure 6.8. Volumetric BMD measurement comparison between the superior region of the calcaneus, the distal radius and distal tibia.

A – Total CSA; B – Total vBMD; C – Tb.vBMD; D – Outer Tb.vBMD; E – Inner Tb.vBMD.
ANOVA (mean (95%CI)) – Total CSA, Total vBMD, Tb.vBMD and Outer Tb.vBMD; Friedman test (median (IQR)) – Inner Tb.vBMD.

Figure 6.9A-D shows the BV/TV^{d} and trabecular microstructure measurement comparison between the superior region of the calcaneus, distal radius and distal tibia. Post-hoc analyses are presented in text as mean (95% CI) differences for the one-way ANOVAs (BV/TV^{d}, Tb.N* and Tb.Th^{d}) and rank sum differences for the Friedman test (Tb.Sp^{d}).

There was a significant effect of the skeletal site on BV/TV^{d}, Tb.N*, Tb.Sp^{d}, but not on Tb.Th^{d}. BV/TV^{d} at the superior region of the calcaneus was higher compared to the distal radius (8.9% (7.6, 10.1%), p<0.001) and distal tibia (7.8% (6.3, 9.3%), p<0.001), as was Tb.N* (distal radius 1.4 mm^{-1} (1.1, 1.6 mm^{-1}), p<0.001; distal tibia (1.3 mm^{-1} (1.1, 1.6 mm^{-1}), p<0.001), whereas Tb.Sp^{d} was lower compared to the distal radius (-19, p<0.001) and distal tibia (-17, p=0.002). There were no differences between the distal radius and distal tibia BV/TV^{d} (-1.1% (-2.6, 0.1%), p=0.23), Tb.N* (-0.0 mm^{-1} (-0.3, 0.3 mm^{-1}), p>0.99) and Tb.Sp^{d} (2, p>0.99).

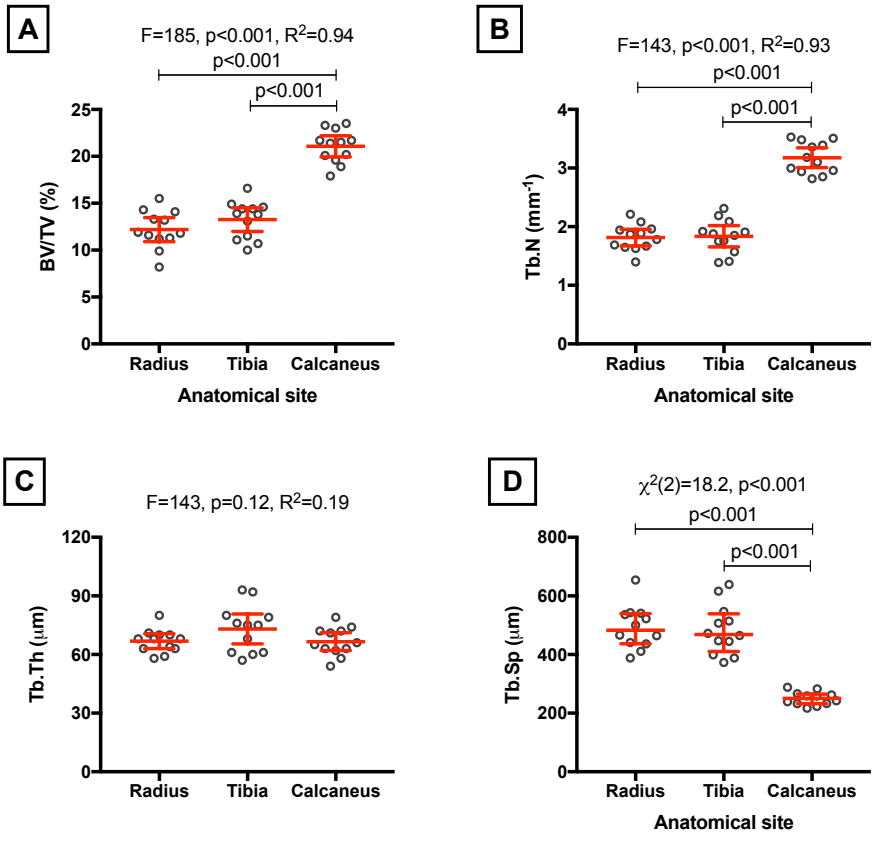

Figure 6.9. BV/TV and trabecular microstructure measurement comparison between the superior region of the calcaneus, the distal radius and distal tibia.

A – BV/TV^{d}; B – Tb.N*; C – Tb.Th^{d}; D – Tb.Sp^{d}.
ANOVA (mean, 95%CI) – BV/TV^{d}, Tb.N*, Tb.Th^{d}; Friedman test (median, IQR) – Inner Tb.vBMD.

Figure 6.10A-C shows the trabecular microstructure measurements for the superior region of the calcaneus following adjustment for the scan integration time (100 ms to 200 ms) in comparison to the distal radius and distal tibia. Post-hoc analyses are presented in text as mean (95% CI) differences from the one-way ANOVAs (adjusted Tb.N* and Tb.Th^{d}) and rank sum differences from the Friedman tests (adjusted Tb.Sp^{d}).

There was a significant effect of the skeletal site on adjusted Tb.N*, similar to that found in the standard Tb.N*. The adjusted Tb.N* was higher at the calcaneus compared to the distal radius (0.8 mm^{-1} (0.5, 1.1 mm^{-1}), p<0.001) and distal tibia (0.8 mm^{-1} (0.6, 0.1 mm^{-1}), p<0.001). Additionally, there was a significant effect of the skeletal site on adjusted Tb.Sp^{d}, similar to the standard Tb.Sp^{d}, which was lower at the calcaneus compared to the distal radius (-19, p<0.001) and distal tibia (-17, p=0.002). There was also a significant effect of the skeletal site on adjusted Tb.Th^{d}, which was not reported with the standard Tb.Th$^{d.}$ The adjusted Tb.Th^{d} was higher at the superior region of the calcaneus compared to the distal radius (14 µm (1, 22 µm), p<0.001), but was not different to the distal tibia (8 µm (-1, 18 µm), p=0.12).

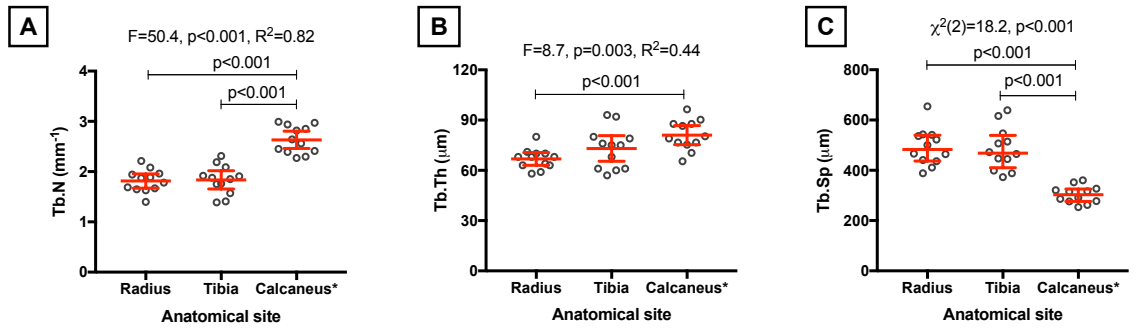

Figure 6.10. Adjusted trabecular microstructure measurements from the superior region of the calcaneus in comparison to distal radius and distal tibia measurements.

A – adjusted Tb.N*; B – adjusted Tb.Th^{d}; C – adjusted Tb.Sp^{d}.
ANOVA (mean (95%CI)) – adjusted Tb.N*, adjusted Tb.Th^{d}; Friedman test (median (IQR)) – adjusted Tb.Sp^{d}.

6.4.5 Skeletal site correlation

6.4.5.1 HR-pQCT: calcaneus, distal radius and distal tibia

For the correlation analysis, 12 participants were analysed for the calcaneus-distal radius comparison and 15 participants were analysed for the calcaneus-distal tibia comparison, due to the availability of acceptable quality HR-pQCT images.

Figure 6.11A-D shows the total and trabecular volumetric BMD correlation analysis between the calcaneus, distal radius and distal tibia. The calcaneus and distal radius was not significantly correlated for total vBMD and inner trabecular vBMD, but had a moderate, borderline significant correlation for outer trabecular vBMD and had a moderate-strong correlation for trabecular vBMD. The calcaneus and distal tibia were significantly correlated for all measurements. Total vBMD had a strong correlation, trabecular vBMD and inner trabecular vBMD had a moderate-strong correlation, and outer trabecular vBMD had a moderate correlation.

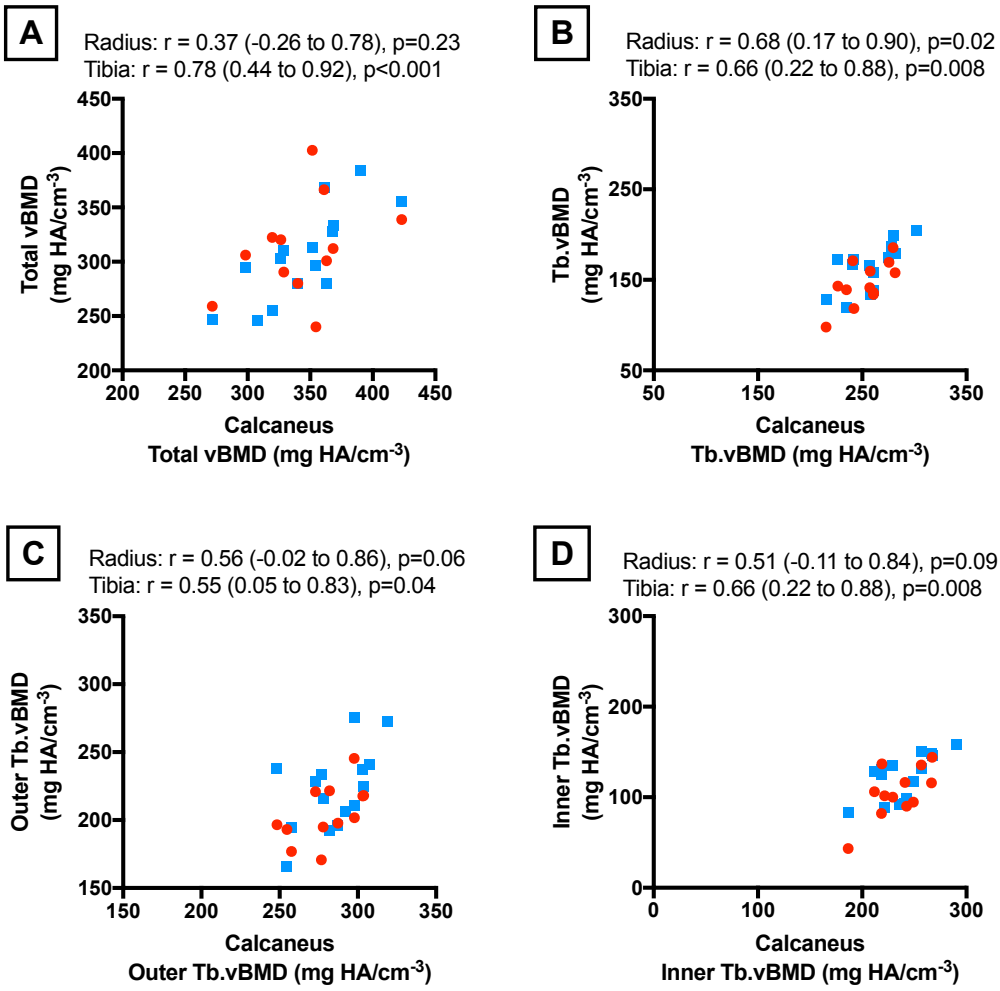

Figure 6.11. Volumetric BMD measurement correlation between the superior region of the calcaneus, the distal radius and distal tibia.

A – Total vBMD; B – Tb.vBMD; C – Outer Tb.vBMD; D – Inner Tb.vBMD.
Red circle – calcaneus vs. radius (n=12); Blue square – calcaneus vs. tibia (n=15).
Pearson's correlation with 95% CI – Total vBMD, Tb.vBMD and Outer Tb.vBMD.
Spearman's correlation with 95% CI – Inner Tb.vBMD.

Figure 6.12A-D shows the BV/TV^{d} and the trabecular microstructure correlation analysis between the calcaneus, distal radius and distal tibia; the corrected calcaneus trabecular microstructure measurements are reported in this analysis.

The calcaneus and distal radius was moderate-strongly correlated for BV/TV^{d}. There was no correlation between the calcaneus and the distal radius for Tb.N*, Tb.Th^{d} and Tb.Sp^{d}. The calcaneus and distal tibia were moderate-strongly correlated for BV/TV^{d}. There were moderate correlations between calcaneus and distal tibia Tb.Th^{d} and Tb.Sp^{d}, and there was no correlation in Tb.N*. Correlation analysis results from the adjusted trabecular microstructure did not differ to the uncorrected trabecular microstructure.

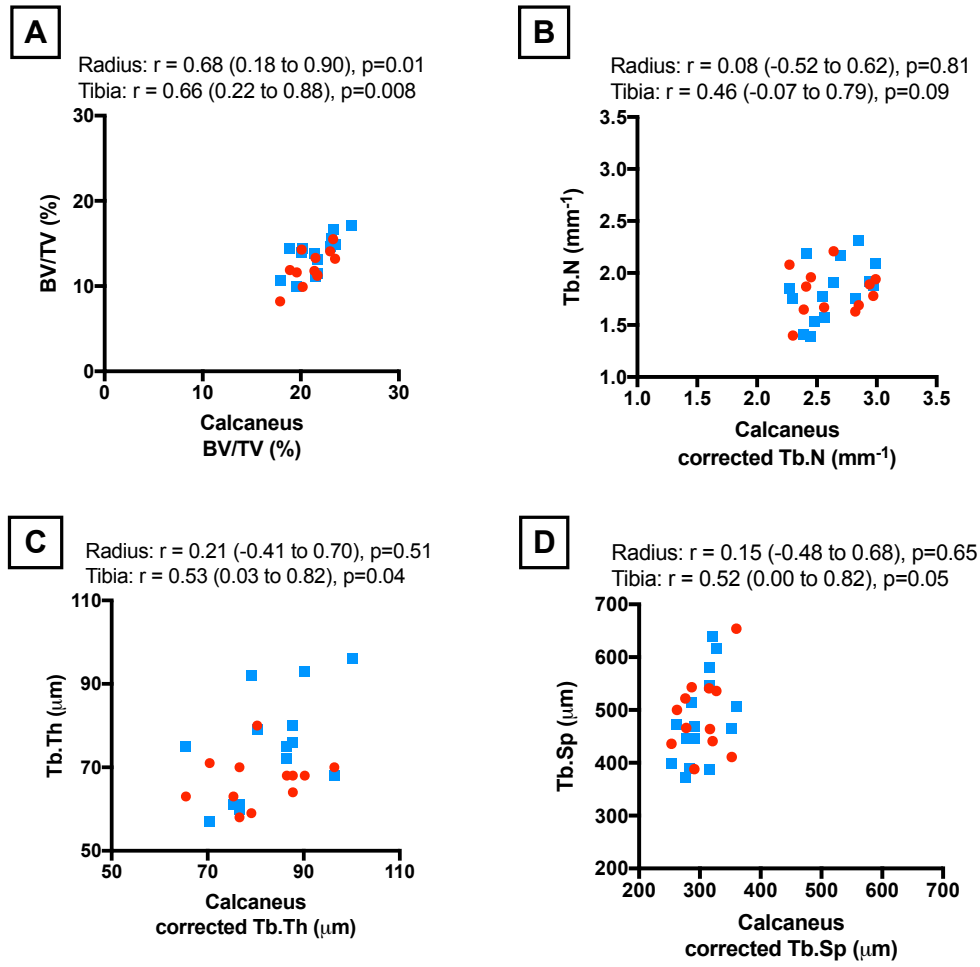

Figure 6.12. BV/TV and trabecular microstructure measurement correlation between the superior region of the calcaneus, the distal radius and distal tibia.

A – BV/TV; B – Tb.N*; C – Tb.Th^{d}; D – Tb.Sp^{d}.
Red circle – calcaneus vs. radius (n=12); Blue square – calcaneus vs. tibia (n=15).
Pearson's correlation with 95% CI – BV/TV^{d}, Tb.N*, Tb.Th^{d}; Spearman's correlation with 95% CI – Tb.Sp^{d}.

6.4.5.2 HR-pQCT vs. DXA

Figure 6.13 shows the correlation analysis between calcaneus, distal radius and distal tibia total vBMD and trabecular vBMD, and lumbar spine, total hip and femoral neck aBMD. No correlations were found between the calcaneus, tibia and radius total vBMD and trabecular vBMD, and the lumbar spine, total hip and femoral neck aBMD.

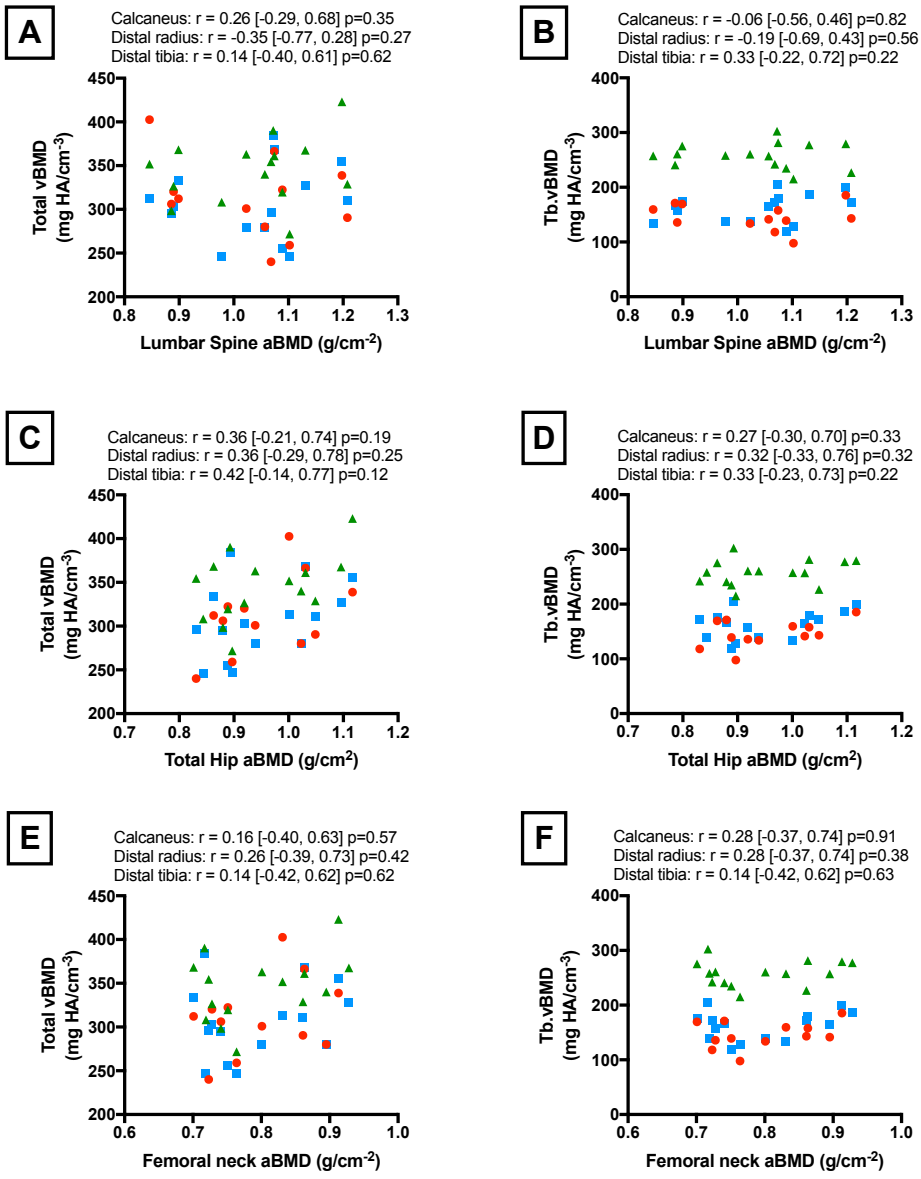

Figure 6.13. Calcaneus, distal radius and distal tibia total and trabecular volumetric BMD correlation with lumbar spine, total hip and femoral neck areal BMD.

Total vBMD vs. Lumbar spine (A), Total hip (C) and Femoral neck aBMD (E).
Trabecular vBMD (Tb.vBMD) vs. Lumbar spine (B), Total hip (D) and Femoral neck aBMD (F).
Red circles – distal radius; Blue squares – distal tibia; Green triangles – calcaneus.
Pearson's correlation with 95% CI – Lumbar spine aBMD; Spearman's correlation with 95% CI – Total hip and Femoral neck aBMD.

6.4.6 Skeletal site vs. height and weight

Table 6.5 shows the correlation analysis between the calcaneus, distal radius and distal tibia volumetric BMD, BV/TV^{d} and trabecular microstructure measurements, and participants height and weight.

The total CSA for each skeleton site was positively correlated with height. Distal radius and distal tibia total vBMD was negatively correlated with height, but the superior region calcaneus was not. However, calcaneus trabecular vBMD, outer and inner trabecular vBMD and BV/TV^{d} were negatively correlated with height, whereas the distal radius and distal tibia were not for these measurements. Distal tibia and the superior region of the calcaneus Tb.Th^{d} was negatively correlated with height, but the distal radius was not. Tb.N* and Tb.Sp^{d} were not significantly correlated with height at any of the skeletal sites.

The total CSA for each skeleton site was positively correlated with weight. In comparison to the volumetric BMD measurements, weight was only correlated with trabecular vBMD at the superior region of the calcaneus, although this had borderline significance (p=0.05). There were no correlations between the distal radius and distal tibia with weight for any of the volumetric BMD measurements. Weight was positively correlated with Tb.N* at the superior region of the calcaneus, and negatively correlated with Tb.Th^{d} and Tb.Sp^{d}. Distal tibia Tb.Th^{d} was also negatively correlated with weight, but not Tb.N* or Tb.Sp^{d}, and weight was not correlated with trabecular microstructure measurements at the distal radius.

Table 6.5. Distal radius, distal tibia and the superior region of the calcaneus volumetric BMD and trabecular microstructure measurement correlation with height and weight.

	Height			Weight		
	Radius	Tibia	Calcaneus	Radius	Tibia	Calcaneus
Total CSA	**0.70 (0.19, 0.91) p=0.01**	**0.82 (0.51, 0.94) p<0.001**	**0.80 (0.47, 0.93) p<0.001**	**0.78 (0.36, 0.94) p=0.004**	**0.91 (0.74, 0.97) p<0.001**	**0.83 (0.55, 0.94) p<0,001**
Total vBMD	**-0.71 (-0.91, -0.20) p=0.01**	**-0.68 (-0.89, -0.24) p=0.007**	-0.37 (-0.75, 0.19) p=0.18	-0.34 (-0.77, 0.31) p=0.28	-0.44 (-0.78, 0.11) p=0.10	-0.06 (-0.57, 0.48) p=0.83
Tb.vBMD	-0.42 (-0.81, 0.22) p=0.18	-0.36 (-0.74, 0.21) p=0.19	**-0.62 (-0.86, -0.14) p=0.02**	-0.22 (-0.71, 0.42) p=0.50	-0.32 (-0.73, 0.24) p=0.24	-0.51 (-0.82, 0.01) p=0.05
Outer Tb.vBMD	-0.53 (-0.85, 0.08) p=0.08	-0.24 (-0.68, 0.32) p=0.38)	-0.43 (-0.78, 0.13) p=0.12	-0.19 (-0.70, 0.45) p=0.56	-0.22 (-0.67, 0.35) p=0.43	-0.40 (-0.77, 0.15) p=0.14
Inner Tb.vBMD[#]	-0.43 (-0.81, 0.21) p=0.16	-0.31 (-0.72, 0.26) p=0.26	**-0.64 (-0.87, -0.18) p=0.01**	-0.22 (-0.72, 0.42) p=0.49	-0.24 (-0.68, 0.33) p=0.40	-0.44 (-0.78, 0.12) p=0.11
BV/TV[d]	-0.42 (-0.81, 0.22) p=0.18	-0.35 (-0.74, 0.22) p=0.20	**-0.63 (-0.87, -0.16) p=0.01**	-0.22 (-0.71, 0.42) p=0.50	-0.33 (-0.73, 0.24) p=0.23	-0.49 (-0.81, 0.04) p=0.06
Tb.N*	-0.50 (-0.84, 0.13) p=0.10	0.15 (-0.41, 0.62) p=0.60	0.38 (-0.19, 0.75) p=0.17	-0.30 (-0.75, 0.35) p=0.34)	0.24 (-0.33, 0.68) p=0.40	**0.69 (0.26, 0.89) p=0.005**
Tb.Th[d]	-0.10 (-0.65, 0.52) p=0.75	**-0.56 (-0.84, -0.06) p=0.03**	**-0.81 (-0.94, -0.49) p<0.001**	0.15 (-0.48, 0.67) p=0.65	**-0.54 (-0.83, -0.02) p=0.04**	**-0.89 (-0.96, -0.68) p<0.001**
Tb.Sp[d,#]	0.55 (-0.05, 0.86) p=0.07	-0.11 (-0.60, 0.44) p=0.69	-0.29 (-0.71, 0.28) p=0.29	0.36 (-0.29, 0.78) p=0.26	-0.17, (-0.64, 0.39) p=0.54)	**-0.62 (-0.86, -0.13) p=0.02**

All correlation data reported with 95% CI and p values (significance p<0.05, measurements in bold). [#] Spearman's correlation.
Distal radius, n=12; Distal tibia and superior region of the calcaneus, n=15.

6.5 Discussion

This Chapter described the evaluation of calcaneus HR-pQCT short-term measurement precision error *in vivo*. In comparison to the relative precision errors reported at the distal radius and distal tibia (Table 6.1), the calcaneus total vBMD and trabecular vBMD were within a similar range (0.9-1.9% vs. 0.5-2.1%) and the trabecular microstructure was towards the lower end of the range reported in the literature (1.4-1.8% vs. 1.0-7.0%). There seemed to be no additional benefit in applying 3D registration over CSA-based registration to align the HR-pQCT images. The calcaneus HR-pQCT image acquisitions seemed to be better tolerated (i.e. lower movement artefacts) by participants than the distal radius, but not the distal tibia image acquisitions. The superior region of the calcaneus also had greater trabecular vBMD and Tb.N* than the distal radius and distal tibia.

The results show that controllable sources of precision error were minimised, such as positioning and movement artefacts. The image registration procedure was important to correct for the repositioning and mid-point reference line placement error. Marginal significance and trends were identified in improving calcaneus total and trabecular vBMD measurement precision errors. This has also been demonstrated at the distal radius and distal tibia in healthy premenopausal women [176, 177]. Also, the precision error for total and trabecular vBMD and trabecular microstructure seems independent of the registration method both in the work described in the Chapter and by Ellouz et al., [177]. MacNeil and Boyd [176] did report marginal improvements with 3D registration compared to CSA-based registration, however, the registration method may have artificially manipulated measurements with transformation of the grey-scale HR-pQCT images. The small changes with correction for angular deviations between the images could be supported by the uniformity of Tb.N* (which $Tb.Th^{d}$ and $Tb.Sp^{d}$ are dependent on) at the distal radius and distal tibia [203, 230]. This uniformity could also be demonstrated in Tb.N* at the superior region of the calcaneus from the slice shifts (Figure 6.6), which also suggests that the precision for calcaneus trabecular microstructure are dependent on movement artefacts rather than repositioning error.

A clinically significant change in calcaneus total vBMD and trabecular vBMD measurements could be reported with a change greater than 3.8% (13.5 mg HA/cm^{-3}) and 2.4-5.3% (6.7-13.2 mg HA/cm^{-3}), respectively. These relative and absolute results are similar to other studies, if the 95% LSC criterion was applied (Table 6.1).

A clinically significant change in Tb.N*, Tb.Th^{d} and Tb.Sp^{d} could be reported with a change greater than 4.4% (0.14 mm^{-1}), 3.9% (3 µm) and 5.0% (10 µm), respectively, which would be lower than those reported from previous studies with the 95% criterion applied (precision error multiplied by 2.77) (Table 6.1). The SD_{RMS} LSC reported by Ellouz et al., [177] was similar to the current study for Tb.N* (0.14-0.22 mm^{-1}) and also trabecular vBMD (5-10 mg HA/cm^{-3}), which are used to calculated Tb.Th^{d} and Tb.Sp^{d}. Furthermore, the precision for plate-like Tb.N* has been reported to be lower than rod-like Tb.N* (0.9-2.3% vs. 3.5-3.6%, respectively) [241] and is lower for cortical vBMD and cortical thickness at more proximal regions of the distal radius and tibia, which are denser and thicker [155]. Therefore, the lower relative precision errors and LSCs for calcaneus trabecular microstructure measurements could be attributed to higher Tb.vBMD and Tb.N* found at the superior region of the calcaneus.

The preliminary comparison of the HR-pQCT images revealed no effect of dominance on the superior region of the calcaneus. Therefore, in agreement with Hildebrandt et al., [249], the non-dominant side should be imaged for the calcaneus HR-pQCT scans, and if contraindicated the dominant side can be used. Determining whether these findings are found with different ages and physical functions, and also in males, is outside of the scope of this work and would require testing in a larger sample size.

Even with the small sample size, large inter-site differences were found between the superior region of the calcaneus and the distal radius and distal tibia. Calcaneal trabecular vBMD, including the outer and inner regions, was 1.4-2.3 fold higher than the distal radius and 1.3-1.9 fold higher than the distal tibia. This was reflected by higher Tb.N* and lower Tb.Sp^{d}, as well as a greater adjusted Tb.Th^{d} compared to the distal tibia. The higher connectivity density and lower Tb.Sp found between calcaneus and distal radius trabecular specimens using micro-CT [228] supports the current HR-pQCT findings. However, making further inferences is difficult due to the lack of correlation between these peripheral sites vBMD and microstructure.

The positive effect of mechanical loading and weight has been well established in relation to calcaneus QUS measurements and BMD [122, 123, 125, 127, 134, 138], as well as BMD, microstructure and geometry at central and other peripheral sites of the skeleton [21, 133, 134, 257, 258]. The Chapter's preliminary findings may indicate a greater weight-bearing influence at the superior region of the calcaneus compared to the distal tibia, as shown by correlations with Tb.N*. The differences between the sites could be explained by the proximity of the respective regions of

interest to the articular surfaces, where compressive strains are higher. The superior region of the calcaneus includes bone that is in contact with the subtalar articular surface, whereas the distal tibia region of interest is located 22.5 mm proximal to the distal articular plateau, and has a larger cortical envelope. Movement of the region of interest towards the distal end of the tibia shows an increase in trabecular vBMD (i.e. increase in total vBMD and decrease in cortical BMC and thickness) [252]. The distal tibia region, as indicated by standard HR-pQCT measurement, shares compression, bending and torsional strains, which have been attributed to the higher cortical vBMD and thicker cortex [252, 259]. Interestingly, trabecular vBMD and Tb.N* at the subchondral proximal tibia and distal femur, which have high compressive mechanical loads with habitual locomotion, are comparable to the superior region of the calcaneus [93]. This preliminary data may suggest that the biological changes at the superior region of the calcaneus could be tapered by its weight bearing properties compared to the distal tibia. The data may also support a use in quantifying the superior region of the calcaneus in mechanical loading investigations.

The correlation between height and some of the HR-pQCT measurements at the skeletal sites align with 'errors' caused by using fixed offsets for obtaining HR-pQCT scans [230, 236]. For the distal radius and distal tibia, the negative correlation between height and the total vBMD can be caused by imaging different sites of the long bone between people with different heights. In shorter people, who likely have shorter radii and tibia lengths, the region of interest would be more proximal compared to taller people due to the fixed offset that is applied from the anatomical landmarks at these sites [236]. Subsequently, shorter people would have a region imaged that has a thicker cortex with a greater cortical vBMD, which would have significant effect on total vBMD [203, 230]. The results in this Chapter would suggest a similar finding at the calcaneus. For example, shorter participants may have a smaller distance between the two fixed anatomical landmarks for the mid-point reference line placement. Applying a fixed offset would then place the superior region of interest more 'superior' compared to taller participants, which may explain why trabecular vBMD increased as height decreased. This does highlight a limitation in applying the current positioning protocol in cross-sectional studies; but this could be overcome by using a relative offset for the scan position and a relative scan area [230].

The site comparison analyses identified moderate to strong correlations for total and trabecular vBMD between the superior region of the calcaneus and distal tibia. Most

of the correlations between the calcaneus and the distal radius were weaker and insignificant, apart from trabecular vBMD. The small sample size in this Chapter limited the power to detect significant correlations between peripheral sites using HR-pQCT and central sites using DXA, whereas other studies have presented significant correlations [253-256]. However, the important comparison to make would be to fracture risk; total, trabecular and cortical vBMD, cortical area and thickness, trabecular number, and estimated bone stiffness and failure load at the distal radius and tibia can predict major osteoporotic fractures in addition to DXA and FRAX [80-82, 221]. Calcaneus QUS measurements and BMD can predict fracture risk [111, 140, 142], but do not seem to provide additional information to DXA measurements at the lumbar spine and hip [141]. It remains to be seen whether additional predictive measurements can be obtained using calcaneus HR-pQCT measurements, particularly in comparison to those identified at the distal radius and distal tibia.

There were limitations to this study that may have implications for the calcaneus precision error measurements and also the site comparison analyses.

The calcaneus HR-pQCT measurements precision error may not be applicable to participants with osteoporosis. Participants with osteoporosis can have more challenging HR-pQCT images to contour and segment [151, 240], which could be anticipated due to the thin and apparent low mineralisation at the calcaneal cortices.

The study was unable to control for all factors in measurement precision error. There were no large deviations in the calibration phantom densities during the measurement period (Figure 2.8). The study applied image registration to the calcaneus HR-pQCT images to correct for repositioning; however this may not eliminate all repositioning errors, as shown with and without repositioning in human cadaveric specimen [176]. Movement artefacts have also been well established due to the scan duration [94, 95, 260] and there is no method to correct for movement artefacts in images.

Movement artefacts were particularly problematic in the distal radius HR-pQCT images compared to the calcaneus and distal tibia. This followed a consistent trend reported in other studies between the distal radius and distal tibia [94, 95, 151, 155]. Here, distal radius HR-pQCT images could not be obtained from all participants; therefore these participants were excluded from the repeated measures analysis. Nonetheless, inclusion of the 15 participants in calcaneus and distal tibia comparisons revealed similar results to those found with 12 participants. The image

quality grades also revealed that the foot position for calcaneus HR-pQCT scans leads to movement artefacts, as this was the only positional difference to the distal tibia scans, which had excellent image quality grades. Therefore, it could be thought that there is scope to minimise movement artefacts and lower precision error in the calcaneus HR-pQCT scans.

A 100 ms integration time was selected for quantification of the precision error for calcaneus HR-pQCT measurements. The estimation of trabecular microstructure measurements at this integration time could be affected by greater image noise (Chapter 4), which may have contributed to the higher Tb.N* and lower trabecular microstructure precision error. The reasons for not choosing the 200 ms integration time for the precision error quantification were: (1) the loss of degrees of freedom for precision error estimation due to the increased likelihood of movement artefact at a 200 ms integration time with the current imaging apparatus (shown in Chapter 5); (2) that the volumetric BMD measurements were not affected by integration time (Chapter 4 and 5); (3) and that there were reasonable correlations for the trabecular microstructure at the superior region of the calcaneus between the 100 ms and 200 ms integration time scans *in vivo* (Chapter 5).

A final limitation was identifying the calcaneus mid-point. The precision error was 1.26 mm (equivalent to 15 HR-pQCT slices) and was poorer than Chapter 5 (0.69 mm). The CV% for the mid-point identification was high in some participants, and may have been influenced by movement of the foot between the scout view acquisitions. As indicated in Chapter 5, the landmark identification and scaling of the scout view may exacerbate this error in comparison to measurements at the distal radius and distal tibia [154]. Whilst this error could be corrected for with image registration in longitudinal studies, the positional error reported in the mid-point identification (e.g. 15 HR-pQCT slices) may have a large impact in cross-sectional studies e.g. ±3% change in total vBMD and a ±4% change in trabecular vBMD (Figure 6.6). The procedure of reference line placement for the calcaneus HR-pQCT scans requires improvement for future studies.

6.6 Conclusion

The Chapter reports the calcaneus vBMD and trabecular microstructure short-term measurement precision error *in vivo* using the first generation XtremeCT. The precision error was comparable to that reported at the distal radius and distal tibia in previous studies, which lends support to the application of the method *in vivo*. The

superior region of the calcaneus has markedly different trabecular vBMD and microstructure compared to the distal radius and distal tibia, and also appears to be a more prominent weight-bearing region compared to the distal tibia.

CHAPTER 7 DISCUSSION

7.1 Main findings

The aim of this thesis was to develop a method to quantify calcaneus vBMD and microstructure using HR-pQCT, which could be applied *in vivo* to monitor disease progression and the response to interventions for osteoporosis management. To achieve this, Chapter 2 to 6 described chronological research aims and objectives specific to developing the method, and determining measurement accuracy and reproducibility.

Chapter 2 described the scanning methods used in the thesis. 3D image registration procedures were presented to (1) spatially align HR-pQCT and micro-CT images and (2) determine a common volume mask between repeat HR-pQCT images, without manipulating image greyscale values i.e. vBMD and microstructure measurements.

Chapter 3 proposed a foot position that aligned the superior and inferior surfaces of the calcaneus parallel to the scout view using human cadaveric feet. This position aimed to keep the surrounding tissues of the foot within the field of view. Local trabecular heterogeneity (vBMD and $Tb.Th^{d}$) was identified along the superior-inferior axis of the bone, and appreciable positional errors were induced by small shifts in the region of interest (±1.64 mm).

Chapter 4 reported that measurements' accuracy from calcaneus HR-pQCT images were comparable to previous validation studies performed at the distal radius and distal tibia. BV/TV^{d} was strongly predicted and was independent of integration time and the region of interest. A 200 ms integration time seemed preferable for the quantification of calcaneus trabecular microstructure (Tb.N* and $Tb.Sp^{d}$) *in situ*, which was best predicted at the superior region of the bone.

Chapter 5 found the calcaneus HR-pQCT scans were well tolerated by participants. Increasing the integration from 100 ms to 200 ms led to a reduction in calcaneus Tb.N*, which exceeded differences that have been associated with fracture risk at the distal radius and distal tibia in previous studies. The superior region of the calcaneus was measurable in all participants; however acquisition of the inferior region was impaired by the participants foot size and the dimension of the XtremeCT field of view.

Chapter 6 found that calcaneus vBMD and trabecular microstructure could be measured with good precision in healthy premenopausal women. The precision

errors were similar between the CSA-based and 3D registration, and therefore either could be used to remove misalignment and find the common volume between repeat calcaneus HR-pQCT images. There were no dominance asymmetries in the calcaneus HR-pQCT measurements. The superior region of the calcaneus also had higher trabecular vBMD and Tb.N* compared to the standard distal tibia measurement region, and these measurements were moderate-strongly correlated with body weight.

7.2 Original contributions and discussion

My original contribution to the research area is a protocol to scan the calcaneus using HR-pQCT *in vivo*. Within the protocol there were several unique contributions that should be considered when utilising the method in studies and in continuing the method development.

7.2.1 Foot positioning within the lower limb cast.

Plantar-flexion at the ankle joint was the only positional change in comparison to the distal tibia HR-pQCT scans. This position was important to prevent surrounding tissues of the foot from crossing the field of view and avoid incomplete projections in the HR-pQCT images, potentially lead to an underestimation of vBMD measurements. This is a specific limitation to the dimensions of the XtremeCT field of view, but not using standard QCT and some pQCT devices. From scanning a small number of men and women (Chapter 5), the correct foot positioning (i.e. surrounding tissues within the field of view) was achieved when imaging the superior region of the calcaneus. However, this was not achieved when imaging the inferior region of the bone. Furthermore, the middle region (between the superior and inferior region, Chapters 3 and 4) in some participants may have also had surrounding tissues crossing the field of view from assessment of the HR-pQCT scout views.

The physical size of the participant's foot was an issue, but also utilising the lower limb cast (provided by the manufacturer for distal tibia HR-pQCT scans) restricted the correct positioning of the foot. The foot positioning and imaging apparatus may have also contributed to the greater presence of movement artefact at the calcaneus compared to in the tibia HR-pQCT images. There was difficulty in standardising the degree of plantar flexion, which affected the common volume between repositioned calcaneus HR-pQCT images. Therefore, even though the

immobilisation of the foot was effective for the calcaneus HR-pQCT scans, positional aids and immobilisation procedures could be developed and implemented to improve the quality of the acquired images.

7.2.2 Calcaneus microstructure accuracy is dependent on the region measured.

The accuracy of the calcaneus BV/TV^{d} and trabecular microstructure (Tb.N* and Tb.Sp^{d}) measured by the first generation XtremeCT was dependent on the region evaluated. The region with the strongest correlation and best accuracy for trabecular microstructure was the superior region when compared to micro-CT measurements. The correlation became weaker and less accurate as the quantities of soft tissue increased (inferior > middle > superior) and as the BV/TV got lower and the trabeculae got thinner (micro-CT Tb.Th: inferior < middle < superior). Dissection of the calcaneus from the foot improved the trabecular microstructure correlation and accuracy, supporting the impact that the surrounding tissues have on the measurements. This was particularly apparent at the inferior region, where there was no correlation for Tb.N* and Tb.Sp^{d} *in situ* and a significant, but weak, correlation following the dissection. Similar improvements in Tb.N* and Tb.Sp^{d} correlation and accuracy were also found between the superior and middle regions following dissection, suggesting that these regional differences were mainly dependent on calcaneal vBMD. The calcaneus CSA between the regions could also influence measurement accuracy (calcaneus CSA: superior < middle < inferior). This may also be apparent between the distal radius and distal tibia, with a greater overestimation of Tb.N* and a greater underestimation of Tb.Sp at the distal tibia [30]. The greater bone CSA may increase x-ray scatter and image noise [156], which may include noise as bone voxels with HR-pQCT image processing [172]. Therefore, even if foot positioning was improved for calcaneus HR-pQCT scans, the estimation of trabecular microstructure measurements may still be better at the superior region due to smaller CSA, combined with the higher vBMD.

BV/TV^{d} at the middle and inferior region could be utilised in studies if the foot positioning is improved, especially when considering that there were the strong correlations between HR-pQCT and micro-CT BV/TV. The middle region may, in fact, have the greatest clinical relevance, as it could be compared to existing data from a similar region of interest using BMD and BUA to determine fracture risk [111, 140, 142] and monitor treatment response [145-147].

7.2.3 Adaptation of the HR-pQCT scan integration time.

Increasing scan integration time from 100 ms significantly improved the correlation and accuracy of the calcaneus trabecular microstructure HR-pQCT measurements (Tb.N* and $Tb.Sp^d$) compared to micro-CT. This work also appears to be the first to demonstrate the affect of integration time on HR-pQCT measurements *in vivo*. Increasing the integration time from 100 ms seemed to remove voxels that are noise from the images and increase the distance between the trabeculae ridges for measurement using the distance transformation method [165, 166]. Subsequently a 200 ms integration time led to a significant decrease in Tb.N* and an increase in $Tb.Th^d$ and $Tb.Sp^d$, with vBMD measurements unperturbed, which supported findings from cadaveric experiments even though there were movement artefacts in the images. This presents a potential option to improve image quality and microstructure accuracy within first generation XtremeCT images.

An increase in the integration time (50 to 100 ms) has been proposed as a necessary adaptation in imaging the knee using HR-pQCT due to the size of the joint [93]. Increasing the integration time would be most useful for the accuracy of measurements that that rely on distance-related calculations (e.g. Tb.N* (Chapter 4), cortical thickness and cortical porosity [162]), and not attenuation-related measurements (e.g. vBMD and BV/TV^d). Potentially adapting the integration time may be useful in imaging sites with greater surrounding tissues or material, such as proximal sites of the extremities or where a cast surrounds a site for immobilisation following a fracture [261]. A limitation from this adaptation is that there would be an increased likelihood of movement artefacts, which distance-related measurement precision is highly sensitive to [94, 95]. Added clinical value may need to be demonstrated before adapting HR-pQCT scan integration time.

7.2.4 Precise calcaneus HR-pQCT measurements can be obtained *in vivo*.

The current development of the procedure to quantify calcaneus HR-pQCT images demonstrates that the short-term precision error was robust for total and trabecular vBMD, and trabecular microstructure. This reflects a reduction in movement artefacts through immobilising the lower limb and of positional errors using an image registration workflow. The resulting measurement precision was comparable to those reported at the distal radius and distal tibia in previous work [79, 151, 155, 177, 195, 240, 241].

The calcaneus HR-pQCT measurements relative precision errors ($CV\%_{RMS}$) were lower than those reported using QUS *in vivo* (2-7% [113]). Therefore, with lower

LSCs and the capacity to complete volumetric and compartmental measurements, HR-pQCT would appear to be more capable in monitoring the intrinsic characteristics of the calcaneus over time compared to QUS. Nonetheless, these devices have different applications within osteoporosis, with QUS as a screening tool [113] and HR-pQCT as a research tool, but with potent clinical promise [234]. Determining whether clinically significant differences can be identified using the calcaneus HR-pQCT LSC would be an important next step, particularly regarding the trabecular microstructure, which appeared more precise than that found at the distal radius and distal tibia. This may make the superior region of the calcaneus an attractive candidate in clinical studies, particularly if investigating exercise studies or the interaction between load-bearing and other treatments.

7.2.5 Calcaneus HR-pQCT image acquisition and processing differences compared to radius and tibia.

Several adaptations to the procedure to image the calcaneus using HR-pQCT have been presented that are different to the measurement of the radius and tibia.

The potential requirement for an increase in scan integration time has been discussed (Section 7.2.3). The calcaneus HR-pQCT scout view dimensions need to be maximised (0-150 mm) to ensure that the calcaneus is properly aligned. This removes anatomical detail compared to the radius and tibia scans, which have narrower scout view dimensions (90-120 mm and 73-103 mm, respectively). There is also difficulty in selecting a single, well-defined landmark to standardised calcaneus reference line positioning, due to the close proximity of the articular surfaces with surrounding bones of the foot. In contrast with the radius and tibia, two anatomical landmarks are selected to identify the mid-point, from which the reference point is determined to begin the calcaneus HR-pQCT image acquisition. The selection of the two landmarks is, however, essential to account for the difference in heel size between participants. This could be important to accommodate relative standardisation of this reference point, in alignment with recent recommendations for radius and tibia HR-pQCT scans [236].

The need for plantar-flexion at the ankle joint led to high variability in the calcaneus common volume between repeat HR-pQCT image acquisitions. The common volume (mean 76%, cropped method (Section 6.4.2.3)) was notably lower than that reported at the radius and tibia (88 and 82%, respectively) using similar methods [177]. Calcaneus total CSA (superior-inferior region) is significantly larger than the distal radius and distal tibia, particularly along the anterior-posterior axis of the bone.

Therefore, a small angular deviation in plantar-flexion at the ankle would be magnified in the calcaneus images, when compared to the same angular deviation at the radius and tibia. The magnified angular deviations would lead to a higher number of slices where the HR-pQCT image mask does not cover the whole calcaneus CSA (Figure 2.21); these slices were subsequently removed prior to image evaluation. Adjusting the manufacturer's common volume cut off threshold (set at 70% and independent from bone size) may be required for the calcaneus HR-pQCT scans to account for these anatomical differences. Otherwise, a high proportion of participants' calcaneus HR-pQCT images could be removed in longitudinal studies.

The processing of the calcaneus HR-pQCT images is more complex. Completing the semi-automated contouring around the periosteal surface took upto 120 minutes in some participant's images, whereas the same procedure in the radius and tibia took approximately 60-75 minutes. Calcaneus cortical segmentation would also be more time expensive to correct for errors in detecting the endocortical boundary, which has been reported to take upto 5 hours per distal radius and distal tibia scan [262], and is consistent with durations reported in our Research Group.

7.3 Limitations

Limitations of the various parts of the work have been described in the relevant Chapters. The following section summarises these limitations.

The first generation XtremeCT device has several physical limitations. The device uses plate model-assumptions to compute trabecular microstructure as the spatial resolution (120-150 μm) is within the range of the physical dimensions of individual trabeculae (50-200 μm) and is the reason for the poor $Tb.Th^{d}$ accuracy [159, 163, 164]. It also has a narrow gantry and field of view, which restricts the accessibility of the device for imaging the calcaneus. Some of these limitations could be overcome using the second generation XtremeCT, which has a slightly larger field of view (+14 mm diameter) and has a superior spatial resolution (95 μm vs. 127-154 μm) that includes more model-independent measurements [97]. Whilst it may improve Tb.Th estimation, most differences between the two XtremeCT devices may be removed using regression equations ($r^2 \geq 0.94$) [190].

The present work only piloted the calcaneus HR-pQCT method in one position *in vivo*; the participant sat upright in a chair with their lower limb fixed in a cast (similar to the tibia HR-pQCT scans). Although this was suited to the equipment that was

available, participants are typically supine for calcaneus measurement using standard QCT and MRI, which may improve body stability and lower the likelihood of movement artefact. Other body positions could also be considered, such as lying on their side and imaging the sagittal plane of the calcaneus (as completed using histomorphometry in cadaveric specimens [197]), and lying prone to image perpendicularly to the superior and inferior surfaces of the main tuberosity body. These different positions may require customised imaging apparatus and potentially be restricted by the dimensions of the XtremeCT gantry.

The work assumed that the HR-pQCT image filtering, segmentation and reconstruction within the standard patient evaluation were applicable to the calcaneus HR-pQCT images. This was selected to maintain consistency with the large body of clinical research at the distal radius and distal tibia, as well as metacarpals, using the first generation XtremeCT. These assumptions may have limitations, such as with changing bone mineralisation [172] and x-ray artefacts (beam hardening and scatter) with a different bone size [156]

In the method development using human cadaveric feet, there was limited availability of specimens and no control over their condition and age. BV/TV^{d} of the specimens was within the range found in the *in vivo* studies (~24% in specimen vs. ~26% *in vivo*), although there were a small number of cadaveric samples towards the maximum value reported *in vivo* (Figure 9.4).

Small sample sizes were used with the developmental nature of the *in vivo* work. These studies may have not been sufficiently powered for the secondary analyses reported. For example, in Chapter 5 the sample size (n=9) may have been too small to gain a reliable adjustment of the trabecular microstructure measurements at a 200ms integration time using 100ms integration time HR-pQCT images, where 30 participants has been recommended for measurement cross-calibrations by the ISCD [263]. In Chapter 6, 15 participants may have been too small to investigate site comparison and correlation analyses. Furthermore, the comparison of the dominant and non-dominant calcaneus was done in 15 healthy premenopausal women, and therefore the findings may not be representative of males and in younger and older individuals.

Identifying the calcaneus mid-point on the scout view was a practical issue, which affected the common volume between repositioned HR-pQCT images. This would also have implications in cross-sectional studies, in which differences or the absence of differences could be due to region of interest placement rather than

bone biology [230]. The mid-point positional error (Chapter 5 and 6) may have also been overestimated with participant movement between the 2 scout views. Re-evaluation using the recently developed HR-pQCT training software [154] may provide a more valid positional error estimate. Improving the contrast between the bone and background may benefit landmark identification, which could be achieved by increasing the scout view x-ray intensity.

The precision errors that have been reported were quantified in healthy, female participants. This may not be representative of males. Furthermore, this may not be representative of older individuals and those that have suffered from osteopenia, which may increase the relative precision error measurements [151].

7.4 Ongoing and future work

Areas of ongoing and future work for the calcaneus HR-pQCT scans include: improving positioning aids, anatomical standardisation between participants, pursuing image-processing methods to quantify the trabecular and cortical bone compartments, the application and development of FE models, and completing population comparison and monitoring studies.

Future work should aim to customise the lower limb positioning aid. This may improve foot alignment in relation to the field of view, standardise foot positioning between repositioned images, and minimise foot and toe movement. Four key features are proposed to achieve this: (1) the sole of the foot is in contact with a platform made from a solid, non-attenuating material, such as the carbon fibre that the lower limb cast is made from. (2) The platform should adjustable to support different degrees of plantar-flexion at the ankle joint, to simplify and standardised foot position within and between participants. (3) An inflatable device, similar to the one used for metacarpal imaging [90], should be positioned to immobilise the mid-foot and toes, acting like a slipper that the foot fits within. (4) The lower limb cast diameter should be widened from the heel insert to the shank, to support positioning in participants with a larger foot size. If the customisation of the positioning aid is successful, longer scan duration could be used and other calcaneal regions could be imaged. Importantly, there may be less restriction of the foot size that can be used for the calcaneus HR-pQCT image acquisition.

Future work should also optimise a procedure to complete anatomical standardisation for the calcaneus HR-pQCT scans. This would remove height dimorphisms between participants, which were potentially identified in Chapter 6. In

accordance with the work by Bonaretti et al. [236], a relative scan position could be defined based on the distance between the plantar-fascia attachment and the superior peak of the tuberosity, or even the participant's height [230]. The scan length can then be collected with an equal number of slices either side of this relative scan position i.e. ±55 slices. Following image acquisition, a relative number of slices would be evaluated. These steps could make the calcaneus HR-pQCT scans more applicable in cross-sectional studies.

With development of the procedure for calcaneus HR-pQCT image acquisition, more advanced image processing could be pursued. Improvements could be made in detecting the calcaneal endocortical boundary by lowering the minimum cortical thickness mask and lowering the threshold used for segmentation; which has only recently been applied to metacarpal joints [264]. Optimising the segmentation of the calcaneal cortex may improve the specificity in identifying local adaptations to extrinsic and environmental stimulus, particularly as adaptations with anti-resorptive and anabolic treatments at the extremities have been mainly located in the cortical envelope [84-86]. Future work could immediately assess the validity and reproducibility of calcaneus trabecular plates, rods and connectivity [265, 266] and fabric anisotropy [199, 219, 267]. The regional assessment of the calcaneus CSA might also be of interest, such as isolating areas of high mechanical loading at the subtalar articular surface and the Achilles tendon attachment. This would require the development of novel image processing scripts that are external to the Scanco IPL, as shown by Sode and colleagues [268].

An ongoing parallel project is investigating FE models of calcaneus trabecular bone using HR-pQCT and micro-CT images. With the available images, the effect of HR-pQCT integration time on mechanical properties can be determined. These developments, combined with improve trabecular and cortical quantification, would improve the geometric and microstructural specificity that is needed for whole tissue level FE models of the calcaneus [269, 270]

Pilot studies are being undertaken to better understand the clinical applicability of the calcaneus HR-pQCT images. Images are being collected from postmenopausal women with T-score ≤ −1.0 (n=25) with the methods reported in Chapter 6. This aims to investigate measurement precision error in participants at higher risk of fracture and provide additional data for the site comparison analyses. This may help to determine whether the superior region of the calcaneus offers similar or additional fracture risk insight compared to the distal tibia, or whether the potential higher weight bearing characteristics blunts trabecular adaptation to biological changes.

Data related to musculoskeletal health are also being collected in these postmenopausal women (as part of a separate study). Calcaneus HR-pQCT measurements could be associated with bone turnover markers, proximal femur QCT and FE measurements, and with physical function and real-time activity monitoring data in these participants, albeit only providing a snapshot in a small sample size. Calcaneus HR-pQCT images are also currently being collected from postmenopausal women prescribed teriparatide through routine clinical care. However, recruitment has been challenging due to the nature of the population and contraindications for study inclusion. Nonetheless, calcaneus BMD and microstructure have not been evaluated in response to anabolic treatments previously. With development, the method may assist in determining whether there is a mechano-interaction with anabolic treatments at peripheral sites of the skeleton, and how the response compares to the distal radius and distal tibia.

7.5 Conclusion

Calcaneus vBMD and trabecular microstructure can be quantified using HR-pQCT *in vivo*. Measurements at the superior region of the calcaneus were accurate and precise, and the region could be imaged within the physical constraints of the HR-pQCT device. Increasing the scan integration time appeared to be an important adaptation to the scan settings for the quantification of calcaneus trabecular microstructure. There was notable heterogeneity in trabecular vBMD and microstructure between different calcaneal regions, with appreciable differences with small positional errors. Continued development in the positioning apparatus, positioning of a relative region of interest and image-processing procedures, would benefit the future application of this method.

CHAPTER 8 REFERENCES

[1] Rho J-Y, Kuhn-Spearing L, Zioupos P. Mechanical properties and the hierarchical structure of bone. Med Eng Phys 1998;20: 92-102.

[2] Pahr DH, Zysset PK. Finite Element-Based Mechanical Assessment of Bone Quality on the Basis of In Vivo Images. Curr Osteoporos Rep 2016;14: 374-385.

[3] Duren DL, Seselj M, Froehle AW, Nahhas RW, Sherwood RJ. Skeletal growth and the changing genetic landscape during childhood and adulthood. Am J Phys Anthropol 2013;150: 48-57.

[4] Gabel L, Macdonald HM, Nettlefold L, McKay HA. Physical activity, sedentary time, and bone strength from childhood to early adulthood: A mixed longitudinal HR-pQCT study. J Bone Miner Res 2017;32: 1525-1536.

[5] Kirmani S, Christen D, van Lenthe GH, Fischer PR, Bouxsein ML, McCready LK, Melton III LJ, Riggs BL, Amin S, Muller R, Khosla S. Bone structure at the distal radius during adolescent growth. J Bone Miner Res 2009;24: 1033-1042.

[6] Henry YM, Fatayerji D, Eastell R. Attainment of peak bone mass at the lumbar spine, femoral neck and radius in men and women: relative contributions of bone size and volumetric bone mineral density. Osteoporos Int 2004;15: 263-273.

[7] Heaney RP, Abrams S, Dawson-Hughes B, Looker A, Marcus R, Matkovic V, Weaver C. Peak bone mass. Osteoporos Int 2000;11: 985-1009.

[8] Walsh JS, Henry YM, Fatayerji D, Eastell R. Lumbar spine peak bone mass and bone turnover in men and women: a longitudinal study. Osteoporos Int 2009;20: 355-362.

[9] Burt LA, Hanley DA, Boyd SK. Cross-sectional versus longitudinal change in a prospective HR-pQCT study. J Bone Miner Res 2017;32: 1505-1513.

[10] Gabel L, Macdonald HM, McKay HA. Sex Differences and Growth-Related Adaptations in Bone Microarchitecture, Geometry, Density, and Strength From Childhood to Early Adulthood: A Mixed Longitudinal HR-pQCT Study. J Bone Miner Res 2017;32: 250-263.

[11] Walsh JS, Henry YM, Fatayerji D, Eastell R. Hormonal determinants of bone turnover before and after attainment of peak bone mass. Clin Endocrinol 2010;72: 320-327.

[12] Sims NA, Martin TJ. Coupling Signals between the Osteoclast and Osteoblast: How are Messages Transmitted between These Temporary Visitors to the Bone Surface? Front Endocrinol (Lausanne) 2015;6: 41.

[13] Szulc P, Naylor K, Hoyle NR, Eastell R, Leary ET. Use of CTX-I and PINP as bone turnover markers: National Bone Health Alliance recommendations to standardize sample handling and patient preparation to reduce pre-analytical variability. Osteoporos Int 2017;28: 2541-2556.

[14] Morris HA, Eastell R, Jorgensen NR, Cavalier E, Vasikaran S, Chubb SAP, Kanis JA, Cooper C, Makris K. Clinical usefulness of bone turnover marker concentrations in osteoporosis. Clin Chim Acta 2017;467: 34-41.

[15] Eastell R, Szulc P. Use of bone turnover markers in postmenopausal osteoporosis. Lancet Diabetes Endocrinol 2017;S2213-8587: 1-16.

[16] von Meyer GH. The classic: The architecture of the trabecular bone (tenth contribution on the mechanics of the human skeletal framework). Clin Orthop Relat Res 2011;469: 3079-3084.

[17] Wolff J. Ueber die Bedeutung der Architectur der Spongiösen Sunstanz für de Frage Vom Knochenwachsthu. Vorläufge Mettheilung. Centralblatt für die meichinschen Wissenschaften 1869;54: 849-851.

[18] Frost HM. Bone "mass" and the "mechanostat": a proposal. Anat Rec 1987;219: 1-9.

[19] Cardoso L, Herman BC, Verborgt O, Laudier D, Majeska RJ, Schaffler MB. Osteocyte apoptosis controls activation of intracortical resorption in response to bone fatigue. J Bone Miner Res 2009;24: 597-605.

[20] Seref-Ferlengez Z, Basta-Pljakic J, Kennedy OD, Philemon CJ, Schaffler MB. Structural and mechanical repair of diffuse damage in cortical bone in vivo. J Bone Miner Res 2014;29: 2537-2544.

[21] Evans AL, Paggiosi MA, Eastell R, Walsh JS. Bone density, microstructure and strength in obese and normal weight men and women in younger and older adulthood. J Bone Miner Res 2015;30: 920-928.

[22] Sornay-Rendu E, Boutroy S, Vilayphiou N, Claustrat B, Chapurlat RD. In obese postmenopausal women, bone microarchitecture and strength are not commensurate to greater body weight: The Os des Femmes de Lyon (OFELY) Study. J Bone Miner Res 2013;28: 1679-1687.
[23] Morin S, Leslie WD. High bone mineral density is associated with high body mass index. Osteoporos Int 2009;20: 1267-1271.
[24] Kazakia GJ, Tjong W, Nirody JA, Burghardt AJ, Carballido-Gamio J, Patsch JM, Link T, Feeley BT, Ma CB. The influence of disuse on bone microstructure and mechanics assessed by HR-pQCT. Bone 2014;63: 132-40.
[25] Vico L, Van Rietbergen B, Vilayphiou N, Linossier MT, Locrelle H, Normand M, Zouch M, Gerbaix M, Bonnet N, Novikov V, Thom CT, Vassilieva G. Cortical and trabecular bone microstructure did not recover at weight-bearing skeletal sites and progressively deteriorated at non-weight-bearing sites during the year following International Space Station missions. J Bone Miner Res 2017;32: 2010-2021.
[26] Haapasalo H, Kontulainen S, Sievänen H, Kannus P, Järvinen M, Vuori I. Exercise-induced bone gain is due to enlargement in bone size without a change in volumetric bone density: A peripheral quantitative computed tomography study of the upper arms of male tennis players. Bone 2000;27: 351-357.
[27] Kontulainen S, Sievänen H, Kannus P, Pasanen M, Vuori I. Effect of long-term impact-loading on mass, size, and estimated strength of humerus and radius of female racquet-sports players: a peripheral quantitative computed tomography study between young and old starters and controls. J Bone Miner Res 2002;17: 2281-2289.
[28] Ireland A, Maden-Wilkinson T, Ganse B, Degens H, Rittweger J. Effects of age and starting age upon side asymmetry in the arms of veteran tennis players: a cross-sectional study. Osteoporos Int 2014;25: 1389-1400.
[29] Skerry TM. One mechanostat or many? Modifications of the site-specific response of bone to mechanical loading by nature and nurture. J Musculoskelet Neuronal Interact 2006;6: 122-127.
[30] Zhou B, Wang J, Yu YE, Zhang Z, Nawathe S, Nishiyama KK, Rosete FR, Keaveny TM, Shane E, Guo XE. High-resolution peripheral quantitative computed tomography (HR-pQCT) can assess microstructural and biomechanical properties of both human distal radius and tibia: ex vivo computational and experimental validations. Bone 2016;86: 58-67.
[31] Kroker A, Plett R, Nishiyama KK, McErlain DD, Sandino C, Boyd SK. Distal skeletal tibia assessed by HR-pQCT is highly correlated with femoral and lumbar vertebra failure loads. J Biomech 2017;5: 43-49.
[32] Zioupos P. Accumulation of in-vivo fatigue microdamage and its relation to biomechanical properties in ageing human cortical bone. J Microsc 2001;201: 270-278.
[33] Wolfram U, Schwiedrzik JJ, Mirzaali MJ, Burki A, Varga P, Olivier C, Peyrin F, Zysset PK. Characterizing microcrack orientation distribution functions in osteonal bone samples. J Microsc 2016;264: 268-281.
[34] Granke M, Makowski AJ, Uppuganti S, Nyman JS. Prevalent role of porosity and osteonal area over mineralization heterogeneity in the fracture toughness of human cortical bone. Journal of Biomechanics 2016;49: 2748-2755.
[35] Cole JH, van der Meulen MCH. Whole bone mechanics and bone quality. Clin Orthop Relat Res 2011;469: 2139-2149.
[36] Consensus development conference: diagnosis, prophylaxis, and treatment of osteoporosis. Am. J. Med. 1993;94: 646-650.
[37] Kanis JA, Melton III LJ, Christiansen C, Johnston CC, Khaltaev N. The diagnosis of osteoporosis. J Bone Miner Res 1994;9: 1137-1141.
[38] Kanis JA, McCloskey EV, Johansson H, Oden A, Melton III LJ, Khaltaev N. A reference standard for the description of osteoporosis. Bone 2008;42: 467-475.
[39] Marshall D, Johnell O, Wedel H. Meta-analysis of how well measures of bone mineral density predict occurrence of osteoporotic fractures. BMJ 1996;312: 1254-1259.
[40] Kanis JA, Johnell O, Oden A, Dawson A, de Laet C, Jonsson B. Ten year probabilities of osteoporotic fractures according to BMD and diagnostic thresholds. Osteoporos Int 2001;12: 989-995.
[41] Compston J, Cooper A, Cooper C, Gittoes N, Gregson C, Harvey N, Hope S, Kanis JA, McCloskey EV, Poole KES, Reid DM, Selby P, Thompson F, Thurston A, Vine N. UK clinical guideline for the prevention and treatment of osteoporosis. Arch Osteoporos 2017;12: 1-24.

[42] Kanis JA, Oden A, Johnell O, Johansson H, De Laet C, Brown J, Burckhardt P, Cooper C, Christiansen C, Cummings S, Eisman JA, Fujiwara S, Gluer C, Goltzman D, Hans D, Krieg MA, La Croix A, McCloskey E, Mellstrom D, Melton III LJ, Pols H, Reeve J, Sanders K, Schott AM, Silman A, Torgerson D, van Staa T, Watts NB, Yoshimura N. The use of clinical risk factors enhances the performance of BMD in the prediction of hip and osteoporotic fractures in men and women. Osteoporos Int 2007;18: 1033-1046.
[43] Dagan N, Cohen-Stavi C, Leventer-Roberts M, Balicer RD. External validation and comparison of three prediction tools for risk of osteoporotic fractures using data from population based electronic health records: retrospective cohort study. BMJ 2017;356: 1-15.
[44] Curtis EM, van der Velde R, Moon RJ, van den Bergh JPW, Geusens P, de Vries F, van Staa TP, Cooper C, Harvey NC. Epidemiology of fractures in the United Kingdom 1988-2012: Variation with age, sex, geography, ethnicity and socioeconomic status. Bone 2016;87: 19-26.
[45] Hernlund E, Svedbom A, Ivergård M, Compston J, Cooper C, Stenmark J, McCloskey EV, Jonsson B, Kanis JA. Osteoporosis in the European Union: medical management, epidemiology and economic burden. A report prepared in collaboration with the International Osteoporosis Foundation (IOF) and the European Federation of Pharmaceutical Industry Associations (EFPIA). Arch Osteoporos 2013;8: 1-115.
[46] van Staa TP, Dennison EM, Leufkens HGM, Cooper C. Epidemiology of fractures in England and Wales. Bone 2001;29: 517-522.
[47] Falahati-Nini A, Riggs BL, Atkinson EJ, O'Fallon WM, Eastell R, Khosla S. Relative contributions of testosterone and estrogen in regulating bone resorption and formation in normal elderly men. J Clin Invest 2000;106: 1553-1560.
[48] Khosla S, Melton III LJ, Atkinson EJ, O'Fallon WM, Klee GG, Riggs BL. Relationship of serum sex steroid levels and bone turnover markers with bone mineral density in men and women: a key role for bioavailable estrogen. J Clin Endocrinol Metab 1998;83: 2266-2274.
[49] Weitzmann MN, Pacifici R. Estrogen deficiency and bone loss: an inflammatory tale. J Clin Invest 2006;116: 1186-1194.
[50] Sowers MR, Jannausch M, McConnell D, Little R, Greendale GA, Finkelstein JS, Neer RM, Johnston J, Ettinger B. Hormone predictors of bone mineral density changes during the menopausal transition. J Clin Endocrinol Metab 2006;91: 1261-1267.
[51] Cauley JA, Ewing SK, Taylor BC, Fink HA, Ensrud KE, Bauer DC, Barrett-Connor E, Marshall L, Orwoll ES. Sex steroid hormones in older men: longitudinal associations with 4.5-year change in hip bone mineral density--the Osteoporotic Fractures in Men Study. J Clin Endocrinol Metab 2010;95: 4314-4323.
[52] Zebaze RMD, Ghasem-Zadeh A, Bohte A, Iuliano-Burns S, Mirams M, Price RI, Mackie EJ, Seeman E. Intracortical remodelling and porosity in the distal radius and post-mortem femurs of women: a cross-sectional study. Lancet 2010;375: 1729-1736.
[53] Crandall CJ, Newberry SJ, Diamant A, Lim YW, Gellad WF, Booth MJ, Motala A, Shekelle PG. Comparative effectiveness of pharmacologic treatments to prevent fractures: an updated systematic review. Ann Intern Med 2014;161: 711-23.
[54] Geusens P, Marin F, Kendler DL, Russo LA, Zerbini CAF, Minisola S, Body JJ, Lespessailles E, Greenspan SL, Bagur A, Stepan JJ, Lakatos P, Casado E, Moericke R, Lopez-Romero P, Fahrleitner-Pammer A. Effects of Teriparatide Compared with Risedronate on the Risk of Fractures in Subgroups of Postmenopausal Women with Severe Osteoporosis: The VERO Trial. J Bone Miner Res 2018.
[55] Saag KG, Petersen J, Brandi ML, Karaplis AC, Lorentzon M, Thomas T, Maddox J, Fan M, Meisner PD, Grauer A. Romosozumab or Alendronate for Fracture Prevention in Women with Osteoporosis. N Engl J Med 2017;377: 1417-1427.
[56] NICE. National Institute for Health and Clinical Excellence: Technology appraisal guidance: Alendronate, etidronate, risedronate, raloxifene, strontium ranelate and teriparatide for the secodnary prevention of osteoporotic fragility fractures in postmenopausal women (amended) (2011). In; 2011.
[57] Lewiecki EM, Binkley N, Morgan SL, Shuhart CR, Camargos BM, Carey JJ, Gordon CM, Jankowski LG, Lee JK, Leslie WD. Best practices for dual-energy x-ray absorptiometry measurement and reporting: International Society for Clinical Densitometry guidance. J Clin Densitom 2016;19: 127-140.
[58] Adams JE. Advances in bone imaging for osteoporosis. Nat Rev Endocrinol 2013;9: 28-42.

[59] Yu EW, Thomas BJ, Brown JK, Finkelstein JS. Simulated increases in body fat and errors in bone mineral density measurements by DXA and QCT. J Bone Miner Res 2012;27: 119-124.
[60] Engelke K, Adams JE, Armbrecht G, Augat P, Bogado CE, Bouxsein ML, Felsenberg D, Ito M, Prevrhal S, Hans DB, Lewiecki EM. Clinical use of quantitative computed tomography and peripheral quantitative computed tomography in the management of osteoporosis in adults: the 2007 ISCD Official Positions. J Clin Densitom 2008;11: 123-162.
[61] Yang L, Burton AC, Bradburn M, Nielson CM, Orwoll ES, Eastell R. Distribution of bone density in the proximal femur and its association with hip fracture risk in older men: the osteoporotic fractures in men (MrOS) study. J Bone Miner Res 2012;27: 2314-2324.
[62] Poole KES, Skingle L, Gee AH, Turmezei TD, Johannesdottir F, Blesic K, Rose C, Vindlacheruvu M, Donell S, Vaculik J, Dungl P, Horak M, Stepan JJ, Reeve J, Treece GM. Focal osteoporosis defects play a key role in hip fracture. Bone 2017;94: 124-134.
[63] Johannesdottir F, Poole KE, Reeve J, Siggeirsdottir K, Aspelund T, Mogensen B, Jonsson BY, Sigurdsson S, Harris TB, Gudnason VG, Sigurdsson G. Distribution of cortical bone in the femoral neck and hip fracture: a prospective case-control analysis of 143 incident hip fractures; the AGES-REYKJAVIK Study. Bone 2011;48: 1268-76.
[64] Fitzpatrick LA, Dabrowski CE, Cicconetti G, Gordon DN, Fuerst T, Engelke K, Genant HK. Ronacaleret, a calcium-sensing receptor antagonist, increases trabecular but not cortical bone in postmenopausal women. J Bone Miner Res 2012;27: 255-62.
[65] Poole KE, Treece GM, Ridgway GR, Mayhew PM, Borggrefe J, Gee AH. Targeted regeneration of bone in the osteoporotic human femur. PLoS One 2011;6: e16190.
[66] Zysset P, Qin L, Lang T, Khosla S, Leslie WD, Shepherd JA, Schousboe JT, Engelke K. Clinical use of quantitative computed tomography-based finite element analysis of the hip and spine in the management of msteoporosis in adults: the 2015 ISCD official positions-part II. J Clin Densitom 2015;18: 359-392.
[67] Engelke K, Lang T, Kholsa S, Qin L, Zysset P, Leslie WD, Shepherd JA, Shousboe JT. Clinical use of quantitative computed tomography-based advanced techniques in the management of osteoporosis in adults: the 2015 ISCD Official Positions - Part III. J Clin Densitom 2015;18: 393-407.
[68] Wong AKO. A comparison of peripheral imaging technologies for bone and muscle quantification: a technical review of image acquisition. J Musculoskelet Neuronal Interact 2016;16: 265-282.
[69] Koivisto J, Kiljunen T, Kadesjo N, Shi XQ, Wolff J. Effective radiation dose of a MSCT, two CBCT and one conventional radiography device in the ankle region. J Foot Ankle Res 2015;8: 1-10.
[70] Dennison EM, Jameson KA, Edwards MH, Denison HJ, Aihie Sayer A, Cooper C. Peripheral quantitative computed tomography measures are associated with adult fracture risk: the Hertfordshire Cohort Study. Bone 2014;64: 13-17.
[71] Sheu Y, Zmuda JM, Boudreau RM, Petit MA, Ensrud KE, Bauer DC, Gordon CL, Orwoll ES, Cauley JA. Bone strength measured by peripheral quantitative computed tomography and the risk of nonvertebral fractures: the osteoporotic fractures in men (MrOS) study. J Bone Miner Res 2011;26: 63-71.
[72] Ireland A, Ferretti JL, Rittweger J. Imaging of the muscle-bone relationship. Curr Osteoporos Rep 2014;12: 486-495.
[73] Crockett K, Arnold CM, Farthing JP, Chilibeck PD, Johnston JD, Bath B, Baxter-Jones ADG, Kontulainen SA. Bone strength and muscle properties in postmenopausal women with and without a recent distal radius fracture. Osteoporos Int 2015;26: 2461-2469.
[74] Swinford RR, Warden SJ. Factors affecting short-term precision of musculoskeletal measures using peripheral quantitative computed tomography (pQCT). Osteoporos Int 2010;21: 1863-1870.
[75] Rinaldi G, Wisniewski CA, Setty NG, Leboff MS. Peripheral quantitative computed tomography: optimization of reproducibility measures of bone density, geometry, and strength at the radius and tibia. J Clin Densitom 2011;14: 367-373.
[76] Wong AK, Beattie KA, Min KK, Merali Z, Webber CE, Gordon CL, Papaioannou A, Cheung AM, Adachi JD. A trimodality comparison of volumetric bone imaging technologies. part II: 1-yr change, long-term precision, and least significant change. J Clin Densitom 2014;18: 260-269.

[77] Tjong W, Kazakia GJ, Burghardt AJ, Majumdar S. The effect of voxel size on high-resolution peripheral computed tomography measurements of trabecular and cortical bone microstructure. Med Phys 2012;39: 1893-1903.
[78] Kazakia GJ, Burghardt AJ, Link TM, Majumdar S. Variations in morphological and biomechanical indices at the distal radius in subjects with identical BMD. J Biomech 2011;44: 257-266.
[79] Wong AK, Beattie KA, Min KK, Webber CE, Gordon CL, Papaioannou A, Cheung AM, Adachi JD. A trimodality comparison of volumetric bone imaging technologies. Part I: Short-term precision and validity. J Clin Densitom 2015;18: 124-135.
[80] Ohlsson C, Sundh D, Wallerek A, Nilsson M, Karlsson M, Johansson H, Mellstrom D, Lorentzon M. Cortical bone area predicts incident fractures independently of areal bone mineral density in older men. J Clin Endocrinol Metab 2016;102: 516-524.
[81] Boutroy S, Khosla S, Sornay-Rendu E, Zanchetta MB, McMahon DJ, Zhang CA, Chapurlat RD, Zanchetta J, Stein EM, Bogado C, Majumdar S, Burghardt AJ, Shane E. Microarchitecture and peripheral BMD are impaired in postmenopausal white women with fracture independently of total hip T-score: an international multicenter study. J Bone Miner Res 2016;31: 1158-1166.
[82] Sornay-Rendu E, Boutroy S, Duboeuf F, Chapurlat RD. Bone microarchitecture assessed by HR-pQCT as predictor of fracture risk in postmenopausal women: The OFELY Study. J Bone Miner Res 2017;32: 1243-1251.
[83] Stein EM, Kepley A, Walker M, Nickolas TL, Nishiyama KK, Zhou B, Liu XS, McMahon DJ, Zhang C, Boutroy S, Cosman F, Nieves J, Guo XE, Shane E. Skeletal structure in postmenopausal women with osteopenia and fractures is characterized by abnormal trabecular plates and cortical thinning. J Bone Miner Res 2014;29: 1101-1109.
[84] Tsai JN, Nishiyama KK, Lin D, Yuan A, Lee H, Bouxsein ML, Leder BZ. Effects of denosumab and teriparatide transitions on bone microarchitecture and estimated strength: the DATA-Switch HR-pQCT study. J Bone Miner Res 2017;32: 2001-2009.
[85] Hansen S, Hauge EM, Jensen J-EB, Brixen K. Differing effects of PTH 1–34, PTH 1–84, and zoledronic acid on bone microarchitecture and estimated strength in postmenopausal women with osteoporosis: An 18-month open-labeled observational study using HR-pQCT. J Bone Miner Res 2013;28: 736-745.
[86] Burghardt AJ, Kazakia GJ, Sode M, de Papp AE, Link TM, Majumdar S. A longitudinal HR-pQCT study of alendronate treatment in postmenopausal women with low bone density: Relations among density, cortical and trabecular microarchitecture, biomechanics, and bone turnover. J Bone Miner Res 2010;25: 2558-2571.
[87] Nilsson AG, Sundh D, Johansson L, Nilsson M, Mellstrom D, Rudang R, Zoulakis M, Wallander M, Darelid A, Lorentzon M. Type 2 diabetes mellitus is associated with better bone microarchitecture but lower bone material strength and poorer physical function in elderly women: a population-based study. J Bone Miner Res 2017;32: 1062-1071.
[88] Sutter S, Nishiyama KK, Kepley A, Zhou B, Wang J, McMahon DJ, Guo XE, Stein EM. Abnormalities in cortical bone, trabecular plates, and stiffness in postmenopausal women treated with glucocorticoids. J Clin Endocrinol Metab 2014;99: 4231-4240.
[89] Nishiyama KK, Pauchard Y, Nikkel LE, Iyer S, Zhang C, McMahon DJ, Cohen D, Boyd SK, Shane E, Nickolas TL. Longitudinal HR-pQCT and image registration detects endocortical bone loss in kidney transplantation patients. J Bone Miner Res 2015;30: 554-561.
[90] Barnabe C, Buie H, Kan M, Szabo E, Barr SG, Martin L, Boyd SK. Reproducible metacarpal joint space width measurements using 3D analysis of images acquired with high-resolution peripheral quantitative computed tomography. Med Eng Phys 2013;35: 1540-1544.
[91] Simon D, Kleyer A, Stemmler F, Simon C, Berlin A, Hueber AJ, Haschka J, Renner N, Figueiredo C, Neuhuber W, Buder T, Englbrecht M, Rech J, Engelke K, Schett G. Age- and sex-Dependent changes of intra-articular cortical and trabecular bone structure and the effects of rheumatoid arthritis. J Bone Miner Res 2017;32: 722-730.
[92] Srikhum W, Virayavanich W, Burghardt AJ, Yu A, Link T, Imboden JB, Li X. Quantitative and semiquantitative bone erosion assessment on high-resolution peripheral quantitative computed tomography in rheumatoid arthritis. J Rheumatol 2013;40: 408-416.
[93] Kroker A, Zhu Y, Manske SL, Barber R, Mohtadi N, Boyd SK. Quantitative in vivo assessment of bone microarchitecture in the human knee using HR-pQCT. Bone 2017;97: 43-48.

[94] Pialat JB, Burghardt AJ, Sode M, Link TM, Majumdar S. Visual grading of motion induced image degradation in high resolution peripheral computed tomography: impact of image quality on measures of bone density and micro-architecture. Bone 2012;50: 111-118.
[95] Pauchard Y, Liphardt AM, Macdonald HM, Hanley DA, Boyd SK. Quality control for bone quality parameters affected by subject motion in high-resolution peripheral quantitative computed tomography. Bone 2012;50: 1304-1310.
[96] Burghardt AJ, Pialat JB, Kazakia GJ, Boutroy S, Engelke K, Patsch JM, Valentinitsch A, Liu D, Szabo E, Bogado CE, Zanchetta MB, McKay HA, Shane E, Boyd SK, Bouxsein ML, Chapurlat R, Khosla S, Majumdar S. Multicenter precision of cortical and trabecular bone quality measures assessed by high-resolution peripheral quantitative computed tomography. J Bone Miner Res 2013;28: 524-536.
[97] Manske SL, Zhu Y, Sandino C, Boyd SK. Human trabecular bone microarchitecture can be assessed independently of density with second generation HR-pQCT. Bone 2015;79: 213-221.
[98] Jorgenson BL, Buie HR, McErlain DD, Sandino C, Boyd SK. A comparison of methods for in vivo assessment of cortical porosity in the human appendicular skeleton. Bone 2015;73: 167-175.
[99] Chang G, Deniz CM, Honig S, Egol K, Regatte RR, Zhu Y, Sodickson DK, Brown R. MRI of the hip at 7 Tesla: feasibility of bone microarchitecture, high-resolution cartilage, and clinical imaging. J Magn Reson Imaging 2014;39: 1384-1393.
[100] Kazakia GJ, Hyun B, Burghardt AJ, Krug R, Newitt DC, de Papp AE, Link TM, Majumdar S. In vivo determination of bone structure in postmenopausal women: a comparison of HR-pQCT and high-field MR imaging. J Bone Miner Res 2008;23: 463-474.
[101] Link TM, Majumdar S, Augat P, Lin JC, Newitt D, Lu Y, Lane NE, Genant HK. In vivo high resolution MRI of the calcaneus: differences in trabecular structure in osteoporosis patients. J Bone Miner Res 1998;13: 1175-1182.
[102] Majumdar S, Link TM, Augat P, Lin JC, Newitt D, Lane NE, Genant HK. Trabecular bone architecture in the distal radius using magnetic resonance imaging in subjects with fractures of the proximal femur. Magnetic Resonance Science Center and Osteoporosis and Arthritis Research Group. Osteoporos Int 1998;10: 231-239.
[103] Wehrli FW, Ladinsky GA, Jones C, Benito M, Magland J, Vasilic B, Popescu AM, Zemel B, Cucchiara AJ, Wright AC, Song HK, Saha PK, Peachey H, Snyder PJ. In vivo magnetic resonance detects rapid remodeling changes in the topology of the trabecular bone network after menopause and the protective effect of estradiol. J Bone Miner Res 2008;23: 730-740.
[104] Folkesson J, Goldenstein J, Carballido-Gamio J, Kazakia G, Burghardt AJ, Rodriguez A, Krug R, de Papp AE, Link TM, Majumdar S. Longitudinal evaluation of the effects of alendronate on MRI bone microarchitecture in postmenopausal osteopenic women. Bone 2011;48: 611-621.
[105] Phan CM, Matsuura M, Bauer JS, Dunn TC, Newitt D, Lochmuller EM, Eckstein F, Majumdar S, Link TM. Trabecular bone structure of the calcaneus: comparison of MR imaging at 3.0 and 1.5 T with micro-CT as the standard of reference. Radiology 2006;239: 488-496.
[106] Rajapakse CS, Bashoor-Zadeh M, Li C, Sun W, Wright AC, Wehrli FW. Volumetric cortical bone porosity assessment with MR imaging: validation and clinical feasibility. Radiology 2015;267: 526-535.
[107] Langton CM, Palmer SB, Porter RW. The measurement of broadband ultrasonic attenuation in cancellous bone. Eng Med 1984;13: 89-91.
[108] Glüer CC, Wu CY, Jergas M, Goldstein SA, Genant HK. Three quantitative ultrasound parameters reflect bone structure. Calcif Tissue Int 1994;55: 46-52.
[109] Njeh CF, Fuerst T, Diessel E, Genant HK. Is quantitative ultrasound dependent on bone structure? A reflection. Osteoporos Int 2001;12: 1-15.
[110] Raum K, Grimal Q, Varga P, Barkmann R, Glüer CC, Laugier P. Ultrasound to assess bone quality. Curr Osteoporos Rep 2014;12: 154-162.
[111] McCloskey EV, Kanis JA, Oden A, Harvey NC, Bauer D, González-Macias J, Hans D, Kaptoge S, Krieg MA, Kwok T, Marin F, Moayyeri A, Orwoll E, Gluër C, Johansson H. Predictive ability of heel quantitative ultrasound for incident fractures: an individual-level meta-analysis. Osteoporos Int 2015;26: 1979-1987.

[112] Moayyeri A, Kaptoge S, Dalzell N, Bingham S, Luben RN, Wareham NJ, Reeve J, Khaw KT. Is QUS or DXA better for predicting the 10-year absolute risk of fracture? J Bone Miner Res 2009;24: 1319-1325.
[113] Krieg MA, Barkmann R, Gonnelli S, Stewart A, Bauer DC, Del Rio Barquero L, Kaufman JJ, Lorenc R, Miller PD, Olszynski WP, Poiana C, Schott AM, Lewiecki EM, Hans D. Quantitative ultrasound in the management of osteoporosis: the 2007 ISCD Official Positions. J Clin Densitom 2008;11: 163-187.
[114] Barkmann R, Dencks S, Laugier P, Padilla F, Brixen K, Ryg J, Seekamp A, Mahlke L, Bremer A, Heller M, Glüer CC. Femur ultrasound (FemUS)--first clinical results on hip fracture discrimination and estimation of femoral BMD. Osteoporos Int 2010;21: 969-976.
[115] Grimal Q, Grondin J, Guerard S, Barkmann R, Engelke K, Glüer CC, Laugier P. Quantitative ultrasound of cortical bone in the femoral neck predicts femur strength: results of a pilot study. J Bone Miner Res 2013;28: 302-312.
[116] Paggiosi MA, Barkmann R, Gluer CC, Roux C, Reid DM, Felsenberg D, Bradburn M, Eastell R. A European multicenter comparison of quantitative ultrasound measurement variables: the OPUS study. Osteoporos Int 2012;23: 2815-2828.
[117] Riggs BL, Melton III LJ, Robb RA, Camp JJ, Atkinson EJ, Peterson JM, Rouleau PA, McCollough CH, Bouxsein ML, Khosla S. Population-based study of age and sex differences in bone volumetric density, size, geometry, and structure at different skeletal sites. J Bone Miner Res 2004;19: 1945-1954.
[118] Melton III LJ, Khosla S, Atkinson EJ, O'Connor MK, O'Fallon WM, Riggs BL. Cross-sectional versus longitudinal evaluation of bone loss in men and women. Osteoporos Int 2000;11: 592-599.
[119] Malaquias TM, Silveira C, Aerts W, De Groote F, Dereymaeker G, Vander Sloten J, Jonkers I. Extended foot-ankle musculoskeletal models for application in movement analysis. Comput Methods Biomech Biomed Engin 2017;20: 153-159.
[120] Sabry FF, Ebraheim NA, Mehalik JN, Rezcallah AT. Internal architecture of the calcaneus: implications for calcaneus fractures. Foot Ankle Int 2000;21: 114-118.
[121] Gefen A, Seliktar R. Comparison of the trabecular architecture and the isostatic stress flow in the human calcaneus. Med Eng Phys 2004;26: 119-129.
[122] Blanchet C, Giguère Y, Prud'homme D, Turcot-Lemay L, Dumont M, Leduc G, Côte S, Laflamme N, Rousseau F, Dodin S. Leisure physical activity is associated with quantitative ultrasound measurements independently of bone mineral density in postmenopausal women. Calcif Tissue Int 2003;73: 339-349.
[123] Pettersson U, Nilsson M, Sundh V, Mellström D, Lorentzon M. Physical activity is the strongest predictor of calcaneal peak bone mass in young Swedish men. Osteoporos Int 2010;21: 447-455.
[124] Nakazono E, Miyazaki H, Abe S, Imai K, Masuda T, Iwamoto M, Moriguchi R, Ueno H, Ono M, Yazumi K, Moriyama K, Nakano S, Tsuda H. Discontinuation of leisure time impact-loading exercise is related to reduction of a calcaneus quantitative ultrasound parameter in young adult Japanese females: a 3-year follow-up study. Osteoporos Int 2014;25: 485-495.
[125] Pye SR, Devakumar V, Boonen S, Borghs H, Vanderschueren D, Adams JE, Ward KA, Bartfai G, Casanueva FF, Finn JD, Forti G, Giwercman A, Han TS, Huhtaniemi IT, Kula K, Lean ME, Pendleton N, Punab M, Silman AJ, Wu FC, O'Neill TW, Group ES. Influence of lifestyle factors on quantitative Heel ultrasound measurements in middle-aged and elderly men. Calcif Tissue Int 2010;86: 211-219.
[126] Shephard RJ, Park H, Park S, Aoyagi Y. Objective longitudinal measures of physical activity and bone health in older japanese: the nakanojo study. J Am Geriatr Soc 2017;65: 800-807.
[127] Min JY, Min KB, Paek D, Cho SI. Side differences in the bone density of the distal radius and calcaneus in Koreans aged 4-86 years. J Clin Densitom 2007;10: 184-188.
[128] Heinonen A, Oja P, Kannus P, Sievänen H, Haapasalo H, Mänttäri A, Vuori I. Bone mineral density in female athletes representing sports with different loading characteristics of the skeleton. Bone 1995;17: 197-203.
[129] Nurmi-Lawton JA, Baxter-Jones AD, Mirwald RL, Bishop JA, Taylor P, Cooper C, New SA. Evidence of sustained skeletal benefits from impact-loading exercise in young females: a 3-year longitudinal study. J Bone Miner Res 2004;19: 314-322.

[130] Ito M, Nakamura T, Ikeda S, Tahara Y, Hashmi R, Tsurusaki K, Uetani M, Hayashi K. Effects of lifetime volleyball exercise on bone mineral densities in lumbar spine, calcaneus and tibia for pre-, peri- and postmenopausal women. Osteoporos Int 2001;12: 104-111.
[131] Fredericson M, Chew K, Ngo J, Cleek T, Kiratli J, Cobb K. Regional bone mineral density in male athletes: a comparison of soccer players, runners and controls. Br J Sports Med 2007;41: 664-668.
[132] Kemmler W, Engelke K, Baumann H, Beeskow C, von Stengel S, Weineck J, Kalender WA. Bone status in elite male runners. Eur J Appl Physiol 2006;96: 78-85.
[133] Heinonen A, Kannus P, Sievänen H, Oja P, Pasanen M, Rinne M, Uusi-Rasi K, Vuori I. Randomised controlled trial of effect of high-impact exercise on selected risk factors for osteoporotic fractures. Lancet 1996;348: 1343-1347.
[134] Engelke K, Kemmler W, Lauber D, Beeskow C, Pintag R, Kalender WA. Exercise maintains bone density at spine and hip EFOPS: a 3-year longitudinal study in early postmenopausal women. Osteoporos Int 2006;17: 133-142.
[135] Slatkovska L, Beyene J, Alibhai SM, Wong Q, Sohail QZ, Cheung AM. Effect of whole-body vibration on calcaneal quantitative ultrasound measurements in postmenopausal women: a randomized controlled trial. Calcif Tissue Int 2014;95: 547-556.
[136] Torvinen S, Kannus P, Sievänen H, Järvinen TA, Pasanen M, Kontulainen S, Nenonen A, Järvinen TL, Paakkala T, Järvinen M, Vuori I. Effect of 8-month vertical whole body vibration on bone, muscle performance, and body balance: a randomized controlled study. J Bone Miner Res 2003;18: 876-884.
[137] Slatkovska L, Alibhai SM, Beyene J, Cheung AM. Effect of whole-body vibration on BMD: a systematic review and meta-analysis. Osteoporos Int 2010;21: 1969-1980.
[138] Wang H, Wan Y, Tam KF, Ling S, Bai Y, Deng Y, Liu Y, Zhang H, Cheung WH, Qin L, Cheng JC, Leung KS, Li Y. Resistive vibration exercise retards bone loss in weight-bearing skeletons during 60 days bed rest. Osteoporos Int 2012;23: 2169-2178.
[139] LeBlanc AD, Schneider VS, Evans HJ, Engelbretson DA, Krebs JM. Bone mineral loss and recovery after 17 weeks of bed rest. J Bone Miner Res 1990;5: 843-850.
[140] Moayyeri A, Adams JE, Adler RA, Krieg MA, Hans D, Compston J, Lewiecki EM. Quantitative ultrasound of the heel and fracture risk assessment: an updated meta-analysis. Osteoporos Int 2012;23: 143-153.
[141] Bauer DC, Glüer CC, Cauley JA, Vogt TM, Ensrud KE, Genant HK, Black DM. Broadband ultrasound attenuation predicts fractures strongly and independently of densitometry in older women. Arch Intern Med 1997;157: 629-634.
[142] Stone KL, Seeley DG, Lui L-Y, Cauley JA, Ensrud K, Browner WS, Nevitt MC, Cummings SR. BMD at multiple sites and risk of fracture of multiple types: long-term results from the study of osteoporotic fractures. J Bone Miner Metab 2003;18: 1947-1954.
[143] Sahota O, San P, Cawte SA, Pearson D, Hosking DJ. A comparison of the longitudinal changes in quantitative ultrasound with dual-energy x-ray absorptiometry: the four-year effects of hormone replacement therapy. Osteoporos Int 2000;11: 52-58.
[144] Frost ML, Blake GM, Fogelman I. Changes in QUS and BMD Measurements with Antiresorptive Therapy: A Two-Year Longitudinal Study. Calcif Tissue Int 2001;69: 138-146.
[145] Ringe JD, Dorst A, Faber H, Ibach K, Preuss J. Three-monthly ibandronate bolus injection offers favourable tolerability and sustained efficacy advantage over two years in established corticosteroid-induced osteoporosis. Rheumatology 2003;42: 743-749.
[146] Leal T, Tevaarwerk A, Love R, Stewart J, Binkley N, Eickhoff J, Parrot B, Mulkerin D. Randomized trial of adjuvant zoledronic acid in postmenopausal women with high-risk breast cancer. Clin Breast Cancer 2010;10: 471-476.
[147] Paggiosi MA, Peel N, McCloskey EV, Walsh JS, Eastell R. Comparison of the effects of three oral bisphosphonate therapies on the peripheral skeleton in postmenopausal osteoporosis: the TRIO study. Osteoporos Int 2014;25: 2729-2741.
[148] Tsai JN, Uihlein AV, Burnett-Bowie SA, Neer RM, Zhu Y, Derrico N, Lee H, Bouxsein ML, Leder BZ. Comparative effects of teriparatide, denosumab, and combination therapy on peripheral compartmental bone density, microarchitecture, and estimated strength: the DATA-HRpQCT Study. J Bone Miner Res 2015;30: 39-45.
[149] Blake GM, Fogelman I. Technical principles of dual energy x-ray absorptiometry. Seminars in Nuclear Medicine 1997;XXVII: 210-228.
[150] Bonnick SL, Lewis LA. Bone densitometry for technologists. In: Press H, editor. Second ed; 2006, p. 27-62.

[151] Paggiosi MA, Eastell R, Walsh JS. Precision of high-resolution peripheral quantitative computed tomography measurement variables: influence of gender, examination site, and age. Calcif Tissue Int 2014;94: 191-201.
[152] Bouxsein ML, Boyd SK, Christiansen BA, Guldberg RE, Jepsen KJ, Müller R. Guidelines for assessment of bone microstructure in rodents using micro-computed tomography. J Bone Miner Res 2010;25: 1468-1486.
[153] Prevrhal S, Engelke K, Kalender WA. Accuracy limits for the determination of cortical width and density: the influence of object size and CT imaging. Phys Med Biol 1999;44: 751-764.
[154] Bonaretti S, Vilayphiou N, Chan CM, Yu A, Nishiyama K, Liu D, Boutroy S, Ghasem-Zadeh A, Boyd SK, Chapurlat R, McKay H, Shane E, Bouxsein ML, Black DM, Majumdar S, Orwoll ES, Lang TF, Khosla S, Burghardt AJ. Operator variability in scan positioning is a major component of HR-pQCT precision error and is reduced by standardized training. Osteoporos Int 2016;28: 245-257.
[155] Engelke K, Stampa B, Timm W, Dardzinski B, de Papp AE, Genant HK, Fuerst T. Short-term in vivo precision of BMD and parameters of trabecular architecture at the distal forearm and tibia. Osteoporos Int 2012;23: 2151-2158.
[156] Sekhon K, Kazakia GJ, Burghardt AJ, Hermannsson B, Majumdar S. Accuracy of volumetric bone mineral density measurement in high-resolution peripheral quantitative computed tomography. Bone 2009;45: 473-479.
[157] Burghardt AJ, Kazakia GJ, Laib A, Majumdar S. Quantitative assessment of bone tissue mineralization with polychromatic micro-computed tomography. Calcif Tissue Int 2008;83: 129-38.
[158] Barrett JF, Keat N. Artifacts in CT: recognising and avoidance. RadioGraphics 2004;24: 1679-1691.
[159] Laib A, Rüegsegger P. Comparison of structure extraction methods for in vivo trabecular bone measurements. Comput Med Imaging Graph 1999;23: 69-74.
[160] Davis KA, Burghardt AJ, Link TM, Majumdar S. The effects of geometric and threshold definitions on cortical bone metrics assessed by in vivo high-resolution peripheral quantitative computed tomography. Calcif Tissue Int 2007;81: 364-371.
[161] Buie HR, Campbell GM, Klinck RJ, MacNeil JA, Boyd SK. Automatic segmentation of cortical and trabecular comaprtments based on a dual threshold technique for in vivo micro-CT bone analysis. Bone 2007;41: 505-515.
[162] Burghardt AJ, Buie HR, Laib A, Majumdar S, Boyd SK. Reproducibility of direct quantitative measures of cortical bone microarchitecture of the distal radius and tibia by HR-pQCT. Bone 2010;47: 519-528.
[163] MacNeil JA, Boyd SK. Accuracy of high-resolution peripheral quantitative computed tomography for measurement of bone quality. Med Eng Phys 2007;29: 1096-1105.
[164] Liu XS, Zhang XH, Sekhon KK, Adams MF, McMahon DJ, Bilezikian JP, Shane E, Guo XE. High-resolution peripheral quantitative computed tomography can assess microstructural and mechanical properties of human distal tibial bone. J Bone Miner Res 2010;25: 746-756.
[165] Laib A, Hildebrand T, Häuselmann J, Rüegsegger P. Ridge number density: a new parameter for in vivo bone structure analysis. Bone 1997;21: 541-546.
[166] Hildebrand T, Rüegsegger P. A new method for the model-independent assessment of thickness in three-dimensional images. J Microsc 1997;185: 67-75.
[167] Laib A, Rüegsegger P. Calibration of trabecular bone structure measurements of in vivo three-dimensional peripheral quantitative computed tomography with 28-um-resolution microcomputed tomography. Bone 1999;24: 35-39.
[168] Parfitt AM, Drezner MK, Glorieux FH, Kanis JA, Malluche H, Meunier PJ, Ott SM, Recker RR. Bone histomorphometry: Standardization of nomenclature, symbols, and units: Report of the asbmr histomorphometry nomenclature committee. J Bone Miner Res 1987;2: 595-610.
[169] Müller R, van Campenhout H, van Damme B, van der Perre G, Dequeker J, Hildebrand T, Rüegsegger P. Morphometric analysis of human bone biopsies: a quantitative structural comparison of histological section and micro-computed tomography. Bone 1998;23: 59-66.
[170] Particelli F, Mecozzi L, Beraudi A, Montesi M, Baruffaldi F, Viceconti M. A comparison between micro-CT and histology for the evaluation of cortical bone: effect of polymethylmethacrylate embedding on structural parameters. J Microsc 2012;245: 302-10.

[171] Stauber M, Müller R. Micro-Computed Tomography: A Method for the Non-Destructive Evaluation of the Three-Dimensional Structure of Biological Specimens. In: Springer, editor. Osteoporosis Methods and Protocols: Springer; 2008. p. 273-292.
[172] Burghardt AJ, Kazakia GJ, Majumdar S. A local adaptive threshold strategy for high resolution peripheral quantitative computed tomography of trabecular bone. Ann Biomed Eng 2007;35: 1678-1686.
[173] Soret M, Bacharach SL, Buvat I. Partial-volume effect in PET tumor imaging. J Nucl Med 2007;48: 932-45.
[174] Hill DLG, Batchelor PG, Holden M, Hawkes DJ. Medical image registration. Phys Med Biol 2001;46: R1-R45.
[175] Pluim JPW, Maintz JBA, Viergever MA. Mutual information based registration of medical images: a survey. IEEE Trans Med Imaging 2003;22: 986-1004.
[176] MacNeil JA, Boyd SK. Improved reproducibility of high-resolution peripheral quantitative computed tomography for measurement of bone quality. Med Eng Phys 2008;30: 792-799.
[177] Ellouz R, Chapurlat R, Van Rietbergen B, Christen P, Pialat JB, Boutroy S. Challenges in longitudinal measurements with HR-pQCT: Evaluation of a 3D registration method to improve bone microarchitecture and strength measurement reproducibility. Bone 2014;63: 147-157.
[178] Boyd SK, Moser S, Kuhn M, Klinck RJ, Krauze PL, Muller R, Gasser JA. Evaluation of three-dimensional image registration methodologies for in vivo micro-computed tomography. Ann Biomed Eng 2006;34: 1587-1599.
[179] Nishiyama KK, Campbell GM, Klinck RJ, Boyd SK. Reproducibility of bone micro-architecture measurements in rodents by in vivo micro-computed tomography is maximized with three-dimensional image registration. Bone 2010;46: 155-161.
[180] Studholme C, Hill DLG, Hawkes DJ. An overlap invariant entropy measure of 3D medical image alignment. Pattern Recognition 1999;32: 71-86.
[181] Nishiyama KK, Macdonald HM, Buie HR, Hanley DA, Boyd SK. Postmenopausal women with osteopenia have higher cortical porosity and thinner cortices at the distal radius and tibia than women with normal aBMD: an in vivo HR-pQCT study. J Bone Miner Res 2010;25: 882-890.
[182] Ashburner J, Friston KJ. Rigid body registration. In: Human Brain Function. Second ed; 2003, p. 635-653.
[183] Schulte FA, Lambers FM, Mueller TL, Stauber M, Müller R. Image interpolation allows accurate quantitative bone morphometry in registered micro-computed tomography scans. Comput Methods Biomech Biomed Engin 2014;17: 539-548.
[184] Pluim JPW, Antoine Maintz JB, Viergever MA. Interpolation artefacts in mutual information-based image registration. Comput Vis Image Underst 2000;77: 211-232.
[185] de Bakker CMJ, Altman AR, Li C, Tribble MB, Lott C, Tseng WJ, Liu XS. Minimizing interpolation bias and precision error in in vivo microCT-based measurements of bone structure and dynamics. Ann Biomed Eng 2016;44: 2518-2528.
[186] Lu Y, Boudiffa M, Dall'Ara E, Bellantuono I, Viceconti M. Development of a protocol to quantify local bone adaptation over space and time: Quantification of reproducibility. J Biomech 2016;49: 2095-2099.
[187] Birkhold AI, Razi H, Weinkamer R, Duda GN, Checa S, Willie BM. Monitoring in vivo (re)modeling: a computational approach using 4D microCT data to quantify bone surface movements. Bone 2015;75: 210-221.
[188] Burt LA, Bhatla JL, Hanley DA, Boyd SK. Cortical porosity exhibits accelerated rate of change in peri- compared with post-menopausal women. Osteoporos Int 2017;28: 1423-1431.
[189] Belavy DL, Beller G, Ritter Z, Felsenberg D. Bone structure and density via HR-pQCT in 60d bed-rest, 2-years recovery with and without countermeasures. J Musculoskelet Neuronal Interact 2011;11: 215-226.
[190] Manske SL, Davison EM, Burt LA, Raymond DA, Boyd SK. The estimation of second-generation HR-pQCT from first-generation HR-pQCT using in vivo cross-calibration. J Bone Miner Res 2017;32: 1514-1524.
[191] Shanbhogue VV, Brixen K, Hansen S. Age- and sex-related changes in bone microarchitecture and estimated strength: A three-year prospective study using HRpQCT. J Bone Miner Res 2016;31: 1541-1549.

[192] Daftary A, Haims AH, Baumgaertner MR. Fractures of the calcaneus: a review with emphasis on CT. RadioGraphics 2005;25: 1215-1226.
[193] Issever AS, Link TM, Newitt D, Munoz T, Majumdar S. Interrelationships between 3T MRI derived cortical and trabecular bone structure parameters and quantitative computed tomography derivedbone mineral density. Magn Reson Imaging 2010;28: 1299-1305.
[194] Ouyang X, Selby K, Lang P, Engelke K, Klifa C, Fan B, Zucconi F, Hottya G, Chen M, Majumdar S, Genant HK. High resolution magnetic resonance imaging of the calcaneus: age-related changes in trabecular structure and comparison with dual x-ray absorptiometry measurements. Calcif Tissue Int 1997;60: 139-147.
[195] Boutroy S, Bouxsein ML, Munoz F, Delmas PD. In vivo assessment of trabecular bone microarchitecture by high-resolution peripheral quantitative computed tomography. J Clin Endocrinol Metab 2005;90: 6508-6515.
[196] Heger L, Wulff K. Computed tomography of the calcaneus: normal anatomy. AJR 1985;145: 123-129.
[197] Rupprecht M, Pogoda P, Mumme M, Rueger JM, Puschel K, Amling M. Bone microarchitecture of the calcaneus and its changes in aging: a histomorphometric analysis of 60 human specimens. J Orthop Res 2006;24: 664-674.
[198] Lin JC, Amling M, Newitt DC, Selby K, Srivastava SK, Delling G, Genant HK, Majumdar S. Heterogeneity of trabecular bone structure in the calcaneus using magnetic resonance imaging. Osteoporos Int 1998;8: 16-24.
[199] Souzanchi MF, Palacio-Mancheno P, Borisov YA, Cardoso L, Cowin SC. Microarchitecture and bone quality in the human calcaneus: local variations of fabric anisotropy. J Bone Miner Res 2012;27: 2562-2572.
[200] Majumdar S, Newitt D, Jergas M, Gies A, Chiu E, Osman D, Keltner J, Keyak J, Genant H. Evaluation of technical factors affecting the quantification of trabecular bone structure using magnetic resonance imaging. Bone 1995;17: 417-430.
[201] Boutroy S, Vilayphiou N, Roux JP, Delmas PD, Blain H, Chapurlat RD, Chavassieux P. Comparison of 2D and 3D bone microarchitecture evaluation at the femoral neck, among postmenopausal women with hip fracture or hip osteoarthritis. Bone 2011;49: 1055-1061.
[202] Boutroy S, Van Rietbergen B, Sornay-Rendu E, Munoz F, Bouxsein ML, Delmas PD. Finite element analysis based on in vivo HR-pQCT images of the distal radius is associated with wrist fracture in postmenopausal women. J Bone Miner Res 2008;23: 392-399.
[203] Boyd SK. Site-specific variation of bone micro-architecture in the distal radius and tibia. J Clin Densitom 2008;11: 424-430.
[204] Cheung AM, Adachi JD, Hanley DA, Kendler DL, Davison KS, Josse R, Brown JP, Ste-Marie LG, Kremer R, Erlandson MC, Dian L, Burghardt AJ, Boyd SK. High-resolution peripheral quantitative computed tomography for the assessment of bone strength and structure: a review by the Canadian Bone Strength Working Group. Curr Osteoporos Rep 2013;11: 136-146.
[205] Campanelli V, Fantini M, Facciolo N, Cangemi A, Pozzo A, Sbarbati A. Three-dimensional morphology of heel fat pad: an in vivo computed tomography study. J Anat 2011;219: 622-631.
[206] Cortet B, Dubois P, Boutroy N, Palos G, Cotten A, Marchandise X. Computed tomography image analysis of the calcaneus in male osteoporosis. Osteoporos Int 2002;13: 33-41.
[207] Cortet B, Chappard D, Boutroy N, Dubois P, Cotten A, Marchandise X. Relationship between computed tomographic image analysis and histomorphometry for microarchitectural characterization of human calcaneus. Calcif Tissue Int 2004;75: 23-31.
[208] Chappard C, Laugier P, Fournier B, Roux C, Berger G. Assessment of the relationship between broadband ultrasound attenuation and bone mineral density at the calcaneus using BUA imaging and DXA. Osteoporos Int 1997;7: 316-322.
[209] Mueller TL, Stauber M, Kohler T, Eckstein F, Müller R, van Lenthe GH. Non-invasive bone competence analysis by high-resolution pQCT: an in vitro reproducibility study on structural and mechanical properties at the human radius. Bone 2009;44: 364-371.
[210] Sundh D, Rudang R, Zoulakis M, Nilsson AG, Darelid A, Lorentzon M. A high amount of local adipose tissue Is associated with high cortical porosity and low bone material strength in older women. J Bone Miner Res 2016;31: 749-757.
[211] Cheung AM, Majumdar S, Brixen K, Chapurlat R, Fuerst T, Engelke K, Dardzinski B, Cabal A, Verbruggen N, Ather S, Rosenberg E, de Papp AE. Effects of odanacatib on the

radius and tibia of postmenopausal women: improvements in bone geometry, microarchitecture, and estimated bone strength. J Bone Miner Res 2014;29: 1786-94.
[212] de Jong JJA, Willems PC, Arts JJ, Bours SGP, Brink PRG, van Geel TACM, Poeze M, Geusens PP, van Rietbergen B, van den Bergh JPW. Assessment of the healing process in distal radius fractures by high resolution peripheral quantitative computed tomography. Bone 2014;64: 65-74.
[213] Fajardo RJ, Cory E, Patel ND, Nazarian A, Laib A, Manoharan RK, Schmitz JE, DeSilva JM, MacLatchy LM, Snyder BD, Bouxsein ML. Specimen size and porosity can introduce error into microCT-based tissue mineral density measurements. Bone 2009;44: 176-184.
[214] Salmon PL, Liu X. MicroCT bone densitometry: context sensitivity, beam hardening correction and the effect of surrounding media. The Open Access Journal of Science and Technology 2014;2: 1-25.
[215] Metcalf LM, Dall'Ara E, Paggiosi MA, Rochester JR, Vilayphiou N, Kemp GJ, McCloskey EV. Validation of calcaneus trabecular microstructure measurements by HR-pQCT. Bone 2018;106: 69-77.
[216] Varga P, Dall'Ara E, Pahr DH, Pretterklieber M, Zysset PK. Validation of an HR-pQCT-based homogenized finite element approach using mechanical testing of ultra-distal radius sections. Biomech Model Mechanobiol 2011;10: 431-444.
[217] Dall'Ara E, Varga P, Pahr D, Zysset P. A calibration methodology of QCT BMD for human vertebral body with registered micro-CT images. Med Phys 2011;38: 2602-2608.
[218] Bland JM, Altman DG. Statistical methods for assessing agreement between two methods of clinical measurement. Lancet 1986;1: 307-310.
[219] Maquer G, Musy SN, Wandel J, Gross T, Zysset PK. Bone volume fraction and fabric anisotropy are better determinants of trabecular bone stiffness than other morphological variables. J Bone Miner Res 2015;30: 1000-1008.
[220] Vilayphiou N, Boutroy S, Szulc P, van Rietbergen B, Munoz F, Delmas PD, Chapurlat R. Finite element analysis performed on radius and tibia HR-pQCT images and fragility fractures at all sites in men. J Bone Miner Res 2011;26: 965-973.
[221] Edwards MH, Robinson DE, Ward KA, Javaid MK, Walker-Bone K, Cooper C, Dennison EM. Cluster analysis of bone microarchitecture from high resolution peripheral quantitative computed tomography demonstrates two separate phenotypes associated with high fracture risk in men and women. Bone 2016;88: 131-137.
[222] Krause M, Museyko O, Breer S, Wulff B, Duckstein C, Vettorazzi E, Glueer C, Puschel K, Engelke K, Amling M. Accuracy of trabecular structure by HR-pQCT compared to gold standard uCT in the radius and tibia of patients with osteoporosis and long-term bisphosphonate therapy. Osteoporos Int 2014;25: 1595-1606.
[223] Wang J, Stein EM, Zhou B, Nishiyama KK, Yu YE, Shane E, Guo XE. Deterioration of trabecular plate-rod and cortical microarchitecture and reduced Bone stiffness at distal radius and tibia in postmenopausal women with vertebral fractures. Bone 2016;88: 39-46.
[224] Tsai JN, Uihlein AV, Burnett-Bowie SM, Neer RM, Derrico NP, Lee H, Bouxsein ML, Leder BZ. Effects of Two Years of Teriparatide, Denosumab, or Both on Bone Microarchitecture and Strength (DATA-HRpQCT study). J Clin Endocrinol Metab 2016;101: 2023-30.
[225] Macdonald HM, Nishiyama KK, Hanley DA, Boyd SK. Changes in trabecular and cortical bone microarchitecture at peripheral sites associated with 18 months of teriparatide therapy in postmenopausal women with osteoporosis. Osteoporos Int 2011;22: 357-362.
[226] Liu XS, Shane E, McMahon DJ, Guo XE. Individual trabecula segmentation (ITS)-based morphological analysis of microscale images of human tibial trabecular bone at limited spatial resolution. J Bone Miner Res 2011;26: 2184-93.
[227] Diederichs G, Link TM, Kentenich M, Schwieger K, Huber MB, Burghardt AJ, Majumdar S, Rogalla P, Issever AS. Assessment of trabecular bone structure of the calcaneus using multi-detector CT: correlation with microCT and biomechanical testing. Bone 2009;44: 976-983.
[228] Eckstein F, Matsuura M, Kuhn V, Priemel M, Müller R, Link TM, Lochmuller EM. Sex differences of human trabecular bone microstructure in aging are site-dependent. J Bone Miner Res 2007;22: 817-824.
[229] Seeram E. Computed tomography: physical principles, clinical applications, and quality control. 4th Edition ed; 2015.

[230] Ghasem-Zadeh A, Burghardt A, Wang XF, Iuliano S, Bonaretti S, Bui M, Zebaze R, Seeman E. Quantifying sex, race, and age specific differences in bone microstructure requires measurement of anatomically equivalent regions. Bone 2017;101: 206-213.
[231] Campbell GM, Tiwari S, Grundmann F, Purcz N, Schem C, Gluer CC. Three-dimensional image registration improves the long-term precision of in vivo micro-computed tomographic measurements in anabolic and catabolic mouse models. Calcif Tissue Int 2014;94: 282-292.
[232] Stein EM, Liu XS, Nickolas TL, Cohen A, Thomas V, McMahon DJ, Zhang C, Yin PT, Cosman F, Nieves J, Guo XE, Shane E. Abnormal microarchitecture and reduced stiffness at the radius and tibia in postmenopausal women with fractures. J Bone Miner Res 2010;25: 2572-2581.
[233] Walker MD, Liu XS, Stein E, Zhou B, Bezati E, McMahon DJ, Udesky J, Liu G, Shane E, Guo XE, Bilezikian JP. Differenes in bone microstructure between postmenopausal Chinese-American and White women. J Bone Miner Res 2011;26: 1392-1398.
[234] Burt LA, Liang Z, Sajobi TT, Hanley DA, Boyd SK. Sex- and site-specific normative data curves for HR-pQCT. J Bone Miner Res 2016;31: 2041-2047.
[235] de Jong JJA, Heyer FL, Arts JJC, Poeze M, Keszei AP, Willems PC, van Rietbergen B, Geusens PP, van den Bergh JPW. Fracture repair in the distal radius in post-menopausal women: a follow-up two years post-fracture using HRpQCT. J Bone Miner Res 2016;31: 1114-1122.
[236] Bonaretti S, Majumdar S, Lang TF, Khosla S, Burghardt AJ. The comparability of HR-pQCT bone measurements is improved by scanning anatomically standardized regions. Osteoporos Int 2017;28: 2115-2128.
[237] Shanbhogue VV, Hansen S, Halekoh U, Brixen K. Use of relative vs fixed offset distance to define region of interest at the distal radius and tibia in high-resolution peripheral quantitative computed tomography. J Clin Densitom 2015;18: 217-225.
[238] Glüer CC, Blake GM, Lu Y, Blunt BA, Jergas M, Genant HK. Accurate assessment of precision errors: How to measure the reproducibility of bone densitometry techniques. Osteoporos Int 1995;5: 262-270.
[239] Baim S, Wilson CR, Lewiecki EM, Luckey MM, Downs RWJ, Lentle BC. Precision assessment and radiation safety for dual-energy x-ray absorptiometry: position paper of the Inter- national Society for Clinical Densitometry. J Clin Densitom 2005;8: 371-378.
[240] Kawalilak CE, Johnston JD, Olszynski WP, Leswick DA, Kontulainen SA. Comparison of short-term in vivo precision of bone density and microarchitecture at the distal radius and tibia between postmenopausal women and young adults. J Clin Densitom 2014;17: 510-517.
[241] Zhou B, Zhang Z, Wang J, Yu YE, Liu XS, Nishiyama KK, Rubin MR, Shane E, Bilezikian JP, Guo XE. In vivo precision of digital topological skeletonization based individual trabecula segmentation (ITS) analysis of trabecular microstructure at the distal radius and tibia by HR-pQCT. Pattern Recognit Lett 2016;76: 83-89.
[242] Leslie WD. Factors affecting short-term bone density precision assessment and the effect on patient monitoring. J Bone Miner Res 2008;23: 199-204.
[243] Glüer CC. Monitoring skeletal changes by radiological techniques. J Bone Miner Res 1999;14: 1952-1962.
[244] Macdonald HM, Nishiyama KK, Hanley DA, Boyd SK. Changes in trabecular and cortical bone microarchitecture at peripheral sites associated with 18 months of teriparatide therapy in postmenopausal women with osteoporosis. Osteoporos Int 2011;22: 357-362.
[245] Hansen S, Hauge EM, Beck Jensen JE, Brixen K. Differing effects of PTH 1-34, PTH 1-84, and zoledronic acid on bone microarchitecture and estimated strength in postmenopausal women with osteoporosis: An 18-month open-labeled observational study using HR-pQCT. J Bone Miner Res 2013;28: 736-745.
[246] Shi L, Wang D, Hung VWY, Yeung BHY, Griffith JF, Chu WCW, Heng PA, Cheng JCY, Qin L. Fast and accurate 3-D registration of HR-pQCT images. IEEE Trans Inf Technol Biomed 2010;14: 1291-1297.
[247] Shaw CN. Is 'hand preference' coded in the hominin skeleton? An in-vivo study of bilateral morphological variation. J Hum Evol 2011;61: 480-487.
[248] Ireland A, Korhonen M, Heinonen A, Suominen H, Baur C, Stevens S, Degens H, Rittweger J. Side-to-side difference in bone strength in master jumpers and sprinters. J Musculoskelet Neuronal Interact 2011;11: 298-305.

[249] Hildebrandt EM, Manske SL, Hanley DA, Boyd SK. Bilateral asymmetry of radius and tibia bone macroarchitecture and microarchitecture: a high-resolution peripheral quantitative computed tomography study. J Clin Densitom 2016;19: 250-254.
[250] Tan Ü. Relationships between hand skill and the excitability of motoneurons innervating the postural soleus muscle in human subjects. International Journal of Neuroscience 1985;26: 289-300.
[251] Graafmans WC, Bouter LM, Lips P. The influence of physical activity and fractures on ultrasound parameters in elderly people. Osteoporos Int 1998;8: 449-454.
[252] Capozza RF, Feldman S, Mortarino P, Reina PS, Schiessl H, Rittweger J, Ferretti JL, Cointry GR. Structural analysis of the human tibia by tomographic (pQCT) serial scans. J Anat 2010;216: 470-481.
[253] Liu XS, Cohen A, Shane E, Yin PT, Stein EM, Rogers H, Kokolus SL, McMahon DJ, Lappe JM, Recker RR, Lang T, Guo XE. Bone density, geometry, microstructure, and stiffness: Relationships between peripheral and central skeletal sites assessed by DXA, HR-pQCT, and cQCT in premenopausal women. J Bone Miner Res 2010;25: 2229-2238.
[254] Vico L, Zouch M, Amirouche A, Frere D, Laroche N, Koller B, Laib A, Thomas T, Alexandre C. High-resolution pQCT analysis at the distal radius and tibia discriminates patients with recent wrist and femoral neck fractures. J Bone Miner Res 2008;23: 1741-50.
[255] Amstrup AK, Jakobsen NFB, Moser E, Sikjaer T, Mosekilde L, Rejnmark L. Association between bone indices assessed by DXA, HR-pQCT and QCT scans in post-menopausal women. J Bone Miner Metab 2016;34: 638-645.
[256] Okazaki N, Burghardt AJ, Chiba K, Schafer AL, Majumdar S. Bone microstructure in men assessed by HR-pQCT: associations with risk factors and differences between men with normal, low, and osteoporosis-range areal BMD. Bone Rep 2016;5: 312-319.
[257] Nilsson M, Sundh D, Ohlsson C, Karlsson M, Mellstrom D, Lorentzon M. Exercise during growth and young adulthood is independently associated with cortical bone size and strength in old Swedish men. J Bone Miner Res 2014;29: 1795-1804.
[258] Watson SL, Weeks BK, Weis LJ, Harding AT, Horan SA, Beck BR. High-intensity resistance and impact training improves bone mineral density and physical function in postmenopausal women with osteopenia and osteoporosis: The LIFTMOR Randomized Controlled Trial. J Bone Miner Res 2017.
[259] Kamer L, Noser H, Blauth M, Lenz M, Windolf M, Popp AW. Bone mass distribution of the distal tibia in normal, osteopenic, and osteoporotic conditions: an ex vivo assessment using HR-pQCT, DXA, and computational modelling. Calcif Tissue Int 2016;99: 588-597.
[260] Sode M, Burghardt AJ, Pialat JB, Link TM, Majumdar S. Quantitative characterization of subject motion in HR-pQCT images of the distal radius and tibia. Bone 2011;48: 1291-7.
[261] de Jong JJA, Arts JJ, Meyer U, Willems PC, Geusens PP, van den Bergh JPW, van Rietbergen B. Effect of a cast on short-term reproducibility and bone parameters obtained from HR-pQCT measurements at the distal end of the radius. J Bone Joint Surg Am 2016;98: 356-362.
[262] Kawalilak CE, Johnston JD, Cooper DML, Olszynski WP, Kontulainen SA. Role of endocortical contouring methods on precision of HR-pQCT-derived cortical micro-architecture in postmenopausal women and young adults. Osteoporos Int 2015;27: 789-796.
[263] International Society for Clinical Densitometry Committee on Standards of Bone Measurement. 2015 ISCD Official Positions - Adult.
[264] Peters M, Scharmga A, de Jong J, van Tubergen A, Geusens P, Arts JJ, Loeffen D, Weijers R, van Rietbergen B, van den Bergh J. An automated algorithm for the detection of cortical interruptions on high resolution peripheral quantitative computed tomography images of finger joints. PLoS One 2017;12: e0175829.
[265] Liu XS, Sajda P, Saha PK, Wehrli FW, Bevill G, Keaveny TM, Guo XE. Complete volumetric decomposition of individual trabecular plates and rods and its morphological correlations with anisotropic elastic moduli in human trabecular bone. J Bone Miner Res 2008;23: 223-235.
[266] Liu XS, Stein EM, Zhou B, Zhang CA, Nickolas TL, Cohen A, Thomas V, McMahon DJ, Cosman F, Nieves J, Shane E, Guo XE. Individual trabecula segmentation (ITS)-based morphological analyses and microfinite element analysis of HR-pQCT images discriminate postmenopausal fragility fractures independent of DXA measurements. J Bone Miner Res 2012;27: 263-272.

[267] Hosseini HS, Maquer G, Zysset PK. uCT-based trabecular anisotropy can be reproducibly computed from HR-pQCT scans using the triangulated bone surface. Bone 2017;97: 114-120.
[268] Sode M, Burghardt AJ, Kazakia GJ, Link TM, Majumdar S. Regional variations of gender-specific and age-related differences in trabecular bone structure of the distal radius and tibia. Bone 2010;46: 1652-1660.
[269] Wong DW, Niu W, Wang Y, Zhang M. Finite element analysis of foot and ankle impact Injury: risk evaluation of calcaneus and talus fracture. PLoS One 2016;11: e0154435.
[270] Smolen C, Quenneville CE. A finite element model of the foot/ankle to evaluate injury risk in various postures. Ann Biomed Eng 2017;45: 1993-2008.

CHAPTER 9 APPENDIX

DXA quality control plots

A

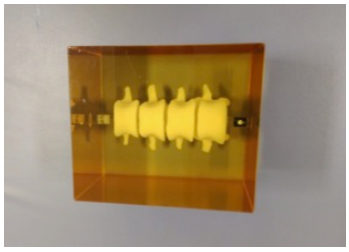

B

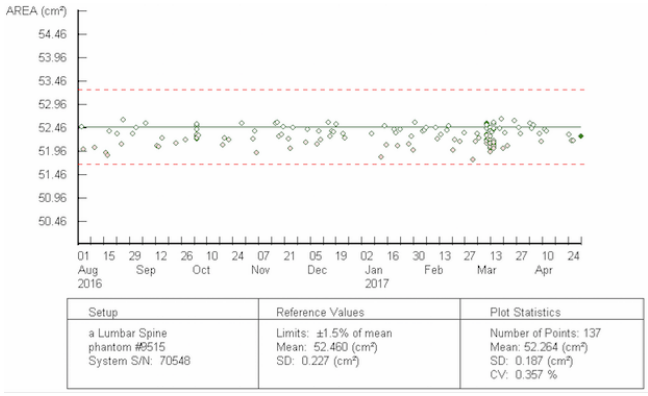

C

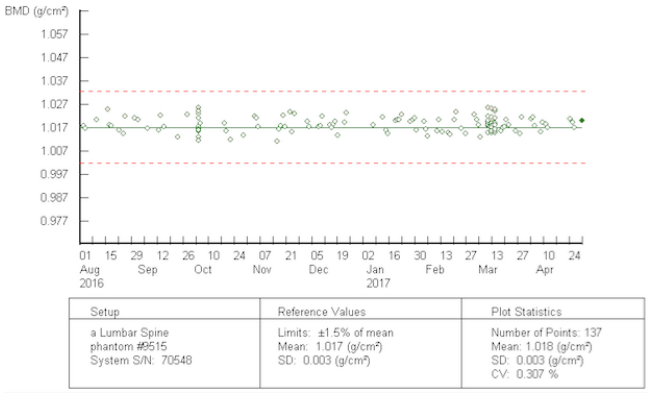

D

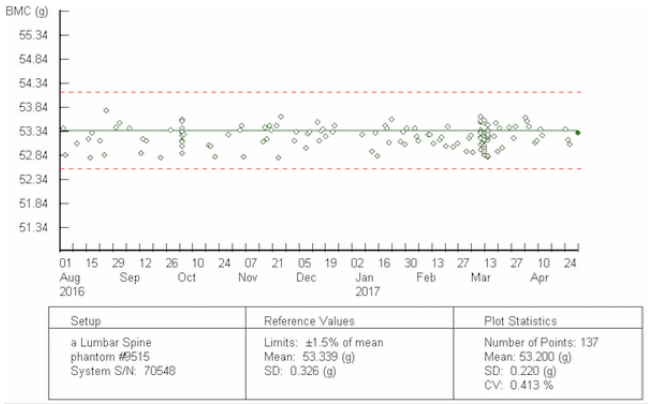

Figure 9.1: Quality control plots for the DXA outcomes

A − Anthropomorphic spine phantom; B − Bone area; C − areal BMD; D − Bone mineral content.

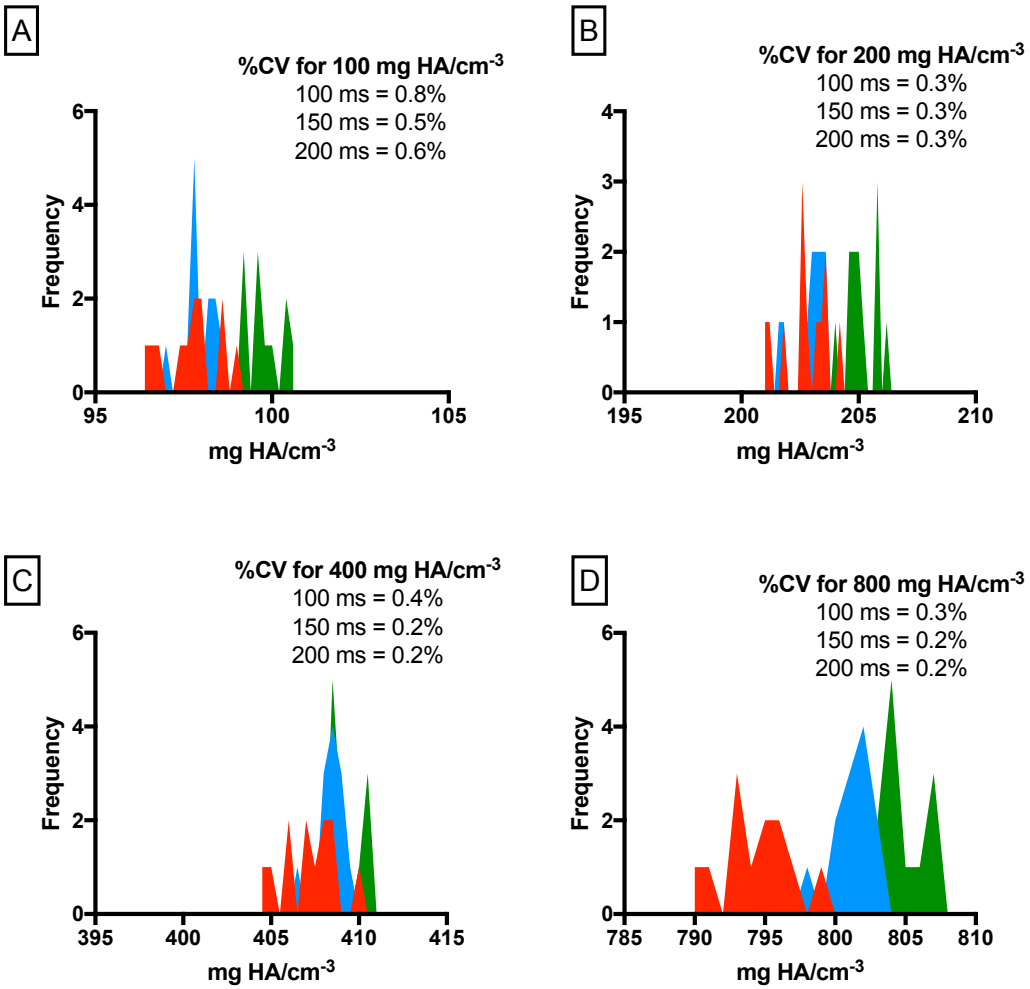

Figure 9.2. HR-pQCT density phantom imaged and quantified at 3 different scan integration times (100, 150 and 200 ms).

A – 100 mg HA/cm^{-3}; B – 200 mg HA/cm^{-3}; C – 400 mg HA/cm^{-3}; D – 800 mg HA/cm^{-3}.
Legend: 100 ms – Red; 150 ms – Blue; 200 ms – Green.

Rigid image registration code

3D registration of two HR-pQCT images

```
! read in the AIM files for the HR-pQCT scan 1 (AIM1) and scan 2 (AIM2).

/read
  -name                 dk0:[microct.data. 0000XXXX.0000XXXX]c000XXXX.aim
  -filename             AIM1

/read
  -name                 dk0:[microct.data. 0000XXXX.0000XXXX]c000XXXX.aim
  -filename             AIM2

! register HR-pQCT scan 1 and 2
/iplreg
/register
  -in1                  AIM1
  -gobj_filename_in1    none
  -in2                  AIM2
  -gobj_filename_in2    none
  -Tmat_file_name       Tmat.DAT
  -orientation_search   0
  -initial_rotation     0.000 0.000 0.000
  -initial_translation  0.000 0.000 0.000
  -delta_rotation       0.100 0.100 0.500
  -delta_translation    0.100 0.100 0.500
  -resolution_scaling   10 4 1
  -delta_scaling        1.000 0.100 0.100
  -tolerance            0.000010
  -min_corr_coef        0.500000
  -min_method           1
  -object_func          1
  -max_nr_iter          1000
  -output_option        1

! transform the common region of the GOBJ from scan 2 to scan 1.

/gobj_to_aim
  -gobj_filename        dk0:[microct.data. 0000XXXX.0000XXXX]c000XXXX.gobj
  -output               GOBJ1
  -peel_iter            0

/gobj_to_aim
  -gobj_filename        dk0:[microct.data. 0000XXXX.0000XXXX]c000XXXX.gobj
  -output               GOBJ2
  -peel_iter            0

/transform
  -in                   GOBJ2
  -out                  OUT1
  -Tmat_file_name       Tmat.DAT
  -img_interpol_option  1
  -el_size_mm_out       -1.000 -1.000 -1.000
  -Tmat_invert          false
```

```
/set_value
  -input                 GOBJ1
  -value_object            10
  -value_background         0

/set_value
  -input                 OUT1
  -value_object            20
  -value_background         0

/add_aims
  -input1                 GOBJ1
  -input2                 OUT1
  -output                 COMB1

/threshold
  -input                 COMB1
  -output                 OVERLAYED_GOBJ1
  -lower_in_perm_aut_al      25
  -upper_in_perm_aut_al      100000.000000
  -value_in_range           127
  -unit                  5

/togobj_from_aim
  -input                 OVERLAYED_GOBJ1
  -gobj_filename
dk0:[microct.data.0000XXXX.0000XXXX]COMMON_FOLLOWUP.GOBJ
  -min_elements             0
  -max_elements             0
  -curvature_smooth         1

! Inverse transform the common region of the GOBJ from scan 1 to scan 2.

/transform
  -in                    GOBJ1
  -out                   OUT2
  -Tmat_file_name          Tmat.DAT
  -img_interpol_option      1
  -el_size_mm_out          -1.000 -1.000 -1.000
  -Tmat_invert             true

/set_value
  -input                 OUT2
  -value_object            20
  -value_background         0

/set_value
  -input                 GOBJ2
  -value_object            10
  -value_background         0

/add_aims
  -input1                 GOBJ2
  -input2                 OUT2
```

```
  -output                 COMB2

/threshold
  -input                  COMB2
  -output                 OVERLAYED_BASELINE_GOBJ
  -lower_in_perm_aut_al      15.000000
  -upper_in_perm_aut_al      100000.000000
  -value_in_range          127
  -unit                  5

/togobj_from_aim
  -input                  OVERLAYED_BASELINE_GOBJ
  -gobj_filename
dk0:[microct.data.0000XXXX.0000XXXX]COMMON_BASELINE.GOBJ
  -min_elements            0
  -max_elements            0
  -curvature_smooth        1
```

3D registration of three HR-pQCT images

! read in the AIM files for the HR-pQCT scan 1 (AIM1), scan 2 (AIM2) and scan 3 (AIM3).

```
/read
  -name                   dk0:[microct.data. 0000XXXX.0000XXXX]c000XXXX.aim
  -filename               AIM1

/read
  -name                   dk0:[microct.data. 0000XXXX.0000XXXX]c000XXXX.aim
  -filename               AIM2

/read
  -name                   dk0:[microct.data. 0000XXXX.0000XXXX]c000XXXX.aim
  -filename               AIM3
```

! register HR-pQCT scan 1 and scan 2.

```
/register
  -in1                    AIM1
  -gobj_filename_in1      none
  -in2                    AIM2
  -gobj_filename_in2      none
  -Tmat_file_name         Tmat1.DAT
  -orientation_search     0
  -initial_rotation       0.000 0.000 0.000
  -initial_translation    0.000 0.000 0.000
  -delta_rotation         0.100 0.100 0.500
  -delta_translation      0.100 0.100 0.500
  -resolution_scaling     10 4 1
  -delta_scaling          1.000 0.100 0.100
  -tolerance              0.000010
  -min_corr_coef          0.500000
  -min_method             1
```

```
  -object_func              1
  -max_nr_iter              1000
  -output_option            1

! register HR-pQCT scan 1 and 3.

/register
  -in1                    AIM1
  -gobj_filename_in1        none
  -in2                    AIM3
  -gobj_filename_in2        none
  -Tmat_file_name           Tmat2.DAT
  -orientation_search       0
  -initial_rotation         0.000 0.000 0.000
  -initial_translation      0.000 0.000 0.000
  -delta_rotation           0.100 0.100 0.500
  -delta_translation        0.100 0.100 0.500
  -resolution_scaling       10 4 1
  -delta_scaling            1.000 0.100 0.100
  -tolerance                0.000010
  -min_corr_coef            0.500000
  -min_method               1
  -object_func              1
  -max_nr_iter              1000
  -output_option            1

! identify the common region between three HRpQCT scans.

/gobj_to_aim
  -gobj_filename            gobj1_file
  -output                 GOBJ1
  -peel_iter                0

/gobj_to_aim
  -gobj_filename            gobj2_file
  -output                 GOBJ2
  -peel_iter                0

/gobj_to_aim
  -gobj_filename            gobj3_file
  -output                 GOBJ3
  -peel_iter                0

/transform
  -in                     GOBJ2
  -out                    GOBJ2_transformed
  -Tmat_file_name           Tmat1.DAT
  -img_interpol_option      1
  -el_size_mm_out           -1.000 -1.000 -1.000
  -Tmat_invert              false

/set_value
  -input                  GOBJ1
  -value_object             10
  -value_background         0
```

```
/set_value
  -input                GOBJ2_transformed
  -value_object           20
  -value_background        0

/add_aims
  -input1               GOBJ1
  -input2               GOBJ2_transformed
  -output               COMB1

/threshold
  -input                COMB1
  -output               COMB1_seg
  -lower_in_perm_aut_al     25.000000
  -upper_in_perm_aut_al     100000.000000
  -value_in_range          127
  -unit                 5

/transform
  -in                   GOBJ3
  -out                  GOBJ3_transformed
  -Tmat_file_name          Tmat2.DAT
  -img_interpol_option     1
  -el_size_mm_out          -1.000 -1.000 -1.000
  -Tmat_invert            false

/set_value
  -input                COMB1_seg
  -value_object           10
  -value_background        0

/set_value
  -input                GOBJ3_transformed
  -value_object           20
  -value_background        0

/add_aims
  -input1               COMB1_seg
  -input2               GOBJ3_transformed
  -output               COMB2_seg

/threshold
  -input                COMB2_seg
  -output               COMMONREGION_allgobjs
  -lower_in_perm_aut_al     25.000000
  -upper_in_perm_aut_al     100000.000000
  -value_in_range          127
  -unit                 5

! Transform and copy the common region to the scan directories (Scan 1, Scan 2
and Scan 3).

/togobj_from_aim
  -input                COMMONREGION_allgobjs
```

```
  -gobj_filename
dk0:[microct.data.0000XXXX.0000XXXX]commonregion_scan1.gobj
  -min_elements             0
  -max_elements             0
  -curvature_smooth         1

/transform
  -in                    COMMONREGION_allgobjs
  -out                    commonregion_allgobj2
  -Tmat_file_name           "Tmat1.DAT"
  -img_interpol_option      1
  -el_size_mm_out           -1.000 -1.000 -1.000
  -Tmat_invert             true

/togobj_from_aim
  -input                  commonregion_gobj2
  -gobj_filename
dk0:[microct.data.0000XXXX.0000XXXX]commonregion_scan2.gobj
  -min_elements             0
  -max_elements             0
  -curvature_smooth         1

/transform
  -in                    COMMONREGION_allgobjs
  -out                    commonregion_gobj3
  -Tmat_file_name           Tmat2.DAT
  -img_interpol_option      1
  -el_size_mm_out           -1.000 -1.000 -1.000
  -Tmat_invert             true

/togobj_from_aim
  -input                  commonregion_gobj3
  -gobj_filename
dk0:[microct.data.0000XXXX.0000XXXX]commonregion_scan3.gobj
  -min_elements             0
  -max_elements             0
  -curvature_smooth         1
```

Chapter 4

A

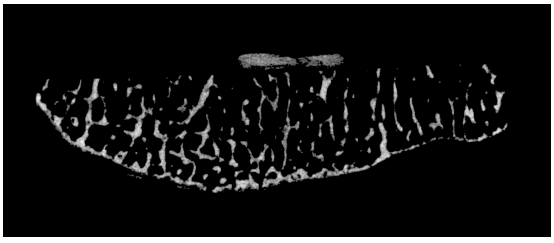

B

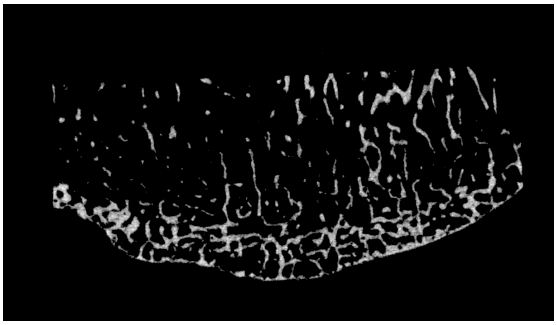

C

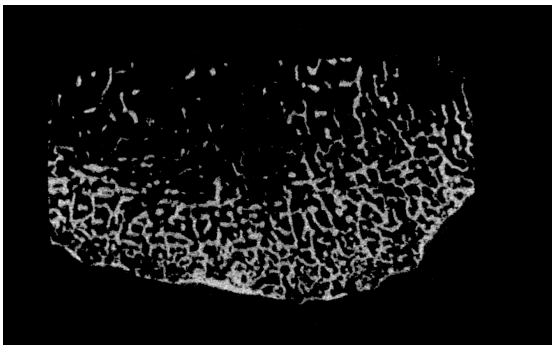

Figure 9.3. Micro-CT images (isotropic 17.4 µm voxel size) of the posterior portions from one human cadaveric calcaneus.

These samples were taken from the region that the Achilles tendon attaches to the calcaneus: A − superior slice; B – Middle slice; C – inferior slice.
Note the thin cortex in comparison to the trabeculae.

Table 9.1. Passing-Bablok analysis for the HR-pQCT vs. Micro-CT trabecular measurement across all regions.

Sample	r	Intercept (95% CI)	Slope (95% CI)	P value
Bone volume/total volume[d] (1)				
IS200	0.98	0.0494 (0.0454, 0.0531)	1.0138 (0.9698, 1.0663)	0.30
IS150	0.98	0.0480 (0.0446, 0.0519)	1.0318 (0.9826, 1.0888)	0.30
IS100	0.99	0.0487 (0.0448, 0.0518)	1.0188 (0.9750, 1.0691)	0.30
EV100	0.99	0.0516 (0.0495, 0.0534)	1.0333 (1.0063, 1.0588)	0.43
Trabecular number (mm^{-1})				
IS200	0.70	0.6919 (0.5834, 0.7946)	0.4032 (0.3493, 0.4574)	0.30
IS150	0.58	0.7776 (0.6377, 0.9095)	0.3329 (0.2659, 0.3947)	0.20
IS100	0.48	0.7787 (0.5839, 0.9432)	0.2833 (0.2162, 0.3571)	0.05
EV100	0.86	0.5624 (0.4612, 0.6565)	0.5279 (0.4716, 0.5785)	0.08
Trabecular thickness[d] (mm)				
IS200	0.73	0.0935 (0.0892, 0.1002)	0.7846 (0.6556, 0.9109)	1.00
IS150	0.72	0.0958 (0.0903, 0.1011)	0.8211 (0.6812, 0.9556)	0.88
IS100	0.75	0.0979 (0.0923, 0.1024)	0.8950 (0.7559, 1.0556)	0.74
EV100	0.77	0.0945 (0.0902, 0.0994)	0.7375 (0.6317, 0.8481)	1.00
Trabecular spacing[d] (mm)				
IS200	0.69	0.2705 (0.2185, 0.3260)	0.7545 (0.6432, 0.8733)	0.08
IS150	0.59	0.2855 (0.2169, 0.3444)	0.7932 (0.6549, 0.9599)	0.20
IS100	0.51	0.2101 (0.1055, 0.2992)	1.1588 (0.9154, 1.4673)	0.05
EV100	0.87	0.2312 (0.1872, 0.2669)	0.7435 (0.6659, 0.8387)	0.08

Abbreviations: *in situ* 100ms (IS100); *in situ* 150ms (IS150); *in situ* 200ms (IS200); *ex vivo* 100ms (EV100).

All r values are statistically significant, $p<0.001$.
A P value <0.05 indicates that there is no linear relationship between the two measurements.

Table 9.2. Passing-Bablok analysis of bone volume fraction data for the different HR-pQCT conditions at the three different regions.

Sample	r	Intercept (95% CI)	Slope (95% CI)	P value
Superior region				
IS200	0.98	0.0619 (0.0558, 0.0693)	0.9101 (0.8385, 0.9852)	0.28
IS150	0.98	0.0609 (0.0547, 0.0709)	0.9271 (0.8393, 1.0045)	0.18
IS100	0.99	0.0608 (0.0555, 0.0675)	0.9187 (0.8558, 0.9903)	0.08
EV100	0.97	0.0596 (0.0551, 0.0661)	0.9771 (0.9034, 1.0235)	0.18
Middle region				
IS200	0.98	0.0527 (0.0481, 0.0559)	0.9500 (0.9051, 1.0082)	0.20
IS150	0.98	0.0520 (0.0474, 0.0552)	0.9536 (0.9081, 1.0227)	0.59
IS100	0.98	0.0517 (0.0479, 0.0551)	0.9631 (0.9209, 1.0229)	0.36
EV100	0.99	0.0519 (0.0488, 0.0532)	1.0243 (1.0000, 1.0609)	0.59
Inferior region				
IS200	0.99	0.0343 (0.0287, 0.0398)	1.1781 (1.0882, 1.2787)	0.98
IS150	0.98	0.0312 (0.0253, 0.0385)	1.2261 (1.1021, 1.3074)	0.72
IS100	0.98	0.0341 (0.0279, 0.0409)	1.1803 (1.0818, 1.3000)	0.98
EV100	0.99	0.0486 (0.0448, 0.0531)	1.0643 (0.9875, 1.1423)	0.36

Abbreviations: *in situ* 100ms (IS100); *in situ* 150ms (IS150); *in situ* 200ms (IS200); *ex vivo* 100ms (EV100).

All r values are statistically significant, $p<0.001$.
A P value <0.05 indicates that there is no linear relationship between the two measurements.

Table 9.3. Passing-Bablok analysis of trabecular number data for the different HR-pQCT conditions at the three different regions.

Sample	r	Intercept (95% CI)	Slope (95% CI)	P value
Superior region				
IS200	0.84	0.4911 (0.3281, 0.6200)	0.5410 (0.4708, 0.6267)	0.18
IS150	0.77	0.5169 (0.3286, 0.6862)	0.4956 (0.4127, 0.5916)	0.18
IS100	0.63	0.5265 (0.2421, 0.7467)	0.4379 (0.3448, 0.5577)	0.08
EV100	0.92	0.4034 (0.2724, 0.5174)	0.6119 (0.5540, 0.6857)	0.04
Middle region				
IS200	0.83	0.7553 (0.6188, 0.9122)	0.3658 (0.2942, 0.4293)	0.59
IS150	0.76	0.7946 (0.6211, 0.9601)	0.3257 (0.2425, 0.3982)	0.84
IS100	0.70	0.6586 (0.3677, 0.8668)	0.3150 (0.2408, 0.4255)	0.36
EV100	0.85	0.5816 (0.3949, 0.7360)	0.5176 (0.4268, 0.6060)	0.59
Inferior region				
IS200	0.11	1.2804 (1.1540, 1.5156)	0.0884 (-0.0350, 0.1537)	0.36
IS150	-0.16	1.3886 (1.1995, 1.6195)	0.0276 (-0.0749, 0.1124)	0.04
IS100	-0.21	1.4500 (1.2459, 1.6750)	0.0002 (-0.0831, 0.0763)	0.04
EV100	0.69	1.1028 (0.9075, 1.2473)	0.2038 (0.1208, 0.3170)	0.72

Abbreviations: *in situ* 100ms (IS100); *in situ* 150ms (IS150); *in situ* 200ms (IS200); *ex vivo* 100ms (EV100).

r values for inferior IS100, p=0.364; inferior IS150, p=0.480; inferior IS200, p=0.650. All other r values were statistically significant, p<0.001.
A P value <0.05 indicates that there is no linear relationship between the two measurements.

Table 9.4. Passing-Bablok analysis of trabecular thickness data for the different HR-pQCT conditions at the three different regions.

Sample	r	Intercept (95% CI)	Slope (95% CI)	P value
Superior region				
IS200	0.35	0.0807 (0.0656, 0.1003)	0.9861 (0.6429, 1.2703)	0.82
IS150	0.32	0.0824 (0.0658, 0.0994)	1.0118 (0.6955, 1.3667)	0.56
IS100	0.36	0.0799 (0.0527, 0.0982)	1.2333 (0.8345, 1.8429)	0.08
EV100	0.48	0.0820 (0.0621, 0.1008)	0.9270 (0.6216, 1.2750)	0.98
Middle region				
IS200	0.69	0.0962 (0.0880, 0.1054)	0.7261 (0.5100, 0.9722)	0.84
IS150	0.67	0.0977 (0.0889, 0.1061)	0.7598 (0.5412, 1.0143)	0.84
IS100	0.72	0.0982 (0.0902, 0.1062)	0.8667 (0.6261, 1.1375)	0.84
EV100	0.77	0.0945 (0.0874, 0.1019)	0.7157 (0.5400, 0.8957)	0.84
Inferior region				
IS200	0.62	0.0901 (0.0798, 0.1069)	0.9826 (0.5816, 1.3333)	0.98
IS150	0.61	0.0899 (0.0789, 0.1068)	1.1329 (0.6618, 1.5238)	0.98
IS100	0.63	0.0927 (0.0809, 0.1062)	1.3047 (0.8429, 1.8824)	0.72
EV100	0.76	0.0957 (0.0854, 0.1061)	0.8217 (0.5667, 1.1429)	0.98

Abbreviations: *in situ* 100ms (IS100); *in situ* 150ms (IS150); *in situ* 200ms (IS200); *ex vivo* 100ms (EV100).

r values for superior IS200, p=0.021; superior IS150, p=0.035; superior IS100, p=0.017; superior EV100, p=0.001; inferior IS200, p=0.003; inferior IS150, p=0.003; inferior IS100, p=0.002. All other r values were statistically significant, p<0.001.

A P value <0.05 indicates that there is no linear relationship between the two measurements.

Table 9.5. Passing-Bablok analysis of trabecular spacing data for the different HR-pQCT conditions at the three different regions.

Sample	r	Intercept (95% CI)	Slope (95% CI)	P value
Superior region				
IS200	0.82	0.1829 (0.0944, 0.2357)	0.8998 (0.7566, 1.1100)	0.56
IS150	0.75	0.1808 (0.0767, 0.2463)	0.9551 (0.7587, 1.2448)	0.82
IS100	0.64	0.1423 (-0.0055, 0.2582)	1.1688 (0.8213, 1.6750)	0.56
EV100	0.93	0.1500 (0.0889, 0.2074)	0.9257 (0.7948, 1.0627)	0.98
Middle region				
IS200	0.82	0.3186 (0.2595, 0.3761)	0.6412 (0.5324, 0.7675)	0.84
IS150	0.76	0.3059 (0.2417, 0.3847)	0.7370 (0.5683, 0.9063)	0.84
IS100	0.73	0.2092 (0.0922, 0.3075)	1.1751 (0.9012, 1.5265)	0.36
EV100	0.88	0.2434 (0.1876, 0.2843)	0.7171 (0.6297, 0.8380)	0.59
Inferior region				
IS200	-0.11	0.5594 (0.0910, 0.6543)	0.2191 (0.0300, 1.2903)	0.36
IS150	-0.25	0.5943 (0.2660, 0.6935)	0.1775 (-0.0680, 1.0571)	0.04
IS100	-0.32	0.5564 (-0.5940, 0.6497)	0.3325 (0.0550, 3.8758)	0.04
EV100	0.60	0.5592 (0.4919, 0.6237)	0.1876 (0.0746, 0.3074)	0.36

Abbreviations: *in situ* 100ms (IS100); *in situ* 150ms (IS150); *in situ* 200ms (IS200); *ex vivo* 100ms (EV100).

r values for inferior IS200, p=0.631; inferior IS150, p=0.268; inferior IS100, p=0.154; inferior EV100, p=0.004. All other r values were statistically significant, p<0.001.
A P value <0.05 indicates that there is no linear relationship between the two measurements.

Table 9.6. Passing-Bablok regression for measurements between the 100 ms and 200 ms integration time calcaneus HR-pQCT images.

	Intercept (95% CI)	Slope (95% CI)	p value
Superior			
Total vBMD, mg HA.cm^{-3}	-4.602 (-52.113, 34.500)	1.012 (0.873, 1.176)	0.699
Tb.vBMD, mg HA.cm^{-3}	-23.182 (-74.937, 5.447)	1.104 (0.983, 1.316)	0.699
Outer Tb.vBMD, mg HA.cm^{-3}	-8.118 (-29.940, 21.799)	1.038 (0.920, 1.111)	0.699
Inner Tb.vBMD, mg HA.cm^{-3} #	-22.611 (-100.807, 10.919)	1.103 (0.947, 1.477)	1.000
BV/TV^{d}, %	-0.013 (-0.059, 0.006)	1.066 (0.971, 1.296)	0.699
Tb.N*, mm^{-1}	-0.641 (-1.989, 0.110)	1.029 (0.816, 1.483)	0.927
Tb.Th^{d}, µm	-0.008 (-0.051, 0.013)	1.336 (1.000, 2.000)	1.000
Tb.Sp^{d}, µm	-0.071 (-0.199, 0.002)	1.504 (1.157, 2.000)	1.000
Inferior			
Total vBMD, mg HA.cm^{-3}	6.014 (-21.595, 20.427)	0.962 (0.898, 1.123)	0.699
Tb.vBMD, mg HA.cm^{-3}	2.714 (-15.426, 10.948)	0.985 (0.931, 1.114)	0.699
Outer Tb.vBMD, mg HA.cm^{-3}	-3.682 (-33.346, 6.478)	1.025 (0.973,1.168)	0.699
Inner Tb.vBMD, mg HA.cm^{-3} #	3.895 (-14.500, 12.241)	0.958 (0.877, 1.160)	1.000
BV/TV^{d}, %	0.001 (-0.014, 0.009)	0.994 (0.933, 1.115)	0.699
Tb.N*, mm^{-1}	-1.715 (-2.506, -0.823)	1.277 (1.031, 1.529)	0.699
Tb.Th^{d}, µm	-0.007 (-0.170, 0.022)	1.583 (0.900, 6.000)	0.699
Tb.Sp^{d}, µm	-0.252 (-0.343, -0.132)	2.317 (1.822, 2.664)	1.000

Data shown for 9 participants.
The Passing-Bablock regression was completed using XLSTAT 2017.4.45706 for Mac.

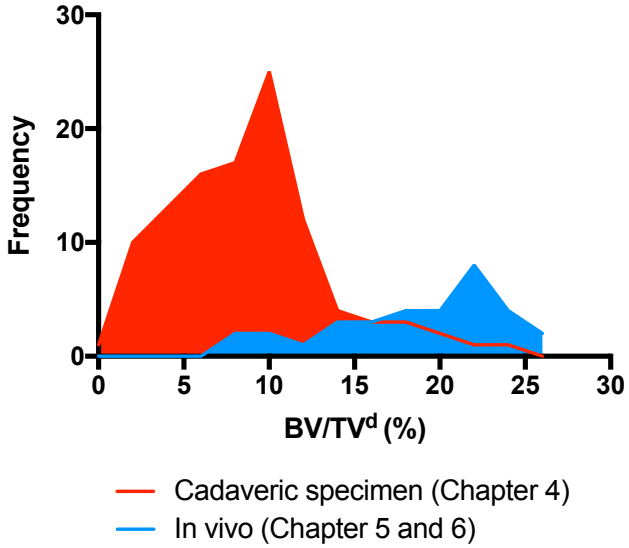

Figure 9.4. Histograms for the distribution of calcaneus BV/TV from the human cadaveric specimen and participants *in vivo*.

Cadaveric specimen (red) – BV/TV from 108 samples from 10 cadavers, located at the superior, middle and inferior regions of the bone.
In vivo (blue) – BV/TV from the superior and inferior regions from 9 participants in Chapter 5, and BV/TV from the superior region of the calcaneus from 15 participants in Chapter 6.

Copyright permissions

Table 9.7. Copyright permissions for the thesis.

Figure	
1.1	Image used with permission from Springer: Pahr, D. H. and Zysset, P. K. Finite Element-Based Mechanical Assessment of Bone Quality on the Basis of *In vivo* Images. Current Osteoporosis Reports (2016), 14(6), 374-385. Page 375, Figure 1.
1.4	Image used with permission from Springer: Cole, J. H. and van der Meulen, M. C. H. Whole bone mechanics and bone quality. Clinical Orthopaedics and Related Research (2011), 468(8), 2139-2149. Page 2140, Figure 1A-B.
1.5	Image used with permission from Elsevier: Curtis, E. M., van der Velde, R., Moon, R. J., van den Bergh, J. P., Geusens, P., de Vries, F., van Staa, T. P., Cooper, C. and Harvey, N. C. Epidemiology of fractures in the United Kingdom 1988–2012: Variation with age, sex, geography, ethnicity and socioeconomic status. Bone (2016), 87, 19-26. Page 23, Figure 2.
1.6B	Image used with permission from Elsevier: Zebaze, R.M.D., Ghasem-Zadeh, A., Bohte, A., Iuliano-Burns, S., Mirams, M., Price, R.I., Mackie, E.J. and Seeman, E. Intracortical remodelling and porosity in the distal radius and post-mortem femurs of women: a cross-sectional study. The Lancet (2010), 375(9727), 1729-1736. Page 1733, Figure 4.
1.8	Image used with permission from Springer: von Meyer, G. H. The Classic: The Architecture of the Trabecular Bone (Tenth Contribution on the Mechanics of the Human Skeletal Framework). Clinical Orthopaedics and Related Research (2011), 469(11), 1-6. Page 2, Plate XVIII Original plate XVIII which includes Figure 1–9.
2.1B	Image used with permission from Springer: Bone Densitometry for Technologists (Second Edition), Sydney Lou Bonnick and Lori Ann Lewis, Densitometry Techniques. Page 50, Figure 2-10.
2.7A	Image used with permission from Springer, Burghardt, A. J., Kazakia, G. J., Laib, A. & Majumdar, S. Quantitative assessment of bone tissue mineralization with polychromatic micro-computed tomography. Calcified Tissue International (2008), 83(2), 129-38. Page 131, Figure 1a.
2.7B	Image used with permission from The Radiological Society of North America (RNSA®), Barrett J F, Kean N. Artifacts in CT: Recognition and avoidance. RadioGraphics 2004; 24: 1679-1691, Figures 3a and 3b.
2.11	Image used with permission from Stauber M. & Muller R. Micro-Computed Tomography: A Method for the Non-Destructive Evaluation of the Three-Dimensional Structure of Biological Specimens. Methods in Molecular Biology 2008, 455, 273-292.
2.13	This research was originally published in JNM. Soret M, Bacharach SL, Buvat I. Partial-volume effect in PET tumor imaging. J Nucl Med.

	2008;48(6):932-45. © by the Society of Nuclear Medicine and Molecular Imaging, Inc.
2.20	2003 IEEE. Reprinted, with permission, from Pluim, J.P.W., Maintz, J.B.A., Viergever, M.A. Mutual information based registration of medical images: a survey, ICC Transactions on Medical Imaging, July 2003.